



Review Article

# Enhancing Transparency and Reproducibility in Finite Element Analysis through Comprehensive Reporting Parameters: A Review

Aun Haider<sup>1a</sup>

<sup>1</sup> Institute of Aeronautics and Avionics, Air University, Islamabad, Pakistan

aunbhutta@gmail.com

DOI : 10.31202/ecjse.1436203

Received: 13.02.2024 Accepted: 24.04.2024

**How to cite this article:**

Aun Haider, " Enhancing Transparency and Reproducibility in Finite Element Analysis through Comprehensive Reporting Parameters: A Review", El-Cezeri Journal of Science and Engineering, Vol: 11, Iss:3, (2024), pp.(212-222).

ORCID: "0009-0000-5279-2829

**Abstract :** This paper highlights the importance of thorough documentation in Finite Element Analysis (FEA) studies to ensure transparency and reproducibility of results. It points out the lack of standardized guidelines for reporting and communication in FEA, which can lead to confusion and hinder evaluation. The paper aims to address this gap by proposing key reporting parameters covering various aspects of FEA studies such as analysis description, model identification, solver settings, and validation techniques. It emphasizes the significance of sensitivity analysis, verification, and validation for establishing the reliability of FEA models. The abstract concludes by advocating for the sharing of FEA models to promote scrutiny and improvement, using a case study to demonstrate how the proposed reporting parameters can enhance the quality and credibility of simulation studies. Additionally, it suggests that as modeling techniques evolve, the reporting parameters should also adapt accordingly, incorporating any supplementary factors that affect the accuracy of FEA models.

**Keywords :** Finite Elements Analysis, Meshing, Pre-processing, Post Processing, Reporting Parameters, Solver Setting, Sensitivity Analysis, Validation, Verification

## 1 Introduction

In the past few decades, Finite Element Analysis (FEA) has played a pivotal role in structural analysis, offering researchers and engineers invaluable insights into structural responses under varying environmental conditions [1]. The continuous evolution of FE codes has significantly enhanced our ability to comprehend complex structural behaviors.

FEA, as a numerical technique, provides an approximate solution to partial differential equations [2]. The process involves discretizing the problem domain to create a mesh model, with elements connecting at nodes. Equations are then solved at these nodes, and discrete nodal values are interpolated across the domain to generate field values. Standard FEA procedure encompasses geometry development, assignment of material properties, mesh discretization, and application of boundary conditions and loads, culminating in the computation of desired results [3].

It is important to note that, strictly speaking, all FE models are inherently imperfect, yet they remain useful tools for representing physical phenomena [4]. The accuracy of these results hinges on effective error control within the FEA process. Modeling errors may arise from assumptions regarding geometry, material models, loads, and boundary conditions, while inadequacies in the mesh can lead to discretization errors. Additionally, numerical schemes themselves may introduce errors [5]. Assessment of errors arising from inherent idealizations during Finite Element Analysis (FEA) necessitates meticulous documentation, serving as a cornerstone for establishing confidence in the accuracy and reliability of FE results [6]. Detailed documentation not only ensures repeatability and reproducibility of FE results but also underscores the importance of investing in both model improvement and comprehensive documentation [7].

## 2 Literature Review

The availability of extensive guidelines on model development, verification, and validation from organizations such as the American Society of Mechanical Engineers (ASME) and the National Agency for Finite Element Methods and Standards (NAFEMS) has significantly contributed to the advancement of Finite Element Analysis (FEA) in various engineering fields [8]. However, a notable gap exists in these standards, as they do not explicitly address critical aspects of reporting and communication of FE studies, resulting in a discrepancy between the widespread application of this tool and the quality of reports [9].

In FEA, intricacies of model definition and development are intrinsically linked with analysis settings and capabilities of FE code [10]. A diverse array of simulation software packages available for structural analysis, each with distinct pre-, solution,

and post-processing algorithms, further complicates matters. Differences in syntax among these FE codes, if not adequately addressed in FE reports, can impede the reproducibility of results across different software platforms [7].

The lack of a standardized documentation basis contributes to a perceived lack of transparency in reported FE studies, hindering the essential processes of verification, validation, and accreditation. Additionally, a prevailing issue is FE analysts' potential unawareness of the limitations inherent in the chosen model and simulation platform, leaving reviewers and users uninformed [11].

Upon reviewing published FE results, it becomes evident that while some simulation parameters are generally reported, the information provided may be insufficient for result reproduction due to a lack of detail about the simulation environment [12]. This study aims not to prescribe best practices in FEA but to introduce reporting parameters that comprehensively assess the overall quality and scientific rigor of simulation studies. By presenting comprehensive information about the simulation environment, solution verification and validation (V & V), and model availability, this paper illustrates these guiding principles [13].

A review of published FE results reveals that few simulation parameters like type of analysis, selection of finite elements, boundary conditions, loads, etc. have generally been reported [14]. In some cases, authors have only indicated the conformance of models with standard modeling practices without commenting on the variability or sensitivity of results. At best, the reported set of parameters has traditionally been minimal to fulfill publication criteria. Unfortunately, sometimes published FE results cannot be reproduced due to insufficient information about the simulation environment [15]. The guidelines presented herein serve as a valuable resource for journal editors and reviewers in the evaluation of manuscripts, helping to identify potential knowledge gaps between theoretical concepts and practical applications of FEA.

While intended for engineers and scientists in academia, industry, and government agencies involved in the preparation, dissemination, and evaluation of simulation studies, readers need to acknowledge that not all considerations may be reported in every FEA study [16]. While justifications for omitted steps must be documented, adherence to these guidelines enhances confidence in disseminating FE results. Nevertheless, these guidelines do not exclude the incorporation of additional details driven by the fidelity of the simulation model.

### **3 Reporting Parameters**

#### **3.1 Analysis Description**

The preamble of a reporting document ideally should offer a comprehensive description of the FE study under consideration.

#### **3.2 Study Objective**

FEA report should elaborate on a research question that the study seeks to answer. In cases where the primary objective is the structural qualification of a component, as opposed to exploring design spaces, it is advisable to include acceptance criteria as part of the report [17].

#### **3.3 Motivation**

The motivation for employing Finite Element Analysis (FEA) should be clearly stated, emphasizing its advantages in comparison to the capabilities or limitations of existing analytical, empirical, or experimental methods.

#### **3.4 Scope**

The report should provide a detailed scope, outlining how FEA of the problem domain will be conducted to generate solution space. This includes a clear description of the methodology, modeling approach, and key steps involved in the FEA process.

#### **3.5 Mathematical Model**

It is advisable to elaborate on the constitutive representation of field variables, presenting a mathematical relationship between required inputs and desired outputs within the FEA framework [18].

#### **3.6 Type**

The type of analysis conducted, whether it be static, dynamic, modal, buckling, thermal analysis, or any other specific type, should be identified in the report.

#### **3.7 Time Scale**

Specify the simulation's time scale in the report to discern the nature of the response, distinguishing between steady-state and transient responses.

### 3.8 System of Units

System of units for FE simulation, such as SI System, British Engineering System, MKS System, etc., should be explicitly stated. It is worth noting that certain Finite Element (FE) codes may not adhere to any specific unit system [11], placing responsibility for unit consistency squarely on the analyst in such cases.

### 3.9 Analysis Hardware and Software

Reporting solution time with the used computer system is essential for providing an assessment of computation costs [19]. Therefore, hardware and software employed for Finite Element Analysis (FEA) should be thoroughly documented. While in-house proprietary codes may be utilized, FEA is generally conducted using commercial software packages encompassing geometry modelers, pre-processors, solvers, and post-processors. Although vendors typically offer sufficient documentation on code verification, it is crucial to include comments on the suitability of these software packages for the intended analysis. Despite claims of upward and downward compatibility by code developers among various versions, it is advisable to report specific software versions used [20].

### 3.10 Related Publications

If there is published work on similar analyses, it is recommended to refer to these publications, as they provide a valuable basis for the verification and validation (V & V) of the current analysis [21].

### 3.11 Highlight

A detailed exposition of the analysis's distinctive features, emphasizing any innovative elements that differentiate it from existing approaches, will augment the overall value of the FEA report.

## 4 Model Identification

### 4.1 Model Name

Assigning an illustrative name to the FE model, differentiating it from similar models, is recommended. Furthermore, enhancing the model's discoverability in research repositories can be achieved by incorporating relevant keywords into its description.

### 4.2 Version

During most investigations, the FE model typically undergoes refinements upon the initial receipt of results, ultimately leading to the adoption of a refined or improved model for reporting FE outcomes. If the developmental history of the model has the potential to contribute valuable insights to the existing knowledge bank, it is advisable to incorporate this information in the report.

### 4.3 Region of Interest

During structural design, identifying areas or regions of interest in the model is essential. Typically, geometric or material transitions, supports, load application regions and fastening mechanisms are major concerns that warrant careful attention.

### 4.4 Related Models

When related models exist, it's important to present the strengths and limitations of these complementing or competing models to adequately justify the employed model.

### 4.5 Utility

Delineating the primary (or secondary, if any) utility of the model in relevant engineering domains is essential.

### 4.6 Case Study

The aircraft wing comprises structural members such as ribs, spars, stringers, and skin [22]. It is designed to accommodate external stores at designated stations. Figure 1 depicts the internal structural members of the aircraft wing. The analysis of the wing rib located at wing stations 2 and 6 is necessary to determine the maximum stress under applied aerodynamic and inertial loads within the flight envelope of the aircraft.

The aircraft wing, being a statically indeterminate structure, exhibits support reactions on the rib (local model) isolated from the wing (global model) that depend on the stiffness of the attached structure. Analytical or empirical analyses of the rib isolated from the wing do not fully account for the stiffness of the global model [23]. Experimental analyses based on strain gauge techniques can provide accurate point values, but interpolating these values is necessary to generate field values for the wing rib. Moreover, the cost and safety implications of conducting actual ground or flight tests can be prohibitive. Therefore, Finite Element (FE) analysis of the wing rib under design load emerges as the most suitable method.

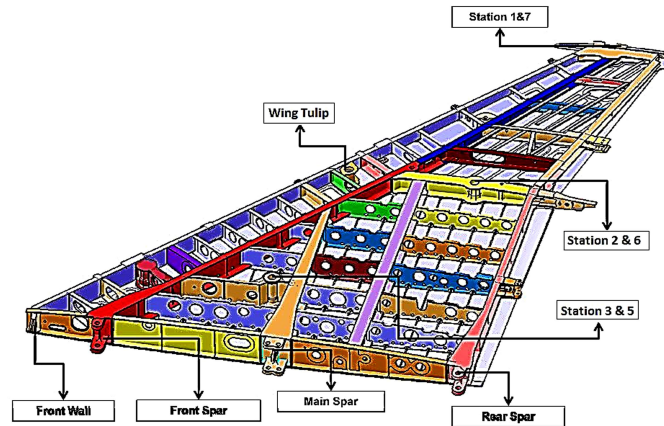


**Figure 1: Wing Internal Structure**

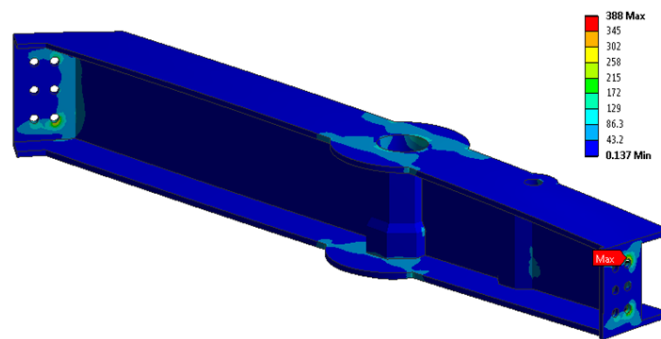


**Figure 2: Wing Rib with Fixed Support**

The CAD model of the wing rib is developed in Ansys Design Modeler® from manufacturing drawings. Appropriate material properties given in aircraft technical publications are assigned to the model. The stiffness of the attached wing structure is represented by elastic support boundary conditions applied at attachment bolt holes. Static structural analysis of the wing rib is carried out at design load.

Analysis of structural members isolated from the global model is generally carried out with fixed support as a boundary condition [24]. This is a conservative approximation that under predicts the performance of local models. As an aircraft wing is a statically indeterminate structure, reaction forces and moments at supports (constraints) depend upon the stiffness characteristics of the wing itself. This necessitates that the stiffness of the global wing model must be represented in a solution of the local rib model.

The application of elastic support introduces a finite stiffness of the global model in a solution of the isolated local model. Elastic support is the most appropriate boundary condition for FE analysis of local models. With elastic supports, it is predicted that the value of maximum stress will be reduced. Therefore, the maximum load-carrying capacity of the wing station can be predicted accurately.

Region of interest are bolt holes used for attachment of rib with wing structure. The SI system of units is used for analysis. FE analysis is performed in Ansys ® Software version 14.5 installed on a workstation with a core i7 Intel processor and 16 GB RAM.

A similar FE study of the same wing rib with fixed support boundary conditions under design load is available [25]. Application of fixed support as a boundary condition for FE analysis of structural members isolated from the global model implies infinite stiffness of the global model. Therefore, it underestimates the maximum load-carrying capacity of the wing rib. Figure 2 presents a stress contour plot for the wing rib under design load with fixed support as boundary conditions. The maximum stress observed is 388 MPa at the bolt hole.

## 5 Model Structure

### 5.1 Coordinate Systems

Defining both global and local coordinate systems in the report is imperative. Without clear definitions, the accurate application of environmental conditions may be compromised, potentially leading to misinterpretation of subsequent results.

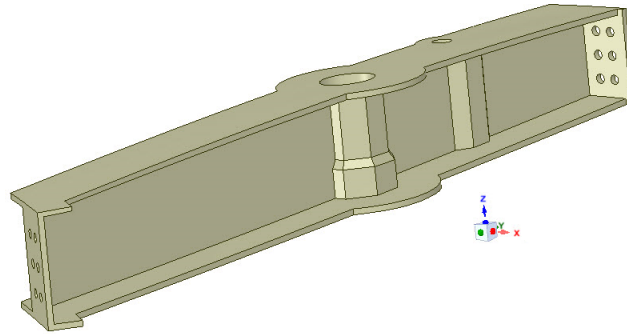


**Figure 3: CAD Model of Wing Rib**

## 5.2 Geometry

Dimensional details in the form of diagrams or sketches can also be included. The present trend is to use computer-aided design (CAD) software like CATIA®<sup>®</sup>, SolidWorks®<sup>®</sup>, AutoCAD®<sup>®</sup>, etc. to develop models. The CAD model then forms a template for downstream FE modeling after its translation from the CAD environment to FE software. In FE software, geometry preparation involves cleaning, simplification, decimation, and symmetric exploitation. Therefore, these preceding steps may also be covered to establish the reproducibility and fidelity of the model.

## 5.3 Material Properties

Relevant material properties such as Modulus of Elasticity, Poisson Ratio, Shear Modulus, etc., should be thoroughly reported. Many Finite Element (FE) codes now include an extensive library of material models, which can be referenced in the report when utilized for analysis.

## 5.4 Environmental Conditions

Environmental conditions for the FE model consist of imposed boundary conditions and applied loads. It is crucial to report necessary details, including magnitude, time history, direction, and application region of these conditions. Furthermore, explaining their physical interpretation and corroborating them with reality is essential to avoid misinterpretation resulting from differences in syntax among various FE codes [26].

In many cases, applied boundary conditions serve as modest representative approximations. A set of boundary conditions offers a range for variation in Finite Element (FE) results. Such scenarios necessitate a comprehensive consideration of boundary condition selection alongside the predicted variation in results [27]. However, there are instances where a specific FE code does not permit the direct application of certain environmental conditions. For example, in cases where torque cannot be directly applied, an equivalent force multiplied by the moment arm is applied through a rigid connection. The FE report must include such workarounds [3].

Finite Element Analysis (FEA) of a mechanical assembly, comprising various interacting components, is indeed relatively intricate. Interactions between these components are typically idealized; for instance, fasteners may be replaced with 1D beam elements, while mating surfaces are often fixed or replaced with frictional contact [28]. It is crucial to document a comprehensive list of interacting components, specifying the type of interaction (e.g., gap, friction, no separation, no penetration) and the attributes of interaction (such as friction coefficient, stiffness, etc.) [29].

## 5.5 Model Calibration

In determining certain simulation parameters, heuristics can be employed in addition to actual experimentation [30]. Therefore, validating these assumptions becomes necessary, and this is achieved by comparing the output from the simulation model with the actual experimental output. Based on the correlation or deviation between these two outputs, the model is calibrated to generate pseudo-true values. If model calibration has been employed, it should be reported for result interpretation.

## 5.6 Case Study

The model of the wing rib is developed in a native CAD environment called Ansys Design Modeler®<sup>®</sup>. Development of CAD model in Design Modeler eliminates translation errors during import of model from CAD to FE environment. Figure 3 presents a CAD model of the wing rib. The linear elastic isotropic material model is used for analysis. Wing rib is assigned material properties of Aluminum Alloy 7050-T7 Yield strength=427 MPa, Modulus of Elasticity=70 GPa and Poisson Ratio=0.33.

Imposed boundary conditions and applied loads are shown in Figure 4. Global coordinates and length scale are presented for visualization. Elastic support represents the stiffness of the attached wing structure. Bolt holes are given free displacement with

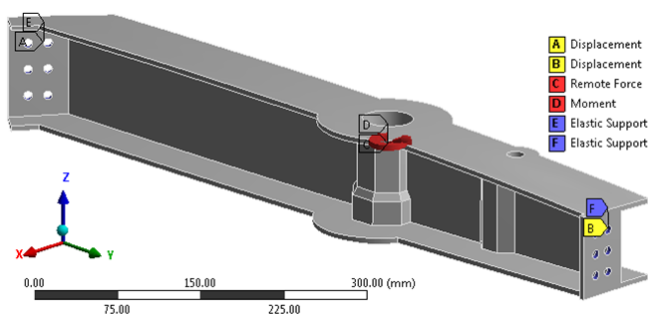


**Figure 4: Loads and Boundary Conditions**

**Table 1: Applied Loads.**

Force Component	Magnitude (kN)	Moment Component	Magnitude (kN.m)
Fx	-3.86	Mx	87.1
Fy	6.9	My	5880
Fz	2.43	Mz	-27.9

linear and rotational stiffness of 99 KN/m and 50 KN.m/rad respectively. Aerodynamic and inertial loads acting on the wing rib are applied as force (8.27 KN) and moment (5881 KN.m) at the spindle of the wing rib. Table 1 presents the components of applied force and moment.

**6 Discretization Scheme**

Mesh characteristics have a direct impact on the accuracy of results [31]. Therefore, it is imperative to report the discretization scheme to assess its adequacy.

**6.1 Element Name**

Names of finite elements used for meshing should be provided, for example, CQUAD4, etc.

**6.2 Element Attributes**

Attributes of finite elements dictate their capability or limitation to capture physical phenomena [32] and should be reported. For example, specifying the type of elements used, such as 1D line (Beam) elements or 2D shell (Triangular or quadrilateral) elements, is essential. Additionally, reporting the number of nodes, shape function, and total degrees of freedom (DOFs) per node is crucial for transparency and accuracy.

**6.3 Mesh density**

In the FE report, it is important to include details about total degrees of freedom (DOFs), nodes, and elements of the mesh, along with illustrations highlighting mesh pattern (e.g., free or mapped) and density (coarse or fine). Variations in mesh density, which may be adjusted to capture stress gradients and geometric discontinuities [33], should be reported. Additionally, the suitability of local and global mesh densities for the current analysis should be discussed.

**6.4 Mesh Convergence**

Finite Element Analysis is performed with progressively finer mesh until an appropriate mesh density is identified, which results in no significant change (less than 5% ) in the primary FE output [34]. Once this mesh density is determined, the solution is considered independent of mesh, and this mesh is later used for all subsequent analyses. A mesh convergence study should be reported to establish the independence of FE results from mesh density. The maximum equivalent stress is typically used as an appropriate FE output for mesh convergence study. If a secondary output is used for this purpose, the relationship between the primary and secondary outputs should be reported. Additionally, the difference between averaged and un-averaged stress values, typically less than 3 % [35], serves as a good indicator of mesh convergence and may also be reported.

**6.5 Mesh Quality**

Mesh quality can be evaluated and presented in the FE report [36] using various mesh metrics such as Element Quality, Aspect Ratio, Skewness, Jacobian, Warping Factor, Maximum corner angle, etc. Additionally, various criteria in terms of average values and allowable percentage of bad elements have been developed to assess mesh quality. Locations of bad elements which have failed assessment criteria should also be reported. It is important to note that a few ill-shaped elements in critical regions of the model can significantly affect the accuracy of results [37]

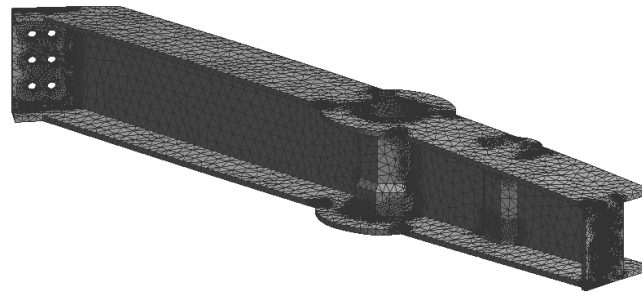


Figure 5: Mesh Model of Wing Rib

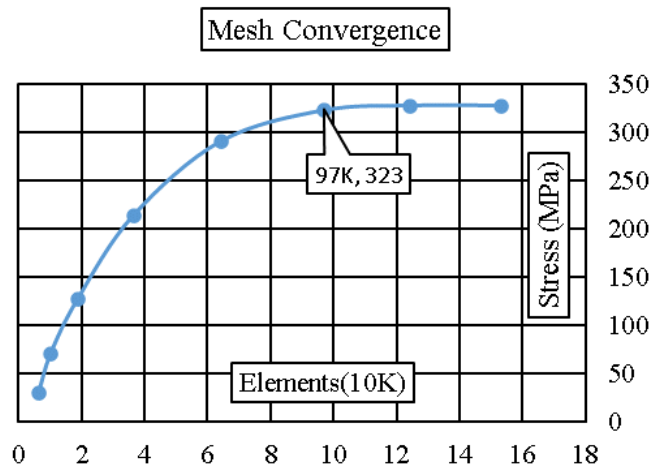


Figure 6: Mesh Convergence Study

**6.6 Case Study**

An unstructured free mesh is employed for the discretization of the problem domain, with tetrahedral-shaped 10-node elements (named Tet10) with quadratic shape functions. The mesh model of the wing rib is illustrated in Figure 5. Both local and global mesh controls have been employed to enhance mesh quality. Mesh refinement has been implemented at regions of load application, constraints, and geometric transitions.

The mesh convergence study is depicted in Figure 6. It is observed that the mesh-independent solution is obtained with a mesh count of 97,000 elements. The average skewness of this mesh is 0.24, where 0 represents the best quality and 1 is the worst. The value of equivalent stress is recorded as 323 MPa. No bad or ill-shaped elements have been observed in the area of stress gradients.

**7 Analysis Setting**

A pre-processor generates an input file for the FE solver, which, based on defined analysis settings, performs computations of the numerical model. If an analyst has opted for default settings, this should be explicitly stated. Otherwise, any relevant changes made to these settings should be reported, including: 1. The type of solver used, whether direct or iterative, should be specified. 2. Numerical algorithms employed, such as Newton’s method, quasi-Newton methods, or Newton-Raphson method, should be mentioned. 3. Convergence Criteria, including the field variable (e.g., displacement, rotation, force, etc.) and associated tolerances, should be clearly defined. During the solution phase, the solver may generate errors and warning messages, which require critical review by the analyst. If certain measures are implemented to address these warnings, they should be documented in the FE report.

**8 Output Parameters**

FE outputs for downstream design analysis must be reported, with commonly reported results including contour plots for deformation, strain, and stress. It is also advisable to report the maximum and minimum magnitude of the field variable on these contour plots. While these plots provide useful visualization of field parameters, care should be taken to avoid misrepresentation through graphical artifacts.

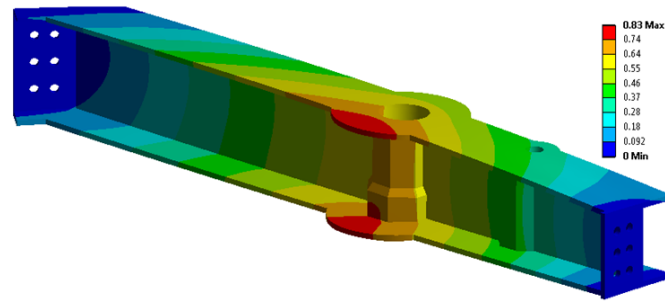


Figure 7: Deformation Field

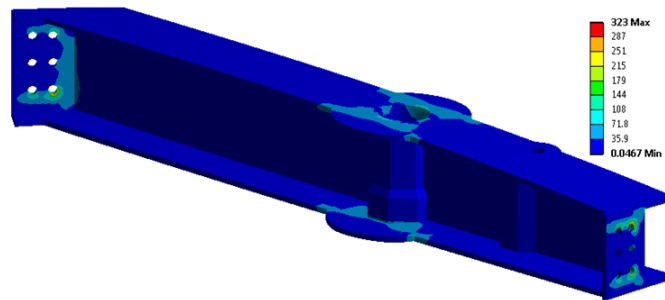


Figure 8: Maximum Stress

## 8.1 Case Study

Default settings in Ansys solver have been utilized for static structural analysis. Figure 7 illustrates the deformation of the wing rib under design load, with maximum deformation (0.83 mm) observed at the spindle. Figure 8 presents von Mises stress distribution for the rib under design load, with the maximum stress (323 MPa) observed at the bolt holes for the attachment of the rib to the wing.

## 9 Sensitivity Analysis

Uncertainty in modeling parameters can significantly impact simulation results. Therefore, sensitivity analysis should be conducted and the influence of such uncertainties on Finite Element (FE) results may be reported. In this approach, input parameters are generated based on probability distributions, and a large number of simulations (generally several thousand) are performed to generate a probability distribution of simulation results. This comprehensive sensitivity analysis should be documented to establish the predictive performance of the model under uncertainty in modeling parameters [38].

### 9.1 Case Study

Max stress under applied load is observed at bolt holes. The original bolt hole diameter is 4 mm. A sensitivity analysis can be performed to determine the effect of the bolt hole on maximum stress. Figure 9 presents the variation in maximum stress with changes in the diameter of bolt holes. The diameter of bolt holes at each side is varied from 3 mm to 5 mm. Minimum stress (286 MPa) is observed when the diameter of the bolt hole is 4.5 mm. Maximum stress is decreased from 323 MPa to 286 MPa (11.4% decrease) by enlarging the diameter of bolt holes from 4 mm to 4.5 mm.

## 10 Verification

Verification and Validation of the model guarantee accurate results with the right balance between computational cost and accuracy. Verification determines that the model has been solved while validation determines correct model has been solved. The following information should be documented [39]; 1. A comparison of inertial properties such as mass, center of gravity, and moment of inertia between the Finite Element (FE) model and the physical/CAD model should be conducted. 2. Reasonable deformation of the body under its weight (i.e., 1 g condition without applied load) 3. Verification of applied boundary conditions under external loads should be conducted to ensure their observance. 4. Equilibrium conditions can be assessed by comparing reaction forces and moments with the applied loads. 5. Code verification of user-developed subroutines

## 11 Validation

The validation process determines that correct equations governing a physical phenomenon have been solved. The following validation steps may be reported [38]; 1. When numerically representing complex physical phenomena, Finite Element (FE)

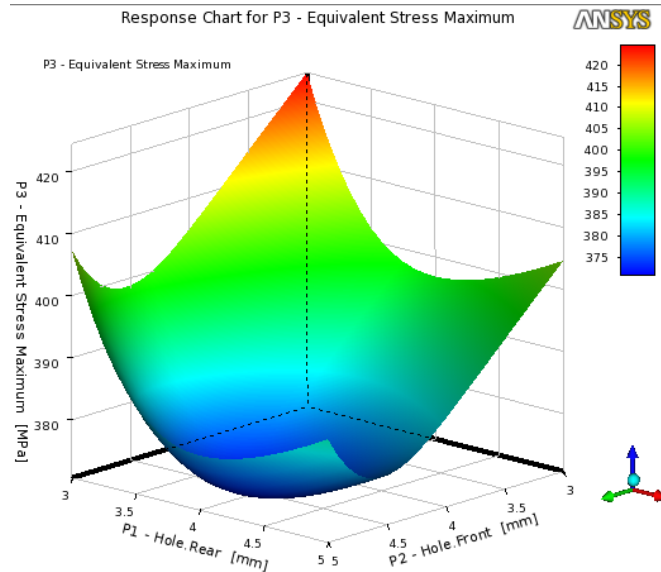


**Figure 9: Response Chart**

analysts inevitably rely on modeling assumptions. It is essential to report and substantiate these assumptions to assess the efficacy of FE models. 2. Correlation with analytical or empirical solutions of a simplified model is essential to validate the accuracy and reliability of numerical solutions. 3. Correlating the current analysis with similar accredited Finite Element (FE) analyses helps validate the reliability and accuracy of the results. 4. Correlating experimental output with simulation results is crucial to validate and verify the accuracy of the Finite Element (FE) analysis. 5. In the Finite Element (FE) report, it is imperative to provide appropriate references for modeling parameters to ensure credibility. 6. The repeatability of FE results on different hardware/operating systems and FE software demonstrated the robustness of digital twins. 7. Error i.e., difference between simulation result and experimental output, should be reported in terms of relevant statistical metrics.

## 12 Results Section

Physical interpretation of FE results should be thoroughly reported. The report should deliberate on how and to what extent these results have answered the posed research question. If the results have not conclusively addressed the question, a new approach or methodology can be recommended. Singularities in Finite Element (FE) outputs, often indicated by values approaching infinity, may arise at locations of constraints, applied loads, or zero radii corners. While it is crucial to report these singularities, they may be excluded from discussion with appropriate justification.

### 12.1 Case Study

By using an elastic support, the maximum stress observed is 323 MPa. This elastic support introduces the stiffness of the global wing model into the solution of the isolated local model. When the stiffness of the global model is made infinite, i.e., a fixed support is used as a boundary condition, the maximum stress increases to 388 MPa. This represents an increase of 20.1% in stress. Therefore, it is concluded that the application of a fixed boundary condition for the local model isolated from a global model under predicts the strength by 20%.

## 13 Availability

Granting public access to the model enables prospective users to evaluate and enhance its capabilities. When access to the model is provided under appropriate distribution conditions and contractual binding, it fosters improvements in the model. 1. Clear licensing terms should be established for the distribution, reuse, and modification of FE models. 2. An online link or web address may be provided for model download, developmental updates, user reviews, and address of queries by the model owner.

## 14 Conclusion

This article elucidates essential considerations for reporting in the context of finite element analysis (FEA). Adherence to these guidelines is poised to yield succinct documentation. FEA report fashioned by these guidelines is designed to encapsulate all pertinent details, enabling a comprehensive understanding of the simulation process and facilitating accurate result reproduction. The application of these guidelines serves to instill confidence in the reproducibility, repeatability, and accountability of FEA studies.

These guidelines offer a valuable resource for researchers, journal editors, and funding agencies, equipping them with a framework to evaluate and ascertain the capabilities, limitations, and usability of simulation models. While it may be impractical for a journal manuscript to comprehensively present and discuss all reporting parameters, the identification of omitted sections can serve as a compass, guiding prospective research directions.

Moreover, these guidelines have the potential to evolve into a foundational reporting standard for FEA studies. Over time, the systematic application of these guidelines may contribute to the establishment of standardized protocols for the exchange of FEA models. Notably, there is a contemporary trend among software vendors and seasoned FEA users who are actively developing subroutines for automated reports within FEA software. Incorporation of these guidelines stands to enhance the fidelity of such subroutines.

It is imperative to acknowledge that these guidelines, while comprehensive, may not be exhaustive and are susceptible to evolution concurrent with ongoing advancements in computer modeling and simulation. Furthermore, their adaptability for multi-domain and multi-physics analyses underscores their relevance in the dynamic landscape of simulation methodologies.

### Acknowledgments

The author acknowledges the facilitation of his department at Air University for providing all the resources for this publication.

### Author Contributions

100 % contribution by AH.

### Competing Interests

The author declares that he has no competing interests.

### References

- [1] S. David Müzel, E. P. Bonhin, N. M. Guimarães, and E. S. Guidi, "Application of the finite element method in the analysis of composite materials: A review," *Polymers*, vol. 12, no. 4, p. 818, 2020.
- [2] L. Sabat and C. K. Kundu, "History of finite element method: a review," *Recent Developments in Sustainable Infrastructure: Select Proceedings of ICRDSI 2019*, vol. 3, no. 121, p. 395, 2020.
- [3] H.-H. Lee, *Finite element simulations with ANSYS Workbench 21*. SDC publications, 2021.
- [4] T. Chandrupatla and A. Belegundu, *Introduction to finite elements in engineering*. Cambridge University Press, 2021.
- [5] K. N. B. R. U. A. Mastoi S., Mugheri A. B. M. and M. R. B., "Solution accuracy of finite element grids," *International Journal of Advanced Research in Engineering and Technology*, vol. 4, no. 17, p. 1127, 2021.
- [6] A. M. Law, "How to build valid and credible simulation models," in *2022 Winter Simulation Conference (WSC)*, p. 128, IEEE, 2022.
- [7] D. Arndt, W. Bangerth, D. Davydov, T. Heister, L. Heltai, M. Kronbichler, M. Maier, J.-P. Pelteret, B. Turcksin, and D. Wells, "The deal. ii finite element library: Design, features, and insights," *Computers & Mathematics with Applications*, vol. 3, no. 128, p. 128, 2021.
- [8] K. Srinivas and S. Motera, "Verifications and validations in finite element analysis (fea)," *Ahmedabad: Advanced Scientific and Engineering Services (AdvanSES)*, vol. 3, no. 128, p. 407, 2020.
- [9] P. M. Kurowski, *Finite element analysis for design engineers*. SAE International, 2022.
- [10] M. Zaheer, P. Lindh, L. Aarniovuori, and J. Pyrhönen, "Comparison of commercial and open-source fem software: A case study," *IEEE Transactions on Industry Applications*, vol. 56, no. 6, p. 6411, 2020.
- [11] I. Magomedov and Z. Sebaeva, "Comparative study of finite element analysis software packages," in *Journal of Physics: Conference Series*, vol. 1515, p. 73, IOP Publishing, 2020.
- [12] D. Marinkovic and M. Zehn, "Survey of finite element method-based real-time simulations," *Applied Sciences*, vol. 9, no. 14, p. 2775, 2019.
- [13] S. Chakraverty, N. Mahato, P. Karunakar, and T. D. Rao, *Advanced numerical and semi-analytical methods for differential equations*. John Wiley & Sons, 2019.
- [14] I. Erhunmwun and U. Ikonmwoosa, "Review on finite element method," *Journal of Applied Sciences and Environmental Management*, vol. 21, no. 5, p. 999, 2018.
- [15] T. Stolarski, Y. Nakasone, and S. Yoshimoto, *Engineering analysis with ANSYS software*. Butterworth-Heinemann, 2018.
- [16] I. Koutromanos, *Fundamentals of finite element analysis: Linear finite element analysis*. John Wiley & Sons, 2018.
- [17] R. Basu, K. Kirkhope, and J. Srinivasan, "Guideline for evaluation of finite elements and results.," *Military Systems Engineering*, p. 64, 2018.
- [18] M. Kuzin, P. Vovk, and O. Kuzin, "Mathematical modelling and mechanics approaches in investigation of structural failure causes," in *MATEC Web of Conferences*, vol. 390, p. 04010, EDP Sciences, 2024.
- [19] S. Georgescu, P. Chow, and H. Okuda, "Gpu acceleration for fem-based structural analysis," *Archives of Computational Methods in Engineering*, vol. 20, no. 11, p. 111, 2019.
- [20] J. Schröder, T. Wick, S. Reese, P. Wriggers, R. Müller, S. Kollmannsberger, M. Kästner, A. Schwarz, M. Igelbüscher, N. Viebahn, *et al.*, "A selection of benchmark problems in solid mechanics and applied mathematics," *Archives of Computational Methods in Engineering*, vol. 28, p. 713, 2021.
- [21] A. Mar and M. Hicks, "A benchmark computational study of finite element error estimation," *International journal for numerical methods in engineering*, vol. 39, no. 23, p. 3969, 2018.
- [22] V. Saravanan, M. Ramachandran, and C. Raja, "A study on aircraft structure and application of static force," *REST Journal on Advances in Mechanical Engineering*, vol. 1, no. 1, p. 1, 2022.
- [23] C. Zhao, A. Alimardani Lavasan, and T. Schanz, "Application of submodeling technique in numerical modeling of mechanized tunnel excavation," *International Journal of Civil Engineering*, vol. 17, p. 75, 2019.
- [24] M. W. Sracic and W. J. Elke, "Effect of boundary conditions on finite element submodeling," in *Nonlinear Dynamics, Volume 1: Proceedings of the 36th IMAC, A Conference and Exposition on Structural Dynamics 2018*, p. 163, Springer, 2019.
- [25] A. H. Bhutta, "Appropriate boundary condition for finite element analysis of structural members isolated from global model.," *NED University Journal of Research*, vol. 18, no. 3, 2021.
- [26] D. Venkatkumar and D. Ravindran, "Effect of boundary conditions on residual stresses and distortion in 316 stainless steel butt welded plate," *High Temperature Materials and Processes*, vol. 38, no. 2019, p. 827, 2019.

- [27] F. Guarracino, A. Walker, and A. Giordano, "Effects of boundary conditions on testing of pipes and finite element modelling," *International Journal of Pressure Vessels and Piping*, vol. 86, no. 2-3, p. 196, 2019.
- [28] R. Omar, M. A. Rani, and M. Yunus, "Representation of bolted joints in a structure using finite element modelling and model updating," *Journal of Mechanical Engineering and Sciences*, vol. 14, no. 3, p. 7141, 2020.
- [29] T. Liu, Q. Zhao, Y. Cao, and J. Yang, "A generic approach for analysis of mechanical assembly," *Precision Engineering*, vol. 54, p. 361, 2020.
- [30] S. Ereiz, I. Duvnjak, and J. F. Jiménez-Alonso, "Review of finite element model updating methods for structural applications," in *Structures*, vol. 41, p. 684, Elsevier, 2022.
- [31] A. Ruggiero, R. D'Amato, and S. Affatato, "Comparison of meshing strategies in the finite element modelling," *Materials*, vol. 12, no. 14, p. 2332, 2020.
- [32] M. S. Petrov and T. D. Todorov, "Properties of the multidimensional finite elements," *Applied Mathematics and Computation*, vol. 391, no. 125, p. 695, 2021.
- [33] A. Nemade and A. Shikalgar, "The mesh quality significance in finite element analysis," *J. Mech. Civ. Eng.*, vol. 17, p. 44, 2020.
- [34] K. Jalammanavar, N. Pujar, and R. V. Raj, "Finite element study on mesh discretization error estimation for ansys workbench," in *2018 International conference on computational techniques, electronics and mechanical systems (CTEMS)*, p. 344, IEEE, 2021.
- [35] H. A. Carson, A. C. Huang, M. C. Galbraith, S. R. Allmaras, and D. L. Darmofal, "Mesh optimization via error sampling and synthesis: An update," in *AIAA Scitech 2020 Forum*, p. 87, 2020.
- [36] W. Kwok and Z. Chen, "A simple and effective mesh quality metric for hexahedral and wedge elements," in *IMR*, p. 325, Citeseer, 2020.
- [37] J. Svetlichny, "Overview of ansys meshing preprocessor capabilities to create high quality meshes," *Open Information and Computer Integrated Technologies*, no. 95, p. 83, 2022.
- [38] C. Oefner, S. Herrmann, M. Keibach, H.-E. Lange, D. Kluess, and M. Woiczinski, "Reporting checklist for verification and validation of finite element analysis in orthopedic and trauma biomechanics," *Medical Engineering & Physics*, vol. 92, p. 25, 2021.
- [39] M. G. Faes, M. Daub, S. Marelli, E. Patelli, and M. Beer, "Engineering analysis with probability boxes: A review on computational methods," *Structural Safety*, vol. 93, no. 102, p. 92, 2021.

Research Article

# Effects of Metoclopramide and Hyoscine-N-Butyl Bromide on Motility of Duodenum in Male Rats and Quantum Computational Analysis

Sleman Yousif Omar<sup>1a</sup>, Emine Kaçar<sup>2b</sup>, Dyari Mustafa Mamand<sup>3c</sup> Rebaz Anwar Omer<sup>4,5d</sup>

<sup>1</sup> University of Raparin, College of Science, Department of Biology, Sulaymaniyah, Iraq

<sup>2</sup> University of Firat, Tip Faculty, Department of Physiology, Elazığ, Türkiye

<sup>3</sup> University of Raparin, College of Science, Department of Physics, Sulaymaniyah, Iraq

<sup>4</sup> Department of Chemistry, Faculty of Science & Health, Koya University, Koya, KOY45, Iraq

<sup>5</sup> Department of Pharmacy, College of Pharmacy, Knowledge University, Erbil 44001, Iraq

rebaz.anwar@koyauniversity.org

DOI : 10.31202/ecjse.1311981

Received: 13.06.2023 Accepted: 24.04.2024

## How to cite this article:

Sleman Yousif Omar, Emine Kaçar, Dyari Mustafa Mamand, Rebaz Anwar Omer, " Effects of Metoclopramide and Hyoscine-N-Butyl Bromide on Motility of Duodenum in Male Rats and Quantum Computational Analysis", El-Cezeri Journal of Science and Engineering, Vol: 11, Iss:3, (2024), pp.(223-233).

ORCID: <sup>a</sup>0000-0002-9796-8063; <sup>b</sup>0000-0002-1562-4620; <sup>c</sup>0000-0002-1215-7094; <sup>d</sup>0000-0002-3774-6071.

**Abstract :** Gastroenteritis accompanied by emesis commonly involves treatment with metoclopramide, a prokinetic agent. Conversely, hyoscine-N-butyl bromide (Buscopan), an anticholinergic compound, impedes acetylcholine's interaction with muscarinic receptors. This study aimed to elucidate the effects of metoclopramide on duodenal motility induced by acetylcholine and to investigate the influence of metoclopramide alone and in combination with hyoscine-N-butyl bromide on duodenal contractility. Duodenal tissue segments, 1 cm apart, were prepared and secured with surgical silk at both ends within an isolated organ bath. Isometric contractions were recorded as the tissue was subjected to various treatments. Acetylcholine (10-4 M) was introduced initially, followed by the addition of metoclopramide (35 M), hyoscine-N-butyl bromide (15 M), and a combination of both (50 M) after a 10-minute incubation period. The responses of the duodenal tissue were characterized by changes in frequency, peak-to-peak amplitude, and amplitude. Additionally, quantum chemical calculations were performed to investigate several chemical properties, with a focus on determining the active center using the Fukui function. The study revealed that metoclopramide significantly enhanced duodenal motility induced by acetylcholine, as evidenced by a notable increase in frequency and amplitude of contractions compared to the control group ( $p < 0.05$ ). Furthermore, the combination of metoclopramide and hyoscine-N-butyl bromide exhibited a synergistic effect, resulting in a more pronounced enhancement of duodenal contractility compared to either drug alone ( $p < 0.01$ ). Quantum chemical calculations identified key chemical properties and elucidated the active center, providing insights into the molecular mechanisms underlying the observed physiological responses.

**Keywords :** Duodenum, Metoclopramide, Hyoscine-N-Butylbromide, DFT.

## 1 Introduction

Smooth muscle, a type of tissue called smooth muscle is an unstriated, involuntary muscle. In the middle is where the nucleus. The smooth muscle will appear homogeneous because it is made up of thin and thick filaments that are not grouped into sarcomeres [1]. 10% of the total muscle mass in the human body is made up of smooth muscle, which includes the gastrointestinal tract, the bladder, and the heart. This muscle is 30 times smaller than skeletal muscle diameter, measuring 1 to 5 micrometers in diameter and 20 to 500 micrometers in length. Although there are many signals of smooth muscle contractions that are comparable to those of skeletal muscle, smooth muscle fibers have an altogether different interior physical appearance [2].

Smooth muscle in each organ displays distinctive characteristics compared to smooth muscle in other organs. Nevertheless, there are generally two approaches to studying both multi-unit and unitary (single-unit) smooth muscle [3]. The major trait of the smooth fibers that make up the numerous units of smooth muscle is that they can contract unintentionally from one another and are mostly controlled by nerve signals. Some of the multi-unit smooth muscles include the cilia and iris of the eye, as well as the piloerector muscle. Hundreds of thousands of smooth muscle fibers make up a single unit of smooth muscle. The strain in muscle fibers can be transferred to the next cell membrane because most cell membranes are neighbors [3].

On the other hand, many gap junctions connected to the cell membrane enable free ion movement between muscle cells and nearby cells in action potentials, enabling muscle fibers to contract collectively. Many internal organs, including the blood

arteries, ureters, bile ducts, and digestive tract, are built of smooth muscle [4]. The uses of smooth muscle are numerous. The stomach and intestine contain several locations that aid in digestion and nutrient absorption. The urinary bladder is made up of smooth muscle, which plays a part in the body's toxin removal and electrolyte balance mechanisms. All veins and arteries contain smooth muscle, which plays a crucial role in regulating blood pressure and tissue oxygenation. The body's organs could not remain upright without these crucial works; they are the most fundamental. The nervous system can also strongly govern various bodily processes through the usage of smooth muscle. A person does not need to be concerned about their blood pressure to acclimate to the increased need for oxygen from practice [5]. Metoclopramide is a crucial gastrokinetic and antiemetic agent used to treat nausea, vomiting, headaches, gastroesophageal reflux disease, and gastroparesis [6], [7].

It is a dopamine (D2) receptor antagonist with a brief half-life that combines 5HT3 and 5HT4 receptor antagonist properties [8]. Metoclopramide has gastrokinetic, antiemetic, and nausea-reducing effects [9]. Without stimulating gastric biliary or pancreatic discharge, it increases upper gastrointestinal tract motility [10]. The enhanced peristalsis of the duodenum causes the motility of gastric discharge to be enlarged, and the jejunum has little impact on the colon's motility [11]. In clinical practice, hyoscine-N-butyl bromide (Buscopan) is used as an Anticholinergic and antispasmodic to treat spontaneous pain or cramping in the stomach [12]. Particularly in cases of gastroenteritis, such as those seen in patients with intestinal obstruction and bad-tempered internal illness (IBS) [13].

The muscarinic M2 and M3 receptors, for instance, are highly tissue-affective for hyoscine-N-butyl bromide in the gastrointestinal tracts' causal smooth muscles [14]. More ongoing research has shown that the nicotinic receptor can also be inhibited by hyoscine-N-butyl bromide (Buscopan) in SH-SY5Y cells and human enteric neurons [14].

The primary objective of this research was to investigate the impact of metoclopramide on the motility of the duodenum and colon induced by acetylcholine. Additionally, the effects of both metoclopramide alone and its combination with hyoscine-N-butyl bromide were examined on the natural contraction and relaxation processes of the duodenum and colon. In order to analyze the structural and compositional attributes of the molecules utilized in this study, the DFT method was employed. Through this approach, crucial parameters and conducted a comparative analysis between the gas and aqueous phases for both protonated and non-protonated species were identified.

## 2 Material and Method

### 2.1 Study Design

A total of 8 male Sprague-Dawley rats, obtained from the Experimental Research Center of Firat University (FÜDAM), were included in the study based on their weight. The animals' abdominal areas were then opened, and the duodenum and colon tissues were quickly removed. The creatures were subsequently severed from their heads. Samples were put in Krebs solution-filled Petri dishes. Because all anesthetic medications affect the smooth muscle, which is used in the study, animals were beheaded without anesthesia. Eight animals were employed to obtain the duodenum and colon tissues, and the controls were the notes that were obtained from the tissue preparation strips made from each animal's tissues.

### 2.2 Krebs Solution

Krebs's solution is a solution that provides physiological conditions in vivo to a certain extent in vitro. By its content, it enables the smooth muscle cells to maintain their contractility properties optimally in vitro. The Krebs content was prepared in mM / L and the pH was adjusted to 7.4.

### 2.3 Isolated Organ Bath

The isolated organ bath system (MAY IOBS 99) with a double wall structure consists of a stand, tank, amplifier, hoppers, circulation pump with thermostat, O2-CO2 mixing tube (HABAS), recording unit, and liquid and gas transport apparatus. The circulating pump with the thermostat is a device that adjusts the distilled water to the desired temperature and circulates in all double-walled parts of the isolated organ bath and warms up. In the current system, the device will be set to 37 C°. In the experiments, 4 wells with a volume of 5 ml will be used. Throughout the whole experiment, the Krebs solution in the chamber will be continuously gasified with a mixture of 95% O2 and 5% CO2 from the inlet in the lower region of the chamber.

The isometric transducer senses the physical forces resulting from isometric contractions in the smooth muscle strips in the chambers and converts them into electrical signals. In the recording unit, the frequency, peak-to-peak, and area parameters generated by contractions of muscle strips in the organ bath will be recorded simultaneously. These recordings are then analyzed to determine the contraction parameters occurring before and after metoclopramide, hyoscine-N-butyl bromide, and metoclopramide + hyoscine-N-butyl bromide in each muscle strip as frequency, peak to peak, and area parameters.

### 2.4 Preparation and Application of Metoclopramide and Hyoscine-N-butyl bromide to be Applied in Isolated Organ Bath

Metoclopramide, whose trade name is metpamide, is 10 mg and hyoscine-N-butyl bromide whose trade name is buscopan is mixed in vortex with 10 mg tablet separately. Metoclopramide and hyoscine-N-butyl bromide solutions were separated into

small plastic Eppendorf tubes and stored at  $-20\text{ }^{\circ}\text{C}$  until they were applied in the organ bath.

## 2.5 Preparation and Application Protocol of Duodenum and Colon Tissues

After decapitation of male animals, the abdominal areas were opened and the proximal colon were removed about 1 cm from the duodenum and cecum, and 2 cm long strips were prepared and fixed with both sides of surgical silk suture at both ends of the apparatus in the isolated organ bath with 1.0 g of tension to the device is suspended and recorded isometric contractions. Waited 1.5 hours for the duodenum and colon strips to adapt to the environment. During this period, the tissues in the wells in the isolated organ bath were taken for 15 min. with Krebs's solution.

After regular spontaneous contractions were observed, contractions were induced by added acetylcholine (Ach) at a dose of  $10^{-4}$  M. Metoclopramide was applied in 3 different protocols after the regulation period. In the first protocol, 35  $\mu\text{M}$  metoclopramide was added to Ach-induced colon and duodenum strips, 15  $\mu\text{M}$  hyoscine-N-butyl bromide to the same strips to be induced with Ach after 1 hour, and lastly 1 hour later to the induced duodenum and colon strips to induce Ach. Hyoscine-N-butyl bromide and metoclopramide were applied together. The effects of metoclopramide alone and hyoscine-N-butyl bromide on duodenal and colon contractions were recorded and examined. The contraction values of the tissues before the application will be used as their control [15].

## 2.6 Statistically Analysis

Based on the information, the statistical analysis was conducted using paired t-tests to compare the results obtained from three different protocols. The data were checked for normal distribution, and the mean  $\pm$ SEM values were determined before and after the duodenum and colon or intestinal contractions were counted. The differences in intestinal contractions after administering metoclopramide alone and with hyoscine-n-butyl bromide on duodenum and colon contractions were examined using t-tests. To determine whether the relationship between the results of the three protocols is statistically significant, the p-values obtained from the t-tests are crucial. In statistical hypothesis testing, a p-value less than or equal to 0.05 is typically considered statistically significant. If the p-value is less than or equal to 0.05, it suggests that the observed differences are unlikely to have occurred due to random chance alone.

Since the significance level was recorded at  $P \leq 0.05$ , this implies that if the p-values obtained from the t-tests for the comparisons between the different protocols are less than or equal to 0.05, then the observed differences are considered statistically significant. If the p-values are greater than 0.05, the differences are not considered statistically significant.

Therefore, the relationship between the results of the three protocols is statistically significant, you would need to review the actual p-values obtained from the t-tests conducted in the SPSS analysis. If the p-values are at or below 0.05, it indicates a statistically significant relationship between the results of the protocols. If the p-values are above 0.05, it suggests that there is not enough evidence to conclude a statistically significant relationship.

## 3 Results and Discussion

Metoclopramide is the derivative of procainamide which has strong efficacy above motility of the duodenum the subdue of the vomiting center in a brain system. Mechanical works differ from any other factor recognized for efficacy in the mechanical movement of smooth muscles. At the same time, the effects of metoclopramide on acetylcholine contractions are caused by the duodenum. This means that metoclopramide works directly on the intestinal wall's postganglionic cholinergic nerve. The cholinergic effect of metoclopramide can be achieved by releasing acetylcholine from nerve extremities or by sensitizing the muscarinic receptors in the smooth muscles. Metoclopramide can disrupt the inhibition caused by the mechanisms of dopamine, tryptamine, noradrogen, and neurological mechanisms in addition to its possible cholinergic mechanisms [16]. Duodenum and colon section were placed in the organ bath chamber, which contained Krebs solution.

A significant increase was observed in the (frequency, peak-peak/peak-to-peak, and area), of the concentrations following the application. This process was repeated under the same conditions and the same results were obtained. As a result of these findings, it was determined that metoclopramide, hyoscine-n-butyl bromide and of metoclopramide, and hyoscine-n-butyl bromide have stimulatory effects on duodenum and colon contraction and relaxation.

Detects the effectiveness of metoclopramide, hyoscine-n-butyl bromide, and both of them. These drugs were applied to the chamber at concentrations of 35  $\mu\text{M}$  metoclopramide, 15  $\mu\text{M}$  hyoscine-n-butyl bromide and 50  $\mu\text{M}$  metoclopramide and hyoscine-n-butyl bromide. After, spontaneous contractions were recorded for 10 to 15 minutes. The mean  $\pm$  Std. Error values were calculated for Frequency, Peak-to-Peak, and Area measurements of isolated Ach-induced duodenum and colon strips from both control rats and rats treated with various substances (metoclopramide, hyoscine-n-butyl bromide, and a combination of both) across different conditions. The results of each dose examination are explained and shown in the table below.

**Table 1: This table shows the (Mean±Std.Error and P value) before and after treatment in duodenum frequency.**

	Frequency	Number	Mean Std. Error	P
(35µm) Metoclopramide	Before treat	8	43.173±10.369	0.001
	After treat		38.479±10.454	
(15 µm) hyoscine-N-butyl bromide	Before treat	8	61.660±14.192	0.05
	After treat.		57.574±13.790	
(35 µm) metoclopramide + (15 µm) hyoscine-N-butyl bromide	Before treat	8	81.731±6.760	0.05
	After treat.		78.838±6.674	

**Table 2: The Mean±Std.Error and P value of peak-peak, before and after treatment in duodenum strips.**

	Frequency	Number	Mean ± Std. Error	P
(35µm) Metoclopramide	Before treat	8	153.382±14.692	0.001
	After treat		177.75±15.170	
(15 µm) hyoscine-N-butyl bromide	Before treat	8	133.173±22.342	0.01
	After treat.		366.633±75.831	
(35 µm) metoclopramide + (15 µm) hyoscine-N-butyl bromide	Before treat	8	173.127±48.847	0.13
	After treat.		189.237±52.989	

### 3.1 Effects of Metoclopramide and Hyoscine-N-butyl bromide on Frequency of Smooth Muscle Contraction and Relaxation in Duodenum

Hyoscine-N-butyl bromide has a significant anticholinergic effect on the human duodenum of smooth muscle by antagonizing the muscarinic receptors  $M_2$  and  $M_3$ , especially in cholinergic spasticity. The specific reduction effectiveness of hyoscine-N-butyl bromide on different parts of the gastrointestinal tract may provide potentially useful information for medical use in the treatment of craps-related visceral pain. Because metoclopramide and hyoscine-n-butyl bromide are anticholinergic, when used for the treatment of intestinal spasms, or abdominal pain was blocked acetylcholine in the duodenum contraction and relaxation [17]. The first table explains the mean ± Std. error effects of metoclopramide alone, hyoscine-n-butyl bromide only, and metoclopramide and hyoscine-n-butyl bromide together on the mechanisms of contraction and relaxation of smooth muscle frequency in the duodenum before and after treatment.

In this analysis, the Mean ±Std. error for the frequency of the isolated Ach-induced duodenum strips control and treated rats with 35 µM metoclopramide, 15 µM hyoscine-N-butyl bromide, and 50 µM metoclopramide and hyoscine-N-butyl bromide concentration respectively. The results recorded as following 34.47 ± 10.45 ( $n = 8$ ), 57.57 ± 13.79 ( $n = 8$ ), 78.83 ± 6.67 ( $n = 8$ ). All of the frequencies of the dose are statistically significantly decreased compared to the control. Respectively, it was observed this metoclopramide only and with hyoscine-n-butyl bromide applied at concentrations of 35 Mm, 15 µM and 50 µM significantly decreased the frequency of contractions. However, the 35 µM drugs showed significantly the highest decreasing frequency ( $P < 0.05$  and  $P < 0.001$ ) in comparison to other drugs as shown in Table 1.

Table 1. This table shows the (Mean±Std.Error and P value) before and after treatment in duodenum frequency.

### 3.2 Effects of Metoclopramide and Hyoscine-N-butyl Bromide on Peak-Peak (Peak to Peak) of Smooth Muscle Contraction and Relaxation in Duodenum

Table 2 shows the mean±Std. error Isolated Ach peak-to-peak decreases or increases in muscle contraction before and after application of metoclopramide alone, hyoscine-n-butyl bromide only, and metoclopramide and hyoscine-n-butyl bromide together influence the mechanisms of contraction and relaxation of duodenal smooth muscle. In this examination, the Mean ± Std. error for the peak-peak of the isolated Ach reduced duodenum strips control and treated rats with 35 µM metoclopramide, 15 µM hyoscine-N-butyl bromide, and 50 µM of mixed (metoclopramide and hyoscine-N-butyl bromide) concentration separately. The results detected as follows 177.71 ± 15.17 ( $n = 8$ ), 366.63 ± 75.83 ( $n = 8$ ), 189.23 ± 52.98 ( $n = 8$ ). The results determined significance for 35 µM metoclopramide ( $P < 0.001$ ) increased peak to peak compared to the control and showed a significant increase in 15 µM hyoscine-N-butyl bromide ( $P < 0.05$ ) determined compared to the control. Whereas, 50 µM both of them (metoclopramide and hyoscine-N-butyl bromide) showed no significance ( $P < 0.05$ ), while these drugs were not effective on the peak-peak as can be seen in Table 2.

### 3.3 Effects of Metoclopramide and Hyoscine-N-butyl bromide on Area of Smooth Muscle Contraction and Relaxation in Duodenum

Tytgat, Guido N. In this experiment, the antispasmodic hyoscine-n-butyl bromide is an anticholinergic that acts on smooth muscle cells in the gastrointestinal tract locally at the muscarinic receptor. As such causes relaxation and reduction in the smooth muscle. Pathologically stimulated gut motility is the basis for spasmolytic special effects and uses in the treatment of abdominal cramping and pain. This dose is available for >50 years [18]. Leslie A. Samuels (2009), in this paper, after proved Hyoscine-N-Butylbromide (HBB) means a quaternary ammonium compound that blocks the effect of acetylcholine at parasympathetic sites (both muscarinic and nicotinic receptors) in smooth muscle, and in secretory glands. It reduces the motility of the gastrointestinal tract and the urogenital tracts and is helpful in the treatment of spasms that regions [19].

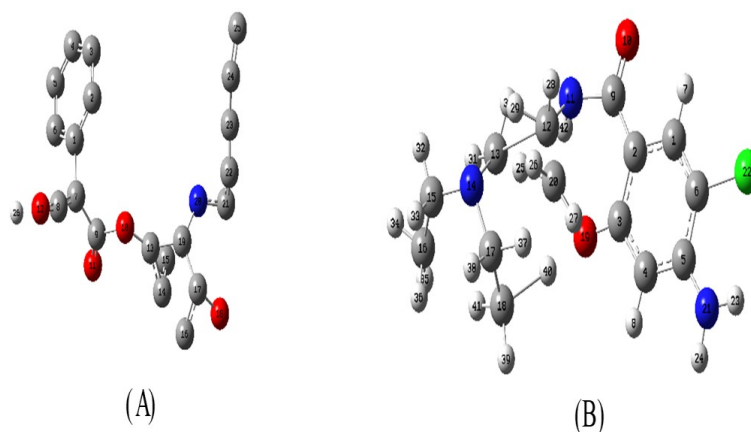


**Figure 1: The optimized molecule structure of (A) hyoscine-N-butyl bromide (B) metoclopramide, is strictly associated with procainamide based on DFT at 6-311G++(d,p) basis set.**

The Mean  $\pm$  Std. error for the amplitude/area of the isolated Ach-induced duodenum strips controls and treated rats how the amounts of muscle before and after the administration of metoclopramide alone, hyoscine-n-butyl bromide alone, and metoclopramide and hyoscine-n-butyl bromide combined affect the mechanisms of contraction and relaxation of duodenal smooth muscle. In this study, the Mean  $\pm$  Std. error for the amplitude/area of the isolated Ach-induced duodenum strips control and treated rats with 35  $\mu$ M metoclopramide, 15  $\mu$ M hyoscine-N-butyl bromide, and 50  $\mu$ M of metoclopramide and hyoscine-N-butyl bromide concentration respectively. The following results determined 370.55  $\pm$  129.89 ( $n = 8$ ), 311.36  $\pm$  85.23 ( $n = 8$ ), 494.27  $\pm$  145.67 ( $n = 8$ ). The result of 50  $\mu$ M of mixed (metoclopramide and hyoscine-N-butyl bromide) compared to the control significantly increased area ( $P < 0.05$ ). On the other hand, the 35  $\mu$ M metoclopramide, and 15  $\mu$ M hyoscine-N-butyl bromide were statistically not significant ( $P < 0.05$ ), while these drugs were not effective on the amplitude as shown in Table 3.

**Table 3: The Mean $\pm$ Std.Error and P value shows amplitude, before and after treatment in duodenum strips.**

	Frequency	Number	Mean $\pm$ Std. Error	P
(35 $\mu$ m) Metoclopramide	Before treat	8	355.43 $\pm$ 120.33	0.092
	After treat		370.555 $\pm$ 129.891	
(15 $\mu$ m) hyoscine-N-butyl bromide	Before treat	8	276.333 $\pm$ 110.11	0.056
	After treat.		311.361 $\pm$ 85.326	
(35 $\mu$ m) metoclopramide + (15 $\mu$ m) hyoscine-N-butyl bromide	Before treat	8	410.974 $\pm$ 125.079	0.03
	After treat.		494.272 $\pm$ 145.272	

#### 4 Electronic Structures

The molecular structures of the studied compounds were optimized using the Density functional theory (DFT) method, the B3LYP hybrid functional, which is a combination of Becke's three parameters (B3) exchange functional with the Lee, Yang, and Parr (LYP) correlation functional, and the 6-311G(d, p) basis set, to speed up the calculations [20]. The Gaussian 09 software package was used to complete all computations [21]. Gauss09 view was used to visualize the optimal structures of the compounds (Fig. 1). The HOMO (highest occupied molecular orbital) and LUMO (lowest unoccupied molecular orbital) frontier molecular orbitals, as well as the molecular electrostatic potential (MEP) of all optimized compounds, were displayed from a gauss perspective. This MEP outlines to illustrate the main size of the molecule, and the color-coded surface shows the position of negative and positive electrostatic potentials as a consequence of drug compound attraction or repulsion.

#### 5 Quantum Chemical Parameters

Using LUMO and HOMO orbital energies, the electron affinity and ionization energy can be expressed as  $A = -E_{LUMO}$ ,  $I = -E_{HOMO}$ , respectively. Softness (S) is a molecular attribute that indicates the degree of chemical reactivity. The reciprocal of softness is called hardness  $\eta$  [22]. The electronegativity can calculate as  $\chi = -\mu$ , the first time proposed by Parr et al and the global electrophilicity power of a ligand as  $w = \mu^2/2\eta$  [23]. When the system receives an additional electronic charge from the environment, this index evaluates the energy stability. Electrophilicity refers to an electrophile's capacity to acquire more electronic charge as well as the system's resistance to exchanging electronic charge with the environment. It is a better description of global chemical reactivity since it comprises information on both electron transport (chemical potential) and

**Table 4: Theoretical calculation of electronic parameters for compound A at protonated and non-protonated species in gas and aqueous phases.**

A	Non-protonated gas phase	Protonated gas phase	Non-protonated aqueous phase	Protonated aqueous phase
EHOMO (eV)	-7.20639506	-7.18054423	-5.74922459	-7.91634049
ELUMO (eV)	-6.570736758	-6.60910483	-5.21996286	-7.42190935
Dipole moment (Debye)	10.6328	17.7123	15.7043	23.1631
Total energy a.u	-1116.8279	-1117.0173	-1116.8121	-1116.8919
Ionization energy (eV)	7.2063	7.1805	5.7492	7.9163
Electron affinity (eV)	6.5707	6.6091	5.2199	7.4219
Band-gap energy (eV)	0.6356	0.5714	0.5292	0.4944
Hardness (eV)	0.31782	0.2857	0.2646	0.2472
Softness (eV)	3.1463	3.4999	3.7788	4.045
Electronegativity (eV)	6.8885	6.8948	5.4845	7.6691
Chemical potential (eV)	-6.8885	-6.8948	-5.4845	-7.6691
Electrophilicity (eV)	74.6507	83.1909	56.8353	118.955
Nucleophilicity (eV)-1	0.0133	0.012	0.0175	0.0084
Transfer electrons	-0.0794	-0.07142	-0.066	-0.0618
$\Delta E$ Back-donation (eV)	0.1753	0.184	2.8632	-1.3533
$\Delta N$	-0.0097	-0.0096	-2.1694	-0.4527
$E_{MEI}$	68.0799	76.5818	51.6153	111.5339
Nucleophugality	81.857	90.3715	62.5845	126.8721
Electrphugality	7.2063	7.18054	5.7492	7.9163

stability (hardness). This equation yields the maximum electron flow between donor and acceptor ( $N_{max}$ ) [24]:

$$\Delta N_{max} = -\mu/\eta \quad (1)$$

To examine the influence of electronic and structural characteristics on the efficiency of the researched medicines attributes, quantum chemical simulations were done using DFT/B3LYP at the 6-311G (d, p) basis set level. The examined inhibitors' geometric and electronic structures were computed by optimizing their bond lengths, bond angles, and dihedral angles. Fig. 1 shows the optimal molecule structures with the lowest energy generated from quantum chemical computations.

Quantum chemical characteristics acquired from DFT calculations, such as the energy of the highest occupied molecular orbital (EHOMO), the energy of the lowest unoccupied molecular orbital (ELUMO), and the energy gap, may be responsible for the inhibitors' inhibitory efficacy. The dipole moment (DM), ionization potential (IP), electron affinity (EA), electronegativity ( $\chi$ ), chemical potential ( $\mu$ ), softness ( $\sigma$ ), hardness ( $\eta$ ), electrophilicity index ( $\omega$ ), maximum electron flow from donor to the acceptor ( $\Delta N_{max}$ ), are collected in Table 4 and 5. Frontier molecular orbital electron densities of the compounds are responsible for charge-transfer complexes and provide a helpful technique for the comprehensive analysis of donor-acceptor interactions. Frontier orbital energies are significant features in a variety of chemical and pharmacological activities [25], [26].

The energy of the HOMO level is proportional to the ionization potential and describes the molecule's sensitivity to electrophile attack. The energy of the LUMO level, on the other hand, is proportional to the electron affinity and indicates the sensitivity to nucleophile attack [27].

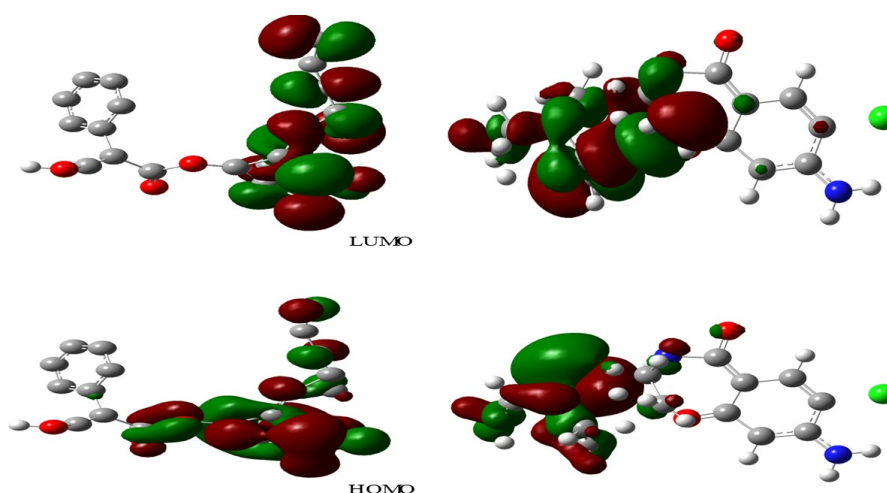
Frontier molecular orbital electron density of the compounds is responsible for charge transfer complexes and provides a helpful means for the comprehensive analysis of donor-acceptor interactions [28], [29]. Frontier orbital energies are significant features in a variety of chemical and pharmacological activities. The energy of the HOMO level is proportional to the ionization potential and describes the molecule's sensitivity to electrophile attack [30]. The energy of the LUMO level, on the other hand, is proportional to the electron affinity and indicates the sensitivity to nucleophile attack [31].

$\Delta E$  is a reactivity function; reducing the value of  $\Delta E$  enhances the inhibitors' reactivity. The narrow energy difference between HOMO and LUMO allows for electron transport and exchange, increasing the reactivity of these molecules (Fig. 2,3). The compound (A) had lower separation energies,  $\Delta E$  (0.63, 0.57, 0.52 and 0.59 eV), than compound (B) (0.905, 0.53, 0.68 and 1.24 eV) which suggests the strongest reactivity of these compounds, as shown in Table 4 and 5. Polar compounds dissociate more readily than non-polar compounds, with the polarity of the structure being described in terms of dipole moment. It's a physicochemical feature of a drug candidate that's commonly employed in medicinal chemistry as a measure of lipophilicity and the drug's ability to pass different biological membranes. When the dipole moment of a pharmacological ingredient rises, so does its solubility in water.

These compounds have a smaller dipole moment (10.63, 17.71, 15.7 and 23.16 D) than Metoclopramide, according to calculations (8.9873, 9.7832, 12.86 and 18.5133 D). This indicates that the inhibitor (A) is more hydrophobic (lipophilic) than the inhibitor (B), which might explain why their biological activities are higher. Electrophilicity is a reactivity descriptor that may be used to define the toxicity of these compounds. It also includes a direct link between reaction rates and the ability to determine an electrophile's function or capacity. The inhibitor (A) had higher electrophilicity indices (74.65, 83.19, 56.83 and 118.95 eV) in gas and aqueous phases for protonating and non-protonated states than Metoclopramide (55.63, 96.73, 76.98 and 22.85 eV), indicating that they have more biological activity. In addition, the calculations revealed that the Hyoscine butyl bromide molecule has a low electronegativity (6.88, 6.89, 484 and 7.66 eV) in gas and aqueous phases for protonating and non-protonated states,

**Table 5: Theoretical calculation of electronic parameters for compound B at protonated and non-protonated species in gas and aqueous phases.**

B	Non-protonated gas phase	Protonated gas phase	Non-protonated aqueous phase	Protonated aqueous phase
EHOMO (eV)	-7.55089139	-7.42789586	-7.60857955	-5.95902449
ELUMO (eV)	-6.64529599	-6.89754567	-6.92285227	-4.71328659
Dipole moment (Debye)	8.9873	9.7832	14.6734	18.5133
Total energy a.u	-1320.7281	-1320.44	-1320.4521	-1320.7801
Ionization energy (eV)	7.5508	7.4278	7.6085	5.959
Electron affinity (eV)	6.6452	6.8975	6.9228	4.7132
Band-gap energy (eV)	0.9055	0.5303	0.6857	1.2457
Hardness (eV)	0.4527	0.2651	0.342	0.6228
Softness (eV)	2.2084	3.771093238	2.9166	1.6054
Electronegativity (eV)	7.098	7.162720765	7.2657	5.3361
Chemical potential (eV)	-7.098	-7.1627	-7.2657	-5.3361
Electrophilicity (eV)	55.6351	96.7371	76.9848	22.8575
Nucleophilicity (eV)-1	0.0179	0.0103	0.0129	0.0437
Transfer electrons	-0.1131	-0.0662	-0.0857	-0.1557
$\Delta E$	-0.10831	-0.3068	-0.3874	1.33562
$\Delta N$	-0.00531	-0.0249	-0.05148	-1.1111
$E_{MEI}$	48.9898	89.8396	70.062	18.1442
Nucleophugality	63.186	104.165	84.5934	28.8166
Electrophugality	7.5508	7.4278	7.6085	5.959

**Figure 2: HOMO and LUMO of A and B compounds in gas phase**

which increases the electron releasing the power of Metoclopramide to the enzyme and, as a result, increases Metoclopramide capacity to be oxidized. A novel reactivity indicator that measures the stability in the energy of the complex is the maximum amount of electronic charge ( $N_{max}$ ) obtained by an inhibitor (acceptor) from the environment (donor). The inhibitor (A) has a larger electron transport, according to the calculations (-0.079, -0.0714, -0.0661, -0.0618) than Metoclopramide (-0.113, -0.066, -0.0857, -0.155). Softness is a molecular attribute that indicates the degree of chemical reactivity. The contact takes place where the softest region of the molecule is [32]. The compounds have higher softness (3.14, 3.49, 3.778 and 4.045 eV) in gas and aqueous phases for protonated and non-protonated states respectively) than Metoclopramide, according to the estimates (2.2, 3.77, 2.91 and 1.6 eV). The computed quantum chemical characteristics of Hyoscine butyl bromide revealed that they had a high biological activity equivalent to Metoclopramide inhibitors, which is in excellent accord with the experimental data. Metoclopramide alone and in combination with hyoscine-n-butyl bromide exhibited different effects depending on the concentration used. Additionally, metoclopramide alone and in combination with hyoscine-n-butyl bromide have an impact on duodenal contractions since these doses block Ach and decrease intestinal motility.

## 6 Electrostatic Potential Map of Selected Molecules

Three-dimensional molecular electrostatic potentials (MEPs) overlaid on the total electron density are beneficial for interpreting long-range interactions between molecules, which benefits in understanding how a ligand binds to its receptor. MEPs consist of some different regions, a negative area can be thought of as a nucleophilic center, whilst positive electrostatic potentials can be thought of as potential electrophilic sites. Furthermore, the electron density's polarization is evident due to the electrostatic potential. They also offer information on the size and shape of molecules. The red and orange portions in these color-coded

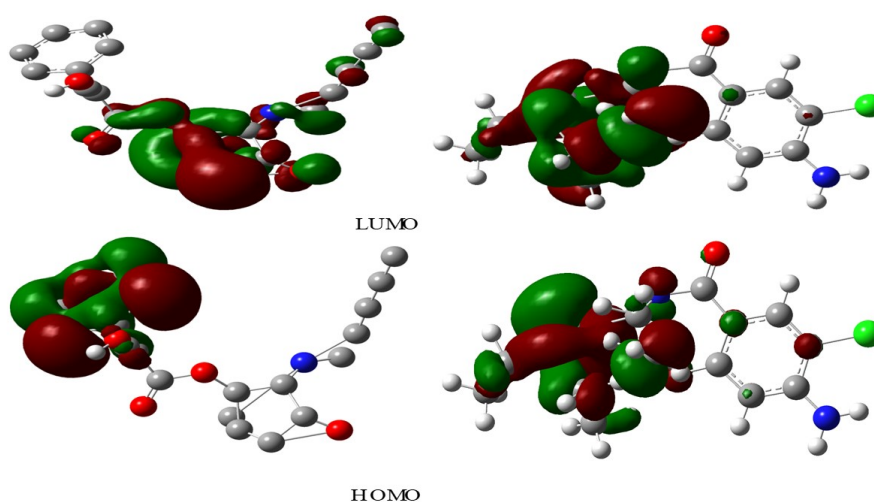


Figure 3: HOMO and LUMO of A and B compounds in the aqueous phase.

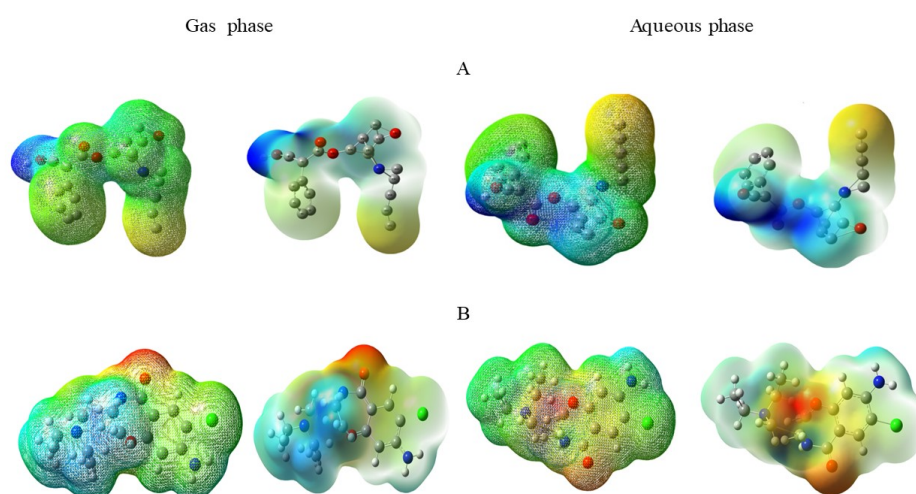


Figure 4: Electrostatic potential map of the selected molecule drugs in gas and aqueous phases.

maps show locations with high electron density, whereas the blue parts reflect electron-poor locales.

These MEP outlines offer a measurement of the molecule's overall size, while the colour-coded surface indicates the position of the positive and negative electrostatic potentials as a result of the positively charged test probe's repulsion or attraction, correspondingly [33], [34]. The oxygen and nitrogen atoms have the strongest negative potential on Hyoscine butyl bromide, as can be shown in Fig. 4. On the other hand, is particularly electron-rich in the oxygen atom regions that have been identified as important for forming a hydrogen bond with the active site of Metoclopramide. The electron-poor sites observed around the oxygen atom of the Hyoscine butyl bromide drug molecule and the rich electron sites located at the edge surface for gas and water phases in protonated and non-protonated states.

## 7 Fukui Function Analysis

The Fukui function defines the electron density after several electrons have been added or removed [35], [36]. It can forecast the location of the molecule's most nucleophilic and electrophilic sites. A finite charge change is used to implement the Fukui function. By default, an entire electron is deleted or added, although the computation is not limited to this value. Electrons in fractional quantities are permitted. When one electron is added, the Fukui equation for the electrophilic attack can be expressed as:

$$f^+ = \rho(N + 1) - \rho(N). \quad (2)$$

Table 6: Calculated Mulliken atomic charges and Fukui functions for inhibitor A, in gas and aqueous phase.

Atom	Gas phase			Aqueous phase		
	$f^+$	$f^-$	$f^0$	$f^+$	$f^-$	$f^0$
1C	-0.005	-0.023	-0.014	0.062	-0.051	0.0055
2C	-0.01	0.021	0.0055	0.29	-0.152	0.069
3C	0.001	0.02	0.0105	0.274	-0.139	0.0675
4C	0.016	-0.048	-0.016	-0.107	0.161	0.027
5C	0.003	0.008	0.0055	0.288	-0.155	0.0665
6C	-0.016	0.041	0.0125	0.303	-0.165	0.069
7C	0	0.012	0.006	0.373	-0.38	-0.0035
8C	-0.009	-0.076	-0.0425	-0.47	0.6	0.065
9C	0.016	0.025	0.0205	-0.612	0.692	0.04
10O	0.056	-0.001	0.0275	0.025	0.011	0.018
11O	0.013	0.031	0.022	0.442	-0.383	0.0295
12O	0.021	0.03	0.0255	0.135	-0.022	0.0565
13C	0.169	0.112	0.1405	-0.426	0.32	-0.053
14C	0.069	0.042	0.0555	0.026	0.097	0.0615
15C	0.277	0.177	0.227	-0.144	0.346	0.101
16C	0.087	0.054	0.0705	-0.195	0.304	0.0545
17C	0.103	0.02	0.0615	-0.353	0.483	0.065
18O	0.086	0.017	0.0515	0.285	-0.084	0.1005
19C	0.025	0.077	0.051	0.007	0.128	0.0675
20N	0.01	0.078	0.044	-0.048	0.042	-0.003
21C	0.023	0.024	0.0235	0.034	-0.01	0.012
22C	-0.032	0.124	0.046	0.084	0.169	0.1265
23C	0.051	-0.001	0.025	0.272	-0.342	-0.035
24C	0.001	0.023	0.012	0.152	-0.263	-0.0555
25C	0.046	0.197	0.1215	0.374	-0.333	0.0205

When one electron is removed, the Fukui equation for the electrophilic attack can be expressed as:

$$f^- = \rho(N) - \rho(N-1). \quad (3)$$

An approach to combine the two Fukui functions is to use the Dual Descriptor. When it is electrophilic, it has a positive value, and when it is nucleophilic, it has a negative value [37]. The difference between the Fukui minus and Fukui plus functions is used to implement it.

$$f(r) = f^+ f^-. \quad (4)$$

The Fukui function can also be used to characterize chemical reactivity in a particular region. Using the condensed Fukui function, this may even be done per atom.

$$f_k^- = q_k(N) - q_k(N-1), \quad (5)$$

$$f_k^+ = q_k(N+1) - q_k(N). \quad (6)$$

The condensed Fukui function is calculated using atomic charges. The atomic charges can be partitioned in a variety of ways. The condensed Fukui functions for Voronoi, Hirshfeld, Mulliken, and, if determined, Bader charges are published by the Fukui computation [38].

Because these atoms have a greater negative charge, Fukui function calculations show that they contain active centers and surplus charges that might serve as a nucleophilic group [39]. The large values of the nucleophilic attack obtained from Fukui function calculations indicate that the molecule has a strong capacity to take electrons. The electrophilic attack site's high score indicates the molecule's great propensity to donate electrons. The tendency of a molecule to give off electrons is represented by the high electrophilic site [40].

## 8 Conclusion

The study found that metoclopramide's anti-emetic effects are boosted by its ability to block dopamine receptors in both central and peripheral areas, akin to how gastrointestinal motility syndrome operates. For patients experiencing cramping-related stomach discomfort, hyoscine-n-butyl bromide is a popular treatment choice. Metoclopramide, at low and high concentrations, reduces gastrointestinal smooth muscle activity, while moderate levels enhance muscle contraction, mainly through intracellular  $Ca^{+2}$  ions. The study utilized isolated organ bath tissue strips from the duodenum and colon, measuring contractions under various drug combinations. Metoclopramide, alone and with hyoscine-n-butyl bromide, displayed concentration-dependent effects on duodenal contractions, blocking acetylcholine and reducing intestinal motility. Chemical analyses showed hyoscine-n-butyl bromide's greater reactivity due to its lower bandgap energy and higher interaction potential compared to metoclopramide. This study enhances our understanding of how these drugs affect gastrointestinal function, providing insights for potential therapeutic applications.

Table 7: Calculated Mulliken atomic charges and Fukui functions for compound B, in gas and aqueous phase.

Atom	Gas phase			Aqueous phase		
	$f^+$	$f^-$	$f^0$	$f^+$	$f^-$	$f^0$
1C	-0.014	0.031	0.0085	0.081	-0.058	0.0115
2C	-0.022	0.054	0.016	0.447	-0.42	0.0135
3C	0.003	0.026	0.0145	-0.296	0.303	0.0035
4C	0.016	-0.022	-0.003	0.404	-0.355	0.0245
5C	-0.011	0.04	0.0145	-0.247	0.257	0.005
6C	-0.017	-0.014	-0.0155	0.133	-0.106	0.0135
7H	0.006	-0.005	0.0005	-0.136	0.17	0.017
8H	0.013	-0.014	-0.0005	-0.178	0.223	0.0225
9C	0.094	-0.129	-0.0175	-0.579	0.618	0.0195
10O	0.023	-0.018	0.0025	0.324	-0.263	0.0305
11N	0.03	-0.018	0.006	0.339	-0.33	0.0045
12C	0.048	0.007	0.0275	0.154	-0.214	-0.03
13C	0.682	0.077	0.3795	0.906	-0.668	0.119
14N	-0.025	0.096	0.0355	-0.154	0.152	-0.001
15C	-0.01	0.033	0.0115	0.419	-0.462	-0.0215
16C	0.142	-0.161	-0.0095	0.65	-0.672	-0.011
17C	-0.037	0.191	0.077	0.173	-0.195	-0.011
18C	-0.064	0.18	0.058	0.687	-0.701	-0.007
19O	-0.068	0.081	0.0065	0.311	-0.298	0.0065
20C	0.357	0.127	0.242	0.157	-0.052	0.0525
21N	0.005	0.001	0.003	0.375	-0.357	0.009
22Cl	0.013	-0.006	0.0035	-0.049	0.118	0.0345

### Authors' Contributions

Sleman Yousif Omar: Laboratory working at Firat University when he was MSc student and data analysis. Emine Kaçar: Supervisor on this work and plan to writing up. Dyari Mustafa Mamand: Theoretical working and data analysis. Rebaz Anwar Omer: Writing up and data analysis.

### Competing Interests

The authors state that there is no conflict of interest in the printing of this manuscript.

### References

- [1] J. Chamley-Campbell, G. R. Campbell, and R. Ross, "The smooth muscle cell in culture," *Physiological reviews*, vol. 59, no. 1, pp. 1–61, 1979.
- [2] R. A. Meiss, "Skeletal muscle and smooth muscle," *Structure*, pp. 152–176, 2003.
- [3] S. McGurk, "Ganong's review of medical physiology–," *Nursing Standard*, vol. 24, no. 20, pp. 30–31, 2010.
- [4] E. Kacar, Z. Ercan, I. Serhatlioglu, A. Sumer, H. Kelestimur, and S. Kutlu, "The effects of apelin on myometrium contractions in pregnant rats," *Cellular and Molecular Biology*, vol. 64, no. 11, pp. 74–79, 2018.
- [5] D. M. Williams and B. K. Rubin, "Clinical pharmacology of bronchodilator medications," *Respiratory Care*, vol. 63, no. 6, pp. 641–654, 2018.
- [6] I. Henzi, B. Walder, and M. Tramer, "Metoclopramide in the prevention of postoperative nausea and vomiting: a quantitative systematic review of randomized, placebo-controlled studies," *British Journal of Anaesthesia*, vol. 83, no. 5, pp. 761–771, 1999.
- [7] C. Maltepe and G. Koren, "The management of nausea and vomiting of pregnancy and hyperemesis gravidarum—a 2013 update," *Journal of Population Therapeutics and Clinical Pharmacology= Journal de la Therapeutique des Populations et de la Pharmacologie Clinique*, vol. 20, no. 2, pp. e184–92, 2013.
- [8] M. Tonini, S. M. Candura, E. Messori, and C. A. Rizzi, "Therapeutic potential of drugs with mixed 5-ht4 agonist/5-ht3 antagonist action in the control of emesis," *Pharmacological research*, vol. 31, no. 5, pp. 257–260, 1995.
- [9] H. S. Smith and A. Laufer, "Opioid induced nausea and vomiting," *European journal of pharmacology*, vol. 722, pp. 67–78, 2014.
- [10] A. R. Van Gool, J. K. Doorduijn, and C. Seynaeve, "Severe akathisia as a side effect of metoclopramide," *Pharmacy world & science*, vol. 32, pp. 704–706, 2010.
- [11] A. O. Ibiloglu, "Metoclopramide induced akathisia: a case report," *Klinik Psikofarmakoloji Bülteni-Bulletin of Clinical Psychopharmacology*, vol. 23, no. 2, pp. 186–189, 2013.
- [12] R. S. Sandler, W. F. Stewart, J. N. Liberman, J. A. Ricci, and N. L. Zorich, "Abdominal pain, bloating, and diarrheain the united states," *Digestive diseases and sciences*, vol. 45, pp. 1166–1171, 2000.
- [13] L. Chang, O. Y. Lee, B. Naliboff, M. Schmulson, and E. A. Mayer, "Sensation of bloating and visible abdominal distension in patients with irritable bowel syndrome," *Official journal of the American College of Gastroenterology| ACG*, vol. 96, no. 12, pp. 3341–3347, 2001.
- [14] S. Evangelista, "Quaternary ammonium derivatives as spasmolytics for irritable bowel syndrome," *Current pharmaceutical design*, vol. 10, no. 28, pp. 3561–3568, 2004.
- [15] S. Y. Omar, D. M. Mamand, R. A. Omer, R. F. Rashid, and M. I. Salih, "Investigating the role of metoclopramide and hyoscine-n-butyl bromide in colon motility," *Aro-The Scientific Journal of Koya University*, vol. 11, no. 2, pp. 109–115, 2023.
- [16] S. Mt-Isa, S. Tomlin, A. Sutcliffe, M. Underwood, P. Williamson, N. M. Croft, and D. Ashby, "Prokinetics prescribing in paediatrics: evidence on cisapride, domperidone, and metoclopramide," *Journal of pediatric gastroenterology and nutrition*, vol. 60, no. 4, pp. 508–514, 2015.
- [17] L. Zhang, J. Song, T. Bai, X. Lu, G. Yang, W. Qian, R. Wang, and X. Hou, "Effects of buscopan on human gastrointestinal smooth muscle activity in an ex vivo model: Are there any differences for various sections?" *European Journal of Pharmacology*, vol. 780, pp. 180–187, 2016.
- [18] J. Stadaas and S. Aune, "The effect of metoclopramide (primperan®) on gastric motility before and after vagotomy in man," *Scandinavian Journal of Gastroenterology*, vol. 6, no. 1, pp. 17–21, 1971.
- [19] L. A. Samuels, "Pharmacotherapy update: Hyoscine butylbromide in the treatment of abdominal spasms," *Clinical Medicine. Therapeutics*, vol. 1, pp. CMT–S1134, 2009.
- [20] H. M. Qadr and D. M. Mamand, "Molecular structure and density functional theory investigation corrosion inhibitors of some oxadiazoles," *Journal of Bio-and Tribo-Corrosion*, vol. 7, no. 4, p. 140, 2021.
- [21] S. Stoll and A. Schweiger, "Easyspin, a comprehensive software package for spectral simulation and analysis in epr," *Journal of magnetic resonance*, vol. 178, no. 1, pp. 42–55, 2006.

- [22] W. Yang and R. G. Parr, "Hardness, softness, and the fukui function in the electronic theory of metals and catalysis." *Proceedings of the National Academy of Sciences*, vol. 82, no. 20, pp. 6723–6726, 1985.
- [23] R. G. Parr, L. v. Szentpály, and S. Liu, "Electrophilicity index," *Journal of the American Chemical Society*, vol. 121, no. 9, pp. 1922–1924, 1999.
- [24] S. Martinez, "Inhibitory mechanism of mimosa tannin using molecular modeling and substitutional adsorption isotherms," *Materials chemistry and physics*, vol. 77, no. 1, pp. 97–102, 2003.
- [25] R. A. Omer, P. Koparir, M. Koparir *et al.*, "Synthesis, experimental and theoretical characterization with inhibitor activity for 1, 2, 4-triazol derivatives," *Indian Journal of Chemistry (IJC)*, vol. 61, no. 12, pp. 1278–1287, 2022.
- [26] R. A. Omer, P. Koparir, K. Sarac, M. Koparir, and D. A. Safin, "A novel coumarin-triazole-thiophene hybrid: synthesis, characterization, admet prediction, molecular docking and molecular dynamics studies with a series of sars-cov-2 proteins," *Journal of Chemical Sciences*, vol. 135, no. 1, p. 6, 2023.
- [27] F. M. Atlam, M. K. Awad, and E. A. El-Bastawisy, "Computational simulation of the effect of quantum chemical parameters on the molecular docking of hmg-coa reductase drugs," *Journal of Molecular Structure*, vol. 1075, pp. 311–326, 2014.
- [28] R. Anwar Omar, P. Koparir, M. Koparir, and D. A. Safin, "A novel cyclobutane-derived thiazole–thiourea hybrid with a potency against covid-19 and tick-borne encephalitis: synthesis, characterization, and computational analysis," *Journal of Sulfur Chemistry*, vol. 45, no. 1, pp. 120–137, 2024.
- [29] P. Koparir, R. Anwar Omar, K. Sarac, M. Koparir, and D. A. Safin, "Novel 1, 2, 4-triazolethiol–thiophen hybrids: Facile synthesis, characterization, admet prediction and molecular docking," *Polycyclic Aromatic Compounds*, pp. 1–15, 2023.
- [30] A. Popova, M. Christov, and T. Deligeorgiev, "Influence of the molecular structure on the inhibitor properties of benzimidazole derivatives on mild steel corrosion in 1 m hydrochloric acid," *Corrosion*, vol. 59, no. 09, 2003.
- [31] I. Obot, S. Kaya, C. Kaya, and B. Tüzün, "Density functional theory (dft) modeling and monte carlo simulation assessment of inhibition performance of some carbohydrazide schiff bases for steel corrosion," *Physica E: Low-dimensional Systems and Nanostructures*, vol. 80, pp. 82–90, 2016.
- [32] I. Obot and N. Obi-Egbedi, "Adsorption properties and inhibition of mild steel corrosion in sulphuric acid solution by ketoconazole: experimental and theoretical investigation," *Corrosion Science*, vol. 52, no. 1, pp. 198–204, 2010.
- [33] D. M. Mamad, R. A. Omer, and K. A. Othman, "Quantum chemical analysis of amino acids as anti-corrosion agents," *Corrosion Reviews*, vol. 41, no. 6, pp. 703–717, 2023.
- [34] R. Omer and R. F. Rashid, "Composition and properties of aspirin through dft analysis," *Journal of Physical Chemistry and Functional Materials*, vol. 6, no. 2, pp. 51–63, 2023.
- [35] H. Wang, X. Wang, H. Wang, L. Wang, and A. Liu, "Dft study of new bipyrazole derivatives and their potential activity as corrosion inhibitors," *Journal of Molecular Modeling*, vol. 13, pp. 147–153, 2007.
- [36] R. A. Omer, K. M. Ahmed, K. A. Omar, W. M. Hamad, D. M. Mamad *et al.*, "N, n-bis (2, 4-dihydroxy benzaldehyde) benzidine: Synthesis, characterization, dft, and theoretical corrosion study," *Journal of Molecular Structure*, vol. 1300, p. 137279, 2024.
- [37] S. R. Stoyanov, S. Gusarov, S. M. Kuznicki, and A. Kovalenko, "Theoretical modeling of zeolite nanoparticle surface acidity for heavy oil upgrading," *The Journal of Physical Chemistry C*, vol. 112, no. 17, pp. 6794–6810, 2008.
- [38] N. O. Eddy, S. R. Stoyanov, and E. E. Ebenso, "Fluoroquinolones as corrosion inhibitors for mild steel in acidic medium; experimental and theoretical studies," *International Journal of Electrochemical Science*, vol. 5, no. 8, pp. 1127–1150, 2010.
- [39] D. M. Mamad, H. H. Rasul, A. H. Awla, and R. A. Omer, "Insight into corrosion inhibition efficiency of imidazole-based molecules: a quantum chemical study," in *Doklady Physical Chemistry*, vol. 511, no. 2. Springer, 2023, pp. 125–133.
- [40] H. H. Rasul, D. M. Mamad, Y. H. Azeez, R. A. Omer, and K. A. Omer, "Theoretical investigation on corrosion inhibition efficiency of some amino acid compounds," *Computational and Theoretical Chemistry*, vol. 1225, p. 114177, 2023.



Research Article

# Manufacturing Lead Time Using the Value Stream Mapping (VSM) Approach in the Oyster Mushroom Baglog Production Process

Nur Islahudin<sup>1a</sup>, Tegar Theo Jodanta<sup>1b</sup>, Rindra Yusianto<sup>2c</sup>

<sup>1</sup> Industrial Engineering Department, Dian Nuswantoro University, Indonesia

<sup>2</sup> Industrial Engineering Department, Dian Nuswantoro University, Indonesia

nur.islahudin@dsn.dinus.ac.id

DOI : 10.31202/ecjse.1409431

Received: 25.12.2023 Accepted: 22.05.2024

**How to cite this article:**

Nur Islahudin, Tegar Theo Jodanta, Rindra Yusianto, " Manufacturing Lead Time Using the Value Stream Mapping (VSM) Approach in the Oyster Mushroom Baglog Production Process ", El-Cezeri Journal of Science and Engineering, Vol: 11, Iss: 3, (2024), pp.(234-245).

ORCID: <sup>a</sup>0000-0001-6814-5028; <sup>b</sup>0009-0005-6451-7855; <sup>c</sup>0000-0002-7983-5865.

**Abstract :** This research focuses on fulfilling demand by reducing the Manufacturing Lead Time (MLT) value at small and medium enterprises (SMEs) of Ungaran mushrooms, which produce baglog for growing oyster mushrooms. This research consists of several stages to optimize the production process for making baglogs in the Ungaran mushroom house, where there is a delay in meeting demand. The first stage of our method is value stream mapping (VSM). This method aims to map the entire process of making a baglog from start to finish. Based on the VSM results, the baglog material mixing process has processes that need improvement. After finding which processes need improvement, the second stage is brainstorming using a fishbone diagram to get the root of the problem in the mixing process. The next stage is looking for root cause analysis of issues in the mixing process. Based on the brainstorming and root cause analysis process, the design and mixing of baglog material tools were improved. Based on the results of the implementation of this tool, it was found that the baglog mixing process time decreased by 58.99 % and the MLT value for the entire baglog production process decreased from 1529,516 minutes to 1405,616 minutes, which is the same as the MLT decrease from 28 days to 26 days.

**Keywords :** Value stream mapping, oyster baglog production, lean manufacturing.

## 1 Introduction

Oyster mushrooms are horticultural plants that can be used as food. Its nutritional content is superior to other mushroom types because it contains good nutrients such as vegetable protein without cholesterol. As an alternative food source, oyster mushrooms can help prevent heart disease and hypertension [1]. Based on data from the Indonesian Ministry of Agriculture, total mushroom consumption in Indonesia reached 39 tons. However, the level of mushroom production in Indonesia has yet to achieve this target. In 2019, Indonesia only managed to produce 33 tons of mushrooms. From these data, it can be concluded that the level of mushroom consumption in Indonesia exceeds the production level. From 2018 to 2020, mushroom production in Semarang Regency experienced a decline. One of Indonesia's small and medium enterprises (SMEs) engaged in mushroom cultivation is "Ungaran Mushroom". The main focus of this company is the cultivation and production of oyster mushroom baglog.

Baglog is a planting medium for oyster mushrooms in the form of a tubular container measuring approximately 15cm x 30cm, generally made from plastic materials such as polypropylene (PP), polyethylene (PE), or polyvinyl chloride (PVC) [2]. The production level that Mushroom Production in Ungaran Mushroom SMEs can achieve is only around 150 baglogs per day, or in one month, it can only produce 3900 baglogs. However, every month, the average demand for oyster mushroom baglog reaches 5000-8000 pcs. This situation indicates that Ungaran Mushroom SMEs need more time to meet demand. Delays in fulfilling this demand impact the buildup of production quantities, resulting in overtime in the production process. The use of overtime certainly causes production costs to increase compared to production during regular working hours. Today's industry employs lean manufacturing to reduce production time and enhance the production lines of companies experiencing waste [3], [4]. Therefore, using the value stream mapping method, we took a system to identify waste in the oyster mushroom baglog production process.

The utilization of overtime poses supplementary difficulties, chief among them being a rise in production expenses in contrast to standard working hours. The Ungaran Mushroom SME's financial sustainability is impacted by this cost increase, which also calls into question the overall efficacy of its operations. Upon realizing that a systematic approach is required to tackle these obstacles, the research shifts its focus to lean manufacturing principles. There needs to be an apparent discrepancy between the market demand and production capacity, which causes delays in order fulfilment and eventually affects output numbers.

Ungaran Mushroom SMEs must increase output over time to meet the growing demand. Although it helps meet urgent needs over time, it also raises production costs, which impacts the SME's overall operational effectiveness and financial sustainability.

Lean manufacturing is a common tactic in reaction to the problems plaguing the industrial landscape. The main goals of lean manufacturing are reduced waste, improved output effectiveness, and process optimization. Ungaran Mushroom SMEs want to shorten lead times and simplify production procedures using lean manufacturing ideas. Value Stream Mapping (VSM) is this study's critical lean manufacturing methodology. Waste, bottlenecks, and inefficiencies in the production system can be found using the VSM approach. The study aims to identify areas for optimization and improvement by mapping the whole value stream, from the delivery of raw materials to the finished product [3], [5]. Ungaran Mushroom SMEs hopes to match production capacity with market demand, improve overall efficiency, and guarantee long-term sustainability in the cutthroat mushroom sector by strategically implementing lean manufacturing ideas and techniques. A systematic approach is required due to the complex relationship between production capacity, market demand, and operational issues in the oyster mushroom cultivation business. Using Value Stream Mapping with lean manufacturing concepts presents Ungaran Mushroom SMEs with a viable way to fix and decrease inefficiencies.

After mapping the process using VSM, the analysis step is critical for initiating improvements to the mapped process. The analysis stage may use Fishbone diagrams and root cause analysis to find potential areas for improvement by the lean manufacturing concepts outlined earlier. Similarly, fishbone diagrams, known as Ishikawa or cause-and-effect diagrams, are handy for root cause analysis. These diagrams aid in the breakdown of complicated problems into their root causes, allowing for more targeted interventions and process changes. Fishbone diagrams provide a structured framework for identifying potential root causes across various dimensions, including people, processes, and equipment. Root cause analysis is a fundamental quality management method that seeks to discover the root causes of problems or faults [6]. Organizations can improve overall efficiency and prevent recurrence by systematically exploring the fundamental reasons deeper.

Optimizing manufacturing lead time has emerged as a pivotal challenge in the industry's dynamic landscape in recent years. Implementing Lean Manufacturing has been recognized as a potent strategy to address this complexity. Notable works such as "Lean Thinking in Manufacturing" Emphasize the importance of implementing lean manufacturing practices and tools to minimize waste and enhance production lead time [7]–[11]. By doing so, manufacturing companies can achieve the desired product with affordable cost and quality, which is essential for their success in the global market [12]. Panigrahi et al. (2023) have contributed valuable insights for manufacturing companies in Oman and other countries that want to implement Lean Manufacturing practices. The study also shows that companies should consider the benefits and risks of each Lean Manufacturing practice before implementing it; a discernible research gap persists, particularly in customizing Lean Manufacturing to confront lead time challenges specific to certain industries [13]–[17].

Several studies have also confirmed the use of value stream mapping, which is used to reduce waste in the production process [18]–[21]. For example, research by Suhardi et al. It uses VSM to reduce waste in Indonesia's garment industry production process. Based on the results of VSM mapping carried out in the garment industry production process, it was found that there was an increase in production process time of 3 minutes and an increase in line efficiency of 6.17%. This research has been good at mapping waste that occurs in the production section of the garment industry and can reduce non-added value to increase the productivity of the production process in the garment industry. This has also been confirmed by several studies using value streams to map waste and reduce it to increase productivity on a production line [21]–[24].

Solving waste reduction problems from the lean manufacturing concept cannot be separated from using tools related to continuous improvement. The VSM method is generally followed by several other methods to support solving manufacturing lead time problems. The follow-up method after VSM that is often used is the analysis method using fishbone diagrams and root cause analysis. This method helps to brainstorm the causes of problems to obtain the root of the problem that will be corrected; many of the studies that use this method to solve problems include [25], [26]. Implementing fishbone analysis to find the root of the problem is quite effective. This is illustrated by related research using fishbone analysis to determine all causes of tank leaks [27]. This research has succeeded in describing the overall causes of the entire tank to enter the following analysis stage. This is also in line with the research above, all of which have successfully described the causes of problems using fishbone diagrams [25], [27]. From the discussion of the issues from other research related to lean manufacturing and root cause analysis, we offer a combination of the VSM method and root cause analysis to solve the problems of the Ungaran Mushroom SMEs.

This study seeks to bridge this gap by actively identifying critical factors that can be seamlessly integrated into the Lean framework, enhancing the effectiveness of minimizing lead time. While existing literature provides a foundation, the proposed research seeks innovation by exploring novel avenues to improve the efficacy of Lean Manufacturing in lead time management. It will specifically focus on integrating emerging technologies, leveraging advanced data analytics, and implementing more streamlined strategies for supply chain management. Envisioning these elements introduces a new dimension to Lean Manufacturing, pushing its boundaries and ensuring a more nuanced and tailored approach to lead time reduction.

The objectives of this research encompass a thorough assessment of the impact of integrating new technologies, identifying critical factors influencing lead time, and evaluating the effectiveness of supply chain management strategies in supporting Lean approaches. Through these objectives, the study aspires to contribute to the academic discourse on Lean Manufacturing

and offer practical insights for industry practitioners seeking to enhance their lead time management strategies. Ultimately, this research provides a comprehensive understanding of how Lean Manufacturing, when strategically customised and integrated with cutting-edge technologies, can significantly minimize manufacturing lead time in a rapidly evolving industrial landscape.

**2 Experimental Methods**

**2.1 Manufacturing Lead Time**

Manufacturing lead time (MLT) is the total amount of time required to process a product, including machine setup time, from the stage of raw materials to the finished product [28], [29]. The following formula is used in the oyster mushroom baglog production process to determine manufacturing lead time:

$$MLT = \sum_{i=1} (T_{suji} + (\frac{Q}{Q_i} \cdot T_{cji}) + T_{noji}) \tag{1}$$

- j = product
- i = workstation
- $T_c$  = setup time for operation
- Q = quantity/number of products
- $Q_i$  = product output in one operation
- $T_{no}$  = non-operation time

**2.2 Value Stream Mapping (VSM)**

Value stream is a complete series of actions that include activities that add value (value added) and those that do not add value (non-value added), which are needed to deliver products through the main process, namely the production flow from raw materials to finished products, to finished products. It reaches the hands of consumers [30]. The manufacturing industry uses value stream mapping to identify waste in the production flow. Once we identify the source of waste, we need to make improvements to eliminate it. The goal of VSM is to carry out mapping focusing on the entire production flow to find system waste and avoid "traps" where optimization at one workstation can sacrifice the overall production flow optimization. The application of VSM is also quoted from process improvement research. Data was obtained before and after the application of VSM to measure the effectiveness of the lean-kaizen concept. Several tangible and intangible benefits from implementing lean were observed in eliminating defects and rework and increased productivity and product quality. Stadnicka and Litwin (2019) apply the integration of VSM with value stream analysis (VSA) and system dynamics analysis (SDA) [3]. The results of this research are in the form of data to develop human resources for the production line. This research shows that VSM is a flexible tool for combining other methods and improvements

The calculation to measure process efficiency in manufacturing can be using the formula [8], [19]:

$$PCE = \frac{VAT}{PLT} \tag{2}$$

- PCE = Process Cycle Efficiency inline production
- VAT = Total Value Added time
- PLT = Total Production lead time

**2.3 Fishbone Diagram And Root Cause Analysis**

Fishbone diagrams are a tool to help identify factors that have the potential to influence problems. Based on research conducted by, a fishbone diagram is a cause-and-effect diagram generally influenced by various factors such as materials, machines, humans, methods, and the environment. In this research, the factors that affect the problem of delays in fulfilling demand are machine, environmental, and method factors. Specifically, the fishbone diagram is often used to conduct cause-and-effect analysis, identifying complex causal interactions for specific problems or events. In defect analysis research on fishing boat manufacturing processes, fishbone diagrams have played a role in identifying defects in human factors, machines, materials, and methods that produce recommendations for Improvement. Apart from that, researchers in China also apply fishbone diagrams in research [31]. This research demonstrates that fishbone diagrams are a tool one can use to identify problems in a case.

A systematic, step-by-step technique based on research is used in root cause analysis, a continuous improvement methodology, to determine the causes of unfavourable events or issues. Step-by-step demonstrates that this strategy requires a systematic process to be implemented. Furthermore, research implies that doing so requires preparation, time, and effort. As a result, one must research every aspect of the undesirable circumstance to identify the issue's primary cause [32]. Root cause analysis is the primary method used in research [33] to pinpoint the source of a case's problem. 3x5 why's is one of the methodologies employed in this study.

## 2.4 Data Collection and Processing

Used primary and secondary data collection to collect data in this research. Preliminary data was collected by directly observing the oyster mushroom baglog production process. Meanwhile, we obtained secondary data from previous research references. We processed the collected data by calculating manufacturing lead time, takt time, value stream mapping, fishbone diagrams, and root cause analysis. Following the data processing, we analyzed this research to propose conclusions. The VSM method yielded results in production process improvements to reduce manufacturing lead time. Figure 1 below illustrates the research process flow.

### 2.4.1 Initiation Stage

This stage is the initial stage to obtain data from the Ungaran mushroom community by observing, mapping and measuring the process time of each baglog making station. At this stage, the times that have added value and those that do not are also measured. A literature study was also carried out to obtain a comprehensive tool for solving problems in the Ungaran Mushroom MSMEs.

### 2.4.2 Calculation Stages

This research begins with calculating the manufacturing lead time at each oyster mushroom baglog production workstation. Manufacturing lead time is the total time needed to process a product from raw materials to finished products, including non-operational time such as machine setup time. The manufacturing lead time calculation is done by adding up the production cycle time at each workstation with the machine setup time and non-operation time at the workstation. Apart from calculating manufacturing lead time, takt time calculations are also carried out to calculate the level of available working time relative to customer demand. If production in the current cycle time is higher than the takt time, there will be a production shortage, so customer demand will not be met.

### 2.4.3 Current State Value Stream Mapping

Current state value stream mapping is carried out after MLT and takt time calculations. Namely, this was in the form of the condition of the production process at Ungaran Mushroom SMEs before repairs were carried out. VSM mapping is carried out in detail, starting from incoming customer demand, which is then received by management and forwarded to the head of production. After that, the head of production plans production (production planning) and procurement of raw materials, then maps the oyster mushroom baglog production process until product delivery arrives for consumers. In VSM mapping, the data displayed is the number of product demands that must be met, product cycle time at each workstation, setup time, non-operation time/transportation time, number of operators, and inventory levels at each workstation. Time in VSM is divided into 2, namely value-added time (processes that provide added value to the product) and non-value-added time (processes that do not offer added value), for example, waiting time or transportation of goods.

### 2.4.4 Analysis and Improvements

After completing the current state value stream mapping, waste identification analysis was carried out along the oyster mushroom baglog production line using a fishbone diagram and the 5 why tools. Fishbone is used to brainstorm all potential causes of waste in the production line, while the 5 why the method is used to identify the root causes of waste sources in a production process. In this stage, an analysis is carried out in the form of 5 why questions (why) this waste can occur five times until the root of the problem is found. Apart from the above techniques, the root cause analysis (RCA) technique is used to get the root cause of the problem. The stage in determining the root of the problem using RCA is to take data on the factors causing the problem from the fishbone diagram that was created previously. Next, identify the root causes of the factors that have been discovered previously. After finding the root cause of the problem, improvements are made through recommendations and implementation to prevent the problem from recurring. After getting to the root of the problem, the next stage is to design improvements using lean manufacturing tools. The improvements focus on reducing waste so that manufacturing lead times can be reduced and consumer demand can be met.

### 2.4.5 Future Value Stream Mapping

This stage is carried out by mapping and measuring again after improving the processing time for each oyster mushroom baglog production station. This stage will provide information on the effects of improvements that have been made, whether there are changes in terms of waste or overall manufacturing lead time.

### 2.4.6 Conclusion

The conclusion from the results of the analysis of improving the production process to reduce manufacturing lead time using the VSM method approach at Ungaran Mushroom SMEs will be a proposal for enhancing the oyster mushroom baglog production process so that it can meet customer demand promptly.

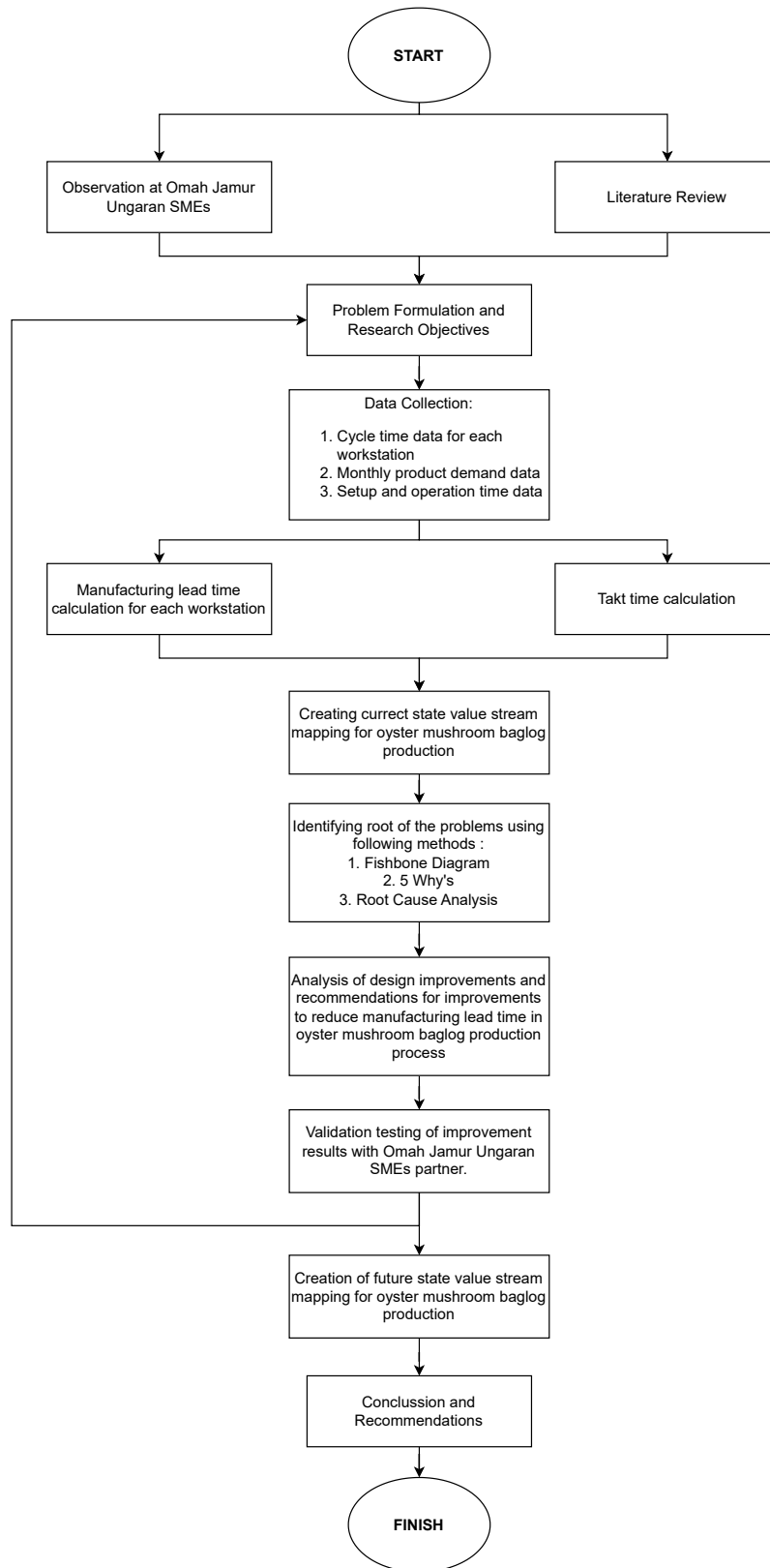


**Figure 1: The flow of the research**

**3 Results and Discussion**

**3.1 Results**

**3.1.1 Manufacturing Lead Time Calculation**

Manufacturing lead time is the time needed to produce a product. Manufacturing lead time consists of a workstation’s production cycle time, setup time, and non-operation time. This research carried out manufacturing lead time calculations daily to meet the average demand at 6462 baglog pcs. Analysis of manufacturing lead time at the oyster mushroom baglog mixing station uses the following formula:

$$MLT = (T_{suji} + (\frac{Q}{Q_i} \cdot T_{cji}) + T_{noji}) = (36 + (\frac{350}{38} \cdot 4,526) + 6) = 71,766 \text{ min} \tag{3}$$

Meanwhile, see the table below to find the MLT value at each workstation.

**Table 1: Manufacturing Lead Time Each Work Station**

Manufacturing Lead Time (Minutes)							
Mixing	Sifting	Packaging	Pressing	Providing Cover	Sterilization	Seeding	Total
71,776	39,818	80,901	56,682	103,858	880,744	295,736	1529,516

Table 1 shows the total daily manufacturing lead time for the oyster mushroom baglog production process, which is 1529.516 minutes. If accumulated over one month, that is 26 effective working days. The monthly manufacturing lead time for producing 6462 baglogs was 39575.73 minutes or 28 days. The delay in the formed manufacturing lead time was two days compared to the effective work time.

**3.1.2 Takt Time Calculation**

Takt time is a process cycle time designed to match customer demand. The following is the calculation of the takt time for oyster mushroom baglog production by considering a working time of 26 days and a month’s demand of 6462 pcs of oyster mushroom baglog:

$$Takttime = \frac{AT}{D} = \frac{37440minutes}{6462pcs} = 5,794 \text{ minutes/pcs} \tag{4}$$

The calculations based on Table 2 indicate that the required takt time to achieve is 5,794 minutes per piece, whereas the current production capacity can only reach 6,124 minutes per piece. This means that the processing time to produce one baglog product in its current condition is 0.33 minutes higher than the target or the equivalent of 5.696 % higher than the predetermined target. We can conclude that the Ungaran Mushroom MSMEs’ current production capacity will result in delays in meeting demand.

**Table 2: Comparison Takt Time for demand 6264 pcs**

Calculation	Current Condition	Target
Actual Time (minutes)	39575,732	37440
Takt Time (minutes/pcs)	6,124	5,794

**3.1.3 Current State Value Stream Mapping**

Value stream mapping is a lean manufacturing tool illustrating the material and information flow throughout a company’s production process. Value stream mapping currently distinguishes between production process activities that contribute value (value added) and those that do not (non-value added). The value stream mapping in the oyster mushroom baglog production process is shown in Figure 2 below. Table 3 supports the explanation from Figure 2.

**Table 3: Description Current State Value Stream Mapping**

Process (P)	Process Name	Qty Operator	Cycle Time (sec)	Non-Added Value/NVA(minutes)	Value Added/VA(minutes)
P1	Mixing	1	271,550	42,000	29,776
P2	Sifting	1	121,460	26,500	13,318
P3	Packaging	1	11,020	35,000	45,901
P4	Pressing	1	9,040	19,000	37,682
P5	Providing Cover	1	19,890	21,000	82,858
P6	Sterilization	1	28826,800	80,000	800,744
P7	Seeding	1	60,180	45,000	250,736
Total		7	29319,940	268,500	1261,015

The current state of value stream mapping results has revealed 1261,016 minutes of value-added time and 268,5 minutes of non-value-added time in the production process. Afterwards, we conducted process cycle efficiency (PCE) measurements to assess the efficiency level of the production process for baglog oyster mushrooms. The following represents the PCE value.

$$PCE = \frac{TotalValueAddedTime}{TotalManufacturingLeadTime} = \frac{1261,016}{1529,516} = 82,45\% \tag{5}$$

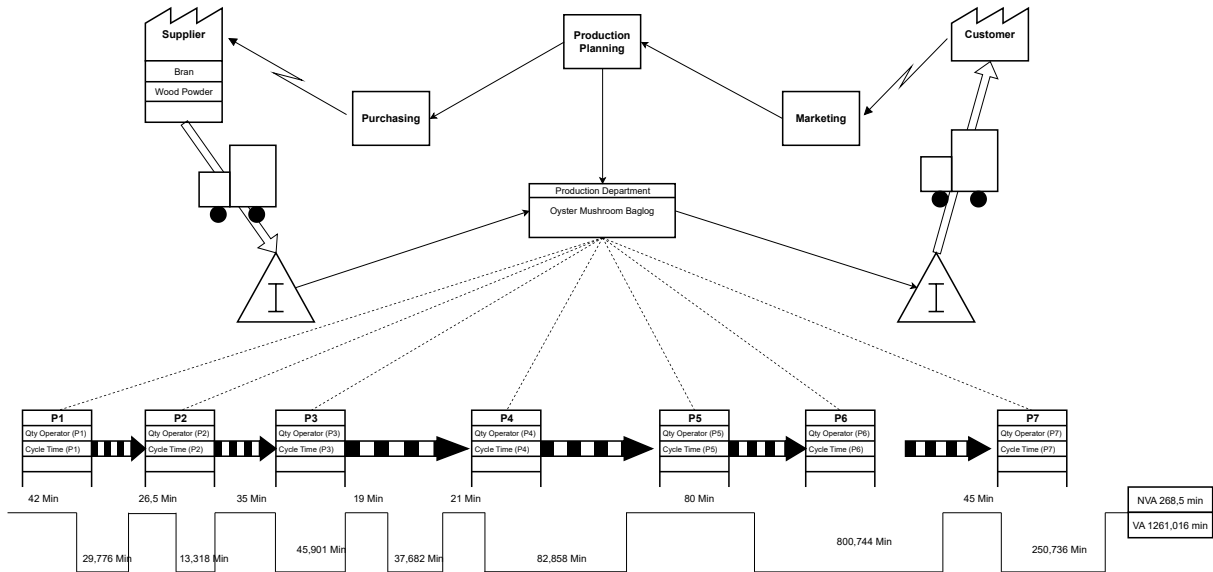


**Figure 2: Current State Value Stream Mapping**

From these calculations, the PCE results obtained from the oyster mushroom baglog production process currently have a process efficiency level of 82,45 %

**3.1.4 Identify Problems Using Fishbone Diagrams**

Fishbone diagrams are a tool to help identify factors that have the potential to influence problems. Fishbone diagrams identified three factors affecting the oyster mushroom baglog production process: machine, method, and environmental factors. Figure 3 shows the results of the fishbone analysis diagram of the oyster mushroom baglog production process:

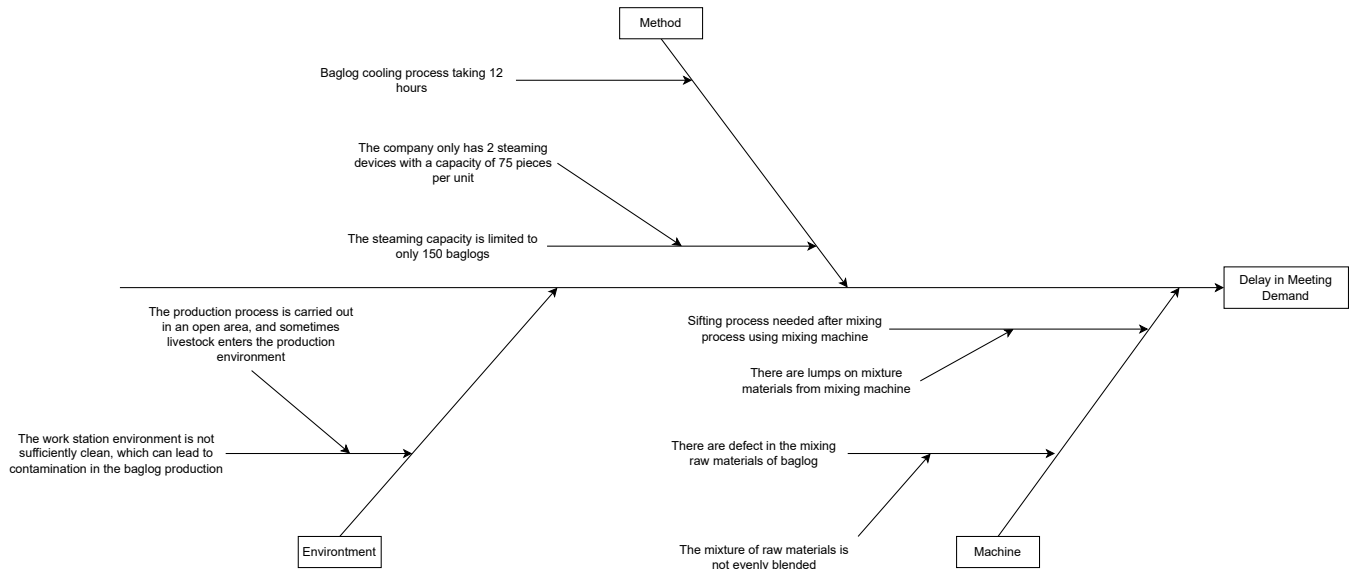


**Figure 3: Fishbone Diagram**

Based on the results of the fishbone diagram above, problems were found in each factor as follows:

- **Machine factor:** The results of mixing baglog raw materials using a mixing machine are currently experiencing clumping, so it requires overprocessing activities in the form of a sieving process.
- **Method factor:** The steaming equipment’s capacity is limited to 150 bags of oyster mushrooms.
- **Environmental factors:** The production floor needs to be cleaner because the space is open, and livestock often enter the production area.

**Table 4: Solution And Target RCA**

Factor	Solution	Detail	Targets
Machine	The mixing machine design uses a stirrer propeller	Make a design for a mixing machine with a stirrer propeller according to the capacity of Mushroom Production Ungaran MSMEs	Get a baglog mixture that is even and without lumps, so it doesn't require a sifting process
Environment	Someone immediately places the results of the mixing baglog into the packaging.	Create a mixing machine design to enter the mixing results into baglog plastic packaging.	An unclean baglog production environment does not contaminate the result of a baglog mixture.
Method	Addition of a steaming tool	Proposing the addition of an oyster mushroom baglog steamer to increase steaming capacity	Increase the steaming capacity of oyster mushroom baglog

**3.1.5 Root Cause Analysis**

The root cause analysis (RCA) process, a research-based, structured, 'step-by-step' method for determining the causes of unfavourable circumstances or issues, is developed from continuous improvement [22]. The outcomes of the root cause investigation into Ungaran Mushroom SME's demand fulfilment delays are as follows at figure 4.

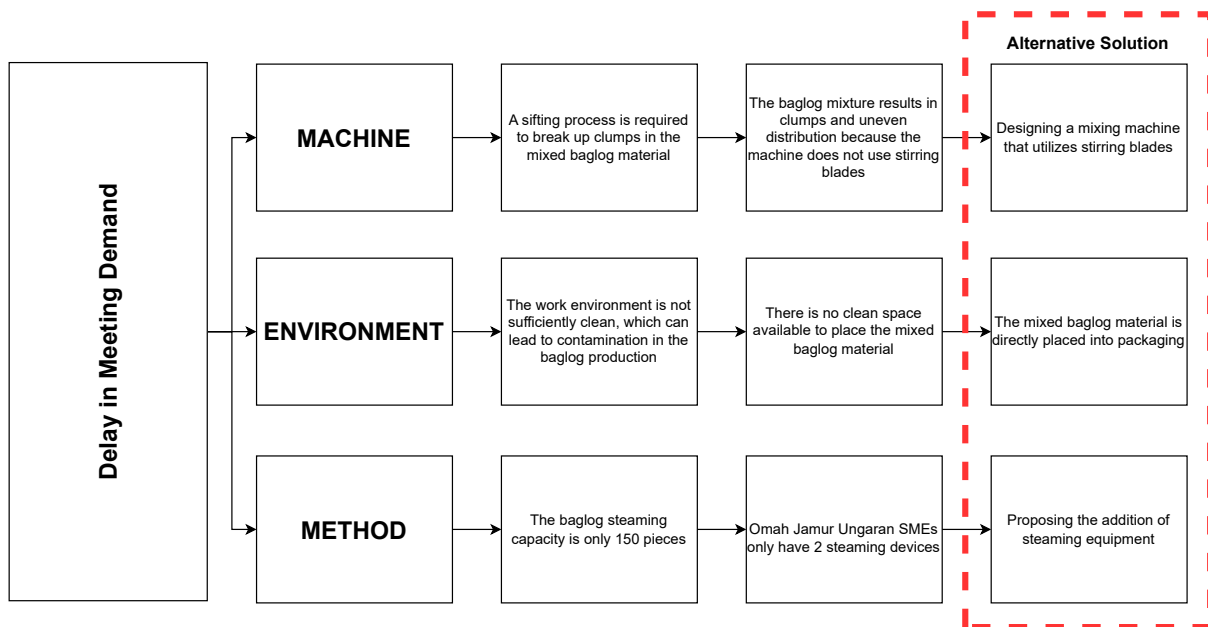


**Figure 4: Root Cause Analysis for Improvements**

From the results of the RCA analysis, we identified alternative solutions for each factor that influenced the problem of delays in fulfilling demand. Details of the solutions and targets to be achieved from each alternative solution created can be seen in Table 4 below.

**3.1.6 Improvements**

Improvements were made based on the results of determining the root of the problem of delays in fulfilling demand. The following is the preparation of corrective actions to reduce manufacturing lead time for oyster mushroom baglog production:

- The lumpy baglog mixture resulting from the mixing process using a mixing machine currently requires an updated stirrer design using a stirrer propeller, and hoping that good mixed results can eliminate overprocessing in the process of sifting the baglog mixture.
- An unclean environment can cause contamination of the baglog. Therefore, pouring the resulting baglog mixture on the production floor is unnecessary. The improvement design involves implementing a filling tank in the mixing machine to enable the direct placement of resulting raw materials into baglog packaging.
- The proposal to add steaming equipment aims to increase the capacity of steaming oyster mushroom baglog in one process at a time. However, Ungaran Mushroom SMEs have been unable to implement this proposal due to high operating costs.

The improvement that Ungaran Mushroom SMEs Production can implement is manufacturing a mixer to overcome the problem of fulfilling the demand for baglogs. We will explore the tool's design and manufacturing process in our other research. After creating an alternative design for a baglog production mixer, the next stage involves manufacturing a mixer to blend ingredients for baglog production. Further research will discuss the outcomes of the baglog raw material mixer design (figure 5).



**Figure 5: Mixer Machine Baglog**

**3.2 Discussion**

Ungaran Mushroom SMEs have achieved results based on the implemented improvements. Comparison of production waiting times after implementing improvements can be seen in table 5 below.

The future state value stream mapping illustrates the flow conditions of the oyster mushroom baglog production process after

**Table 5: Comparison MLT After Improvements**

Workstations	Before (Minutes)	After (Minutes)
Mixing	71,776	29,429
Sifting	39,818	0
Packaging	80,901	39,167
Pressing	56,682	56,682
Providing Cover	103,858	103,858
Sterilization	880,744	880,744
Seeding	295,736	295,736
<b>Total</b>	<b>1529,516</b>	<b>1405,616</b>

we have implemented improvements shown in Figure 6. Table 6 supports the explanation from Figure 6.

**Table 6: Description Future State Value Stream Mapping**

Process (P)	Process Name	Qty Operator	Cycle Time (sec)	Non-Added Value/NVA(minutes)	Value Added/VA(minutes)
P1	Mixing	1	271,550	20,000	9,429
P2	Packaging	1	7,000	10,000	29,167
P3	Pressing	1	9,040	19,000	37,682
P4	Providing Cover	1	19,890	21,000	82,858
P5	Sterilization	1	28826,800	80,000	800,744
P6	Seeding	1	60,180	45,000	250,736
<b>Total</b>		<b>6</b>	<b>29194,460</b>	<b>195,000</b>	<b>1210,616</b>

There is an increase in PCE in future state value stream mapping. The following is the PCE calculation after implementing improvements to the oyster mushroom baglog production process:

$$PCE = \frac{TotalValueAddedTime}{TotalManufacturingLeadTime} = \frac{1210,616}{1405,616} = 86,13\% \tag{6}$$

Table 7 shows a recapitulation of improvements that have been made at the sieving station for the baglog production process. Decrease in the percentage of activities worth NVA from 17,55% to 13,87 % . The production results can reach the target takt time of 5,627 minutes/pcs. PCE increased from 82,45% to 86,13% . There was a reduction in manufacturing lead time for the oyster mushroom baglog production process per day from 1529,516 minutes to 1405,616 minutes. There was also a reduction in the total manufacturing lead time for the baglog production process per month from 28 days to 26 days.

Based on the results of the calculations and analysis of the value stream mapping, the lean manufacturing approach enhances the efficiency of processes within the company, as concluded. This research finding is consistent with several previous studies addressing similar topics. Researchers and practitioners have developed various frameworks for implementing lean, which can enhance the company's benefits by reducing occurring waste [20], [33], [34].

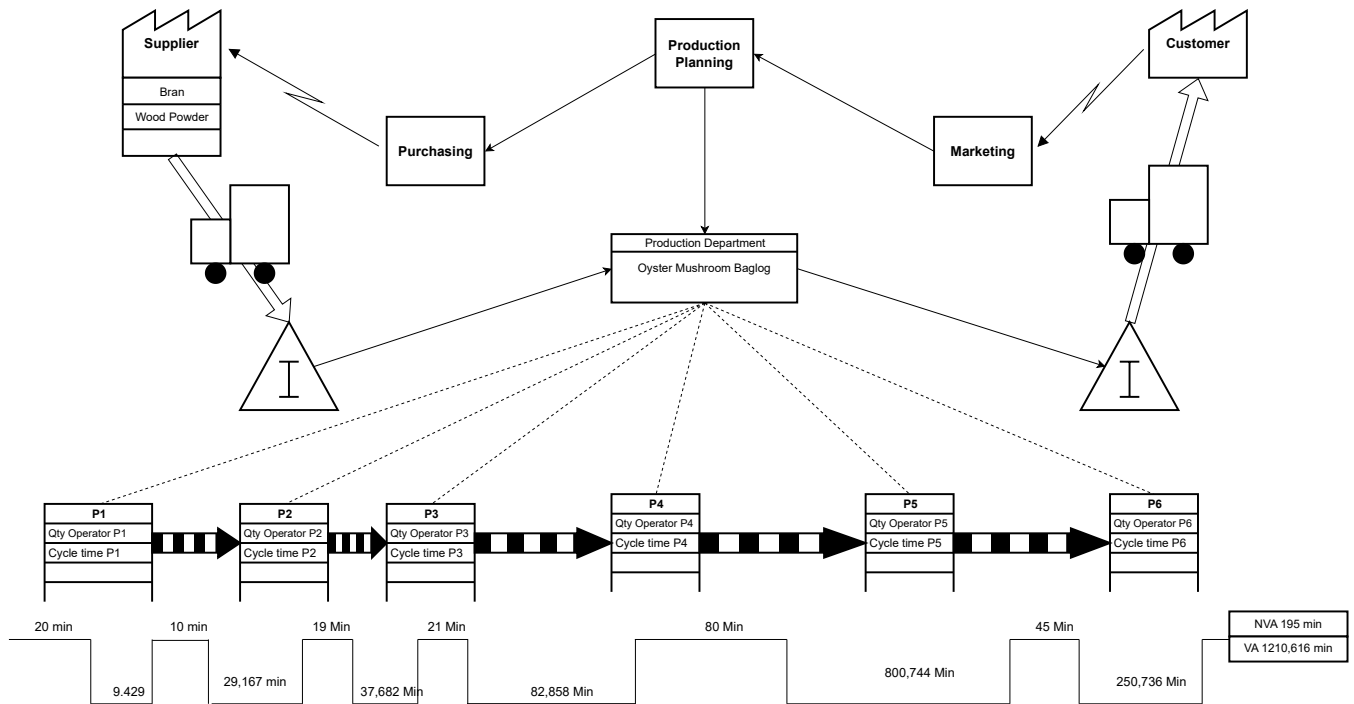


Figure 6: Future State Value Stream Mapping

Table 7: Comparison Results

Comparison	Before	After
Station	7	6
NVA	17,55%	13,87%
Takt Time	6,124 minutes/pcs	5,627 minutes/pcs
PCE	82,45%	86,13%
MLT	1529,516 minutes	1405,616 minutes
Total MLT	28 days	26 days

The research findings are thoroughly analyzed and interpreted in the discussion part, which also situates them within the larger framework of previously published works and industry standards. The Value Stream Mapping (VSM) method assesses how well the implemented improvements reduced Manufacturing Lead Time (MLT) in the oyster mushroom baglog production process. The study aimed to investigate the influence of extended MLT on demand fulfilment delays at UMKM Mushroom Production Ungaran, which affects the timely delivery of oyster mushroom baglogs to customers. To satisfy the average monthly demand of 6462 baglogs, the production process’s identified MLT was 39575,73 minutes, or 28 days, longer than the intended 26 days. VSM, one of the lean manufacturing principles, was used to find and remove waste.

Many academics have stressed the importance of lead time minimization in lean manufacturing to improve operational efficiency [7]. The concepts of Lean Thinking, as promoted by Womack and Jones, emphasize how crucial it is to eliminate waste to produce value effectively. This is consistent with the primary goal of the current study, which is to lower MLT by optimizing the oyster mushroom baglog production process. The proposed research addresses a particular issue in the oyster mushroom baglog producing industry, adding to the body of information already in existence. Although Lean Manufacturing strategies have been extensively studied in a variety of industries [8], [11], [33], the customization of lean methodologies to address the particular issues associated with mushroom cultivation still needs to be discovered. To pinpoint the main causes of manufacturing process delays, the study used techniques including Fish-bone Diagrams and Root Cause Analysis. The investigation uncovered capacity limitations in the steaming process, inadequate environmental cleanliness, and machine-related problems. These results align with research using fish-bone diagrams to effectively identify and examine variables affecting different production processes.

In addition, the research conducted Root Cause Analysis using the 3x5 whys technique to determine the underlying causes of delays in meeting demand methodically. This methodological strategy aligns with earlier studies that stress the significance of using systematic analysis to identify the root causes of unfavourable events [32]. The suggested fixes, which address environmental issues and involve improving the mixing process by revamping the mixing machine and adding an infill tank, show how lean principles may be used in real-world situations. These answers align with academic suggestions that support the use of lean tools to improve process efficiency [13], [16], [35], [36]. When the recommended changes were subsequently

implemented, MLT significantly decreased, demonstrating the effectiveness of the lean solutions. The findings show that the number of workstations sifting has reduced, the Process Cycle Efficiency (PCE) has increased by 3,68% and the MLT has decreased by 3213,718 minutes (2 days). This lead time reduction aligns with the larger lean manufacturing objective of reducing non-value-added processes.

When comparing the before and after situations, it was evident that the enhanced production process had a favourable effect on many necessary performance measures. The optimization of the baglog mixing process is shown in the decrease in the number of sieving workstations, which enhances operational efficiency. The value-added time to total lead time ratio has improved overall, as seen by the rise in PCE from 82,45% to 86,13%. The revised mixing machine has addressed the root causes found in the Fishbone Diagram and Root Cause Analysis with a stirrer propeller and the addition of a steaming tool. The new designs are intended to improve the overall cleanliness of the production environment, provide an even baglog mixture, and remove pointless processes.

The research results significantly contribute to the wider discussion on lean manufacturing, especially for small and medium-sized businesses (SMEs) that grow mushrooms. Lean approaches are adaptable and effective when customized to handle industry-specific difficulties, as demonstrated by Mushroom Production Ungaran's implementation of lean principles.

#### 4 Conclusions

The results of manufacturing lead time calculations for the baglog production process, totalling 39575,73 minutes or 28 days, have proven the delay in fulfilling one month's demand. The demand, which should met within an adequate working time of 26 days, highlighted the need for Improvement. The root cause analysis identified issues such as lumps in the raw material mixture leading to overprocessing through a sieving process, unhygienic environmental factors contributing to potential contamination, and limited steaming capacity causing delays. To address these challenges, the researchers developed an improvement plan involving redesigning the mixing machine with a stirrer propeller to ensure an even mixture without lumps. The mixing machine design also incorporated an infill tank, facilitating the direct placement of mixed raw materials into baglog packaging, eliminating the need for pouring onto the production floor. Implementation of these improvements resulted in reduced workstations, a 3,68% increase in Process Cycle Efficiency (PCE), attainment of the takt time target of 5,627 minutes/pcs, and a decrease in total manufacturing lead time to meet the average monthly demand of 6,462 pcs baglog from 28 days to 26 days.

#### Acknowledgments

Nur Islahudin is an assistant professor in the Industrial Engineering Program at Dian Nuswantoro University. He completed his undergraduate studies at Pancasila University, Jakarta, majoring in Industrial Engineering, and pursued his master's degree at the Bandung Institute of Technology in the Engineering and Industrial Management Program. Before his academic career, the author gained over nine years of practical experience in the automotive industry. My research interests include production systems, quality systems, scheduling systems, and manufacturing engineering.

#### Authors' Contributions

All authors contributed to writing this journal according to their experts and fields.

#### Competing Interests

This research team and I declare no conflict of interest in implementing this research.

#### References

- [1] M. Hultberg, T. Prade, H. Bodin, A. Vidakovic, and H. Asp, "Adding benefit to wetlands – Valorization of harvested common reed through mushroom production," *Science of The Total Environment*, vol. 637-638, pp. 1395–1399, Oct. 2018. [Online]. Available: <https://linkinghub.elsevier.com/retrieve/pii/S0048969718317418>
- [2] W. A. Wan Mahari, W. Peng, W. L. Nam, H. Yang, X. Y. Lee, Y. K. Lee, R. K. Liew, N. L. Ma, A. Mohammad, C. Sonne, Q. Van Le, P. L. Show, W.-H. Chen, and S. S. Lam, "A review on valorization of oyster mushroom and waste generated in the mushroom cultivation industry," *Journal of Hazardous Materials*, vol. 400, p. 123156, Dec. 2020. [Online]. Available: <https://linkinghub.elsevier.com/retrieve/pii/S0304389420311456>
- [3] D. Stadnicka and P. Litwin, "Value stream mapping and system dynamics integration for manufacturing line modelling and analysis," *International Journal of Production Economics*, vol. 208, pp. 400–411, Feb. 2019. [Online]. Available: <https://linkinghub.elsevier.com/retrieve/pii/S0925527318304894>
- [4] A. Erceg, "Lean manufacturing application in the frozen goods industry," *Journal of ekonomi*, vol. 4, no. 2, pp. 57–62, 2022. [Online]. Available: <https://dergipark.org.tr/en/pub/ekonomi/issue/70173/1182631>
- [5] S. Kumar, A. K. Dhingra, and B. Singh, "Process improvement through Lean-Kaizen using value stream map: a case study in India," *Int J Adv Manuf Technol*, vol. 96, no. 5-8, pp. 2687–2698, May 2018. [Online]. Available: <http://link.springer.com/10.1007/s00170-018-1684-8>
- [6] D. D. Shinde, S. Ahirrao, and R. Prasad, "Fishbone Diagram: Application to Identify the Root Causes of Student–Staff Problems in Technical Education," *Wireless Pers Commun*, vol. 100, no. 2, pp. 653–664, May 2018. [Online]. Available: <http://link.springer.com/10.1007/s11277-018-5344-y>
- [7] J. P. Womack and D. T. Jones, "Lean Thinking—Banish Waste and Create Wealth in your Corporation," *J Oper Res Soc*, vol. 48, no. 11, pp. 1148–1148, Dec. 1997. [Online]. Available: <https://www.nature.com/doi/10.1038/sj.jors.2600967>
- [8] S. G. Gebeyehu, M. Abebe, and A. Gochel, "Production lead time improvement through lean manufacturing," *Cogent Engineering*, vol. 9, no. 1, p. 2034255, Dec. 2022. [Online]. Available: <https://www.tandfonline.com/doi/full/10.1080/23311916.2022.2034255>
- [9] R. Hardcopf, G. J. Liu, and R. Shah, "Lean production and operational performance: The influence of organizational culture," *International Journal of Production Economics*, vol. 235, p. 108060, May 2021. [Online]. Available: <https://linkinghub.elsevier.com/retrieve/pii/S0925527321000360>

- [10] S. Gupta and S. K. Jain, "A literature review of lean manufacturing," *International Journal of Management Science and Engineering Management*, vol. 8, no. 4, pp. 241–249, Nov. 2013. [Online]. Available: <https://www.tandfonline.com/doi/full/10.1080/17509653.2013.825074>
- [11] R. Sharma, M. Kasher, L. Zhang, N. Mani, and B. Lai, "Application of Lean Manufacturing Principles in Optimizing Factory Production," in *2018 IEEE MIT Undergraduate Research Technology Conference (URTC)*. Cambridge, MA, USA: IEEE, Oct. 2018, pp. 1–4. [Online]. Available: <https://ieeexplore.ieee.org/document/9244796/>
- [12] S. Yaşar, M. YEŞİLYURT, O. GÜNAYDIN, E. Levent, and T. KÜÇÜKÖMEROĞLU, "Dövme kalıplarında aşınma mekanizmaları," *El-Cezeri*, vol. 8, no. 1, pp. 202–219. [Online]. Available: <https://dergipark.org.tr/en/pub/ecjse/article/819457>
- [13] S. Panigrahi, K. K. Al Ghafri, W. R. Al Alyani, M. W. Ali Khan, T. Al Madhagy, and A. Khan, "Lean manufacturing practices for operational and business performance: A PLS-SEM modeling analysis," *International Journal of Engineering Business Management*, vol. 15, p. 184797902211478, Jan. 2023. [Online]. Available: <http://journals.sagepub.com/doi/10.1177/18479790221147864>
- [14] F. Abu, H. Gholami, M. Z. Mat Saman, N. Zakuan, and D. Streimikiene, "The implementation of lean manufacturing in the furniture industry: A review and analysis on the motives, barriers, challenges, and the applications," *Journal of Cleaner Production*, vol. 234, pp. 660–680, Oct. 2019. [Online]. Available: <https://linkinghub.elsevier.com/retrieve/pii/S0959652619322449>
- [15] D. E. Ufua, T. Papadopoulos, and G. Midgley, "Systemic Lean Intervention: Enhancing Lean with Community Operational Research," *European Journal of Operational Research*, vol. 268, no. 3, pp. 1134–1148, Aug. 2018. [Online]. Available: <https://linkinghub.elsevier.com/retrieve/pii/S0377221717307166>
- [16] N. Kumar, S. Shahzeb Hasan, K. Srivastava, R. Akhtar, R. Kumar Yadav, and V. K. Choubey, "Lean manufacturing techniques and its implementation: A review," *Materials Today: Proceedings*, vol. 64, pp. 1188–1192, 2022. [Online]. Available: <https://linkinghub.elsevier.com/retrieve/pii/S2214785322018284>
- [17] Ö. DEMİRCİ and T. GÜNDÜZ, "Combined application proposal of value stream mapping (vsm) and methods time measurement universal analysis system (mtm-uas) methods in textile industry," *Endüstri Mühendisliği*, vol. 31, no. 2, pp. 234–250, 2020. [Online]. Available: <https://dergipark.org.tr/en/pub/endustrimuhendisligi/issue/56362/728061>
- [18] B. Suhardi, M. Hermas Putri K.S, and W. A. Jauhari, "Implementation of value stream mapping to reduce waste in a textile products industry," *Cogent Engineering*, vol. 7, no. 1, p. 1842148, Jan. 2020. [Online]. Available: <https://www.tandfonline.com/doi/full/10.1080/23311916.2020.1842148>
- [19] M. A. Sayid Mia, M. Nur-E-Alam, and M. K. Uddin, "Court Shoe Production Line: Improvement of Process Cycle Efficiency by Using Lean Tools," *LFJ*, vol. 17, no. 3, pp. 135–146, Sep. 2017. [Online]. Available: [http://revistapielarieincaltaminte.ro/revistapielarieincaltaminteresurse/en/fisiere/full/vol17-nr3/article3\\_ol17\\_issue3.pdf](http://revistapielarieincaltaminte.ro/revistapielarieincaltaminteresurse/en/fisiere/full/vol17-nr3/article3_ol17_issue3.pdf)
- [20] J. Singh and H. Singh, "Application of lean manufacturing in automotive manufacturing unit," *IJLSS*, vol. 11, no. 1, pp. 171–210, Jan. 2020. [Online]. Available: <https://www.emerald.com/insight/content/doi/10.1108/IJLSS-06-2018-0060/full/html>
- [21] S. Patel, D. Mistry, and M. Shah, "A process improvement methodology for effective implementation of value stream mapping integrated with foreman delay survey," *Innov. Infrastruct. Solut.*, vol. 6, no. 3, p. 137, Sep. 2021. [Online]. Available: <https://link.springer.com/10.1007/s41062-021-00512-1>
- [22] G. D. Koltun, S. Feldmann, D. Schutz, and B. Vogel-Heuser, "Model-document coupling in aPS engineering: Challenges and requirements engineering use case," in *2017 IEEE International Conference on Industrial Technology (ICIT)*. Toronto, ON: IEEE, Mar. 2017, pp. 1177–1182. [Online]. Available: <http://ieeexplore.ieee.org/document/7915529/>
- [23] D. E. Ufua, A. S. Ibadunni, M. O. Akinbode, C. G. Adeniji, and B. E. Kehinde, "Value stream mapping, a tool for optimum implementation of systemic lean intervention: a case study of a livestock commercial farm in Nigeria," *IJSOM*, vol. 39, no. 3, p. 399, 2021. [Online]. Available: <http://www.inderscience.com/link.php?id=116123>
- [24] C. Valmohammadi and A. A. Dadashnejad, "Value stream mapping implementation: an operational view," *IJPQM*, vol. 32, no. 3, p. 307, 2021. [Online]. Available: <http://www.inderscience.com/link.php?id=113612>
- [25] J. Lin, X. Fang, Y. Zhang, and Y. Lian, "Application of Plan-Do-Check-Action cycle and fishbone diagram analysis in optimizing surgical procedures to improve satisfaction degree of doctor-nurse-patient," *Ann Eye Sci*, vol. 5, pp. 2–2, Mar. 2020. [Online]. Available: <http://aes.amegroups.com/article/view/5060/html>
- [26] V. Girish, "Identifying the Perspectives of Domestic Tourists Visiting Puducherry of India During the COVID-19 Pandemic: A Fishbone Diagram Analysis," *Tourism (Zagreb, Online)*, vol. 70, no. 1, pp. 127–130, Dec. 2021. [Online]. Available: <https://hrak.srce.hr/267981>
- [27] T. Luo, C. Wu, and L. Duan, "Fishbone diagram and risk matrix analysis method and its application in safety assessment of natural gas spherical tank," *Journal of Cleaner Production*, vol. 174, pp. 296–304, Feb. 2018. [Online]. Available: <https://linkinghub.elsevier.com/retrieve/pii/S0959652617326410>
- [28] M. Groover and G. Jayaprakash, *Automation, Production Systems, and Computer-integrated Manufacturing*, ser. Always learning. Pearson Education Limited, 2015. [Online]. Available: <https://books.google.co.id/books?id=t2fXoAEACAAJ>
- [29] B. Fahimnia, L. H. S. Luong, B. Motevallian, R. M. Marian, and M. M. Esmail, "Analyzing & Formulation of Product Lead Time," 2008.
- [30] R. Sundar, A. Balaji, and R. S. Kumar, "A Review on Lean Manufacturing Implementation Techniques," *Procedia Engineering*, vol. 97, pp. 1875–1885, 2014. [Online]. Available: <https://linkinghub.elsevier.com/retrieve/pii/S1877705814034092>
- [31] Guangdong University of Science & Technology, Dongguan, China and J. Qiu, "Construction and Empirical Analysis of Environmental Cost Early-warning Model for Manufacturing Enterprises Based on Fishbone Diagram," *FMR*, vol. 3, no. 3, Jul. 2019. [Online]. Available: [http://www.isaacpub.org/images/PaperPDF/FMR\\_100062\\_019051410441567231.pdf](http://www.isaacpub.org/images/PaperPDF/FMR_100062_019051410441567231.pdf)
- [32] R. Sweis, A. Moarefi, M. H. Amiri, S. Moarefi, and R. Saleh, "Causes of delay in Iranian oil and gas projects: a root cause analysis," *IJESM*, vol. 13, no. 3, pp. 630–650, Sep. 2019. [Online]. Available: <https://www.emerald.com/insight/content/doi/10.1108/IJESM-04-2018-0014/full/html>
- [33] G. Yadav, S. Luthra, D. Huisingsh, S. K. Mangla, B. E. Narkhede, and Y. Liu, "Development of a lean manufacturing framework to enhance its adoption within manufacturing companies in developing economies," *Journal of Cleaner Production*, vol. 245, p. 118726, Feb. 2020. [Online]. Available: <https://linkinghub.elsevier.com/retrieve/pii/S0959652619335966>
- [34] I. Leksic, N. Stefanic, and I. Veza, "The impact of using different lean manufacturing tools on waste reduction," *Adv produc engineer manag*, vol. 15, no. 1, pp. 81–92, Mar. 2020. [Online]. Available: <http://apem-journal.org/Archives/2020/Abstract-APEM15-1081 - 092.html>
- [35] E. Lamani, A. Ahmad, and M. B. Ahmad, "Lean manufacturing implementation to reduce waste on weighing scale assembly line," *International Journal of Emerging Trends in Engineering Research*, vol. 8, no. 1, pp. 1–2, 2020.
- [36] J. Du, Y. Xue, V. Sugumaran, M. Hu, and P. Dong, "Improved biogeography-based optimization algorithm for lean production scheduling of prefabricated components," *ECAM*, vol. 30, no. 4, pp. 1601–1635, May 2023. [Online]. Available: <https://www.emerald.com/insight/content/doi/10.1108/ECAM-04-2021-0311/full/html>

Research Article

# A New Non-Destructive Multidimensional Yield Determination Method Approach for Walnut Crop

Remzi Gürfidan<sup>1a</sup>, Enes Açıkgozlu<sup>2b</sup>, Mevlüt Ersoy<sup>3c</sup>

<sup>1</sup> Computer Programming Department, Yalvaç Technical Sciences Vocational School, Isparta University of Applied Science, Isparta, Türkiye

<sup>2</sup> Computer Programming Department, Keçiborlu Technical Sciences Vocational School, Isparta University of Applied Science, Isparta, Türkiye

<sup>3</sup> Computer Engineering, Faculty Of Engineering and Natural Sciences, Süleyman Demirel University, Isparta, Türkiye

remzigurfidan@isparta.edu.tr

DOI : 10.31202/ecjse.1435709

Received: 12.02.2024 Accepted: 13.05.2024

**How to cite this article:**

Remzi Gürfidan, Enes Açıkgozlu, Mevlüt Ersoy, " A New Non-Destructive Multidimensional Yield Determination Method Approach for Walnut Crop ", El-Cezeri Journal of Science and Engineering, Vol: 11, Iss: 3, (2024), pp.(246-255).

ORCID: "0000-0002-4899-2219; <sup>b</sup>0000-0001-7293-883X; <sup>c</sup>0000-0003-2963-7729.

**Abstract :** Walnut has an important place in agricultural production and research on it covers various fields. In this study, machine learning algorithms were used for non-destructive estimation of walnut productivity. The researchers developed a setup using audio recordings and images to determine the fullness and void status of walnuts. These data were processed with various machine learning algorithms and the results were evaluated. The algorithms used in the study include RESNET50, DenseNET121, VGG16 and CNN. However, when the results obtained are analyzed, it is seen that the VGG16 algorithm gives the most successful results with 99.79% accuracy and 91.42% val\_accuracy values using imagenet weights. These results were found to be quite successful compared to similar studies in the literature. In future studies, it is aimed to expand the obtained dataset and increase the val\_accuracy value even more. In addition, similar methods are planned to be applied on other nuts such as hazelnuts and almonds. This could be an important step to increase productivity in agricultural production. In conclusion, this study on walnut yield estimation using non-destructive methods offers a new and effective approach in agricultural applications. The use of machine learning algorithms offers potential in various areas such as increasing productivity in walnut production and detecting diseases.

**Keywords :** Machine learning, non-destructive yield determination, nut non-destructive yield calculation, walnut yield determination.

## 1 Introduction

Walnut is a kind of nut with a very high nutritional value that is frequently consumed all over the world [1]. Walnuts contain important nutrients for human metabolism such as Omega-3 fatty acids, antioxidants, protein and fiber content, minerals, and vitamins. Many people consume walnuts in their daily diet routine due to different diseases or for balanced and regular nutrition. People's consumption habits may vary. Walnuts can be consumed raw, that is, fresh, roasted, in flour or milk form. The commonly preferred way of consuming walnuts is to consume them by separating them from the shell after drying. Since walnut food is a hard-shelled food, producers and consumers try to make maximum use of this product [2]. In addition to the edible inner part of the walnut, the inedible hard shells are used as firewood. Walnut shells are used as biomass fuel just like wood, providing secondary gain.

Determining the quality of walnuts, which are widely consumed globally, is based on different criteria. These quality criteria include shell quality, colour, inner walnut, taste and aroma and oil content. Among all these criteria, it is the walnut content that consumers pay the most attention to. Because this parameter constitutes the most important part of the price paid for walnuts. In this food, which is a shelled food and there are limited ways to get an idea about the inside without breaking it, situations such as internal rot, shrivelling and drying of the inner walnut occur. To overcome these handicaps, the inside of the nut must be visualized. Processes such as x-ray technology and ultrasound, which can perform this process, are encountered with radioactive radiation (radiation). Consumption of foods that have undergone these processes carries very unfavourable risks. To overcome these risks, methods such as appearance criteria, weight measurement, shell colour and texture, and flash tests can be tried. However, the reliability of none of these methods can be guaranteed.

The aim of this study is to introduce a reliable, fast, and healthy methodology that will enable the estimation of the inner walnut portion of walnut, which is a nut food, with an innovative approach without breaking the shell and without being exposed to radiation. With the proposed method, it will be possible to estimate how many grams of inner walnut and how many grams of shell can be obtained from the tested walnut in its current state without any crushing. The importance of realizing this process is

to show the transparent yield of the walnuts purchased by the users. In addition to this, the producer and the state or the merchant who makes bulk purchases are to determine the financial values by keeping the correct yield value in the purchase and sale. We aim to minimize the amount of loss called waste, which is taken into account in the trade of this business. For this purpose, we offer an approach that guarantees that the product remains completely healthy, free from any chemical testing or radiological measurements. In the study, walnuts will be placed in the data collection device and 5-second collision sound recordings will be taken. These sound recordings will then be processed and converted first into a signal and then into a histogram graph. As a second step, the walnut will be cracked, and the shell and the inner part will be weighed separately on a precision balance to create a data set. At the end of the proposed methodology, the inner and shell weights of the uncracked walnut will be estimated from the images. At the end of the training, validation accuracy values of 0.9142%, 0.9004%, 0.8455% and 0.4452% were obtained from VGG16, CNN, DenseNet121 and ResNet50 algorithms, respectively. As can be seen from the values, the best performance was achieved by using the VGG16 algorithm using imagenet weights.

In the second part of the study, methods and techniques used in crop yield, yield and quality calculations will be reviewed. In the third section, the technical infrastructure of the methodology proposed in this study will be presented by explaining the findings obtained. In the fourth section, a comparison of the proposed methodology with similar studies will be made and the findings will be discussed. In the last section, the conclusions and future goals of the study will be shared.

## 2 Related Works

Scholars have conducted investigations on a wide range of walnut-related topics. These research focus on the productivity of walnuts, the isolation of walnut species, and the separation of shell and kernel. Scholars have investigated several approaches and procedures for the detachment of the walnut's shell and kernel components. An et al. collected 1200 spectra of three different types of walnut materials after the shells were shattered using near infrared (NIR) spectroscopy. NIR spectroscopy was used to assess the walnut shell and kernel discriminating accuracy. Based on SVM and ELM, a shell-kernel classification model was constructed. The effects of various preprocessing techniques on the accuracy of model recognition are compared. Overall, the SVM and ELM-based shell kernel classification model created for this study demonstrated 97.11% and 97.78% accuracy for the validation set [3]. In order to address common issues with current airflow screening, such as incomplete shell-inner kernel discrimination, high costs, and low efficiency of manually assisted screening, Zhang et al. propose a YOLOX deep learning-based walnut shell-inner kernel detection method [4]. This method makes use of machine vision and deep learning technologies. In order to automatically segment the images and detect natural foreign objects of various sizes (such as fleshy leaf debris, dried leaf debris, and gravel dust) as well as man-made foreign objects (such as paper scraps, packaging material, plastic scraps, and metal parts), they apply two different convolutional neural network structures to walnut images in this study. In 101 test photos, the suggested technique can accurately segment 99.5% of the object regions, and in 277 validation images, it can correctly categorize 95% of the foreign items [5].

The detection of mold within and on the surface of walnuts has been the subject of increased investigation by certain researchers. In order to achieve the non-destructive detection of walnut mold, An et al. developed a walnut mold prediction model utilizing near-infrared spectroscopy in this article. The spectra were pre-processed using a combination of detrending and smooth, multiplicative scattering correction (MSC). The pre-processed spectra's 900–1700 nm band was used to extract features using principal component analysis (PCA), successive projection algorithm (SPA), and competitive adaptive reweighted resampling (CARS). The development of support vector machine (SVM) and extreme learning machine (ELM) models led to 100% accuracy in the identification of rotten walnuts [6]. In this study, Hu et al. assess and distinguish between moldy and normal walnuts using terahertz transmission imaging technology. To determine the filling rate of walnuts, image processing is applied to physical samples with varying internal dimensions. The overall identification accuracy of the three established qualitative discrimination models—SVM, RF and KNN-reaches 90.83%, 97.38%, and 97.87%, respectively [1].

In certain areas, scientists have made more progress in their efforts to classify and identify walnut species. These studies also address more specialized topics like yield calculation. Arndt et al. devised a technique that employs Fourier transform near-infrared (FT-NIR) spectroscopy in conjunction with chemometrics to differentiate between seven distinct geographic origins of walnuts. This analytical instrument is user-friendly, rapid, and versatile. 212 ground and freeze-dried walnut samples that were harvested over the course of three consecutive years (2017-2019) had their NIR spectra gathered. After applying and assessing 50,545 distinct preprocessing combinations, we refined the data preprocessing and used linear discriminant analysis (LDA), which was subsequently verified by nested cross-validation. Thus, this intricate approach can be applied to resolve economically significant issues, like differentiating between Chinese and European walnuts [7]. The suitability of the hyperspectral imaging (HSI) approach for precisely identifying and visualizing Chinese walnut types is examined by Jiang et al. Between 400 and 1000 nm, hyperspectral images of 400 Chinese walnuts, 200 samples of the Ningguo variety, and 200 samples of the Lin'an variety were obtained. To create classification models, three distinct modelling techniques were applied independently: support vector machines (SVM), k-nearest neighbour (KNN), and partial least squares-discriminant analysis (PLS-DDA). With correct classification rates (CCR) of 97.33%, 95.33%, and 92.00% in the calibration, cross-validation, and prediction sets, respectively, the PLS-DA model constructed from the raw full spectrum performed best, according to the results. These findings demonstrated

the exceptional potential of the HSI features and their applicability as a dependable instrument for the establishment of an online identification system for Chinese walnut cultivars [8].

Using chemometric techniques, Peng *et al.* created a regression model for the moisture content of walnut kernels based on NIR diffuse reflectance spectroscopy. The prediction model under these conditions had a squared correlation coefficient ( $R^2$ ) of 0.9865 and a root mean square prediction error (RMSEP) of 0.0017. The study's findings provide a workable technique for quickly determining the moisture content of walnut kernels [9]. Zhu *et al.* want to quickly and accurately classify ten walnut species produced in four provinces by utilizing machine learning techniques in conjunction with Fourier transform mid-infrared spectroscopy. Three different types of models were built using five machine learning classifiers to differentiate between four geographical origins, identify varieties derived from the same origin, and categorize all ten varieties from the four origins. The spectrum was denoised and smoothed using a wavelet transform approach prior to modelling. According to the results, the classification of four distinct origins (accuracy = 96.97%) and the identification of varieties under the same origin performed the best (accuracy = 100% for some origins), while the discrimination of all 10 varieties was the least desirable (accuracy = 87.88%). Additionally, it was demonstrated that random forests (RF) yielded the worst outcomes, whereas back-propagation neural networks (BPNN) offered the highest model performance [10].

In order to assess the quality and quantity of the interior of walnuts and other nuts whose shells are opaque to the naked eye, researchers have experimented with both destructive and non-destructive methods. An optimization model for EU processing planning that a walnut exporter faces was given by Brunner-Parra *et al.* Detailed information from the fruit, including its size, colour, and flaws, was incorporated into our model. Our model became a decision assistance system when it was integrated into a web application. We were able to improve earnings by 9.8% in our computational studies, and in certain circumstances, producers were able to increase their profits by 34% [11]. Qui *et al.*'s work introduces a novel non-destructive technique that uses radiomics and Low Field Magnetic Resonance Imaging (LF-MRI) to evaluate the quality of walnut kernels. The hard shell of walnuts makes it challenging to judge their quality. Radiomics approaches were employed to extract, select, and reduce the dimensionality of features from MRI pictures by analysing the features of the walnut kernel Low Field Nuclear Magnetic Resonance (LF-NMR) relaxation curve and LF-MRI imaging. Using six optimal classification algorithms, ten significant features that are significantly linked to walnut kernel souring were found, and machine learning models were constructed. With a 93.52% test accuracy, 92.78% test recall score, and 96.81% test F1 score, Random Forest (RF) models demonstrated excellent performance [12]. Gao *et al.* suggested combining machine learning with X-ray imaging and image processing technologies to address the issue of low accuracy in walnut mass identification caused by relatively unchanging density. Following the extraction of the form and texture of the walnut characteristic parameters and the kernel shape characteristic parameters, mass prediction models may be constructed by applying image processing technology to separate the kernels from the background of the walnut X-ray picture. Using RBF, an  $R^2$  value of 0.889% was found [13].

An adaptive neuro-fuzzy interface system (ANFIS) was employed by Rezaei *et al.* to forecast the percentage and quality of walnut kernels. Fuzzy and artificial neural network (ANN) learning methods are used in ANFIS. As model inputs, 100 genotypes of walnuts from the Iranian province of Golestan were analyzed for a total of 14 morphological features. ANFIS was able to estimate the percentage of walnut kernels with a coefficient of determination ( $R^2$ ) of 99%, according to data modelling. Additionally, kernel quality detection had a 99% accuracy rate. These findings demonstrated that the most beneficial approach for creating the ANFIS model is to combine the fuzzy c-means (FCM) method with a hybrid training algorithm [14]. The improved whale optimization algorithm (IWOA) was proposed by Zhang *et al.* as a new feature selection technique for walnut kernel protein inversion from hyperspectral images. The model that combined spectral and textural information performed better and produced the best prediction results when compared to models that only used spectral information. The  $R^2$  and RMSE for the calibration group were 0.9047 and 11.1382 g/kg, respectively. The validation group's RMSE was 18.9288 g/kg and  $R^2$  was 0.8537. The findings demonstrated that it is possible to accurately estimate the protein content of walnuts by combining specific wavelengths with textural characteristics using IWOA [15]. A novel technique for non-destructively identifying shriveled kernels in in-shell walnuts was presented by Zhai *et al.* The technique relies on machine learning combined with weight and picture data. First, an industrial charge-coupled device camera and an electronic scale were used to gather weight and picture data for walnut samples. Then, in order to distinguish between the walnuts with wrinkled kernels, three different types of models were developed: a support vector machine (SVM), a back-propagation particle swarm optimization technique (PSO-BP), and partial least squares-linear discriminant analysis. All of the approaches' classification efficiencies were thoroughly compared in order to identify the best one. With an accuracy rate of 97%, the SVM algorithm produced the best results [2].

The discovery of specific disorders linked to walnuts is another area in which the experts have expanded their investigation. The goal of Anagnostis's and his team's study is to develop a quick and accurate object detection system that can identify walnut tree leaves afflicted with anthracnose in order to be used in actual agricultural situations. By comparing the expert classifications with the system's anticipated classes, 279 of the 379 trees in the orchard were utilized to examine the efficacy and resilience of the object detector [16]. Of these, 100 trees were chosen at random to train the detector.

In order to determine and develop the ideal conditions for walnut farming and harvesting, researchers have expanded their investigations. Yang and colleagues employed a hybrid approach of artificial neural network (ANN) and genetic algorithm

(GA) to derive a model of the drying-assisted walnut cracking process along with the ideal parameters for execution. Using air compression technology, walnuts were dried to various moisture contents (10%, 15%, 20%, and 25%) at various infrared temperatures (40, 45, 50, and 55 degrees Celsius) and air velocities (1, 2, 3, and 4 m/s). Subsequently, the dehydrated walnuts were split into three loading directions: longitudinal, vertical, and suture. With coefficients of determination of 0.996, 0.998, 0.990, 0.991, and 0.993 for DT, SEC, HR, WR, and SR, respectively, the ANN model has a good capacity for prediction [17]. Huang et al. used walnut in Wensu County, Aksu District, Xinjiang as the research object in order to address the issues of low accuracy of crop evapotranspiration (ETc) estimation in arid places and optimize ETc for precision irrigation in agriculture. However, Deep learning sequence models including LSTM, GRU, and BiLSTM were used to forecast crop evapotranspiration (ETc) of walnut in arid regions under various micro-irrigation strategies based on multivariate time series data of walnut production [18].

Studies of this kind are being conducted on other nuts, like walnuts. An effective methodology for categorizing hazelnut variants was presented by Taner et al. The dataset with pictures of 17 different types of hazelnuts was used to train the suggested model. It was discovered that the suggested model has an accuracy rate of 98.63%. Other nut dataset's classification performance can be enhanced by adapting the CNN model shown in this paper. The collection consists of 250 photos per image class, with a total of 17 classes [19]. In order to categorize cashew kernels into five groups based on the butts and fragments of first-class fancy whole cashew kernels, Vidyarthi et al. recommended using deep convolutional neural networks (DCNNs) in conjunction with image processing. Model evaluators like sensitivity, specificity, precision, accuracy, and F1-score were used to compare the performance of four DCNN models—Inception-V3, ResNet50, VGG-16, and a custom model—that were implemented [20].

In this study, the physical parameters of walnut kernels, walnut oil and DF from nine different varieties were analyzed. In addition, the effect of genotype, crop year and the interaction between the two on the color parameters of walnut oil and DF was studied [21]. Hakimi et al. evaluated 31 quantitative and qualitative characteristics of seven superior walnut genotypes comparable to 'Jamal', 'Lara' and 'Serr' varieties [22]. There are also comprehensive reviews of walnut nuts in the literature. The aim of the existing reviews is to provide an overview of the bioactive compounds present in the different structural parts of walnut by-products and elderberry fruits, which offer a specific or common activity relevant to human health and the conservation of agricultural products in the context of sustainable development [23].

### 3 Material and Method

In this section, you will find a title with detailed and technical information about the dataset. Then the machine learning methods performed with the dataset will be explained.

#### 3.1 Dataset Collection

The walnuts used in the data collection phase belonged to the same species of walnuts, called Chandler, from one region. In the system shown in Figure 1, a walnut is first placed in a chamber containing a sensitive microphone. Considering that the placed walnuts can be of different sizes, it is ensured that the placed walnuts are always at the same height through the laser distance sensor before hitting the walnut with the moving rod. Until the laser distance sensor detects the placed walnut, the platform is pushed upwards by means of a rotating shaft connected to the stepper motor end. If the sensor detected the walnut in the first placement, the platform is first pulled down and then the platform is pushed upwards until the distance sensor detects the walnut again. After the height of the nut is adjusted, the nut is tapped with the help of a rod connected to the end of the servo motor. The tapping process is achieved by the servo motor lifting the rod up 45 degrees and lowering it again. In order to ensure that the servo motor can easily hit the walnut, the required height was created with a fixed platform.

The sound waves produced by hitting the walnut were recorded to the computer in mp3 file format by means of a microphone. A computer and an Arduino Uno control card connected to the computer were used for all these operations. The sound files recorded through the computer were numbered separately for each nut. The recorded sounds were converted from mp3 file format to wav format.

Audio files in Wav format are converted into a graph in frequency space so that they can be processed as images. In this way, audio files are converted into a form that machine learning algorithms can learn. Examples of frequency images obtained from walnuts are shown in Table 1. After the image conversion process was completed, the walnuts were crushed and separated into shell and kernel walnuts. Each walnut was weighed separately with a precision balance and clustered by the ratio of the total weight to the weight of the inner walnut. This clustering was used to determine the class to which the related walnut image would belong.

The obtained numerical values and examples of class identification are shown in Table 2. A total of 1457 walnuts were used to create the dataset.

As seen in Table 2, the percentage value obtained from the ratio of the total weight of the walnut and the amount of walnut kernel obtained was used to determine the class to which the walnuts belonged. Class values vary between 1-9. While 1 is the least productive walnut class, 9 is the most productive walnut class.

**Table 1: Examples of frequency domain images obtained from walnuts.**

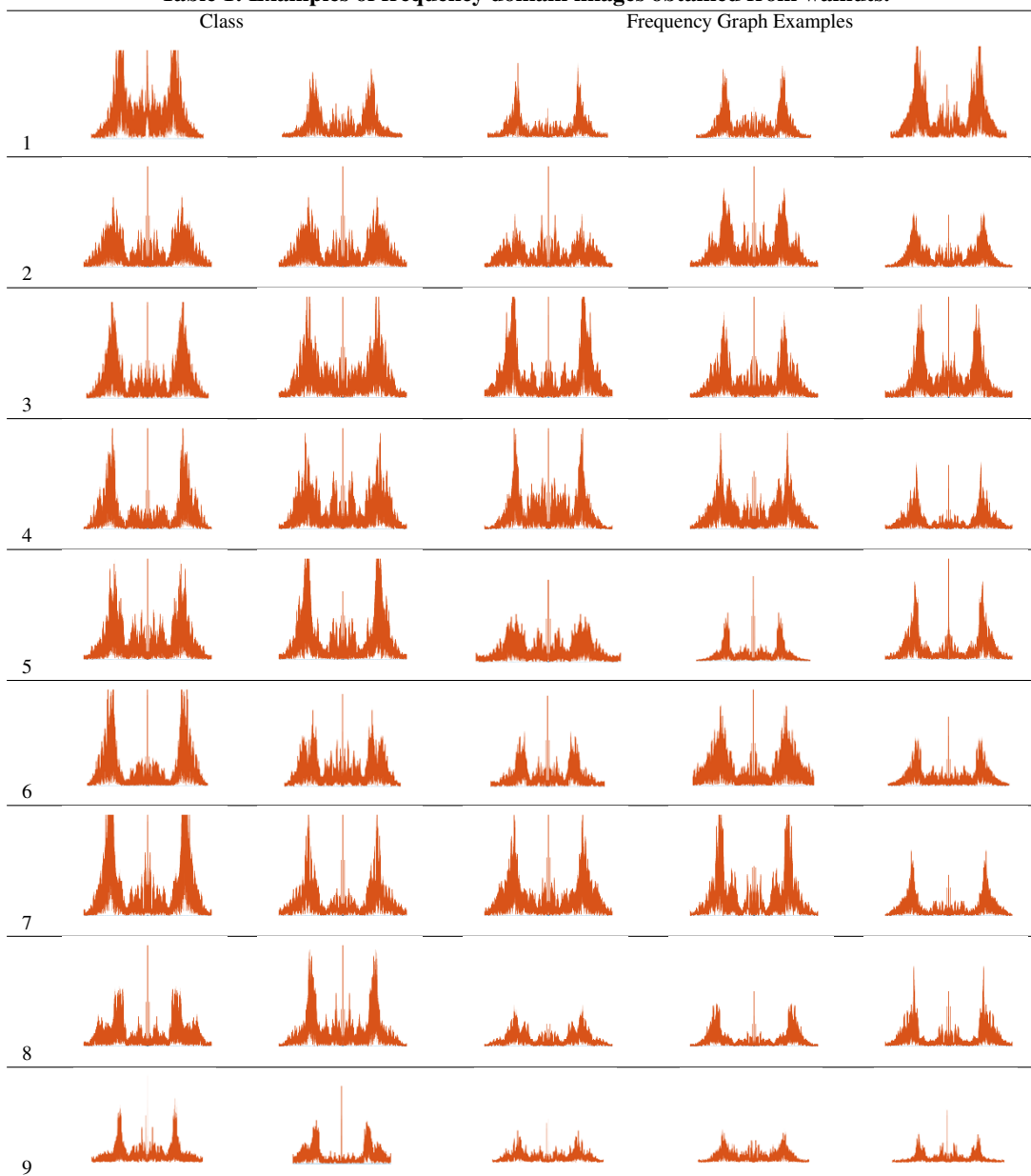


**Table 2: Numerical data obtained from walnuts and classification criteria.**

Walnut No	Total Weight	Shell Weight	Kernel Weight	Internal Yield Rate	Class Type
...	...	...	...	...	...
22	8	4	4	50.00	6
23	8	5	3	37.50	4
...	...	...	...	...	...
124	7	4	3	42.86	5
125	7	3	4	57.14	8
...	...	...	...	...	...
420	10	7	3	30.00	2
421	10	4	6	60.00	8
...	...	...	...	...	...
890	6	3	3	50.00	6
891	6	3	3	50.00	6
...	...	...	...	...	...
1456	9	5	4	44.44	5
1457	9	5	4	44.44	5

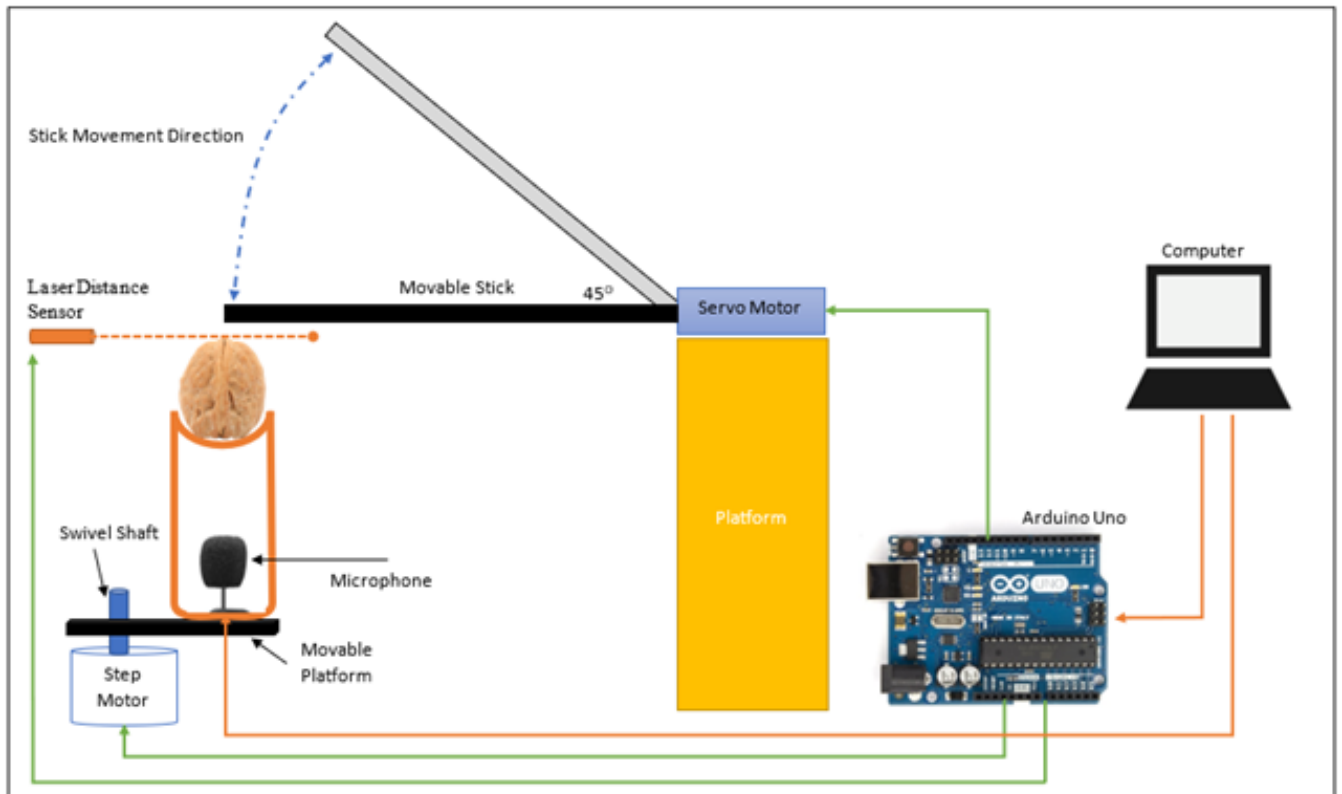


Figure 1: Architecture of the data collection setup

Table 3: Architectural Variable Values of Algorithms.

Model	VGG16	CNN	DenseNet121	ResNet50
Architecture Variables				
Weights	imagenet	-	imagenet	imagenet
Activation Function	softmax	ReLU, softmax	softmax	ReLU, softmax
Loss	Categorical crossentropy	Categorical crossentropy	Categorical crossentropy	Categorical crossentropy
Optimizer	adam	adam	adam	adam
Epochs	20	20	20	20
Validation Split	0.2	0.2	0.2	0.2

### 3.2 Machine Learning Models and Hyperparameters

Machine Learning models include algorithms used in fields such as data analysis and pattern recognition. These algorithms are used to identify patterns in data sets and predict future data. Commonly used algorithms such as VGG16, DenseNet121, CNN, and ResNet50. VGG16 is a convolutional neural network containing 16 layers. In this model, weights are learnable parameters and are removed from the data set during training. Activation functions determine the outputs of neurons in each layer and influence the learning capacity of the model. Generally, ReLU (Rectified Linear Unit) and Softmax function are preferred. The loss function measures the difference between the model’s actual labels and its predictions. Mean Squared Error or cross entropy are frequently used loss functions. The optimizer algorithm is used to update the model’s weights during training. Methods such as Stochastic Gradient Descent and Adam optimizer are frequently preferred. Epochs indicate how many times the data set is processed by the model during the training process. This can increase the model’s ability to recognize more patterns and generalize. Validation split allows a portion of the data set to be reserved for validation during training. This helps prevent overfitting of the model and increases its generalization ability. These variables are important factors that affect the performance of Machine Learning models. Architecture values of the machine learning models used in this study are shown in Table 3.

In this section, since the accuracy values obtained from the ResNet50 algorithm were found to be quite low, re-trials were carried out by increasing the learning number. However, it was clearly seen in the following chapters that it could not reach the

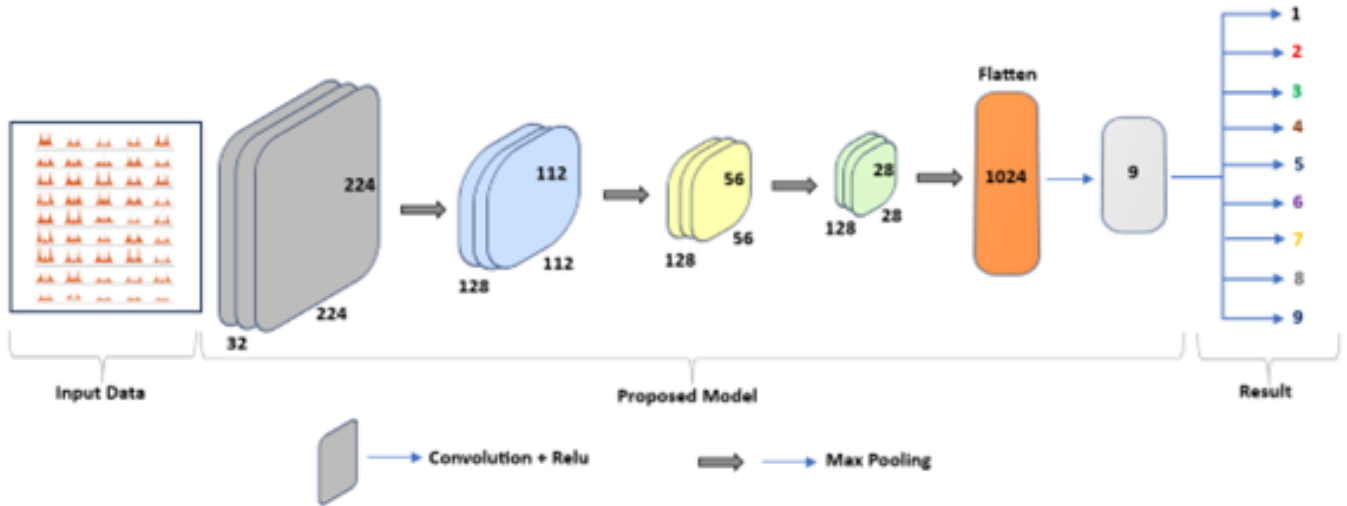


Figure 2: CNN architecture used for model training

Table 4: Accuracy, loss, sharpness and sensitivity values as a result of training machine learning algorithms.

Metrics/Algorithms	VGG16	CNN	DenseNet121	RESNET50
Accuracy	0.9979	0.9990	0.9474	0.5227
Loss	0.0199	0.0031	0.2710	1.3054
Recall_m	0.9979	0.9990	0.8708	0.2487
Precision_m	0.9989	0.9990	0.9928	0.8093
F1_m	0.9983	0.9990	0.9269	0.3655
Val_Accuracy	0.9142	0.9004	0.8455	0.4452
Val_Loss	0.4290	0.6611	0.5421	1.3789
Val_Recall	0.9068	0.8963	0.7357	0.2500
Val_Precision_m	0.9435	0.9103	0.8867	0.8217
Val_F1_m	0.9225	0.9029	0.8023	0.3643

desired level of success, and the reasons for this were discussed.

Figure 2 shows the CNN architecture prepared for model training. The highest accuracy value in the training results was obtained from the CNN architecture. However, it ranks second among all models in terms of validation accuracy value. It also shows the same degrees in F1 score metric values. For this reason, the numerical results prove that the CNN architecture prepared is successful.

#### 4 Result and Discussion

In this section, accuracy, loss and other metric values obtained from machine learning algorithms will be presented. The performances of the trained algorithms will be compared with each other. Recall, precision, accuracy, f1\_m and loss values will be given together with validation measurements so that the results obtained are as clear as possible for the readers and the success of the trained model can be clearly seen. Four different machine learning methods were tried to train the data set. These algorithms are VGG16, CNN, DenseNet121 and Resnet50. We believe that the best efficiency that can be obtained from training with the data set will be obtained by observing the results of these four algorithms.

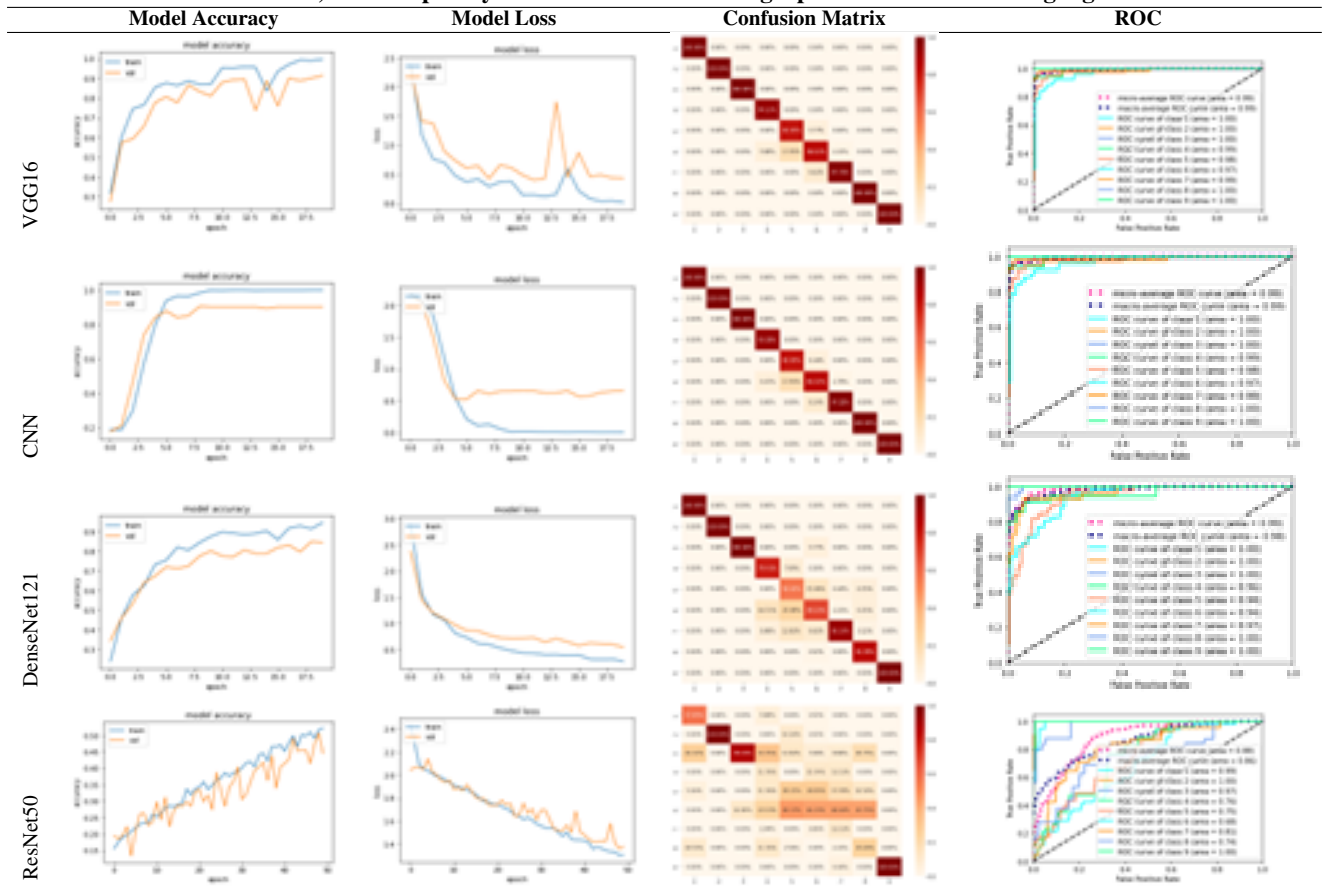
In machine learning, precision and recall are metrics used to evaluate the performance of classification models. In addition to these metrics, the terms val\_precision and val\_recall refer to the precision and recall values calculated on the validation set. Precision indicates how many of the instances that a classification model predicts as positive are actually positive. Precision measures how few false positives (instances predicted as positive by the model that are actually negative) are made. A high precision value indicates the reliability of the model by showing that most of the samples that your model predicts as positive are actually positive. The precision value can be calculated as in Equation 1. TP: True Positives, FP: False Positives;

$$Precision = TP / (TP + FP) \tag{1}$$

Recall shows how many true positives (instances that the model correctly predicts as positive) are captured. Sensitivity is important to minimize the cases where your model misses true positives (false negatives). A high recall value indicates that your model captures most of the true positives. FN: False Negatives, the Recall value can be calculated as in Equation 2.

$$Recall = TP / (TP + FN) \tag{2}$$

**Table 5: Success, loss complexity metric and ROC Curve graphs of machine learning algorithms.**



**val\_precision** is the precision value calculated on the validation set. It indicates how many of the samples that the model predicts as positive in the validation set are actually positive. **val\_recall** is the sensitivity value calculated on the validation set. It shows how much of the true positives are captured in the validation set. Table 5 shows the accuracy, loss graphs, complexity matrix and ROC curve graphs obtained from the machine learning algorithms.

When the accuracy and loss graph obtained after training the ResNet50 algorithm is examined, it is seen that the train and validation lines progress in a zigzag manner. There may be several reasons for this situation. In such cases, if the data set is small or the diversity of your data set is insufficient, your model may tend to overfit the data. In this case, your model may fluctuate during training. In addition, if the model is too complex or has too many parameters, it may be more difficult for the model to learn during training, which may cause fluctuations. Considering these reasons, it is seen that the ResNet50 algorithm is not successful on the existing dataset and is inadequate. As can be seen from the confusion matrix and ROC graph, the model performs a very unsuccessful classification. It has been determined that the other algorithms are close to each other both graphically and in terms of their classification success. Of these three algorithms, it is clearly seen that VGG16 and CNN algorithms are very close to each other and show more successful results than the results of the other two algorithms.

When the studies on similar topics in the literature are examined, it is seen that the success rate obtained is quite promising. The success rates and the metrics shown in the study provide more detailed information than other studies. Although many studies complete the study by giving only Accuracy value, in this study, Accuracy and Val\_accuracy values are given together and model learning is transparently revealed. Table 6 shows the year, methodology, technique, dataset, study purpose, and success status of similar studies. In addition, the precision and recall values shown in Table 4 clearly show the precision and accuracy of the model.

The novelty and perspective positions that this study brings to the literature can be explained as follows;

- The study introduces a non-destructive method for estimating walnut yield using machine learning algorithms. This contributes to the existing literature by providing an innovative approach that does not require physical destruction of walnuts for evaluation.
- The study introduces a new method of data collection using voice recordings to assess the fullness and void status of walnuts. This extends existing techniques for collecting data in agricultural studies and potentially inspires similar approaches in other crop yield prediction research.

**Table 6: Comparison table of studies similar to this study according to different criteria**

Ref.	Year	Dataset	Technique	Aim	Metrics
An et.al. [3]	2022	1200 spectrum image	SVM, ELM, GA+ELM	Classification of walnut shell, kernel and Diaphragma juglandis Fructus (DJF) structures	Accuracy: 97.11%
Taner et.al. [19]	2021	4250 images	CNN	Classification of hazelnut species by image	Accuracy: 98.63%
Jiang et.al. [8]	2021	400 images	PLS-DA, KNN, SVM	Correctly identifying Chinese walnut varieties	Accuracy: 97,33%
Peng et.al. [9]	2021	136	MLR, PCR, PLS, SVR	Estimation of moisture content in walnut kernels	R <sup>2</sup> : 98.65%
Rong et.al. [5]	2019	378 images	CNN	Detection of foreign substances inside the walnut	Accuracy: 95%
Anagnostis et.al. [16]	2021	379 images	VGG16, YOLO, RESNET50	Detecting infected leaves on walnut trees on the tree	Accuracy: 87%
Qiu et.al. [12]	2024	Approximately 1000 walnuts	SVM, SGD, KNN, RF, LightGBM, XGBoost	Walnut internal quality was evaluated with LF-MRI technology.	Accuracy: 93.52%
Gao et.al. [13]	2022	-	RBF	Estimation of walnut internal mass by X-Ray technology	R <sup>2</sup> : 88.9%
Rezaei et.al. [14]	2022	100 walnuts	Anfis	Estimating walnut kernel percentage and kernel quality	R <sup>2</sup> : 99%
Zhang et.al. [4]	2023	185 walnuts, 2753 images	YOLOx, YOLOv3, Faster-RCNN, SSD	Realization of walnut shell and kernel separation	Accuracy: 96.3%
Zhang et.al. [15]	2022	30 walnuts	SVM, RF, BPNN	Walnut kernel protein inversion from hyperspectral image	R <sup>2</sup> : 85%
Hu et.al. [1]	2022	2445 walnuts	SVM, RF, KNN	Identify and analyze normal walnuts and moldy walnuts	Accuracy: 97.8%
Zhai et.al. [2]	2020	-	SVM, PSO-BP	Detecting shriveled kernels from walnut image and weight information	Accuracy: 97%
This Work	2024	1457 walnuts and images	VGG16, CNN, RESNET50, DENSENET121	Yield estimation from walnut sound frequency plane images	Val_Accuracy: 91.42 %

• The study mentions plans to apply similar processing techniques to different nuts such as hazelnuts and almonds. This extension of the methodology broadens the applicability of the findings beyond walnuts, demonstrating their potential generalizability across a variety of nuts.

## 5 Conclusion

In this study, machine learning algorithms were trained to non-destructively predict the yield of walnuts. With the help of a mechanism prepared for the realization of the study, audio recordings were taken, which we thought would allow us to obtain the occupancy and vacancy status of all walnuts under equal conditions. These records were taken in the frequency plane and their images were recorded so that the image algorithms could process them. To classify the images, the value obtained from the ratio of the whole weight of the walnut to the inner walnut was recorded as the class label. When the accuracy and loss results obtained from different machine learning algorithms were evaluated, the most successful VGG16 algorithm was using imagenet weights to obtain Accuracy of 99.79% and Val\_accuracy of 91.42%. When the results obtained are compared with similar studies in the literature, it can be seen that successful results have been achieved. In future studies, it is aimed to further increase the Val\_accuracy value by increasing the amount of data. In addition, similar processing processes are planned to be applied to different nuts such as hazelnuts and almonds.

## Authors' Contributions

RG: training of machine learning algorithms, interpretation of results, literature and conclusion section author. EA: design of the data collection system and creation of the data set, author of the introduction and literature section. ME: author of the training of machine learning algorithms, interpretation of results and discussion section.

## Competing Interests

The authors declare that they have no conflict of interest.

## References

- [1] J. Hu, H. Shi, C. Zhan, P. Qiao, Y. He, and Y. Liu, "Study on the Identification and Detection of Walnut Quality Based on Terahertz Imaging," *Foods* 2022, Vol. 11, Page 3498, vol. 11, no. 21, p. 3498, 2022.
- [2] Z. Zhai, Z. Jin, J. Li, M. Zhang, and R. Zhang, "Machine learning for detection of walnuts with shriveled kernels by fusing weight and image information," *Journal of Food Process Engineering*, vol. 43, no. 12, p. e13562, 2020.
- [3] M. An, C. Cao, Z. Wu, and K. Luo, "Detection Method for Walnut Shell-Kernel Separation Accuracy Based on Near-Infrared Spectroscopy," *Sensors* 2022, Vol. 22, Page 8301, vol. 22, no. 21, p. 8301, 2022.
- [4] Y. Zhang, X. Wang, Y. Liu, Z. Li, H. Lan, Z. Zhang, J. Ma, Y. Zhang, X. Wang, Y. Liu, Z. Li, H. Lan, Z. Zhang, and J. Ma, "Machine Vision-Based Chinese Walnut Shell-Kernel Recognition and Separation," *Applied Sciences* 2023, Vol. 13, Page 10685, vol. 13, no. 19, p. 10685, 2023.
- [5] D. Rong, L. Xie, and Y. Ying, "Computer vision detection of foreign objects in walnuts using deep learning," *Computers and Electronics in Agriculture*, vol. 162, pp. 1001–1010, 2019.
- [6] M. An, C. Cao, S. Wang, X. Zhang, and W. Ding, "Non-destructive identification of moldy walnut based on NIR," *Journal of Food Composition and Analysis*, vol. 121, p. 105407, 2023.
- [7] M. Arndt, A. Drees, C. Ahlers, and M. Fischer, "Determination of the Geographical Origin of Walnuts (*Juglans regia* L.) Using Near-Infrared Spectroscopy and Chemometrics," *Foods* 2020, Vol. 9, Page 1860, vol. 9, no. 12, p. 1860, 2020.
- [8] H. Jiang, L. Ye, X. Li, and M. Shi, "Variety Identification of Chinese Walnuts Using Hyperspectral Imaging Combined with Chemometrics," *Applied Sciences* 2021, Vol. 11, Page 9124, vol. 11, no. 19, p. 9124, 2021.
- [9] D. Peng, Y. Liu, J. Yang, Y. Bi, and J. Chen, "Nondestructive Detection of Moisture Content in Walnut Kernel by Near-Infrared Diffuse Reflectance Spectroscopy," *Journal of Spectroscopy*, vol. 2021, pp. 1–9, 2021.
- [10] H. Zhu, J.-L. Xu, A. Biancolillo, A. Antonio, and D. Archivio, "Authentication and Provenance of Walnut Combining Fourier Transform Mid-Infrared Spectroscopy with Machine Learning Algorithms," *Molecules* 2020, Vol. 25, Page 4987, vol. 25, no. 21, p. 4987, 2020.
- [11] C. F. Brunner-Parra, L. A. Croquevielle-Rendic, C. A. Monardes-Concha, B. A. Urrea-Calfuñir, E. L. Avanzini, and T. Correa-Vial, "Web-Based Integer Programming Decision Support System for Walnut Processing Planning: The MeliFen Case," *Agriculture* 2022, Vol. 12, Page 430, vol. 12, no. 3, p. 430, 2022.
- [12] Z. Qiu, Y. Bian, F. Wang, T. Huang, and Z. Wang, "A novel method for detection of internal quality of walnut kernels using low-field magnetic resonance imaging," *Computers and Electronics in Agriculture*, vol. 217, p. 108546, 2024.
- [13] T. Gao, S. Zhang, H. Sun, and R. Ren, "Mass detection of walnut based on X-ray imaging technology," *Journal of Food Process Engineering*, vol. 45, no. 8, p. e14034, 2022.
- [14] M. Rezaei, A. Rohani, and S. S. Lawson, "Using an Adaptive Neuro-fuzzy Interface System (ANFIS) to Estimate Walnut Kernel Quality and Percentage from the Morphological Features of Leaves and Nuts," *Erwerbs-Obstbau*, vol. 64, no. 4, pp. 611–620, 2022.
- [15] Y. Zhang, Z. Tian, W. Ma, M. Zhang, and L. Yang, "Hyperspectral detection of walnut protein contents based on improved whale optimized algorithm," *International Journal of Agricultural and Biological Engineering*, vol. 15, no. 6, pp. 235–241, 2022.
- [16] A. Anagnostis, A. C. Tagarakis, G. Asiminari, E. Papageorgiou, D. Kateris, D. Moshou, and D. Bochtis, "A deep learning approach for anthracnose infected trees classification in walnut orchards," *Computers and Electronics in Agriculture*, vol. 182, p. 105998, 2021.
- [17] T. Yang, X. Zheng, S. K. Vidyarthi, H. Xiao, X. Yao, Y. Li, Y. Zang, and J. Zhang, "Artificial Neural Network Modeling and Genetic Algorithm Multiobjective Optimization of Process of Drying-Assisted Walnut Breaking," *Foods* 2023, Vol. 12, Page 1897, vol. 12, no. 9, p. 1897, 2023.
- [18] H. Huang, Y. Song, Z. Fan, G. Xu, R. Yuan, and J. Zhao, "Estimation of walnut crop evapotranspiration under different micro-irrigation techniques in arid zones based on deep learning sequence models," *Results in Applied Mathematics*, vol. 20, p. 100412, 2023.
- [19] A. Taner, Y. B. Öztekin, and H. Duran, "Performance analysis of deep learning cnn models for variety classification in Hazelnut," *Sustainability (Switzerland)*, vol. 13, no. 12, p. 6527, 2021.
- [20] S. K. Vidyarthi, S. K. Singh, R. Tiwari, H. W. Xiao, and R. Rai, "Classification of first quality fancy cashew kernels using four deep convolutional neural network models," *Journal of Food Process Engineering*, vol. 43, no. 12, p. e13552, 2020.
- [21] A. Rabadán, J. E. Pardo, R. Gómez, and M. Álvarez-Ortí, "Evaluation of physical parameters of walnut and walnut products obtained by cold pressing," *LWT*, vol. 91, pp. 308–314, 2018.
- [22] Y. Hakimi, Z. Taheri, and A. Rahmani, "Morphological, pomological, and biochemical evaluation of several superior walnut (*Juglans regia* L.) genotypes," *Genetic Resources and Crop Evolution*, 2024.
- [23] A. Sandu-Bălan (Tăbăcariu), I.-L. Ifrim, O.-I. Patriciu, I.-A. Ștefănescu, and A.-L. Finaru, "Walnut By-Products and Elderberry Extracts—Sustainable Alternatives for Human and Plant Health," *Molecules*, vol. 29, no. 2, 2024.



Research Article

# The Development of an IoT-based Cyber-Physical System for Parkinson's Disease Patients Using ML Prediction Algorithm

Sakthisudhan K<sup>1a</sup>, Wahyu Pamungkas<sup>2b</sup>, Anggun Fitriani Isnawati<sup>2c</sup>, Umar Ali Ahmad<sup>3d</sup>, Mohan Raj S<sup>4e</sup>, and Reza Rendian Septiawan<sup>3f</sup>

<sup>1</sup> Dept. Of Electronics & Communication Engg., Dr.N.G.P. Institute of Technology, Coimbatore, India

<sup>2</sup> Faculty of Telecommunications and Electrical Engg., Institute Teknologi Telkom Purwokerto, Purwokerto, Indonesia

<sup>3</sup> School of Electrical Engineering, Telkom University, Indonesia.

<sup>4</sup> Dept. Of Electronics & Communication Engg., M.Kumarasamy College of Engg., India

drkssece@gmail.com

DOI : 10.31202/ecjse.1419630

Received: 15.01.2024 Accepted: 22.05.2024

## How to cite this article:

Sakthisudhan Karuppanan, Wahyu Pamungkas, Anggun Fitriani Isnawati, Umar Ali Ahmad, Mohan Raj S, Reza Rendian Septiawan, "The Development of an IoT-based Cyber-Physical System for Parkinson's Disease Patients Using ML Prediction Algorithm", El-Cezeri Journal of Science and Engineering, Vol: 11, Iss: 3, (2024), pp.(256-266).

ORCID: "0000-0002-8876-3015"; <sup>b</sup>0000-0002-4328-8900; <sup>c</sup>0000-0001-9570-9239; <sup>d</sup>0000-0001-9285-297X; <sup>e</sup>0000-0000-0000-0000;

<sup>f</sup>0009-0009-4707-5062.

**Abstract :** Most people in the present eternal world are stressed and wrecked with diseases because of genetic, environmental, and emotional factors. Some of these diseases are incurable but different hopeful and life-extending treatment methods have been developed. An example is Parkinson's which causes degeneration in the brain and spinal cord with the most noticeable signs identified to be trembling, stiffness, slowness of movement, and difficulty in walking. Dementia is a form of brain condition symptomized by depression and anxiety that worsens as a result of Parkinson's and also makes it hard for the affected individuals to sleep at night. However, the prototypes of the treatment methods are hypothesized to limit the capacities of people with this disease. There is also a lack of diagnostic instruments to determine the precise status of some diseases, leading to the development of wearable sensors to diagnose Parkinson's disease (PD) in its earliest stages when treatment is most effective. In this work we propose a prototype to detect brain waves and other forms of human records through the installation of some effective sensors to determine the improvement in the central nervous system for the patients. A machine learning with prediction algorithm was adopted to observe the progress of the patients as well as to store the data in the cloud automatically to ensure reliable analysis of performance at any period. Furthermore, the prediction system is developed based on the fuzzy k-nearest neighbor (FKNN) for better classification. The proposed prototype is expected to assist in monitoring the patients in several ways other than just measuring vitals such as heart rate, blood pressure, and temperature.

**Keywords :** Parkinson's disease, Fuzzy k-nearest neighbor, Sensors, Cloud platform.

## 1 Introduction

Embedded systems are very important in the design of different electronic devices due to the ease of onboarding in microcontrollers and the primary role in prototypes. It has also been stated that 98% of all microprocessors are normally used in embedded systems. Moreover, the advancement of Internet of Things (IoT) and subsequent integration into cyber-physical systems have opened up new avenues for healthcare applications [1]. The management of Parkinson's disease (PD) can specifically benefit from these technologies through the provision of continuous monitoring and personalized care for affected individuals [2]. PD is a neurodegenerative condition that causes motor deficits such as tremors, stiffness, and bradykinesia at any stage. The management of these symptoms and the design of a monitoring strategy to determine the progression of disease are important for ensuring appropriate care and timely interventions. However, these activities are not present in the conventional treatment methods, leading to limited insights and delayed responses.

A system combining IoT devices, data collection sensors, and prediction algorithm was proposed to develop a comprehensive framework for continuous monitoring and predictive analysis to address the challenges identified. The integration of wearable sensors, ambient monitoring devices, and smart home technologies into system is to ensure the collection of real-time data on different physiological and environmental parameters. The rich dataset serves as the foundation for developing prediction algorithm to anticipate symptom exacerbation, falls, or medication needs. This is necessary because the requirements to ensure continuous monitoring of symptoms as well as the variations in motor function are one of the obstacles associated with the management of PD. A solution is offered by IoT technology by enabling remote monitoring of patients in real-time to allow

medical practitioners to monitor the progress and make informed decisions regarding the appropriate therapy and any necessary alterations to medication.

Embedded systems have been applied in designing several treatment methods throughout the world [3]. These systems were applied in the proposed prototype in addition to machine learning with prediction algorithm. The purpose was to detect brain waves through sensors with the main objective of determining the efficiency of treatment on patients and storing the data in the cloud. Moreover, prediction algorithm was included to habitually monitor the performance of the patients with a focus on the heart rate, blood pressure, temperature, and others. It is important to state that sensors can be placed in different parts of the human body such as the head with the assistance of a cap to detect the brain waves regularly.

IoT-based cyber-physical system was designed for Parkinson's patients in this study through the adoption of prediction algorithm to ensure better quality of life. The process focused on integrating sensors, wearable devices, and machine learning algorithms to collect and analyze data in real-time. The reason was to predict and detect the occurrence of motor symptoms to ensure proactive intervention and personalized care. This study is divided into several parts including Chapter I which explains the introduction, Chapter II discusses the latest study on symptom measurement, Chapter III reviews related works, Chapter IV presents the methods, Chapter V which presents the results and discussion session, and Part VI is the conclusions.

## 2 The Current State of Symptom Measurement

PD shows significantly different symptoms among individuals diagnosed with the condition. The symptoms range from mild in the earlier stage and are often unnoticed, starting from one side of the body and getting worse on the other [4]. These early symptoms can be measured based on the movement of PD-affected patients with a focus on a particular part or any side of the body. Meanwhile, the analysis of the early signs and symptoms is important to avoid serious complications [5]. For example, the tremor in a limb is often detected through the shivering of hands and fingers, and this can be resolved by rubbing the hands of the affected patients. Stiffness can also occur in any part of the body causing pain in the muscles with limited range of motions limited. Furthermore, disease can make the patients move slower, leading to a high increase in the time consumption rate [6]. It also causes automatic loss of movement which can lead to unconscious movements such as eye blinking, often smiling, and arm swinging during walking as well as change of speech in the form of monotone with the usual inflections [7]. In some other cases, the writing can become scribbled due to the defect known as micro-phobia. Moreover, certain nerve cells such as neurons often break down gradually in PD mainly due to the production of a liquid known as dopamine in the brain [8].

PD is believed to be hereditary in a situation where several members of a family are affected by disease but the occurrence is not common when compared to others such as genetic markers containing a smaller form of risk and exposure to certain toxins [9]. Several studies have also reported that the brain has some Lewy bodies containing clumps of microscopic markers within the brain cells considered to be the main cause of PD. An important example is alpha-synuclein which is a natural and widespread protein. Moreover, some of the risk factors of disease depend on age, heredity, sex, and exposure to toxins. This is confirmed by the results of a previous study that PD is rarely experienced by young adults [10], but sometimes starts in middle age and ordinarily in late life. As previously stated, heredity is another factor but the risk is very low except the number of family members affected is low. Furthermore, men are more likely to have disease than women and the people continuously exposed to herbicides and pesticides have a slightly increased risk rate.

Some of the complications of PD include dementia which is associated with difficulty in thinking and is also considered the next stage of disease [11]. However, the cognitive problem is responsive to medications and this is simpler because of the therapy provided for depression which has been initially caused by PD. The emotional changes often found among the affected individuals include fear, anxiety, and loss of motivation. Moreover, the people experience slowed swallowing which leads to drooling and subsequently problems with eating and chewing, choking, and poor nutrition. PD also causes sleeping problems and diseases such as waking up frequently even at night, falling asleep during the day [12], and rapid eye movement during sleep. Some other problems include constipation due to a slower digestive tract, dizziness or lightheadedness when the blood pressure drops suddenly, and difficulty in perceiving differences in certain odors. There is also fatigue and the later stage which causes loss of energy and pains in all parts of the body, specifically the joints. One of the major defects of PD is that sexual desire or performance can be decreased for the affected individuals [13]. Previous study showed that this problem can be moderated through regular aerobic exercises. Another study also stated that caffeine, a substance in coffee, tea, and cola, can also be a risk factor for PD [14].

## 3 Related Works

A diagnostics tool was developed by [15] for the characterization of a progressive mobility disease to ensure early detection and monitoring of the pathology. This system has the capability of defining modulation of the muscle indexes in real-time through wireless nodes in EMG placed on lower limbs. It was designed using the Altera Cyclone V to convert the data acquired into a binary signal which was subsequently used to determine the muscular indexes and retain information throughout the process. The results of the study were observed to agree with those reported in other clinical literature.

Another study by [16] focused on an easily accessible sensor system designed to monitor the motor symptoms of the cardinal organs. The symptoms identified include rigidity in body parts and the production of tremors in people with PD. At the initial stage, data were directly measured from system but the ability of the sensor system to distinguish between the pre-optimization and post-optimization scenarios was determined in the subsequent stage. The sensor system was developed by integrating three sensing modalities including inertial motion, muscle activity, and force. The specific machine-learning model was able to achieve an average accuracy rate of 90.9% and the feedback was used to assist clinicians in conducting a thorough review. The results from both stages were found to be quite promising and provided an opportunity for additional study.

The study conducted by [17] was used to develop a method to monitor the performance of patients using wearable devices with inertial depth entity. A new wavelet was used to analyze the data collected based on a single wrist-worn smartwatch and was observed to have high detection performance for tremor bradykinesia and dyskinesia. It was also confirmed to be suitable for long-term monitoring of patients at home. Moreover, [18] designed another method by combining data from the inertial sensor worn on the body of patients into multi-dimensional figures to automatically identify dissimilar prescription states. System included signal processing algorithms, time-frequency analysis, and tremor decomposition which were used to calculate the mean frequency, signal power, sparsity, average jerk, and spatial features. The datasets were later tested using a Support Vector Machine (SVM) and the results showed an accuracy of 78%.

The measurement of samples through a non-invasive method to locate the actual position of patients was suggested by [19], [20]. SVM with Principal Component Analysis (PCA) was applied to determine the principal components to be considered in diagnosing PD. The opportunity was used to describe the relationship between SWM and RFE as well as SWM and PLA. Furthermore, the dataset was analyzed through the adoption of incremental, MCS, and hybrid search methods. Another study by [21] also used the voice signals of patients to develop a classification system through the application of algorithms and Random Forests. The statistics, sentences, and pronunciation of particular words were used as the data. The objective determination of the character types in speech signals was proposed to be achieved through an accurate categorization model. Therefore, the highest possible average accuracy obtained for the data acquired was 66.5%.

The motor adjustment in the kinematic constraint related to dissimilar stages of PD was proposed to be categorized in another study. The postural behavior was evaluated using Computerized Dynamic Post-urography equipment based on the analysis of the center of pressure time series to determine Kinematic parameters. The test was in the form of a customized clinical Test of Sensory interface on Balance (mcTSIB), Confines of Stability (LOS), and Cadenced Weight Shift [22]. Furthermore, another system was proposed to differentiate PD from other neurological diseases using Gait characteristics. The feature vectors of the patients were analyzed individually and classified using Gaussian radial basis functions through the SVM. The detection accuracy was calculated to be approximately 83.33% while the feature vectors were determined using the statistical tools. The main drawback was that system could not be used to determine a particular stage of disease but rather to monitor the progress [23].

An effective medical care system developed through IoT was provided for PD patients. The process focused on obtaining the motion metrics virtually by attaching wearable sensors to the clothing of the patients. The sensors were monitored on mobile devices such as tablets and cell phones to virtually retrieve the motion metrics [24]. System was beneficial due to the competence and ability to maximize resources to advance the understanding of the patients. Moreover, the study fully reflected value control, study strategy, and provided an opportunity to understand disease treatment as well as the participation of the patients in the process [25], [26]. Another method was also proposed to adequately distinguish PD patients from normal people using gene expression information [27]. System combined the foundation of a binary-coded genetic algorithm with an extreme learning machine. This hybrid binary-coded generic system was observed to have some complications and problems. However, the application of information about gene expression was able to sufficiently distinguish PD patients from normal people and also determined the subset of genes considered responsible for disease.

A user interface considered suitable for older people with PD was recommended by [28], [29]. System operated on an open-source platform using a mobile device and the interactive interface was designed with a large font, a massive button, an innovative visual line, and considerable feature enrichment appropriate for elderly PD patients. The interface had a high level of accuracy due to the presence of a voice button function, a selectable reply message, and simplicity in the usage through a web browser and a search engine. Another study by [30] primarily focused on monitoring the posture and gait of individuals diagnosed with PD. This was achieved through a wireless body region sensor network consisting of wearable sensors that provided a report of posture and gait kinematic data in real-time and wirelessly. The device was implanted within the human body to ensure it did not interfere with the normal activities of the patients. The purpose was to retrieve data in a natural environment without the patients feeling they were being watched. Moreover, the phenomenon in which the movement performance at home was different from the clinic was later defined as the "white coat performance".

Another method was suggested to diagnose PD by combining stack generalization with a supplementary neural network [31]. System was used to retrieve a speech dataset consisting of different sound recordings from the User Computer Interface (UCI) machine learning repository. This method was further compared with traditional feed-forward backpropagation and complementary neural networks. The results showed that the proposed method had a high level of precision and allowed

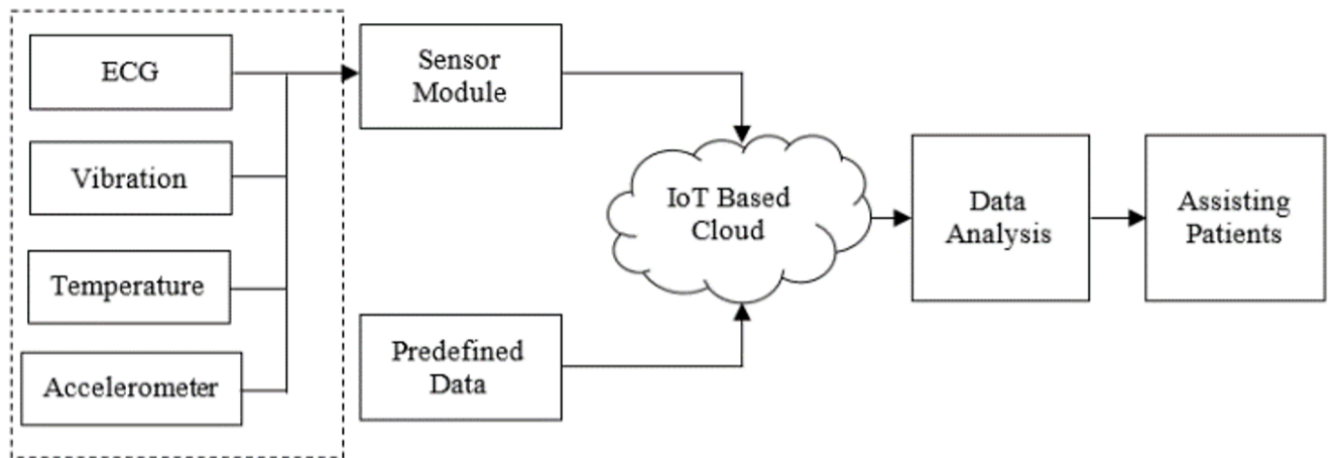


**Figure 1: Block diagram of a proposed system.**

neural networks to perform more effectively. System was proposed by [32] to save time, ensure more efficiency in determining the posture, and improve the healing process through precautionary recognition classification. This was achieved through the adoption of three types of classifiers as well as significant use of the feature extraction concept. The classifiers categorized the trial samples based on the recognition provided by the training samples, and each classifier relied on its unique categorization.

The wearable gait aid system was expanded to predict the episodes of FOG, ensure patients receive physical assistance when necessary, and determine the feasibility of the device. Moreover, the FOG event prediction method identified a decline in the influence of the gait cycle (GC) on the peak-to-peak value of the toe floor response. The device was capable of detecting a reduction in the gait cycle and subsequently providing the user with a stimulus to prompt knee joint flexion through the control mechanism [33]. Furthermore, an effective method was developed by [34] through the profound belief network and assistance of a significant number of resilient individuals to analyze a PD system. A characteristic blocking process was set up to serve as an impulse to the deep belief network and worn to produce a similar template for the voices to identify specific voices for each individual. The accuracy of this system was recorded to be 94% and higher compared to other methods tested, leading to the determination of its effectiveness in diagnosing PD.

## 4 Study Methodology

### 4.1 Microcomputing System

The main dependent of the prototype developed was the microcontroller. Arduino, which was an open-source hardware containing a variety of microprocessors and controllers, was used as the microcontroller in this study. Moreover, interfaces are usually designed between a wide variety of expansion boards and circuits, especially when each board possesses set of digital and analog input/output pins. Boards and interfaces for serial communication were combined with the Universal Serial Bus (USB) to load programs into the computer. Integrated Development Environments (IDEs) were also included based on the processing language projects. The serial Arduino boards applied had a level shifter circuit to alter between RS232 logic levels and transistor-transistor logic (TTL) manner.

### 4.2 Wearable Sensor Technology

Sensors are quite important in identifying potentially problematic aspects of PD patients. Therefore, several sensors were installed in the proposed prototype including ECG, vibration, temperature, and accelerometer to determine some parameters such as temperature, pressure, heartbeat, vibration, and others. The sensors had higher and lower sensitivities and the appropriate option was selected for the patients. For example, the accelerometer range for normal patients is usually 10-12Hz while PD patients have 40-60Hz. The heartbeat sensors could also detect the changes in the amount of blood in the finger with respect to time and were integrated for pulse sensing applications as shown in the Figure 1.

### 4.3 Cloud Storage

The cloud storage was mainly used in the proposed prototype to upload the status report of the patients obtained through measurements. The data for normal patients had been previously uploaded while those related to PD patients were uploaded continuously to determine the abnormal conditions. Think Speak, which was IoT platform, was used due to its ability to store different forms of data and accessibility through a computer with internet connectivity to analyze the data and visualize the

result. The sensor data were sent to the Think Speak platform from Arduino and other compatible devices, and the results were used to easily identify the mode of the patients.

#### 4.4 Machine Learning with Predictive Algorithm

A machine learning algorithm was used to analyze available data and make predictions. The application of this algorithm is because it is the simplest to avoid issues of local minima, gain a fast mechanism on regression analysis, and offer good generalization performance. The algorithm also has the ability to approximate complex mappings and significantly reduces the time needed for training. The data obtained in the study were uploaded to the cloud allocated with IP address followed by the measurement of quality prediction with accuracy for different iterations using predictive algorithm through statistics of known discrete values. Moreover, the probability of outcome was determined based on a set of input data and only one predictor was used to reduce the complexity. The review of previous studies showed that a significant number of common classifiers in machine learning have been used to diagnose PD. This was considered necessary due to the importance of selecting an appropriate classifier in solving the problems associated with the disease. The complexity of the architecture was reduced in this study by introducing the fuzzy k-nearest neighbor (FKNN) algorithm while keeping the same level of accuracy. The FKNN was developed by Keller et al. based on the premise that fuzzy logic concepts could be used to assign degrees of membership to different classes while considering the distance between an object and its k-nearest neighbors. The points lost to the query point are believed to have a significantly higher contribution to the membership function of respective classes when compared to those that are far away from neighbors. The winning class normally has a higher membership function value compared to the other classes. The uniqueness and competitive advantage of the FKNN is the ability to assign an optimistic value to each projected class.

The KNN is a non-parametric pattern classification method that assigns a class based on the high prevalence among the k-nearest neighbors of the pattern being classified. Meanwhile, the FKNN method is an improved variation of the KNN designed using fuzzy set theory where the fuzzy memberships of samples are not usually assigned to distinct classes as observed in KNN but rather designated to a variety of categories based on the following formula shown in Equation (1) as in

$$U_i(x) = \frac{\sum_{p=1}^k U_{ip} \left( \frac{1}{\|X-X_p\|^{\frac{2}{m-1}}} \right)}{\sum_{p=1}^k \left( \frac{1}{\|X-X_p\|^{\frac{2}{m-1}}} \right)}, \tag{1}$$

where  $p = 1, 2, 3, \dots, K$  and  $i = 1, 2, 3, \dots, C$  are the number of nearest neighbors and classes respectively. The determination of the membership scale contribution of each neighbor requires using the fuzzy strength parameter  $m$  to define how heavily the distance is weighted, and its value is commonly set from one to infinity. Moreover, the Euclidean distance is normally used to calculate the distance metric.  $U_{ip}$  is the degree of membership of the pattern  $X_k$  from the training set to the class  $i$  and can be calculated shown in Equation (2) as in

$$U_{ip}(X_k) = \begin{cases} 0.51 + 0.49 \left( \frac{n_p}{K} \right), \\ 0.49 \left( \frac{n_p}{K} \right), \end{cases} \tag{2}$$

where  $n_p$  is the numbers of neighbors which belong to the  $p^{th}$  class.

The calculation of all memberships for the query sample was followed by the allocation to the class with the highest membership value. The results from several studies show that feature extraction is an extremely important part of the classifier modeling process, particularly for medical applications. The purpose is to turn an input parameter vector into a feature vector and lower the dimensionality of the feature vector. These tasks are normally accomplished by lowering the dimensionality of the input parameter vector. Moreover, PCA is a well-known feature extraction tool that searches for the most important changes in the initial feature space with the main objective of improving the classification process, in terms of accuracy and efficiency. This study focused on determining the effectiveness of using PCA for feature extraction in PD diagnosis problems.

The FKNN model was later applied for classification using the feature set newly constructed by PCA and the initial stage of the process was to configure all the parameters. The fuzzy strength was identified to have a sizeable influence on the performance of the FKNN algorithm and this led to the adoption of an experimental method to determine the ideal value for the parameter. The main concept was to supply the fuzzy membership value  $m$  with a range of  $[1, 2]$  and a step size of 0.01 followed by a test on the classification performance using a 10-fold cross-validation on numerous numbers of neighbors  $k$ . Moreover, the average accuracy reached by FKNN for each of the possible values of  $m$  was determined through cross-validation analysis. The value with the highest level of accuracy on average was selected as optimal for the fuzzy strength parameter. This process was followed by the application of the FKNN classifier to the feature set reduction to compute the classification accuracy and an average of the results were later calculated.

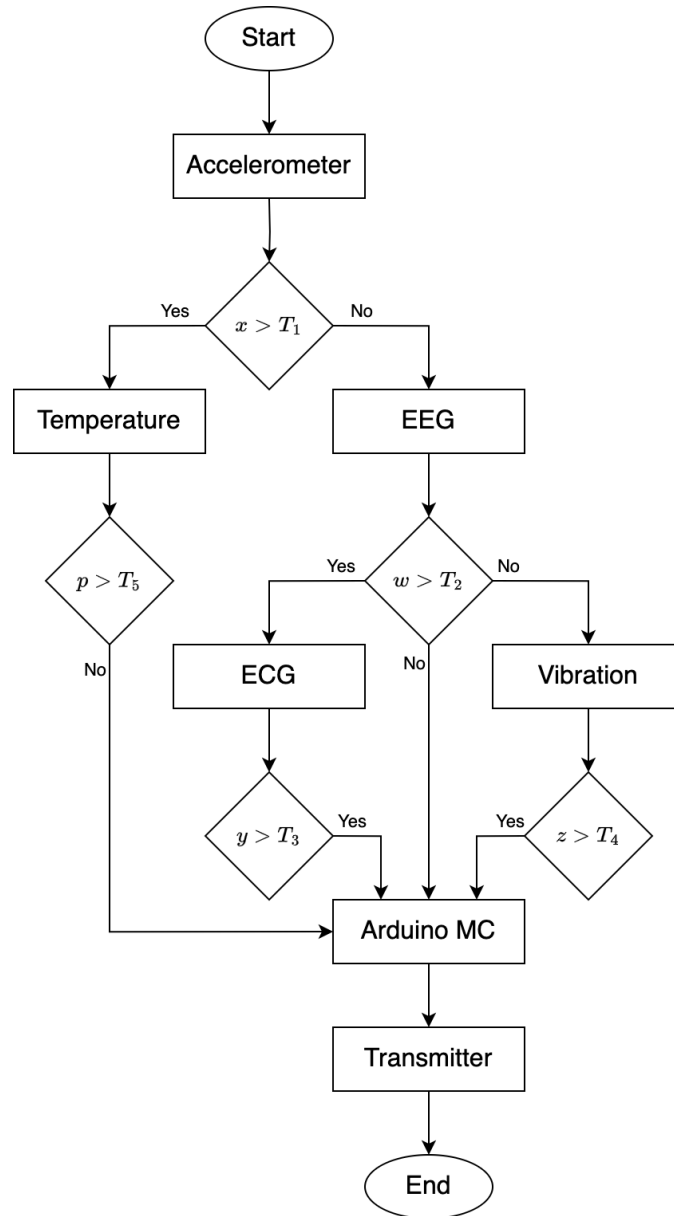


Figure 2: Flowchart of normal condition.

#### 4.5 Methodology

The operations of the proposed prototype mainly depended on the sensor data uploaded to the cloud storage to provide a new treatment option for PD patients. Prediction algorithm was used to regularly track the progress of the patients and automatically save the information to the cloud. The data from the cloud were used to consistently analyze the performance of the patients. Moreover, the sensors could be placed in the body of the patients through different means such as the head through the assistance of a cap to detect the brain waves regularly. System did not have the capacity to provide complete relief to the patients but it could assist in reaching the lifetime.

#### 4.6 Data Analysis

##### 4.6.1 Normal Condition

The condition of PD patients was mainly determined through the comparison with normal persons. This was achieved through the processes described in the flow presented in the Figure 2.

The Pseudo code for the Normal Condition is described as follows:

- Start the program
- IF  $x > T_1$ , then ENTER Temperature AND EEG

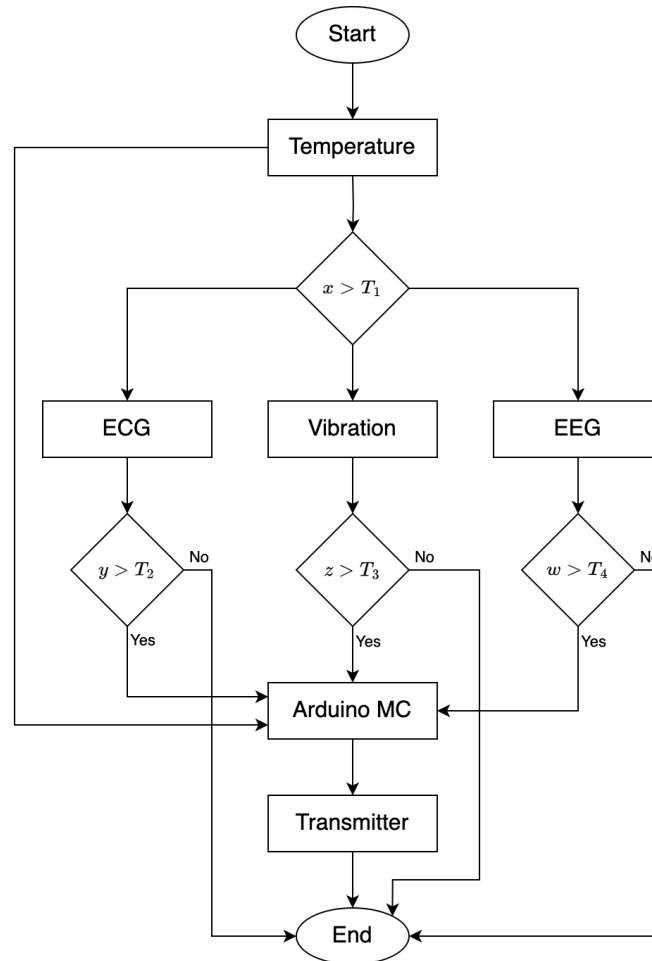


Figure 3: Flowchart of abnormal condition.

- IF Temperature  $p < T_5$ , then ENTER Arduino MC
- IF EEG  $w > T_2$ , then ENTER ECG and Vibration
- IF ECG  $y > T_3$ , then ENTER Arduino MC  
ELSE STOP
- IF Vibration  $z > T_4$ , then ENTER Arduino MC  
ELSE STOP
- Stop the program

#### 4.6.2 Abnormal Condition

The functional flow of the abnormal condition was easily diagnosed through the proposed prototype. The rate of risk zone for the patients was defined to alert the caretaker. This was achieved by measuring the temperature first followed by the other parameters such as heartbeat and vibration. PD was characterized by an abnormally high degree of synchronization of the quantitative EEG signal rate in the frequency range of 13–30 Hz and other conditions stated in Figure 3.

The Pseudo code for the Abnormal Condition is described as follows:

- Start the program
- IF  $x > T_1$ , then CHECK ECG, VIBRATION, and EEG
- IF ECG  $y > T_2$ , then ENTER Arduino MC  
ELSE STOP
- IF EEG  $w > T_4$ , then ENTER Arduino MC  
ELSE STOP
- IF Vibration  $z > T_4$ , then ENTER Arduino MC ELSE STOP  
item Stop the program

**Table 1: Performance comparison.**

Method	Accuracy (%)	Sensitivity (%)	Specificity (%)	Positive Predictivity (%)
Fuzzy k-nearest neighbor	94.14	96.03	90.91	94.77
SVM	91.63	93.33	88.76	93.33
Decision Tree	87.45	89.54	83.72	90.73
Naïve Bayes	88.07	92.11	81.32	89.17

## 5 Results and Discussions

The values from the vibration, temperature, EEG, ECG, and accelerometer sensors were analyzed to decide whether the condition of the patients was abnormal or normal. The proposed prototype captured brain metabolism and Prediction Algorithm was used to foresee the incentive associated with a specific range of the data obtained. Moreover, the diagnostics and analysis of different conditions were expected to increase the awareness of the physical therapist about the discomfort level of the patients. The proposed prototype ensured a ray of hope tempered with realism and was developed through the use of a MATLAB simulation environment and an Intel i7 CPU with NVIDIA GPU 1650 ti. Data were obtained from participants consisting of senior citizens in different age categories with an average age of 64.52 years old and the overall sample size was 239.

The normalization process was conducted to prevent numerical difficulties during the computation and to ensure the characteristics extracted in higher range ranges did not overpower those in lower ranges. Moreover, 10-fold cross-validation was used to objectively measure the classification generalization. The most important advantage of this method was that each of the test sets was autonomous, thereby increasing the dependability of the outcomes. One of the ten subsets was selected at random to serve as the test set for each iteration while the remaining nine were used as the training set. The process was followed by the computation of the standard deviation of the total error for all ten sets. The data were partitioned according to the participants selected with the assurance of having the same sample proportion in each of the data subsets as the population. The purpose was to guarantee that the classification performance in each subset was the same. Furthermore, the conduct of 10-fold cross-validation just once could not produce sufficient classification accuracies for comparison. It is also not possible to predict the accuracy of a model at any given iteration with absolute certainty because the division of datasets was inherently random. Therefore, 10-fold cross-validation was conducted ten times to obtain an accurate evaluation of the functionality of the datasets, and the average of the results was determined.

The effectiveness of the proposed prototype was evaluated through the application of the FKNN classifier to the original feature space and the results were compared with the Naive Base, Decision Tree, and SVM classifiers. The performance of the proposed prototype was evaluated based on classification accuracy, sensitivity, specificity, and positive predictivity, which are represented as shown in Equation (3), (4), (5), and (6) as follow

$$\text{Accuracy (\%)} = \left( \frac{TP + TN}{TP + TN + FP + FN} \right) \times 100, \quad (3)$$

$$\text{Sensitivity (\%)} = \left( \frac{TP}{TP + FN} \right) \times 100, \quad (4)$$

$$\text{Specificity (\%)} = \left( \frac{TN}{TN + FP} \right) \times 100, \text{ and} \quad (5)$$

$$\text{Positive predictivity (\%)} = \left( \frac{TP}{TP + FP} \right) \times 100. \quad (6)$$

The results obtained from comparing the classifiers are presented in the following Table 1. The FKNN method had a 94.14% accuracy rate while the Decision Tree, SVM, and Naive base algorithms had 87.45%, 91.63%, and 88.07%, respectively. Moreover, the FKNN had the highest sensitivity and specificity values with 96.03% and 90.91%, respectively. The FKNN also recorded the greatest positive predictivity rate of 94.77%, while the SVM, DT, and NB had 93.33%, 90.73%, and 89.17%, respectively.

The results showed that FKNN had the best level of accuracy with 94.14% while the Naive Base had the worst. The FKNN also had the least False Negative (FN) and False Positive (FP) conditions compared to the other methods while the Naive Base had the most as presented in the following Figure 4.

The sensitivity comparison in Figure 5 showed that the FKNN had the highest value of 96.03% while the Decision Tree had the lowest with 89.54%. This was associated with the existence of the fewest FN or highest TP in the FKNN compared to the other methods while the Decision Tree had the opposite. This sensitivity comparison graph can be seen in Figure 5. Moreover, specificity usually measures the ability of a model to correctly identify negative instances or true negatives. It also quantifies the proportion of actual negative instances correctly classified. The parameter can be used to compare the number of TN and FP and is considered useful in scenarios where negative instances need to be correctly identified such as medical diagnostics. The results showed that the FKNN had the highest specificity of 90.91% and this was an indication the method had the most TN and less FP values compared to the others. Meanwhile, the Naive Base had the lowest value of 81.32% which showed the method contained the lowest TN and most FP values as presented in Figure 6.

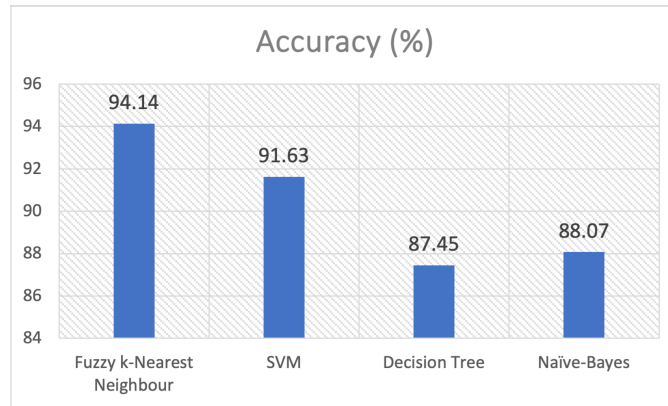


**Figure 4: Accuracy comparison.**

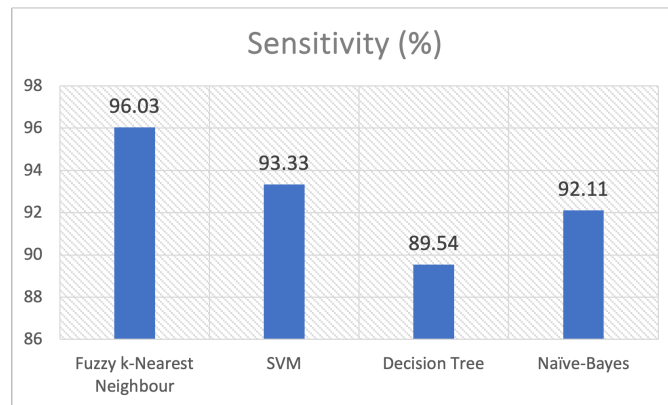


**Figure 5: Sensitivity comparison.**

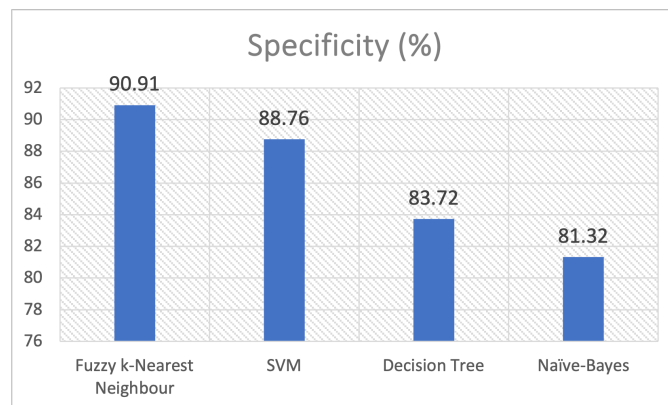


**Figure 6: Specificity comparison.**

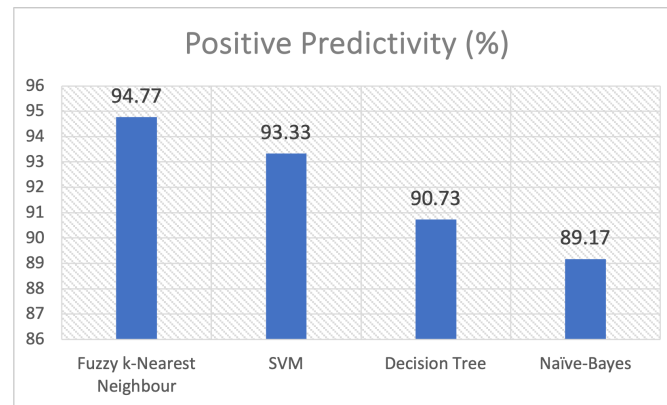


**Figure 7: Positive predictive comparison.**

Positive predictive value (PPV) is a performance metric used in classification tasks to measure the accuracy of the positive predictions made by a model. It is defined as the ratio of true positive predictions to the total number of positive predictions. The phenomenon shows that PPV quantifies the proportion of positive predictions considered to be correct. The results showed that the FKNN had the highest value of 94.77% as indicated by the most TP and least FP values recorded compared to the other methods. Meanwhile, the Naive Base had the worst value of 89.17% which showed the existence of the least TP and most FP values. The result of positive predictive value can be seen in Figure 7

## 6 Conclusions

In conclusion, the prototype was proposed to make PD patients live easier daily lives without any sort of disturbances. This was achieved using individuals with severe cases of PD as the primary participants and the results showed that the prototype was reliable, cost-effective, and correctly monitored the ability of the sensors used to perform several functions. The prototype was expected to reduce the mortality rate and liberate users from both day and night clinical assistance. Moreover, the FKNN-based prediction algorithm developed was found to be more accurate than other algorithms as showed by the 94.14% accuracy recorded.

## Authors' Contributions

In this study, all authors studied and designed the article.

## Competing Interests

The authors declare that they have no conflict of interest.

## References

- [1] H. Xu, W. Yu, D. Griffith, and N. Golmie, "A survey on industrial internet of things: A cyber-physical systems perspective," *IEEE Access*, vol. 6, pp. 78 238–78 259, 2018.
- [2] A. J. Espay, P. Bonato, F. B. Nahab, W. Maetzler, J. M. Dean, J. Klucken, B. M. Eskofier, A. Merola, F. Horak, A. E. Lang, R. Reilmann, J. Giuffrida, A. Nieuwboer, M. Horne, M. A. Little, I. Litvan, T. Simuni, E. R. Dorsey, M. A. Burack, K. Kubota, A. Kamondi, C. Godinho, J.-F. Daneault, G. Mitsi, L. Krinke, J. M. Hausdorff, B. R. Bloem, and S. Papapetropoulos, "Technology in parkinson's disease: Challenges and opportunities," *Movement Disorders*, vol. 31, pp. 1272–1282, 9 2016.
- [3] K. N. R. Challa, V. S. Pagolu, G. Panda, and B. Majhi, "An improved approach for prediction of parkinson's disease using machine learning techniques." *IEEE*, 10 2016, pp. 1446–1451.
- [4] R. Djaldetti, I. Ziv, and E. Melamed, "The mystery of motor asymmetry in parkinson's disease," *The Lancet Neurology*, vol. 5, pp. 796–802, 9 2006.
- [5] K. R. Chaudhuri, P. Odin, A. Antonini, and P. Martinez-Martin, "Parkinson's disease: The non-motor issues," *Parkinsonism & Related Disorders*, vol. 17, pp. 717–723, 12 2011.
- [6] R. BENECKE, J. C. ROTHWELL, J. P. R. DICK, B. L. DAY, and C. D. MARSDEN, "Disturbance of sequential movements in patients with parkinson's disease," *Brain*, vol. 110, pp. 361–379, 1987.
- [7] N. Miller, E. Noble, D. Jones, and D. Burn, "Life with communication changes in parkinson's disease," *Age and Ageing*, vol. 35, pp. 235–239, 5 2006.
- [8] H. Braak and E. Braak, "Pathoanatomy of parkinson's disease," *Journal of Neurology*, vol. 247, pp. II3–II10, 4 2000.
- [9] A. C. Belin and M. Westerlund, "Parkinson's disease: A genetic perspective," *The FEBS Journal*, vol. 275, pp. 1377–1383, 4 2008.
- [10] A. Ascherio and M. A. Schwarzschild, "The epidemiology of parkinson's disease: risk factors and prevention," *The Lancet Neurology*, vol. 15, pp. 1257–1272, 11 2016.
- [11] I. G. McKeith and D. Burn, "Spectrum of parkinson's disease, parkinson's dementia, and lewy body dementia," *Neurologic Clinics*, vol. 18, pp. 865–883, 11 2000.
- [12] C. L. Comella, "Sleep disorders in parkinson's disease: An overview," *Movement Disorders*, vol. 22, pp. S367–S373, 2007.
- [13] K. M. Smith and N. Dahodwala, "Sex differences in parkinson's disease and other movement disorders," *Experimental Neurology*, vol. 259, pp. 44–56, 9 2014.
- [14] D. K. Simon, C. M. Tanner, and P. Brundin, "Parkinson disease epidemiology, pathology, genetics, and pathophysiology," *Clinics in Geriatric Medicine*, vol. 36, pp. 1–12, 2 2020.
- [15] V. Annese, G. Mezzina, V. Gallo, V. Scarola, and D. D. Venuto, "Wearable platform for automatic recognition of parkinson disease by muscular implication monitoring." *IEEE*, 6 2017, pp. 150–154.

- [16] P. Angeles, Y. Tai, N. Pavese, S. Wilson, and R. Vaidyanathan, "Automated assessment of symptom severity changes during deep brain stimulation (dbs) therapy for parkinson's disease." *IEEE*, 7 2017, pp. 1512–1517.
- [17] A. Wagner, N. Fixler, and Y. S. Resheff, "A wavelet-based approach to monitoring parkinson's disease symptoms." *IEEE*, 3 2017, pp. 5980–5984.
- [18] V. Ramji, M. Hssayeni, M. A. Burack, and B. Ghoraani, "Parkinson's disease medication state management using data fusion of wearable sensors." *IEEE*, 2017, pp. 193–196.
- [19] H. Ma, T. Tan, H. Zhou, and T. Gao, "Support vector machine-recursive feature elimination for the diagnosis of parkinson disease based on speech analysis." *IEEE*, 12 2016, pp. 34–40.
- [20] S. Afroz, T. M. N. U. Akhund, T. Khan, M. U. Hasan, R. Jesmin, and M. M. Sarker, *Internet of Sensing Things-Based Machine Learning Approach to Predict Parkinson*, 2024, pp. 651–660.
- [21] M. Vadovsky and J. Paralic, "Parkinson's disease patients classification based on the speech signals." *IEEE*, 1 2017, pp. 000321–000326.
- [22] C. Godinho, V. Ferret-Sena, J. Brito, F. Melo, and M. S. Dias, "Postural behavior and parkinson's disease severity." *IEEE*, 12 2016, pp. 1–6.
- [23] S. Shetty and Y. S. Rao, "Svm based machine learning approach to identify parkinson's disease using gait analysis." *IEEE*, 8 2016, pp. 1–5.
- [24] M. G. Krokidis, G. N. Dimitrakopoulos, A. G. Vrahatis, C. Tzouveleakis, D. Drakoulis, F. Papavassileiou, T. P. Exarchos, and P. Vlamos, "A sensor-based perspective in early-stage parkinson's disease: Current state and the need for machine learning processes," *Sensors*, vol. 22, p. 409, 1 2022.
- [25] C. F. Pasluosta, H. Gassner, J. Winkler, J. Klucken, and B. M. Eskofier, "An emerging era in the management of parkinson's disease: Wearable technologies and the internet of things," *IEEE Journal of Biomedical and Health Informatics*, vol. 19, pp. 1873–1881, 11 2015.
- [26] O. d'Angelis, L. D. Biase, L. Vollero, and M. Merone, "Iot architecture for continuous long term monitoring: Parkinson's disease case study," *Internet of Things*, vol. 20, p. 100614, 11 2022.
- [27] V. Sachnev and H. J. Kim, "Parkinson disease classification based on binary coded genetic algorithm and extreme learning machine." *IEEE*, 4 2014, pp. 1–6.
- [28] Y.-W. Bai, C.-C. Chan, and C.-H. Yu, "Design and implementation of a user interface of a smartphone for the parkinson's disease patients." *IEEE*, 1 2015, pp. 257–258.
- [29] K.-M. Giannakopoulou, I. Roussaki, and K. Demestichas, "Internet of things technologies and machine learning methods for parkinson's disease diagnosis, monitoring and management: A systematic review," *Sensors*, vol. 22, p. 1799, 2 2022.
- [30] Z. Dong, H. Gu, Y. Wan, W. Zhuang, R. Rojas-Cessa, and E. Rabin, "Wireless body area sensor network for posture and gait monitoring of individuals with parkinson's disease." *IEEE*, 4 2015, pp. 81–86.
- [31] P. Kraipeerapun and S. Amornsamankul, "Using stacked generalization and complementary neural networks to predict parkinson's disease." *IEEE*, 8 2015, pp. 1290–1294.
- [32] A. Bourouhou, A. Jilbab, C. Nacir, and A. Hammouch, "Comparison of classification methods to detect the parkinson disease." *IEEE*, 5 2016, pp. 421–424.
- [33] A. Uehara, H. Kawamoto, and Y. Sankai, "Development of gait assist method for parkinson's disease patients with fog in walking." *IEEE*, 9 2016, pp. 1502–1507.
- [34] A. H. Al-Fatlawi, M. H. Jabardi, and S. H. Ling, "Efficient diagnosis system for parkinson's disease using deep belief network." *IEEE*, 7 2016, pp. 1324–1330.



Research Article

# Thermodynamic and Optimization Comparison of a Solar-Powered Compressor-Assisted Combined Absorption Refrigeration and Power Systems

Chinedu F. Okwose<sup>1a</sup>, Mustafa Tunay<sup>1b</sup>, Muhammad Abid<sup>2c</sup>, Michael Adedeji<sup>3d</sup>, Victor Adebayo<sup>3e</sup>, Tahir A H. Ratlamwala<sup>4f</sup>, Muhammad A. Rabbani<sup>1g</sup>

<sup>1</sup> Faculty of Engineering, Cyprus Science University, Ozankoy-Girne, via Mersin 10, Turkey

<sup>2</sup> Department of Energy Systems Engineering, Faculty of Integrated Technologies, Brunei Darussalam University, Jalan Tungku Link BE 1410, Bandar Seri Begawan, Brunei Darussalam

<sup>3</sup> Department of Energy System Engineering, International Cyprus University, Haspolat-Lefkosa Via Mersin, Turkey

<sup>4</sup> Department of Engineering Science, National University of Sciences and Technology, Karachi, Pakistan

mustafatunay@csu.edu.tr

DOI : 10.31202/ecjse.1434603

Received: 09.02.2024 Accepted: 22.05.2024

## How to cite this article:

Chinedu F. Okwose, Mustafa Tunay, Muhammad Abid, Michael Adedeji, Victor Adebayo, Tahir A H. Ratlamwala, Muhammad A. Rabbani, "Thermodynamic and Optimization Comparison of a Solar-Powered Compressor-Assisted Combined Absorption Refrigeration and Power Systems", El-Cezeri Journal of Science and Engineering, Vol: 11, Iss: 3, (2024), pp.(267-282).

ORCID: <sup>a</sup>0000-0003-0827-4578; <sup>b</sup>0000-0001-8843-621X; <sup>c</sup>0000-0001-6579-6212; <sup>d</sup>0000-0002-7532-3563; <sup>e</sup>0000-0002-9237-7678;

<sup>f</sup>0000-0003-3314-5807; <sup>g</sup>0000-0002-0980-5054.

**Abstract :** The operation and performance of three different combined absorption refrigeration and power systems is presented in this study. The systems are based on the single, double, and triple effect absorption refrigeration cycles with ammonia-water as working fluid pairs all powered by solar thermal energy. The thermodynamic performance of these modified combined absorption cycles have been analyzed for typical thermal boundary conditions and design parameters. The simulation results show that when the compressor pressure ratio increases from 1 to 2, the heat source inlet temperatures can be reduced by 27% (111.3°C to 81.1°C) in the single effect system, 16% (182.1°C to 152.5°C) in the double effect system, and 34% (228.3°C to 150.3°C) in the triple effect system. The exergy efficiency of the triple effect system increases from 38% to 64% for a 75-kW cooling load system. These proposed systems provide a better way to optimise the utilisation of heat sources with moderate temperatures.

**Keywords :** Absorption Refrigeration, Compression Ratio, Power, Cooling, Triple Effect

## 1 Introduction

The cooling & refrigeration needs in many countries keep increasing as a consequence of global warming experienced worldwide [1]. This increasing requirement for comfort & high cooling loads needs to be met using environmentally responsible means to prevent further damage to the earth's atmosphere. An example of such an option is cooling and refrigeration using vapor absorption systems. Unlike popular and commercially available vapor compression systems, vapor absorption systems don't make use of chlorofluorocarbon (CFC) and hydrofluorocarbon (HCFC) refrigerants that can cause the ozone layer depletion and also act to trap heat in the lower atmosphere leading to climate change [2]–[5]. This makes absorption cooling and refrigeration systems more environmentally friendly in comparison. Additionally, they can be powered by waste low grade heat thereby greatly reducing their electricity usage [6].

Several working fluids are used in vapor absorption systems which all have different input conditions and advantages. Hugo et al. [7] investigated the performance of six different working fluid pairs used in absorption refrigeration systems. The working fluid pairs considered are H<sub>2</sub>O-LiBr, NH<sub>3</sub>-H<sub>2</sub>O, NH<sub>3</sub>-LiNO<sub>3</sub>, NH<sub>3</sub>-NaSCN, H<sub>2</sub>O-LiCl, and H<sub>2</sub>O-CaCl<sub>2</sub>. They found in their study that the fluid pairs that use H<sub>2</sub>O as the refrigerant are more efficient compared to the ones utilizing NH<sub>3</sub> as the refrigerant. However, water as the refrigerant will make sub-zero cooling/refrigeration impossible because it will freeze at said temperature (0°C). Ammonia as the refrigerant in a working fluid pair on the other hand allows sub-zero cooling.

The inlet temperature of the heat supplied to the generator of the system from an external source is a vital factor in the operation of absorption cooling systems. The driving heat of the system is needed for fluid separation in the generator/desorber. This inlet heat temperature is thus dependent on the type of working fluid pair in the system and also the number of stages of separation. For instance, single effect LiBr-H<sub>2</sub>O systems require heat at about 70°C while the double and triple-effect systems require about 150°C and 200°C respectively. NH<sub>3</sub>-H<sub>2</sub>O systems require higher temperatures in comparison; the single effect systems operate at about 90°C, the double effect systems at about 170°C, and the triple effect systems at over 200°C [8]–[10].

In a bid to reduce the minimum operating temperatures of vapor absorption systems, researchers developed a model that incorporates a compressor into the system. The compressor can be placed between the evaporator and the absorber or between the generator and the condenser [11], [12]. Shu et al. [6] found that the generator temperature of a triple effect  $\text{NH}_3\text{-H}_2\text{O}$  cooling system can be reduced by up to  $50^\circ\text{C}$  when coupled with a compressor. Chen et al. [13] examined the operational efficiency of a compressor-assisted double-effect absorption refrigeration system. This system which uses a [mmim] DMP/ $\text{CH}_3\text{OH}$  working fluid exhibited its best performance when a compressor is placed between the evaporator and absorber. Their study also showed that placing the compressor between the two generators is an acceptable configuration option. According to Boer et al. [14], placing a compressor between the evaporator and the absorber has many functions. These include increasing the deflation range, increasing absorption temperature, and decreasing generation temperature.

In addition to reducing the inlet heat temperature requirement in absorption cooling systems, the introduction of the compressor also increases the performance. However, the additional compression work of the system needs to be considered. There have already been numerous researches conducted on absorption cycles that include a turbine/expander for cogeneration of cooling and power.

Demirkaya et al. [15] examined the Goswami cycle, which integrates power generation and cooling using  $\text{NH}_3\text{-H}_2\text{O}$ . Praveen Kumar et al. [16] explored the impact of operational temperatures on a combined cycle involving ammonia absorption refrigeration (AAR) and the Kalina cycle. They reported the system's effective first law and exergy efficiencies as 13% and 48%, respectively. Shu et al. [6] conducted a simulation to assess the thermal performance of a proposed compressor-assisted triple-effect  $\text{LiBr}/\text{H}_2\text{O}$  absorption cooling cycle coupled with a Rankine cycle driven by high-temperature waste heat. Their findings demonstrated that the integrated compressor enhances the thermal efficiency of multi-effect absorption refrigeration. The development of these combined cooling and power cycles makes it possible to have a hybrid compressor-assisted absorption cooling system that is capable of generating the needed compression work in the system. These self-sufficient compressor-aided systems have been the subject of various research. Agheniaey et al. [17] obtained a second law efficiency of 11.56% in their study of a novel absorption refrigeration cycle with an expander and compressor. Ayou et al. [18] also performed a study on an integrated compressor booster for a power and refrigeration cycle. Their system is a modified single effect  $\text{NH}_3\text{-H}_2\text{O}$  cycle which they showed can conveniently operate in 3 distinct modes; cooling, power, and coproduction. In their research, Chinedu et al. [19] conducted a study on a compressor-assisted two-stage triple-effect absorption cycle designed for both power generation and cooling purposes. This system consists of a power sub-system and an absorption-compressor sub-system, with ammonia-water mixture as the working fluid.

Chinedu et al. [20] demonstrated that the inlet temperature of the heat source was reduced by  $50^\circ\text{C}$  compared to the traditional two-stage triple-effect absorption system. They investigated compressor-assisted single, double, and triple-effect absorption refrigeration cycles for power and cooling using thermal energy from evacuated tube collectors. Their findings indicate that the net power output decreased by 88%, while the cooling output increased slightly by 5.2% for the single-effect cycle.

The research on the hybrid compressor-assisted vapor absorption  $\text{NH}_3\text{-H}_2\text{O}$  systems for cooling and power generation has all been focused on the single effect cycles. There appears to be no study available on multi-effect compressor-assisted vapor absorption  $\text{NH}_3\text{-H}_2\text{O}$  systems for cooling and power generation. This paper therefore aims to fill this gap by providing an analysis of  $\text{NH}_3\text{-H}_2\text{O}$  double, and triple-effect systems working according to this configuration. This study investigates the operation and performance of three combined absorption refrigeration and power systems utilizing solar thermal energy. The systems are based on single, double, and triple-effect absorption refrigeration cycles, employing ammonia-water as the working fluid pairs. Through analysis of thermodynamic performance under typical thermal boundary conditions and design parameters, the study evaluates the modified combined absorption cycles. Also, it will be simulated using the engineering equation solver (EES) tool. The performance characteristics will be assessed by increasing the pressure ratio ( $P_{\text{rcom}}$ ) of each system from 1 to 2, according to the given input conditions.

## 2 Unit Description and Working Principle

This section describes the three systems considered in this study. Each of the systems is based on the typical single effect, two-stage double-effect and two-stage triple-effect  $\text{NH}_3/\text{H}_2\text{O}$  vapor absorption cycles extensively described in [21]. Two-stage ammonia/water absorption systems offer the potential for increased efficiency (coefficient of performance) or increased temperature lift (difference between lowest temperature and the heat rejection temperature) compared to single-stage cycles. They are basically two single effect systems; Two-stage implies that two solution circuits are included in the system and double/triple effect implies that a certain amount of heat is used more than once to generate refrigerant vapor. In each of the systems, the term "strong solution" represents a solution that is strong with refrigerant ( $\text{NH}_3$ ), while "weak solution" represents a solution that is weak with refrigerant.

### 2.1 Single Effect Combined Absorption Refrigeration and Power (SECARP) System

The main components of the SECARP are: generator, condenser, evaporator, absorber, expander, solution pump, superheater, rectifier, and solution heat exchanger. The evaporator works at the low pressure of the system, the absorber works at the



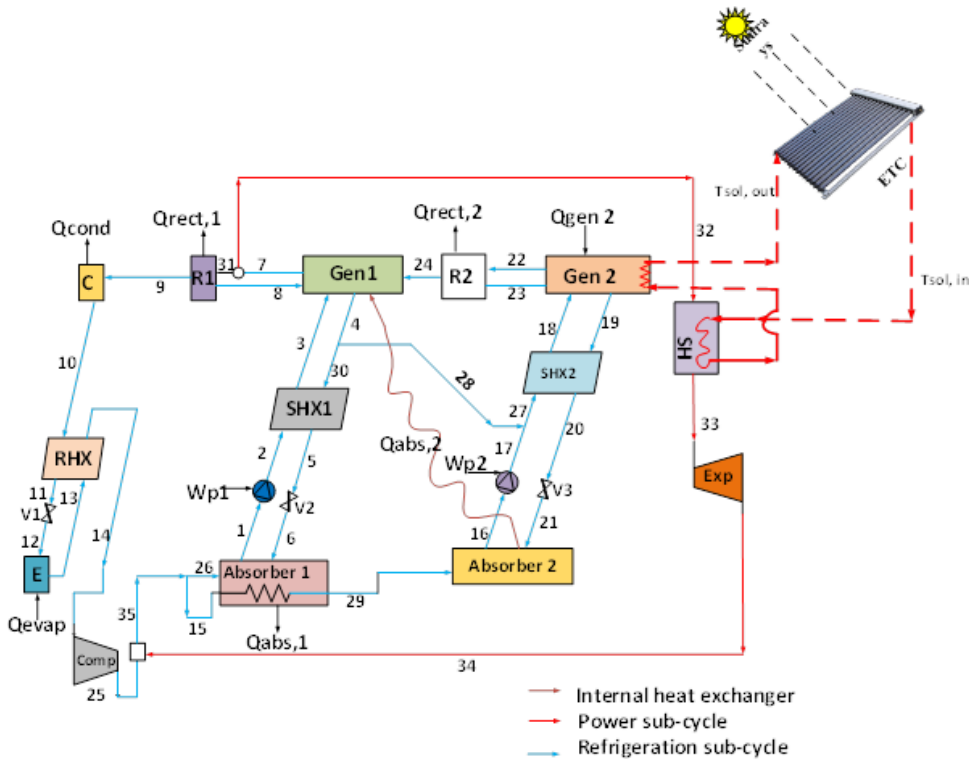


**Figure 2: The Solar Powered DECARP Cycle**

valve (REV). It is then throttled in the to reduce the pressure which will also lead to a drop in its temperature. The low temperature refrigerant (state 12) now proceeds into the evaporator (EVA) where the cooling effect occurs. This is achieved by passing heat from the space/water that needs cooling into the evaporator. The refrigerant at state 13, after leaving the evaporator, then passes through the REV where it provides the cooling required for the initial pre-cooling in the REV. This same process will also ensure that the emerging refrigerant at state 14 is in a superheated vapor state, which then goes through the compressor to increase its pressure to that of the absorber.

After leaving the generator at state 7, a portion of the refrigerant is separated (state 19) and is passed into the superheater (SH). Here, heat from the external source (evacuated tube solar collector) is used to raise the temperature of the refrigerant until it becomes a superheated vapor. This then goes into the expander (state 20) where it expands, creating mechanical work. The refrigerant exiting the expander (state 21) mixes with that leaving the compressor forming state 17 which flows into the absorber.

The weak solution (water) leaving at state 4, after exchanging heat with the strong solution (state 3) in the SHX, flows through the solution expansion valve (SEV) which will reduce its pressure to that of the absorber. The weak solution and the refrigerant are then mixed in the absorber when the absorber heat ( $Q_{abs}$ ) rejected.

**2.2 Double Effect Combined Absorption Refrigeration and Power (DECARP) System**

The DECARP system shown in Fig. 2 consists of two single effect absorption cycles working in tandem and the process of fluid separation is done in 2 generators operating at the same pressure. The left stage of the system is identical to the SECARP system and also undergoes the same processes from states 1 to 14. The second stage consists of the absorber2, pump2, solution heat exchanger2, generator2, and rectifier2.

The combination of the heat rejected from absorber2 and rectifier2 is supplied to generator1 to aid fluid separation. The refrigerant emerging from rectifier2 (state 24) is mixed with the strong solution (state 3) in generator1. After the separation in generator1, a portion of the weak solution (state 4) is extracted and mixed with the state 17. The mixture (state 27) then passes through SHX2 where it gains heat which increases its temperature before flowing into generator2. The refrigerant utilized for power generation in the system is extracted from the stream leaving generator1 (state 7). This ensures that a sufficient amount of the refrigerant is available before the separation making it possible to have power generation even with a low refrigerant split ratio.

The portion of the refrigerant that goes into cooling in the evaporator leaves the RHX at state 14 and then goes into the compressor. The compressed refrigerant then mixes with the refrigerant leaving the expander and the mixture (state 35) is then

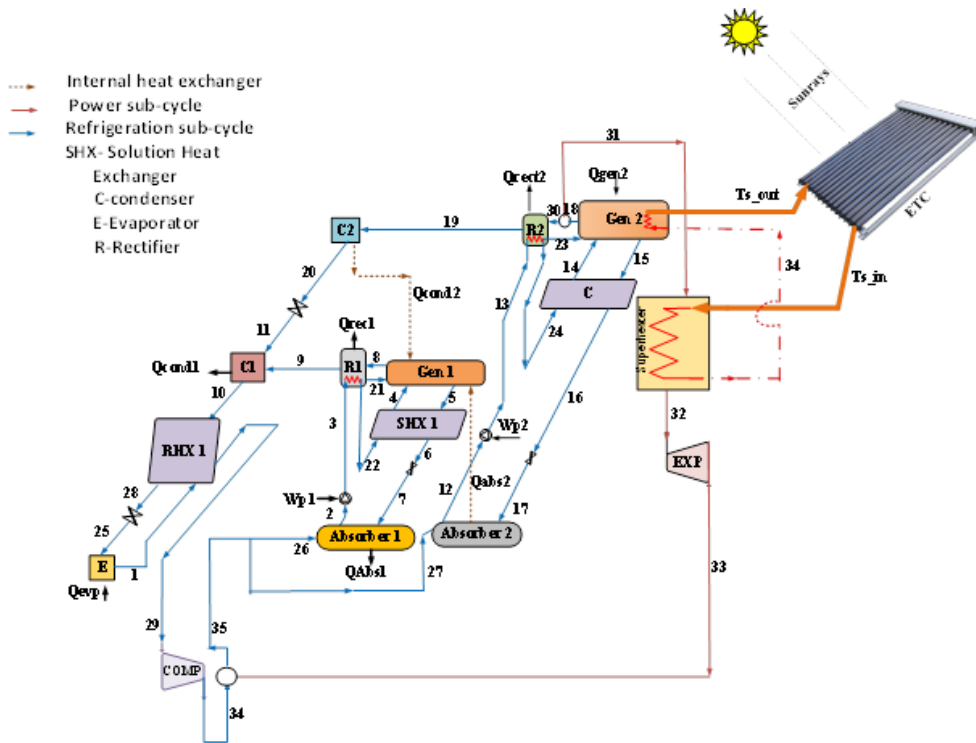


Figure 3: The Solar Powered TECARP Cycle

shared into both absorbers. The share of the refrigerants flowing into absorber2 (state 15) is first passed through absorber1 without mixing. Here, it gains heat which increases its temperature before finally flowing into absorber 2.

### 2.3 Triple effect combined absorption refrigeration and power (TECARP) system

Fig.3 shows the TECARP cycle which uses rejected heat from a coupled high-pressure single effect cycle to drive an inner stage single effect cycle. Similar to the DECARP cycle, it also comprises two generators for fluid separation and two absorbers for reabsorption. The difference however is that the inner and outer stages operate at different generator temperatures. The pressure of the outer stage generator is higher than that of the inner stage which means that each stage will have its separate condenser. The heat required by the generator of the inner cycle is provided by a combination of the Thermal energy rejected in the outer stage generator and absorber.

The refrigerant from rectifier 2 (state 19) is passed into condenser 2. The emerging saturated refrigerant (state 20) then passes through an expansion valve which reduces its pressure to that of condenser 1. Here, it mixes with the refrigerant exiting rectifier 1 and the mixture is then condensed and leaves at state 10.

The same process of refrigerant extraction also occurs in the TECARP cycle. A portion of the refrigerant leaving the outer stage generator is extracted (state 31) and passed through the superheater. The high temperature refrigerant (state 32) expands in the expander chamber consequently generating the power in the system. The refrigerant leaving the evaporator (state 1) after going through the RHX is passed through the compressor which increases its pressure according to the  $P_{com}$ . After leaving the compressor, the compressed refrigerant (state 34) mixes with the refrigerant exiting the expander (state 33) and the resultant mixture (state 35) is separated into two streams; one flowing into absorber 1 (state 26) and the other flowing into absorber 2 (state 27).

### 3 The System Modelling

In the following section, equations based on the mass, concentration, energy, and exergy balance of each component of the three cycles are presented. The equations governing the first and second law performance of the systems are also presented. Tables 1-3 give the energy and exergy balance equations used for the thermodynamic analysis of each component in the three systems analyzed and calculate the exergy destruction rate of each constituent, the exergy at every state point should be defined. Also, chemical and physical exergy was included. The specific physical exergy at every state point (Table 3) is given as [22]:

$$ex_{ph,i} = (h_1 - h_0) - T_0(s_i - s_0) \tag{1}$$

where  $h_0$  and  $s_0$  are the specific enthalpy and entropy for a temperature of  $25^\circ\text{C}$  and Pressure of 101.3 kPa. The specific chemical exergy of the ammonia water at each state point is expressed as [23]:

$$ex_{ch,i} = \frac{z_i}{M_{NH_3}} e_{ch,NH_3}^0 + \frac{1 - z_i}{M_{H_2O}} e_{ch,H_2O}^0 \tag{2}$$

where  $e_{ch,NH_3}^0$  and  $e_{ch,H_2O}^0$  are the normal molar specific exergies of  $NH_3$  and  $H_2O$ ,  $M$  is molar mass. At each state point, the overall specific exergy is expressed as [24]:

$$ex_i = ex_{ph,i} + ex_{ch,i} \tag{3}$$

The cycle steady-state flow exergy balance equation is [25]:

$$\sum_{i \in IN(u)} ex_i m_i - \sum_{i \in OUT(u)} ex_i m_i + \tau_u \dot{Q}_u - \dot{W}_u = E \cdot x_{D,u} \tag{4}$$

The exergy flow related to inlet and outlet mass flow are the first two terms on the left. Where  $\dot{Q}_u$  and  $\dot{W}_u$  are the heat and work transfer rates that go in and out of the system and  $E \cdot x_{D,u}$  is the unit exergy destruction rate. The cycle energy efficiency ( $\eta_1$ ) is given as [26]:

$$\eta_1 = \frac{\dot{W}_{net} + \dot{Q}_{cold}}{\dot{Q}_{gen2} + \dot{Q}_{sh}} \tag{5}$$

where  $\dot{W}_{net}$  is the expander output power minus the pump and compressor work,  $\dot{Q}_{des2}$  and  $\dot{Q}_{sh}$  are the desorber and super heater heat input.

The exergy efficiency ( $\eta_{ex}$ ) of the combined cycle are [18]:

$$\eta_{ex} = \frac{\dot{W}_{net} + E \cdot x_{cold}}{E \cdot x_{gen2} + E \cdot x_{sh}} \tag{6}$$

Combined absorption cycles for dual-production have separate thermodynamic quality, which is not comparable in adding them to the performance evaluation criteria. Therefore, energetic and exergetic performance indicators should, therefore, be considered based on the thermodynamic quality of the useful outputs. In order to evaluate the cooling output of the cycle, the exergy of the cold output should be split by a practical second-law efficiency ( $\eta_{II,ref}$ ) for vapor compression refrigeration cycles. The effective energy and effective exergy efficiency are given as [16], [18]:

$$\eta_{I,eff} = \frac{\dot{W}_{net} + \frac{E \cdot x_{cold}}{\eta_{II,ref}}}{\dot{Q}_{gen2} + \dot{Q}_{sh}} \tag{7}$$

$$\eta_{ex,eff} = \frac{\dot{W}_{net} + \frac{E \cdot x_{cold}}{\eta_{II,ref}}}{E \cdot x_{gen2} + E \cdot x_{sh}} \tag{8}$$

The total exergy destruction rate ( $E \cdot x_{D,total}$ ) represents the lost work potential of driving thermal energy and should be minimised. It can be calculated by adding the sum of individual unit exergy destruction rates. The non-dimensional exergy destruction in each unit is the ratio of its exergy destruction to the cycle's total exergy destruction:  $(E \cdot x_{D,u}) / (E \cdot x_{D,total})$ .

In order to analyze the performance of the different absorption cooling systems, the following assumptions have been made:

- The analysis is made under steady state conditions.
- $NH_3 - H_2O$  solution is at saturated state when leaving the generator & absorber, and refrigerant is at a saturated state when leaving condenser & evaporator.
- Heat losses & pressure drops in the components are negligible.
- The pump process & pressure reduction in the valves are adiabatic.
- The refrigerant vapour concentration at rectifier exits is 0.999.

The design parameters considered for the 3 systems are presented in Table 4. For the purpose of comparison, these parameters are used in all the systems. The refrigerant separation ratio (RSR) determines the amount of the refrigerant that will be passed to the expander for power production and the solution circulation ratio (SCR) is defined as the ratio of the strong solution flow rate to the refrigerant flow rate [27].

**Table 1: Energy and Exergy Destruction Equations for the SECARP System**

Component	Energy is Different from Exergy	Exergy Balance
Pump	$W_p = m_1(h_2 - h_1)$	$E \cdot x_1 + W_p = E \cdot x_2 + E \cdot x_{dest.pump}$
Solution heat exchanger	$m_4 h_4 + m_{16} h_{16} = m_3 h_3 + m_5 h_5$	$E \cdot x_4 + E \cdot x_{16} = E \cdot x_3 + E \cdot x_5 + E \cdot x_{dest.shx}$
Absorber	$m_6 h_6 + m_{17} h_{17} = m_1 h_1 + Q_{Abs}$	$E \cdot x_6 + E \cdot x_{17} + E \cdot x_{cw2.in} = E \cdot x_1 + E \cdot x_{cw2.out} + E \cdot x_{dest.Abs}$
Generator	$m_3 h_3 + m_8 h_8 = m_7 h_7 + Q_{Gen}$	$E \cdot x_3 + E \cdot x_8 = E \cdot x_7 + E \cdot x_{dest.Gen}$
Condenser	$Q_{con} = m_9(h_9 - h_{10})$	$E \cdot x_9 + E \cdot x_{cw1.in} = E \cdot x_{10} + E \cdot x_{cw1.out} + E \cdot x_{dest.con}$
Rectifier	$m_{18} h_{18} = m_8 h_8 + m_9 h_9 + Q_{Rec}$	$E \cdot x_{18} = E \cdot x_8 + E \cdot x_9 + E \cdot x_{dest.Rec}$
Evaporator	$Q_{Eva} = m_{13}(h_{13} - h_{12})$	$E \cdot x_{12} + E \cdot x_{cf.in} = E \cdot x_{13} + E \cdot x_{cf.out} + E \cdot x_{dest.Eva}$
Refrigerant sub-cooler	$m_{10} h_{10} + m_{13} h_{13} = m_{11} h_{11} + m_{14} h_{14}$	$E \cdot x_{10} + E \cdot x_{13} = E \cdot x_{11} + E \cdot x_{14} + E \cdot x_{dest.Rsc}$
Expander	$W_{Exp} = m_{20}(h_{20} - h_{21})$	$E \cdot x_{20} = E \cdot x_{21} + W_{Exp} + E \cdot x_{dest.Exp}$
Compressor	$W_{Com} = m_{14}(h_{15} - h_{14})$	$E \cdot x_{14} + W_{Com} = E \cdot x_{15} + E \cdot x_{dest.Com}$
Super heater	$Q_{sh} = m_{19}(h_{20} - h_{19})$	$E \cdot x_{19} + E \cdot x_{hs.in} = E \cdot x_{20} + E \cdot x_{hs.int} + E \cdot x_{dest.sh}$

**Table 2: Energy and Exergy Destruction Equations for the DECARP System**

Component	Energy is Different from Exergy	Exergy Balance
Pump 1	$W_{p1} = m_1(h_2 - h_1)$	$E \cdot x_1 + W_{p1} = E \cdot x_2 + E \cdot x_{dest.pump1}$
Solution heat exchanger 1	$m_2 h_2 + m_{30} h_{30} = m_3 h_3 + m_5 h_5$	$E \cdot x_2 + E \cdot x_{30} = E \cdot x_3 + E \cdot x_5 + E \cdot x_{dest.shx1}$
Absorber 1	$m_6 h_6 + m_{15} h_{15} + m_{26} h_{26} = m_1 h_1 + m_{29} h_{29} + Q_{Abs1}$	$E \cdot x_6 + E \cdot x_{15} + E \cdot x_{26} + E \cdot x_{cw2.in} = E \cdot x_1 + E \cdot x_{29} + E \cdot x_{cw2.out} + E \cdot x_{dest.Abs1}$
Generator 1	$m_3 h_3 + m_8 h_8 + m_{24} h_{24} + Q_{Rec2} + Q_{Abs2} = m_4 h_4 + m_7 h_7 + Q_{Gen1}$	$E \cdot x_3 + E \cdot x_8 + E \cdot x_{24} + E \cdot x_{Rec2} + E \cdot x_{Abs2} = E \cdot x_4 + E \cdot x_7 + E \cdot x_{dest.Gen1}$
Pump 2	$W_{p2} = m_{16}(h_{17} - h_{16})$	$E \cdot x_{16} + W_{p2} = E \cdot x_{17} + E \cdot x_{dest.pump2}$
Solution heat exchanger 2	$m_{19} h_{19} + m_{27} h_{27} = m_{18} h_{18} + m_{20} h_{20}$	$E \cdot x_{19} + E \cdot x_{27} = E \cdot x_{18} + E \cdot x_{20} + E \cdot x_{dest.shx2}$
Generator 2	$m_{18} h_{18} + m_{23} h_{23} + m_{sh} h_{hs.int} = m_{19} h_{19} + m_{22} h_{22} + m_{sh} h_{hs.out} + Q_{Gen2}$	$E \cdot x_{18} + E \cdot x_{23} + E \cdot x_{hs.int} = E \cdot x_{19} + m_{22} + E \cdot x_{hs.out} + E \cdot x_{dest.Gen2}$
Condenser	$Q_{con2} = m_9(h_9 - h_{10})$	$E \cdot x_9 + E \cdot x_{cw1.in} = E \cdot x_{10} + E \cdot x_{cw1.out} + E \cdot x_{dest.con2}$
Rectifier 1	$m_{31} h_{31} = m_8 h_8 + m_9 h_9 + Q_{Rec1}$	$E \cdot x_{31} = E \cdot x_8 + E \cdot x_9 + E \cdot x_{dest.Rec1}$
Rectifier 2	$m_{25} h_{22} = m_{23} h_{23} + m_{24} h_{24} + Q_{Rec2}$	$E \cdot x_{22} = E \cdot x_{23} + E \cdot x_{24} + E \cdot x_{dest.Rec2}$
Absorber 2	$m_{21} h_{21} + m_{29} h_{29} = m_{16} h_{16} + Q_{Abs1}$	$E \cdot x_{21} + E \cdot x_{29} + E \cdot x_{cw3.in} = E \cdot x_{16} + E \cdot x_{cw3.out} + E \cdot x_{dest.Abs2}$
Super heater	$Q_{sh} = m_{32}(h_{33} - h_{32})$	$E \cdot x_{32} + E \cdot x_{hs.in} = E \cdot x_{33} + E \cdot x_{hs.int} + E \cdot x_{dest.sh}$

**Table 3: Energy and Exergy Destruction Equations for the TECARP System**

Component	Energy is Different from Exergy	Exergy Balance
Pump 1	$W_{p1} = m_2(h_3 - h_2)$	$E \cdot x_2 + W_{p1} = E \cdot x_3 + E \cdot x_{dest.pump1}$
Solution heat exchanger 1	$m_5 h_5 + m_{22} h_{22} = m_4 h_4 + m_6 h_6$	$E \cdot x_5 + E \cdot x_{22} = E \cdot x_4 + E \cdot x_6 + E \cdot x_{dest.shx1}$
Absorber 1	$m_7 h_7 + m_{26} h_{26} = m_2 h_2 + Q_{Abs1}$	$E \cdot x_7 + E \cdot x_{26} + E \cdot x_{cw2.in} = E \cdot x_2 + E \cdot x_{cw2.out} + E \cdot x_{dest.Abs1}$
Generator 1	$m_4 h_4 + m_2 h_2 + Q_{con2} + Q_{Abs2} = m_5 h_5 + m_8 h_8 + Q_{Gen1}$	$E \cdot x_4 + E \cdot x_{21} + E \cdot x_{con2} + E \cdot x_{Abs2} = E \cdot x_5 + E \cdot x_8 + E \cdot x_{dest.Gen1}$
Condenser 1	$m_9 h_9 + m_{11} h_{11} = m_{10} h_{10} + Q_{con1}$	$E \cdot x_9 + E \cdot x_{11} + E \cdot x_{cw1.in} = E \cdot x_{10} + E \cdot x_{cw1.out} + E \cdot x_{dest.con2}$
Pump 2	$W_{p2} = m_{12}(h_{13} - h_{12})$	$E \cdot x_{12} + W_{p2} = E \cdot x_{13} + E \cdot x_{dest.pump2}$
Solution heat exchanger 2	$m_{15} h_{15} + m_{24} h_{24} = m_{14} h_{14} + m_{16} h_{16}$	$E \cdot x_{15} + E \cdot x_{24} = E \cdot x_{14} + E \cdot x_{16} + E \cdot x_{dest.shx2}$
Generator 2	$m_{14} h_{14} + m_{23} h_{23} + m_{sh} h_{hs.int} = m_{15} h_{15} + m_{18} h_{18} + m_{sh} h_{hs.out} + Q_{Gen2}$	$E \cdot x_{14} + E \cdot x_{23} + E \cdot x_{hs.int} = E \cdot x_{15} + m_{18} + E \cdot x_{hs.out} + E \cdot x_{dest.Gen2}$
Condenser 2	$Q_{con2} = m_{19}(h_{19} - h_{20})$	$E \cdot x_{19} + E \cdot x_{cw4.in} = E \cdot x_{20} + E \cdot x_{cw4.out} + E \cdot x_{dest.con2}$
Rectifier 1	$m_3 h_3 + m_8 h_8 = m_9 h_9 + m_{21} h_{21} + m_{22} h_{22} + Q_{Rec1}$	$E \cdot x_3 + E \cdot x_8 = E \cdot x_9 + E \cdot x_{21} + E \cdot x_{22} + E \cdot x_{dest.Rec1}$
Rectifier 2	$m_{13} h_{13} = m_{30} h_{30} = m_{19} h_{19} + m_{23} h_{23} + m_{24} h_{24} + Q_{Rec2}$	$E \cdot x_{13} + E \cdot x_{30} = E \cdot x_{19} + E \cdot x_{23} + E \cdot x_{24} + E \cdot x_{dest.Rec2}$
Evaporator	$Q_{Eva} = m_{25}(h_1 - h_{25})$	$E \cdot x_{25} + E \cdot x_{cf.in} = E \cdot x_1 + E \cdot x_{cf.out} + E \cdot x_{dest.Eva}$
Refrigerant sub-cooler	$m_1 h_1 + m_{10} h_{10} = m_{28} h_{28} + m_{29} h_{29}$	$E \cdot x_1 + E \cdot x_{10} = E \cdot x_{28} + E \cdot x_{29} + E \cdot x_{dest.Rsc}$
Expander	$W_{Exp} = m_{32}(h_{33} - h_{32})$	$E \cdot x_{32} = E \cdot x_{33} + W_{Exp} + E \cdot x_{dest.Exp}$
Compressor	$W_{Com} = m_{29}(h_{34} - h_{29})$	$E \cdot x_{29} + W_{Com} = E \cdot x_{34} + E \cdot x_{dest.Com}$
Absorber 2	$m_{17} h_{17} + m_{27} h_{27} = m_{12} h_{12} + Q_{Abs1}$	$E \cdot x_{17} + E \cdot x_{27} + E \cdot x_{cw3.in} = E \cdot x_{12} + E \cdot x_{cw3.out} + E \cdot x_{dest.Abs2}$
Super heater	$Q_{sh} = m_{31}(h_{32} - h_{31})$	$E \cdot x_{31} + E \cdot x_{hs.in} = E \cdot x_{32} + E \cdot x_{hs.int} + E \cdot x_{dest.sh}$

**Table 4: Assumed Input Parameters for the Simulation of the 3 Systems**

Parameter	SECARP	DECARP	TECARP
Total mass flow rate (kg/s)	1	1	1
Solution heat exchanger and Refrigerant sub-cooler effectiveness	0.85	0.85	0.85
Pump and compressor efficiency	0.80	0.80	0.80
Expander efficiency	0.85	0.85	0.85
Condenser and Absorber temperature (°C)	35	35	35
Evaporator exit temperature (°C)	-10	-10	-10
Cooling water inlet/outlet temperature (°C)	30/35	30/35	30/35
Chilled fluid (ethelyne) inlet/outlet temperature (°C)	-1/-10	-1/-10	-1/-10
Refrigerant separation ratio	$\frac{m_{19}}{m_7}$	$\frac{m_{32}}{m_7}$	$\frac{m_{31}}{m_{18}}$
Solution circulation ratio	$\frac{x_9 - x_4}{x_3 - x_4} = 9$	$\frac{x_{24} - x_{19}}{x_{18} - x_{19}} = 19$	$\frac{x_{19} - x_{15}}{x_{14} - x_{15}} = 30$

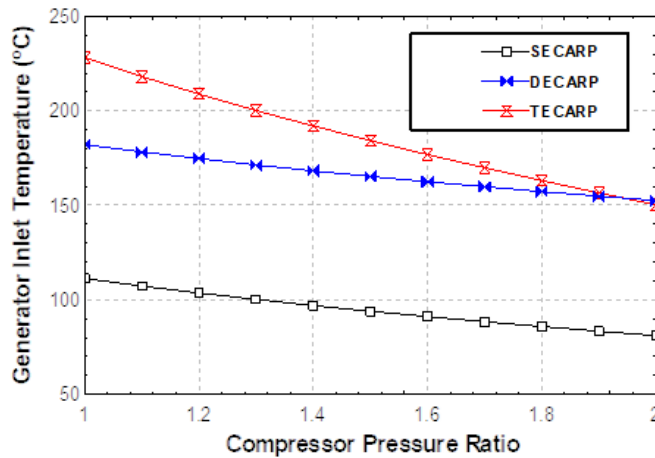


Figure 4: Effect of Compression Ratio on the Generator Inlet Temperatures

**4 Results and Discussion**

The inclusion of the compressor in these systems is to enable them operate at lower temperatures compared to the traditional vapor absorption cycles. As explained earlier, the power consumption of the pumps and the compressors in all three systems is provided by expander output power. For each of the systems to be self-sufficient, the amount of the refrigerant separated for the turbine operation has to exactly what would be needed to power the compressors and pumps. This will be determined by the refrigerant split ratio (RSR) of the respective systems. All the power generated is consumed by the solution pump and compressor.

As the compression pressure ratio  $P_{com}$  increases, the mechanical compression process enhances the heat transformation process. Consequently, the required driving heat source temperature  $t_{hs,in}$  drops when the  $P_{com}$  increases, as shown in Fig. 4. In the TECARP system, as  $P_{com}$  increases from 1 to 2, the generator inlet temperature reduces from  $228^{\circ}C$  to  $150^{\circ}C$  in the TECARP system, representing a 34.78% decrease. In comparison, the SECARP system experiences a 21.73% decrease in the generator temperature while the decrease in the DECARP system is 16.25%.

Fig. 5 shows the effect of increasing the  $P_{com}$  on the compression work in all three systems. As expected, when the  $P_{com}$  increases from 1 to 2, the compression work in the systems also increases. The figure shows that at  $P_{com} = 1$ , the compression work in all three systems is zero but as the pressure ratio increases, the value also increases up to the final values of about 6 kW, 7 kW, and 7.5 kW in the SECARP, DECARP, and TECARP systems respectively.

Figure 6 also shows the amount of vapour that needs to be produced by the generator in order for the system to run on its own, that is, to power the solution pump and mechanical compressor. This figure shows that as  $P_{com}$  increases, the RSR also increases in all three systems. This is because the systems will require more refrigerant for power production to cover the increasing compression work as shown in Fig. 5. However, it is observed that the RSR to ensure autonomous operation in the TECARP system starts from about 0.22 and increases to about 0.79 as the  $P_{com}$  increases. This is as a result of the design arrangement of the TECARP system in which the refrigerant is extracted from the exit of the high pressure generator where the mass flow rate is low.

Fig. 7 shows the energetic implications of the compression process on the three cycles. The cooling output of the cycles decrease as the  $P_{com}$  increases from 1 to 2. The cooling load of the SECARP and DECARP systems reduce as the  $P_{com}$  increases. This is because the RSR also has to increase to cover for the increasing compression work. The cooling load of the TECARP system is however hardly affected as shown in the figure. This is because of the design of the TECARP system where the inner cycle is unaffected by the refrigerant extraction for power generation and since majority of the refrigerant that goes into the evaporator comes from the inner cycle, the cooling load will be hardly affected.

In reality the cooling systems often serve fixed loads, so they have to supply the same amount of cooling throughout their operation. Also, for the solar powered systems that are being considered in this study, intermittent heat supply associated with solar thermal systems can be a problem for fixed load supply. These systems should therefore be able to adjust its heat source temperature requirements to produce the same cooling load by adjusting the  $P_{com}$ . Fig. 8a, 8b, 8c show the effect of pressure ratio increase in the SECARP, DECARP, and TECARP systems respectively. The cooling loads in each system has been fixed as 60 kW and 75 kW. The effect on the generator inlet temperatures and the RSR in the systems are illustrated. The figures show that for the 3 cycles, the 60 kW systems require less operating generator temperatures affirming that the operating temperature increases as the system size increases. However, the RSR is more in the 60 kW systems as they have to compensate for less amount of refrigerant from the generators compared to the 75 kW systems.

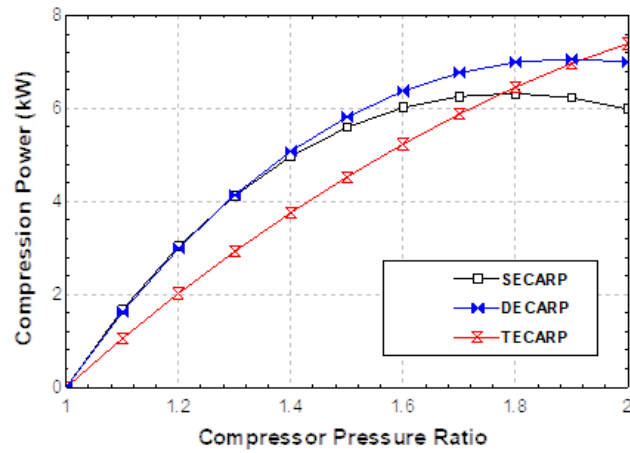


Figure 5: Effect of Compression Ratio on the Compression Power

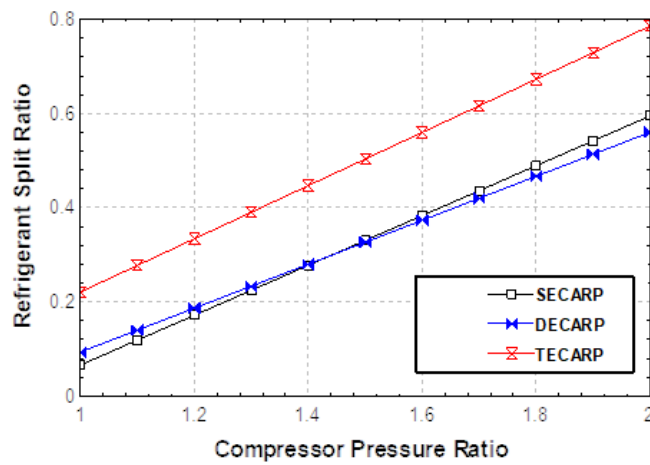


Figure 6: Effect of Compression Ratio on the Refrigerant Split Ratio (RSR) Required for Self-Sufficiency

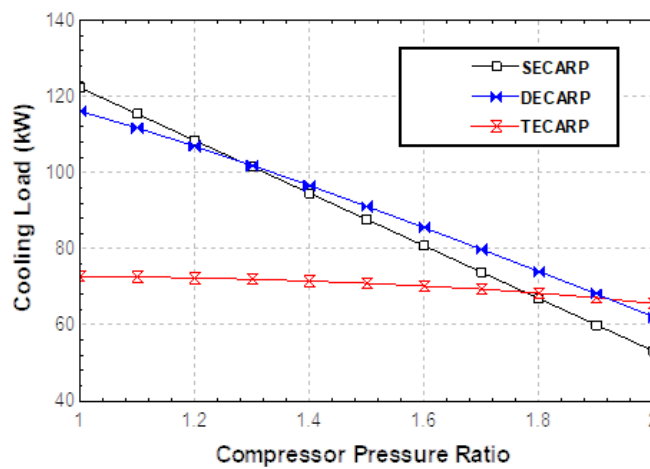


Figure 7: Effect of Compression Ratio on the Cooling Loads

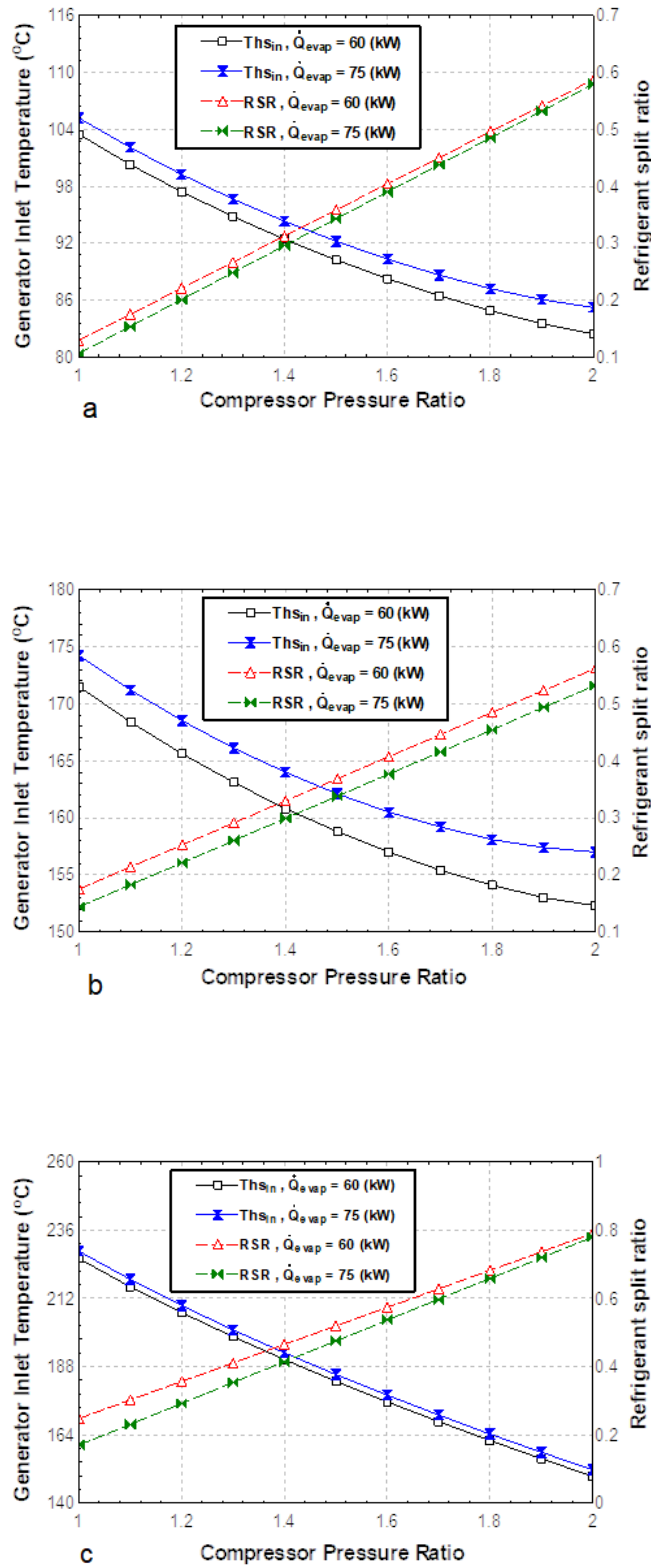


Figure 8: Effect of the Compression Pressure Ratio on the Generator Inlet Temperature and the RSR in (a) – SECARP (b) – DECARP (c) – TECARP for Fixed Cooling Loads

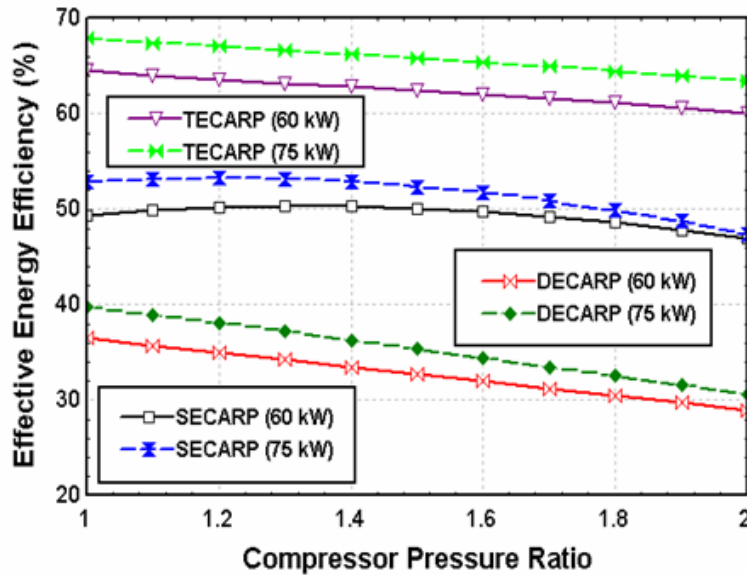


Figure 9: Effect of the Compressor Pressure Ratio on the Effective Energy Efficiency for Fixed System Sizes of the Three Cycles

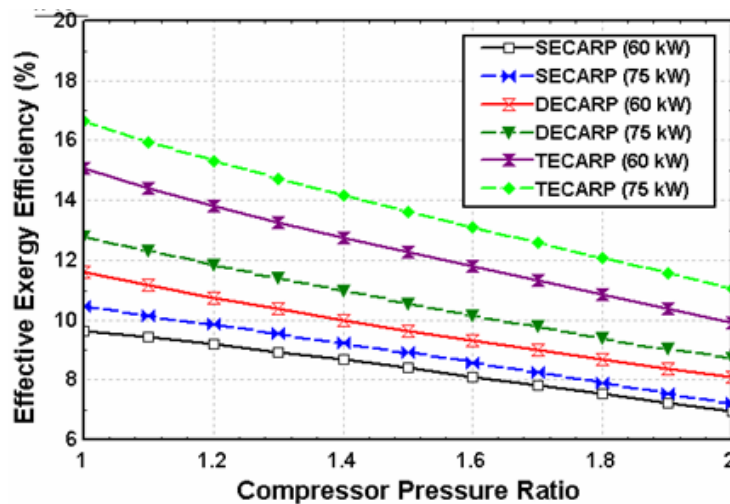


Figure 10: Effect of the Compressor Pressure Ratio on the Effective Exergy Efficiency for Fixed System Sizes of Three Cycles

Fig. 9 and Fig. 10 show the effect of varying the compression ratio on the effective energy and exergy efficiencies respectively. As the Prcom increases from 1 to 2, the performance of all the 3 systems reduce. The DECARP system can be seen to perform better than the SECARP system when comparing their effective energy efficiencies but the SECARP system performs better in terms of effective exergy efficiency. However, it is observed that the performance of the TECARP system increases as the Prcom increases. The performance of the TECARP system also decreases as the Prcom increases. Both the effective energy and exergy efficiencies decrease with increase in Prcom. The figures also show that the performance of the 75 kW system is better in all the 3 systems.

Fig.11 shows the share of the exergy destruction of each of the components in each of the three systems at Prcom = 2 for 75 kW cooling load. The combined destruction rate is taken for 2 of the same component in a system. e.g. for the 2 condensers in the TECARP system. In this figure, it can be observed that exergy destruction in the absorber is highest for all the systems. The main reason for this is the mass transfer between the internal streams, as well as the heat transfer that takes place between the NH<sub>3</sub>/H<sub>2</sub>O working fluid pair and the external cooling water circuit. The relatively lower exergy destruction contribution in the generators are due to the assumed perfect thermal capacitance match between the heat source fluid and the NH<sub>3</sub>/H<sub>2</sub>O mixture in the generator, which minimizes exergy destruction.

The summary of the results obtained from the simulation of the three systems for 75 kW cooling load and Prcom = 2 is

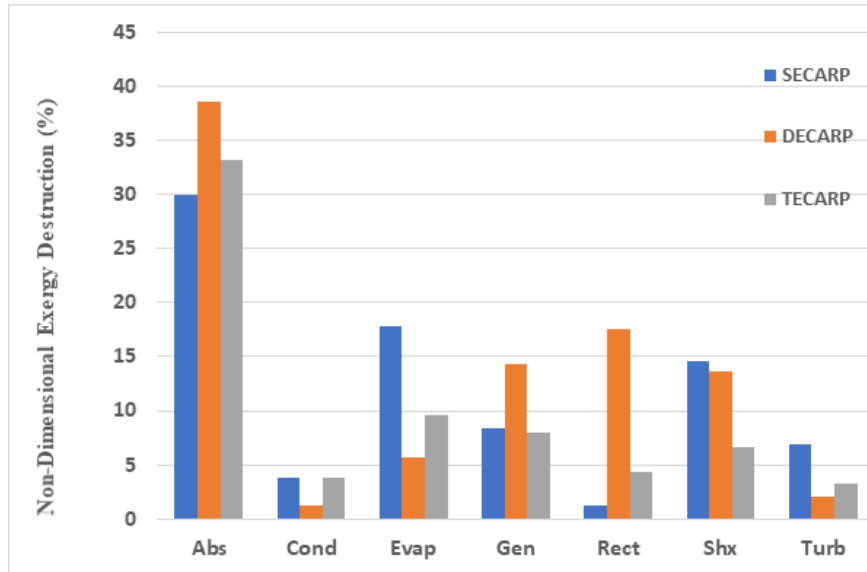


Figure 11: Non-Dimensional Exergy Destruction for Major Components in the 75 kW Systems at Prcom=2

Table 5: System Output Results for the Three Systems at Prcom = 2 and 75 kW Cooling Load

Parameter	SECARP	DECARP	TECARP
Pump1 work (kW)	1.245	1.245	0.9967
Pump2 work (kW)	-	1.197	0.809
Compressor work (kW)	8.461	8.792	8.594
Expander work output (kW)	9.749	11.24	10.49
Absorber1 heat load (kW)	252.7	190	110.9
Absorber2 heat load (kW)	-	128.9	91.8
Condenser1 heat load (kW)	74.18	77.1	65.71
Condenser2 heat load (kW)	-	-	9.318
SHX1 heat load (kW)	140	230	128.4
SHX2 heat load (kW)	-	186	22.94
RSC heat load (kW)	7.203	7.485	7.319
Generator1 load (kW)	244.6	175.5	101.1
Generator2 load (kW)	-	190.4	89.13
Rectifier1 heat load (kW)	5.001	14.31	4.327
Rectifier2 heat load (kW)	-	46.62	74.93
Super heater heat load (kW)	3.233	12.6	1.433
Cooling exergy (kW)	5.524	5.74	5.611
Heat source input exergy, $\Delta(Ex)_{hs}$ (kW)	38.16	60.68	35.95
Effective energy efficiency (%)	7.5	9.2	20.8
Effective exergy efficiency (%)	48.4	30.8	52.3

presented in Table 5. The state point properties for each of the three systems are also presented in Tables 6-8.

#### 4.1 Comparison of the Systems with Similar Studies in Literature

The modification of vapor absorption systems with either an expander, a compressor, or a combination of both have been previously studied by various researchers. The expander integration provides added power generation from the vapor absorption system to cover power needs when necessary. In its case, the integration of the compressor helps to reduce the inlet temperature required for the fluid separation in the generator. A combination of the two gives a hybrid system capable of providing both cooling/refrigeration and power generation and at a lower operating temperature. The three systems evaluated in this study are compared to other modified systems in literature as presented in Table 9.

The systems selected for the comparison have either an integrated expander, compressor, or both. The effective performance of the systems with the integrated expander are listed in the table while the inlet temperature reduction achieved for the systems with integrated compressors are listed. The systems with both integrated compressor and expander therefore have both the inlet temperature reduction and the performances listed.

The results show that the systems with integrated expanders are able to operate on high pressure ratios (3.5-4) which results in a high effective exergy efficiency (~ 42%) for the single and triple effect hybrid systems operating on  $NH_3 - H_2O$ . On the other hand, the systems with integrated compressors are able to reach pressure ratios of around 2. The single effect  $NH_3 - LiNO_3$  system showed a 24°C inlet temperature reduction. In comparison, the single effect hybrid  $NH_3 - H_2O$  system presented in this study has a 31°C temperature reduction and an effective exergy efficiency of 48.4%.

**Table 6: Thermodynamic Properties of the SECARP System at Prcom = 2 and 75 kW Cooling Load**

State	$T^{\circ}C$	P (kPa)	$m'$ (kg/s)	x	h (kJ/kg)	s (kJ/kg.K)	$E \cdot x$ (kW)
1	35	556.1	1	0.5562	-78.14	0.366	39.66
2	35.13	1350	1	0.5562	-76.9	0.3668	40.66
3	67.09	1350	1	0.5562	72.16	0.8263	52.7
4	79.94	1350	0.8476	0.4772	121.8	0.9844	32.33
5	43.65	1350	0.8476	0.4772	-43.35	0.491	17.03
6	43.79	556.1	0.8476	0.4772	-43.35	0.494	16.26
7	66.97	1350	0.1532	0.9936	1394	4.535	55.55
8	66.97	1350	0.000782	0.5562	69.3	0.818	0.04094
9	47.22	1350	0.06361	0.999	1332	4.346	22.68
10	35	1350	0.06361	0.999	165.6	0.5802	19.94
11	11.35	1350	0.06361	0.999	52.32	0.1982	19.98
12	-11.07	278.1	0.06361	0.999	52.32	0.2186	19.59
13	-10	278.1	0.06361	0.999	1231	4.694	9.695
14	26.26	278.1	0.06361	0.999	1344	5.102	9.164
15	89.02	556.1	0.06361	0.999	1477	5.177	16.21
16	37.13	1350	1	0.5562	-67.83	0.3961	40.99
17	49.27	556.1	0.1524	0.9959	1386	4.912	36.97
18	66.97	1350	0.0644	0.9936	1394	4.535	23.35
19	66.97	1350	0.08882	0.9936	1394	4.535	32.2
20	80.24	1350	0.08882	0.9936	1430	4.639	32.68
21	30.69	556.1	0.08882	0.9936	1321	4.703	21.24

**Table 7: Thermodynamic Properties of the DECARP System at Prcom = 2 and 75 kW Cooling Load**

State	$T^{\circ}C$	P (kPa)	$m'$ (kg/s)	x	h (kJ/kg)	s (kJ/kg.K)	$E \cdot x$ (kW)
1	35	556.1	1	0.419806	-76.653	0.381	7.037
2	35.1	1349.8	1	0.419806	-75.4081	0.383	7.982
3	86.4	1349.8	1	0.419806	154.5751	1.072	32.3
4	101.2	1349.8	0.921843	0.369599	231.2098	1.268	36.67
5	45.2	1349.8	0.918253	0.369599	-19.2477	0.544	4.808
6	45.3	556.1	0.918253	0.369599	-19.2477	0.547	4.013
7	90.8	1349.8	0.14841	0.971023	1481.799	4.784	55.19
8	90.8	1349.8	0.003355	0.419805	175.0014	1.129	0.1204
9	47.2	1349.8	0.066101	0.999	1331.602	4.346	23.57
10	35	1349.8	0.066101	0.999	165.5233	0.58	20.71
11	11.35	1350	0.06361	0.999	52.32	0.1982	19.98
12	-11.1	278.1	0.066101	0.999	52.28945	0.218	20.36
13	-10	278.1	0.066101	0.999	1231.206	4.695	10.07
14	26.3	278.1	0.066101	0.999	1344.44	5.102	9.523
15	88.1	556.1	0.063308	0.983772	1492.155	5.224	16.17
16	101.2	556.1	1.040555	0.208758	292.2798	1.326	37.75
17	101.3	1349.8	1.040555	0.208758	293.4297	1.327	38.76
18	139.4	1349.8	1.044145	0.209311	471.3539	1.778	83.99
19	151.7	1349.8	0.977247	0.158551	546.0175	1.907	91.5
20	109.1	1349.8	0.977247	0.158551	355.685	1.435	42.98
21	112.2	556.1	0.977247	0.158551	355.685	1.438	42.29
22	138.8	1349.8	0.087367	0.777087	1813.496	5.516	38.76
23	138.8	1349.8	0.020469	0.209311	461.3503	1.754	1.594
24	101.2	1349.8	0.066898	0.950816	1530.361	4.911	25.31
25	89	556.1	0.066101	0.999	1477.444	5.177	16.84
26	88.1	556.1	0.081747	0.983772	1492.155	5.224	20.89
27	101.3	1349.8	1.044145	0.209311	293.2158	1.327	38.92
28	101.2	1349.8	0.00359	0.369599	231.2098	1.268	0.1428
29	45.3	556.1	0.063308	0.983772	1349.522	4.799	15.16
30	101.2	1349.8	0.918253	0.369599	231.2098	1.268	36.53
31	90.8	1349.8	0.069456	0.971023	1481.799	4.784	25.83
32	90.8	1349.8	0.078954	0.971023	1481.799	4.784	29.36
33	152.6	1349.8	0.078954	0.971023	1641.361	5.189	32.44
34	87.3	556.1	0.078954	0.971023	1504.471	5.257	20.04
35	88.1	556.1	0.145055	0.983772	1492.155	5.224	36.84

**Table 8: Thermodynamic Properties of the TECARP System at Prcom = 2 and 75 kW Cooling Load**

State	$T^{\circ}C$	P (kPa)	$m'$ (kg/s)	x	h (kJ/kg)	s (kJ/kg.K)	$E_x$ (kW)
1	-10.03	277.7	0.06461	0.999	1231	4.695	9.827
2	35	555.4	1	0.5559	-78.19	0.3659	39.54
3	35.08	1350	1	0.5559	-77.2	0.3659	40.54
4	64.04	1350	1	0.5559	55.56	0.7775	50.59
5	70.98	1350	0.9451	0.5302	83.86	0.8682	43.75
6	41.34	1350	0.9451	0.5302	-52.04	0.4553	31.65
7	39.13	555.4	0.9451	0.5302	-52.04	0.4584	30.79
8	67.02	1350	0.05558	0.9936	1394	4.536	20.15
9	47.22	1350	0.0549	0.999	1332	4.346	19.57
10	35	1350	0.06461	0.999	165.6	0.5805	20.24
11	35.01	1350	0.009713	0.999	340.1	1.145	3.103
12	69.04	555.4	0.2525	0.3555	89	0.8678	3.489
13	69.34	3252	0.2525	0.3555	92.2	0.8678	4.298
14	150.6	3252	0.2525	0.3555	479.8	1.879	26.03
15	156.1	3252	0.2428	0.3298	505.4	1.93	26.25
16	137	3252	0.2428	0.3298	411	1.704	19.61
17	92.4	555.4	0.2428	0.3298	411	1.757	15.83
18	150	3252	0.05315	0.8897	1665	4.842	27.64
19	73.91	3252	0.009713	0.999	1300	3.923	4.379
20	69.04	3252	0.009713	0.999	340.1	1.107	3.214
21	67.02	1350	0.000678	0.5559	69.46	0.8186	0.0354
22	36.03	1350	1	0.5559	-72.87	0.38	40.69
23	150	3252	0.001986	0.3555	470.7	1.858	0.1994
24	133.6	3252	0.2525	0.3555	388.9	1.661	19.53
25	-11.1	277.7	0.06461	0.999	52.28	0.2185	19.9
26	95	555.4	0.0549	0.999	1492	5.216	14.12
27	95	555.4	0.009713	0.999	1492	5.216	2.498
28	11.34	1350	0.06461	0.999	52.28	0.198	20.29
29	26.26	277.7	0.06461	0.999	1344	5.103	9.295
30	150	3252	0.0117	0.8897	1665	4.842	6.084
31	150	3252	0.04145	0.8897	1665	4.842	21.56
32	161.6	3252	0.04145	0.8897	1699	4.922	22
33	83.07	555.4	0.04145	0.8897	1446	5.046	9.985
34	89.02	555.4	0.06461	0.999	1477	5.177	16.45
35	95	555.4	0.1061	0.9563	1465	5.139	26.13

**Table 9: Comparison of Hybrid Absorption Cooling Systems**

Integrated Absorption System	Working Fluid	Reference	Prcom	Temperature Reduction $\delta T_{hs,in}$	Effective Energy Efficiency (%)	Effective Exergy Efficiency (%)
Single effect-expander	$NH_3 - H_2O$	[15]	4	-	7	42
Double effect-expander	$NH_3 - H_2O$	[28]	3.5	-	16.8	42.7
Triple effect-expander	$NH_3 - H_2O$	[28]	3.5	-	14.6	41.8
Single effect-compressor	$NH_3 - LiNO_3$	[29]	2	24	-	-
Triple effect-compressor-expander	$LiBr - H_2O$	[6]	2.2	50	-	-
Single effect-compressor-expander	$NH_3 - H_2O$	Present study	2	31	7.5	48.4
Double effect-compressor-expander	$NH_3 - H_2O$	Present study	2	29	9.2	30.8
Triple effect-compressor-expander	$NH_3 - H_2O$	Present study	2	78	20.8	52.3

The triple effect compressor-absorber hybrid system operating on  $LiBr - H_2O$  was able to provide a  $50^{\circ}C$  inlet temperature reduction. The triple effect  $NH_3 - H_2O$  hybrid system presented in this study can provide a  $78^{\circ}C$  inlet temperature reduction and its effective exergy efficiency reaches 52.3%. This shows the large benefits that the hybrid triple effect systems can gain in comparison to the other systems, especially in terms of the inlet temperature reduction.

**5 Conclusion**

This research analyses three compressor-assisted absorption cycles for refrigeration and power using ammonia water as working fluid. The conclusions are as follows :

- The incorporation of a compressor to the three systems result in the heat source temperature (ths,in) reducing in all the systems. Increasing the compression ratio from 1 to 2 reduces 'ths,in' in the SECARP system from  $111.3^{\circ}C$  to  $81.1^{\circ}C$  representing a 27% reduction. The reduction in the DECARP system is from  $182.1^{\circ}C$  to  $152.5^{\circ}C$  representing a 16% and the temperature in the TECARP system drops from  $228.3^{\circ}C$  to  $150.3^{\circ}C$  representing a 34% reduction.
- The refrigerant split ratio (RSR) needed to ensure self-sufficiency in the TECARP system increases from 0.22 to 0.79. This is significantly higher compared to the SECARP and DECARP systems.
- The performance analysis of the systems shows that the TECARP system experience a much bigger benefit from integrating the compressor in the system. The results show that while the energetic and exergetic performance of the SECARP and DECARP systems reduce as the Prcom increases, the TECARP system's performance increases with

increase in Prcom.

- The exergy analysis of the systems reveal that the largest destruction rate occurs in the absorbers of each of the three systems. Also, the absorber in the DECARP system experiences the highest exergy destruction.

This study may provide a new efficient way to produce low-temperature heat source to provide power and cooling by using mid-temperature heat sources. The systems analyzed can utilize heat from a solar thermal collector for instance to provide both cooling and power when needed. The option of self-sufficiency in the cooling mode of the systems also make them prime candidates for operation in remote locations where grid electricity may be non-existent. Analysis of the systems show that the TECARP system will be most suitable for this application as it offers the biggest inlet operating temperature reduction and the best performance of the three systems.

### Acknowledgment

The authors would like to acknowledge Cyprus Science University, Brunei Darussalam University, International Cyprus University and National University of Sciences and Technology.

### Authors' Contributions

In this study, all authors studied and designed the article.

### Competing Interests

The authors declare that they have no conflict of interest.

### References

- [1] Molly, "Proof of climate change: How do we cool a heating world?," Sept. 2018.
- [2] H. Chua, H. Toh, A. Malek, K. Ng, and K. Srinivasan, "A general thermodynamic framework for understanding the behaviour of absorption chillers," *International Journal of Refrigeration*, vol. 23, no. 7, pp. 491–507, 2000.
- [3] S. A. Khan, "Comparative analysis of single and double effect liBr-water absorption system," in *4th International Conference on Recent Innovations in Sciences Engineering and Management*, 2016.
- [4] Minnesota Pollution Control Agency, "Chlorofluorocarbons (cfc) and hydrofluorocarbons (hfc),"
- [5] J. Wang, B. Wang, W. Wu, X. Li, and W. Shi, "Performance analysis of an absorption-compression hybrid refrigeration system recovering condensation heat for generation," *Applied Thermal Engineering*, vol. 108, pp. 54–65, 2016.
- [6] G. Shu, J. Che, H. Tian, X. Wang, and P. Liu, "A compressor-assisted triple-effect h<sub>2</sub>O-liBr absorption cooling cycle coupled with a rankine cycle driven by high-temperature waste heat," *Applied Thermal Engineering*, vol. 112, pp. 1626–1637, 2017.
- [7] V. H. F. Flores, J. C. Román, and G. M. Alpiéz, "Performance analysis of different working fluids for an absorption refrigeration cycle," *American Journal of Environmental Engineering, DOI*, vol. 10, pp. 1–10, 2014.
- [8] J. Deng, R. Wang, and G. Han, "A review of thermally activated cooling technologies for combined cooling, heating and power systems," *Progress in energy and combustion science*, vol. 37, no. 2, pp. 172–203, 2011.
- [9] V. Eveloy and D. S. Ayou, "Sustainable district cooling systems: Status, challenges, and future opportunities, with emphasis on cooling-dominated regions," *Energies*, vol. 12, no. 2, p. 235, 2019.
- [10] A. Shirazi, R. A. Taylor, G. L. Morrison, and S. D. White, "Solar-powered absorption chillers: A comprehensive and critical review," *Energy conversion and management*, vol. 171, pp. 59–81, 2018.
- [11] J.-S. Kim, F. Ziegler, and H. Lee, "Simulation of the compressor-assisted triple-effect h<sub>2</sub>O/liBr absorption cooling cycles," *Applied Thermal Engineering*, vol. 22, no. 3, pp. 295–308, 2002.
- [12] M. Udayakumar *et al.*, "Studies of compressor pressure ratio effect on gaxac (generator-absorber-exchange absorption compression) cooler," *Applied Energy*, vol. 85, no. 12, pp. 1163–1172, 2008.
- [13] W. Chen *et al.*, "Investigation of [mmim]dmp/ch<sub>3</sub>oh absorption refrigeration thermodynamic performances," *Journal of Engineering Thermophysics*, vol. 34, pp. 689–693, 2013.
- [14] D. Boer, M. Valles, and A. Coronas, "Performance of double effect absorption compression cycles for air-conditioning using methanol-tgdme and tfe-tgdme systems as working pairs: Performances de cycles à compression absorption à double effet pour le conditionnement d'air utilisant les couples méthanol-tgdme ou tfe-tgdme," *International Journal of Refrigeration*, vol. 21, no. 7, pp. 542–555, 1998.
- [15] G. Demirkaya, R. Vasquez Padilla, D. Y. Goswami, E. Stefanakos, and M. M. Rahman, "Analysis of a combined power and cooling cycle for low-grade heat sources," *International Journal of Energy Research*, vol. 35, no. 13, pp. 1145–1157, 2011.
- [16] G. P. Kumar, R. Saravanan, and A. Coronas, "Simulation studies on simultaneous power, cooling and purified water production using vapour absorption refrigeration system," *Applied Thermal Engineering*, vol. 132, pp. 296–307, 2018.
- [17] S. Aghniaey and S. M. S. Mahmoudi, "Exergy analysis of a novel absorption refrigeration cycle with expander and compressor," *Indian Journal of Scientific Research*, vol. 1, pp. 815–822, 2014.
- [18] D. S. Ayou, J. C. Bruno, and A. Coronas, "Integration of a mechanical and thermal compressor booster in combined absorption power and refrigeration cycles," *Energy*, vol. 135, pp. 327–341, 2017.
- [19] C. F. Okwose, M. Abid, and T. A. Ratlamwala, "Performance analysis of compressor-assisted two-stage triple effect absorption refrigeration cycle for power and cooling," *Energy Conversion and Management*, vol. 227, p. 113547, 2021.
- [20] C. F. Okwose, M. Abid, and T. A. H. Ratlamwala, "Performance evaluation of compressor assisted multi-effect absorption refrigeration cycles for power and cooling using evacuated tube collectors," *International Journal of Exergy*, vol. 32, no. 3, pp. 227–248, 2020.
- [21] K. E. Herold, R. Radermacher, and S. A. Klein, *Absorption chillers and heat pumps*. CRC press, 2016.
- [22] V. Zare, S. Mahmoudi, and M. Yari, "An exergoeconomic investigation of waste heat recovery from the gas turbine-modular helium reactor (gt-mhr) employing an ammonia-water power/cooling cycle," *Energy*, vol. 61, pp. 397–409, 2013.
- [23] R. Misra, P. K. Sahoo, and A. Gupta, "Thermoeconomic evaluation and optimization of an aqua-ammonia vapour-absorption refrigeration system," *International Journal of Refrigeration*, vol. 29, no. 1, pp. 47–59, 2006.
- [24] S. Salehi and M. Yari, "Exergoeconomic assessment of two novel absorption-ejection heat pumps for the purposes of supermarkets simultaneous heating and refrigeration using nascn/nh<sub>3</sub>, lino<sub>3</sub>/nh<sub>3</sub> and h<sub>2</sub>O/nh<sub>3</sub> as working pairs," *International Journal of Refrigeration*, vol. 101, pp. 178–195, 2019.

- [25] A. Yıldız and M. A. Ersöz, "Energy and exergy analyses of the diffusion absorption refrigeration system," *Energy*, vol. 60, pp. 407–415, 2013.
- [26] A. Vidal, R. Best, R. Rivero, and J. Cervantes, "Analysis of a combined power and refrigeration cycle by the exergy method," *Energy*, vol. 31, no. 15, pp. 3401–3414, 2006.
- [27] X. Zhang, L. Cai, and T. Chen, "Energetic and exergetic investigations of hybrid configurations in an absorption refrigeration chiller by aspen plus," *Processes*, vol. 7, no. 9, p. 609, 2019.
- [28] D. S. Ayou, J. C. Bruno, and A. Coronas, "Combined absorption power and refrigeration cycles using low-and mid-grade heat sources," *Science and Technology for the Built Environment*, vol. 21, no. 7, pp. 934–943, 2015.
- [29] R. Ventas, A. Lecuona, A. Zacañas, and M. Venegas, "Ammonia-lithium nitrate absorption chiller with an integrated low-pressure compression booster cycle for low driving temperatures," *Applied Thermal Engineering*, vol. 30, no. 11-12, pp. 1351–1359, 2010.

Research Article

# Exploring the Influence of Various Solvents on the Structural, Optical, and Spectroscopic Properties of MgO

Bast Ahmed Mohammed<sup>1a</sup>, Rebaz Obaid Kareem<sup>2b\*</sup>, Niyazi Bulut<sup>3c</sup>, Tuna Demirci<sup>4d</sup>, Erdem Elibol<sup>4e</sup>, Filiz Ercan<sup>6f</sup>, Ismail Ercan<sup>5g</sup>, Tankut Ates<sup>7h</sup>, Omer Kaygili<sup>3i</sup>

<sup>1</sup> Department of Applied Physics, College of Science, Charmo University, Chamchamal, Iraq

<sup>2</sup> Physics Department, College of Science, University of Halabja, 46018, Halabja, Iraq

<sup>3</sup> Department of Physics, Faculty of Science, Firat University, Elazig, Türkiye

<sup>4</sup> Scientific and Technological Research Laboratory, Düzce University, Düzce, Türkiye

<sup>5</sup> Department of Electrical and Electronics Engineering, Faculty of Engineering, Düzce University, Türkiye

<sup>6</sup> College of Science, Basic and Applied Scientific Research Center, Nanomaterials Technology Unit, Imam Abdulrahman Bin Faisal University, Dammam, Saudi Arabia

<sup>7</sup> Department of Engineering Basic Sciences, Faculty of Engineering and Natural Sciences, Malatya Turgut Özal University, Battalgazi, Malatya, Türkiye

obedrebaz9@gmail.com

DOI : 10.31202/ecjse.1457824

Received: 24.03.2024 Accepted: 28.05.2024

## How to cite this article:

Bast Ahmed Mohammed, Rebaz Obaid Kareem, Niyazi Bulut, Tuna Demirci, Erdem Elibol, Filiz Ercan, Ismail Ercan, Tankut Ates, Omer Kaygili, " Exploring the Influence of Various Solvents on the Structural, Optical, and Spectroscopic Properties of MgO", El-Cezeri Journal of Science and Engineering, Vol: 11, Iss: 3, (2024), pp.(283-287).

ORCID: <sup>a</sup>0009-0004-3774-633X; <sup>b</sup>0000-0001-6273-1309; <sup>c</sup>0000-0003-2863-7700; <sup>d</sup>0000-0001-8933-4944; <sup>e</sup>0000-0003-0328-5534;

<sup>f</sup>0000-0002-3533-0726; <sup>g</sup>0000-0001-6490-3792; <sup>h</sup>0000-0002-4519-2953; <sup>i</sup>0000-0002-2321-1455.

**Abstract :** Magnesium oxide (MgO) samples were manufactured at different temperatures using various solvents of water and ethanol. MgO structure was also modeled and its vibration modes were calculated. The kind of solvent as-used in the synthesis and calcination temperature caused changes in the lattice parameter, crystallinity, and crystallite size. The crystallite size increased with increasing production temperature for both series of the MgO. The morphology and bandgap energy were also affected significantly by the solvent and calcination temperature.

**Keywords :** MgO, Bandgap energy.

## 1 Introduction

As an economical magnesium composite, magnesium oxide (MgO) is the primary and essential basic refractory mineral and can be employed in steel and iron commercial applications. MgO can be created through either natural or artificial processes. MgO can be found naturally as magnesium carbonate or artificially through the use of magnesium chloride derived from salts and seawater [1]. MgO is composed of  $Mg^{2+}$  and  $O^{2-}$  ions. In this substance, the d-orbital is unoccupied due to the chemical configuration of the ions [2]. MgO maintains a high degree of stability in both oxidizing and reducing atmospheres, withstanding temperatures of up to 2300°C and 1700°C, respectively [3]. Due to its low cost, resistance to corrosive environments, and a high melting point of 2800 °C, MgO is one of the essential substances [4]. MgO possesses a bandgap energy of 7.8 eV, making it a good insulator due to the absence of free electrons in its outer shell [2]. MgO is a type of ionic ceramic [5]. The molecular system of MgO consists of Mg and O atoms distributed along one-half of the diagonals of the cube [6], [7]. The main goal of the present study is to investigate the effects of the calcination temperature and the kind of solvent on the structural, morphological, and optical properties of MgO.

## 2 Materials and Methods

A cubic crystal structure of MgO illustrated in Figure 1a was designed using crystallography. Traditionally, experimental methods have been employed to study molecular structures, but due to their complexity and cost, computational approaches have gained popularity in recent years for their efficiency and ability to provide valuable insights. Our primary objective is to precisely optimize MgO's molecular structure and comprehend its electronic properties. MgO structure was investigated extensively using the B3LYP/6-31g method, and we extended our analysis to MgO's vibrational characteristics. Employing Fourier transform infrared (FTIR) calculations with the same basis set and method, we explore the material's vibrational modes and delve into the intricate interactions between magnesium and oxygen atoms. Eight solutions, each of 250mL of 0.4M magnesium nitrate hexahydrate (Merck), were prepared in different beakers using distilled water and ethanol (Sigma-Aldrich) as the solvents of the first and second groups. These solutions were stirred in a magnetic stirrer for 180 minutes without heating and then were put into an oven at 90°C for 48 hours. After drying, the as-obtained powders were heated in an electric furnace at 740, 840, 940,

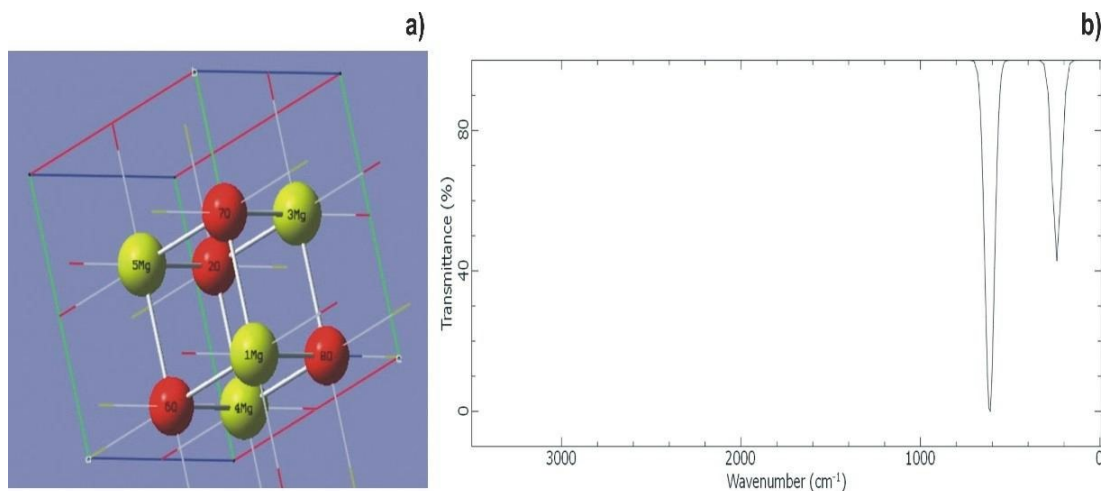


**Figure 1:** a) The cubic crystal structure (red and green colors represent O<sup>2-</sup> and Mg<sup>2+</sup> ions), and b) FTIR spectrum of MgO

and 1040°C for 90 minutes for each group. According to the as-used solvent and heating temperature, the samples were named W740, W840, W940, and W1040 for the group prepared by distilled water, and the rest ones prepared by ethanol were referred to as E740, E840, E940, and E1040. A Rigaku Benchtop Miniflex diffractometer with  $CuK_{\alpha}$  radiation was used to collect the XRD data. An FEI-Quanta FEG 250 scanning electron microscope was used for analyzing the morphology. A Spectro UV-Vis double-beam spectrophotometer UVD-3200 was used to investigate the optical properties.

### 3 Results and Discussion

In FTIR calculations, we simulated the absorption of infrared radiation by the MgO system, which results in the excitation of molecular vibrations. These vibrations arise from the harmonic motion of atoms around their equilibrium positions in the optimized structure. The interpretation of the FTIR peaks shown in Figure 1b allows us to discern various molecular vibrations, such as stretching and bending modes of chemical bonds. By analyzing the intensities, frequencies, and shapes of these FTIR peaks, we can draw conclusions about the stability, symmetry, and electronic properties of the MgO system. Overall, the FTIR calculation represents a significant step towards a comprehensive characterization of MgO and paves the way for further investigations into its multifaceted properties.

In Figure 1b, we observe two prominent peaks that can be unequivocally linked to the stretching of the Mg-O bonds. These peaks are discernible as characteristic features in the graph, and their positions and intensities signify the specific vibrations associated with the Mg-O chemical bonds. Upon closer examination, the first peak, located at the lower wavenumber region, indicates the stretching vibrations of the Mg-O bonds. As the frequency increases along the x-axis, this peak exhibits its distinctive intensity, which arises from the collective movement of atoms within the MgO lattice. This stretching motion is a fundamental characteristic of the MgO molecular structure and can be identified through its unique spectral fingerprint. Likewise, the second peak, situated at the higher wavenumber range, also reflects the stretching of the MgO bonds. Although it appears at a different frequency compared to the first peak, it serves as another signature of the bonding behavior between Mg and O atoms in the material.

Figure 2a shows the XRD patterns of the as-produced MgOs and all the patterns are in a very good harmony with the standard data for MgO (JCPDS pdf no:87-0652) with the cubic crystal structure. These patterns indicate that all the samples have only a single phase of the MgO. The peaks belonging to the diffraction planes of (111), (200), and (220) are detected for all the samples. Some changes in the intensities and shifts in the positions of these peaks are seen. The lattice parameter ( $a$ ), unit cell volume ( $V$ ), crystallite size ( $t$ ) and dislocation density ( $\delta$ ) of the MgOs were estimated using the following relations, respectively [8]:

$$a = d\sqrt{h^2 + k^2 + l^2} \quad (1)$$

$$V = a^3 \quad (2)$$

$$t = \frac{0.9\lambda}{\beta \cos\theta} \quad (3)$$

$$\delta = \frac{1}{t^2} \quad (4)$$

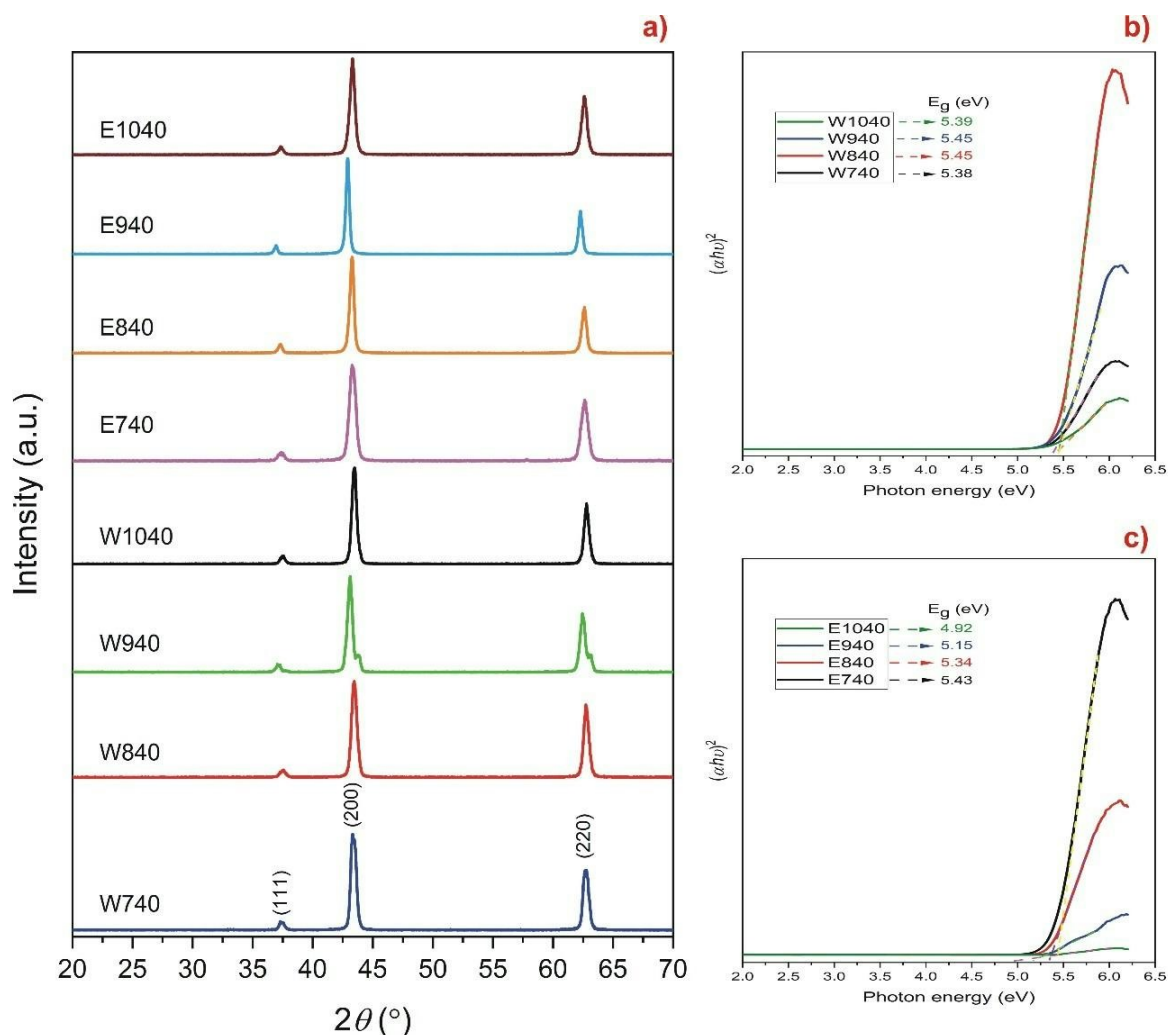


**Figure 2:** a) XRD patterns, and Tauc plots of the samples prepared with b) water and c) ethanol

**Table 1: XRD analysis results.**

Sample	a(nm)	$V(nm)^3$	t(nm)	$\delta(nm)^{-2}$	$X_C\%$
E740	0.4175	0.0728	19.21	0.0027	92.5
E840	0.4178	0.0729	25.55	0.0015	95.2
E940	0.4211	0.0747	36.14	0.0008	95.8
E1040	0.4174	0.0727	39.48	0.0006	94.1
W740	0.4184	0.0732	31.91	0.0010	93.8
W840	0.4172	0.0726	39.96	0.0006	93.7
W940	0.4126	0.0702	45.93	0.0005	93.6
W1040	0.4167	0.0724	59.37	0.0003	94.5

where  $d$  is the interplanar distance,  $\beta$  is the full width at half maximum and  $\lambda$  is the wavelength. Also, the crystallinity (XC) percent for each sample is listed in Table 1. The kind of solvent and calcination temperature are affected the lattice parameter and crystallite size. For two series, it is observed that the crystallite size increases with the calcination temperature. This finding is in a perfect agreement with the literature [8], [9]. For both series, the dislocation density decreases with the increasing production temperature and its small values indicate that the as-manufactured samples have high crystallinity [10]. High crystallinity values listed in Table 1 support this.

The optical bandgap energy ( $E_g$ ) value for each sample was calculated using the following Tauc method [11]:

$$\alpha hv = A(hv - E_g)^n \quad (5)$$

where  $\alpha$  is the absorption coefficient,  $h\nu$  is the photon energy,  $A$  is a constant, and  $n$  is an exponent related to the type of electronic transitions ( $n = 1/2$  for the directly allowed transition). The as-calculated values of the bandgaps and Tauc plots

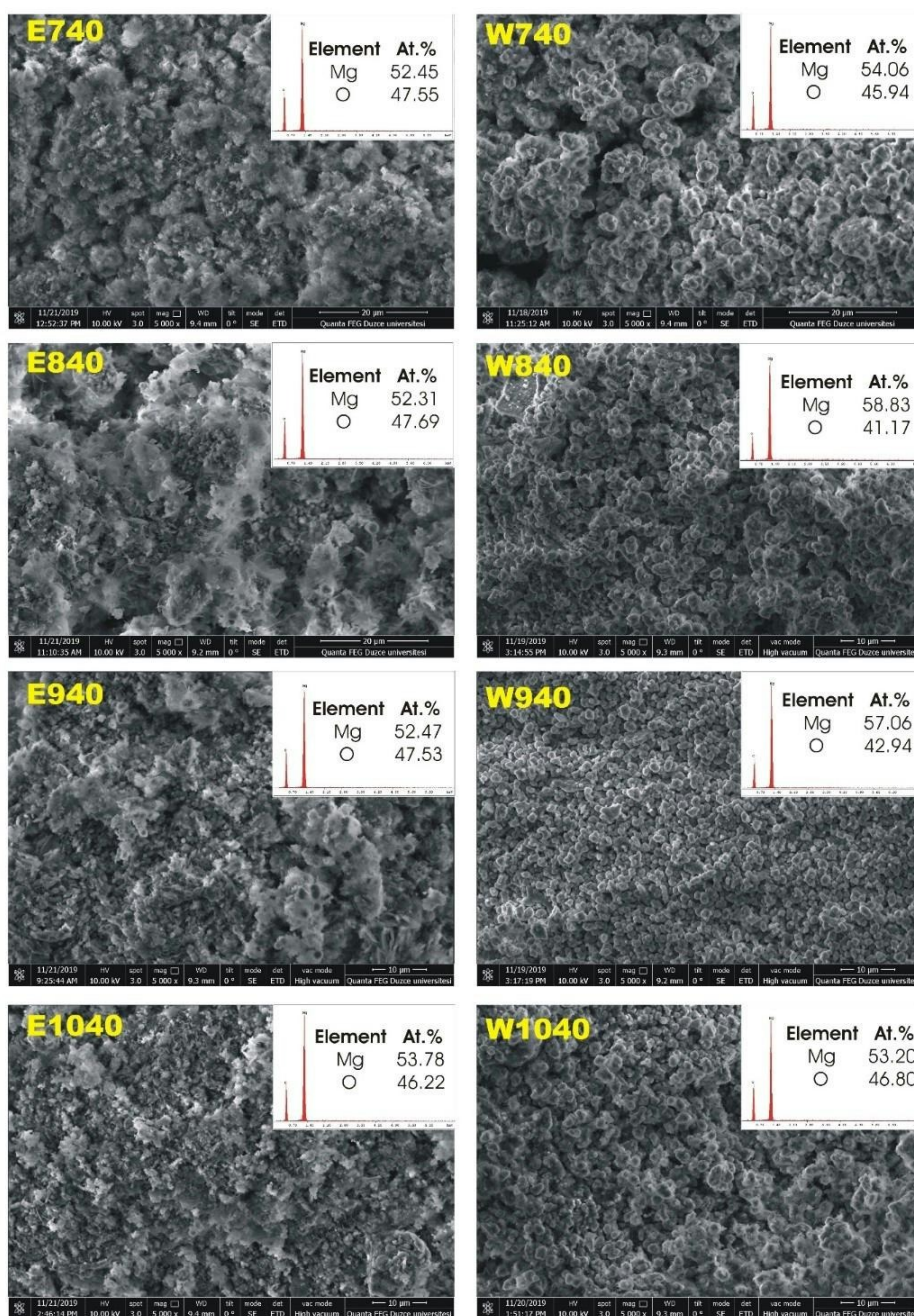


Figure 3: SEM and EDX analyses

of all the samples are shown in Figure 2b and Figure 2c. The Eg values are affected by both the solvent and manufacturing temperature.

For the samples of the E series, Eg decreases with increasing temperature. The as-calculated bandgap values are in the limits reported in the literature [12]–[14].

Figure 3 illustrates the morphological analysis for each sample. Both groups of MgO samples have fine-grained structures. Compared to the E group, the samples of the W group are composed of greater particles, which supports the XRD results. The EDX analyses confirm the MgO structure and verify that all the samples are composed of only Mg and O. The morphology is affected from the type of the solvent and calcination temperature.

#### 4 Conclusion

The MgOs were prepared at different temperatures from 740 to 1040°C with a temperature step of 100°C for the solvents of ethanol and distilled water. It was observed that the crystallite size increased with the increase in the production temperature. The crystallinity, optical bandgap energy, morphology, and lattice parameter were affected by the type of solvent and calcination temperature.

#### Authorship contribution statement

B. Ahmad: R.O. Kareem: N. Bulut: Conceptualization, Writing-review & editing. T. Demirci: E. Elibol: F. Ercan: I. Ercan: T. Ates, O. Kaygili: Conceptualization, Methodology, Investigation

#### Declaration of competing interest

The authors declare that they have no known competing financial interests or personal relationships that could have appeared to influence the work reported in this paper.

#### References

- [1] A. Jassim, S. Salmatori, and J. Jassam, "Sustainable manufacturing process applied to produce magnesium oxide from sea water," in *IOP Conference Series: Materials Science and Engineering*, vol. 757, p. 012021, IOP Publishing, 2020.
- [2] I. Ercan, O. Kaygili, T. Ates, B. Gunduz, N. Bulut, S. Koytepe, and I. Ozcan, "The effects of urea content on the structural, thermal and morphological properties of mgo nanopowders," *Ceramics International*, vol. 44, no. 12, pp. 14523–14527, 2018.
- [3] C. L. Wetteland, J. de Jesus Sanchez, C. A. Silken, N.-Y. T. Nguyen, O. Mahmood, and H. Liu, "Dissociation of magnesium oxide and magnesium hydroxide nanoparticles in physiologically relevant fluids," *Journal of Nanoparticle Research*, vol. 20, pp. 1–17, 2018.
- [4] D. Jesthi, A. Nayak, B. Routara, and R. Nayak, "Evaluation of mechanical and tribological properties of glass/carbon fiber reinforced polymer hybrid composite," *International Journal of Engineering*, vol. 31, no. 7, pp. 1088–1094, 2018.
- [5] R. Salomão, L. Bittencourt, and V. Pandolfelli, "Aspects of magnesium oxide hydration in refractory castables compositions," *Ceramica*, vol. 52, pp. 146–150, 2006.
- [6] W. G. Johnston and J. J. Gilman, "Dislocation velocities, dislocation densities, and plastic flow in lithium fluoride crystals," *Journal of Applied Physics*, vol. 30, no. 2, pp. 129–144, 1959.
- [7] J. Amodeo, S. Merkel, C. Tromas, P. Carrez, S. Korte-Kerzel, P. Cordier, and J. Chevalier, "Dislocations and plastic deformation in mgo crystals: a review," *Crystals*, vol. 8, no. 6, p. 240, 2018.
- [8] G. Monnet, "Investigation of precipitation hardening by dislocation dynamics simulations," *Philosophical Magazine*, vol. 86, no. 36, pp. 5927–5941, 2006.
- [9] L. Huang, Z. Yang, and S. Wang, "Influence of calcination temperature on the structure and hydration of mgo," *Construction and Building Materials*, vol. 262, p. 120776, 2020.
- [10] N. Pathak, S. K. Gupta, C. Prajapat, S. Sharma, P. Ghosh, B. Kanrar, P. K. Pujari, and R. Kadam, "Defect induced ferromagnetism in mgo and its exceptional enhancement upon thermal annealing: a case of transformation of various defect states," *Physical Chemistry Chemical Physics*, vol. 19, no. 19, pp. 11975–11989, 2017.
- [11] I. Sutapa, A. Wahid Wahab, P. Taba, and N. Nafie, "Dislocation, crystallite size distribution and lattice strain of magnesium oxide nanoparticles," in *Journal of Physics: Conference Series*, vol. 979, p. 012021, IOP Publishing, 2018.
- [12] J. Tauc, R. Grigorovici, and A. Vancu, "Optical properties and electronic structure of amorphous germanium," *physica status solidi (b)*, vol. 15, no. 2, pp. 627–637, 1966.
- [13] R. Sreekanth, J. Pattar, A. Anupama, and A. Mallikarjunaswamy, "Synthesis of high surface area and plate-like magnesium oxide nanoparticles by ph-controlled precipitation method," *Applied Physics A*, vol. 127, pp. 1–9, 2021.
- [14] S. Kiran, H. B. Albargi, G. Afzal, U. Aimun, M. N. Anjum, M. B. Qadir, Z. Khaliq, M. Jalalah, M. Irfan, and M. Abdullah, "A zadirachta indica-assisted green synthesis of magnesium oxide nanoparticles for degradation of reactive red 195 dye: a sustainable environmental remedial approach," *Applied Water Science*, vol. 13, no. 10, p. 193, 2023.

Research Article

# Synthesis and Characterization of Zinc Phthalocyanines Containing 2-Hydroxy-6-methoxyisonicotinic Acid Moieties

Nesuhi Akdemir<sup>1a</sup>, Aslı Yıldırım<sup>1b</sup>,

<sup>1</sup> Department of Chemistry, Amasya University, Amasya, Türkiye

nasuhi55@hotmail.com

DOI : 10.31202/ecjse.1434699

Received: 10.02.2024 Accepted: 21.05.2024

**How to cite this article:**

Nesuhi Akdemir, Aslı Yıldırım, " Synthesis and Characterization of Zinc Phthalocyanines Containing 2-Hydroxy-6-methoxyisonicotinic Acid Moieties", El-Cezeri Journal of Science and Engineering, Vol: 11, Iss:3, (2024), pp.(288-297).

ORCID: <sup>a</sup>0000-0003-4684-6450; <sup>b</sup>0000-0002-3949-295X.

**Abstract :** Novel zinc phthalocyanines were synthesized by the reaction of phthalonitriles containing methyl 2-hydroxy-6-methoxyisonicotinate. These compounds were obtained via aromatic nucleophilic substitution reactions. All compounds have been determined by elemental analysis, FT-IR, NMR, MS and electronic absorption. The solubility of phthalocyanines is very low in DMSO and DMF but high in alkaline aqueous solution. The UV-Vis spectra of the Zn(II) phthalocyanines were recorded in different concentration in DMF, DMSO and also in different solvents as DMF, DMSO, and water. Peripheral substitute zincphthalocyanines (5 and 7) showed aggregation in water. Nonperipheral substitute zincphthalocyanine (7) showed monomeric behavior in DMSO, DMF, and water. Beer's law was obeyed for zinc phthalocyanines.

**Keywords :** Methyl 2-Hydroxy 6-methoxyisonicotinate, Phthalonitrile, Water Soluble Phthalocyanines.

## 1 Introduction

Phthalocyanines are aromatic chemical compounds that have many applications [1], [2]. These are dyes and pigments [3], liquid crystal [4], [5], optical applications [6], [7], HIV inactivation [8], [9], electrochromism [10], [11], molecular solar cells [12], [13], chemical sensors [13]–[15], semiconductors for organic field-effect transistors [16], [17], and photodynamic therapy [18]–[20]. Phthalocyanines, whose central atom can contain 70 different metals, have high thermal and chemical stability. While unsubstituted phthalocyanines are insoluble in common organic solvents and water, substituted ones are soluble. Phthalocyanines must contain some groups such as carboxyl in order to be soluble in water [21]. Various substituents can be added to the periphery, nonperiphery or axial positions of phthalocyanines. These substituents are macrocyclic moieties [22]–[24], thiol [25], naphthalene-amide groups [26], phenol groups [27]–[29], pyridine derivatives [30], [31], alcohols [32], [33]. In this study, the synthesis and characterization of water soluble zinc phthalocyanines containing 2-Hydroxy-6-methoxyisonicotinic Acid, a pyridine derivative, in peripheral and nonperipheral positions, and their UV-Vis spectra in different solvents and concentrations are reported.

## 2 Experimental Methods

### 2.1 Materials

IR spectra was recorded on a Perkin Elmer Frontier FT-IR Spectrometer as KBR pellets. UV-VIS spectra were recorded on a Perkin Elmer Lambda 35 UV/VIS Spectrometer. <sup>1</sup>H-NMR and <sup>13</sup>C-NMR studies were done on an Agilent 600 MHz spectrometer (Giresun University NMR Laboratory). Mass spectra were measured on an Agilent GC-MSD - 7890B GC-5977MSD (Amasya University-AUMAULAB). Elemental analyses were performed on a Leco Truspect Micro Analyzer. Methyl 2-hydroxy-6-methoxyisonicotinate, 4,5-dichlorophthalonitrile, 3- or 4-Nitrophthalonitrile were synthesized by following the procedure reported in [34]–[37].

### 2.2 Synthesis

**Synthesis of Methyl 2-(2-Chloro-4,5-dicyanophenoxy)-6-methoxyisonicotinate (2):** Methyl 2-hydroxy-6-methoxyisonicotinate 6,24g (34,10 mmol) was dissolved in dry DMF (50 mL) under nitrogen atmosphere at 70°C and K<sub>2</sub>CO<sub>3</sub> 7,03g (50,94 mmol) was added. After stirring for 2h, a solution of 4,5-dichlorophthalonitrile 6,68g (33,91 mmol) in dry DMF (70 mL) was added dropwise over 5h. The reaction mixture was stirred at 70°C under nitrogen atmosphere for 72 h. The mixture was then poured in to ice-water (400 g). The precipitate was filtered off washed with (10% w/w) NaOH solution and water until the filtrate was neutral. Recrystallization from ethanol gave a compound 2. The product is soluble in methanol, Ethyl alcohol, Ethyl acetate, acetone, THF, 1,4-dioxane, acetonitrile, Toluene, benzene, chlorobenzene, DMF, DMSO, DCM, CHCl<sub>3</sub> and insoluble in hexane.

Yield: 6.91 g (59%); mp: 155°C; anal. calcd. for  $C_{16}H_{10}ClN_3O_4$ : C, 55.91; H, 2.93; N, 12.23%. Found: C, 55.71; H, 2.83; N, 12.34%. FT-IR  $:\nu_{max}$ ,  $cm^{-1}$  3102 (Aromatic CH), 3036, 2962 (aliphatic CH), 2901, 2743, 2581, 2237 (CN), 2023, 1730 (Ester C=O), 1623, 1592, 1575, 1564, 1490, 1447, 1399, 1376, 1251, 1157, 1029, 772, 536.  $^1H$  NMR (400 MHz,  $CDCl_3$ ,  $\delta$ , ppm) 7.94-7.17 (m, Aromatic and Pyridine CH, 5H), 3.99 (s,  $OCH_3$ , 3H), 3.74 (s,  $OCH_3$ , 3H).  $^{13}C$  NMR ( $CDCl_3$ ): $\delta$ , ppm 164.53 (C=O), 163.72, 160.26, 153.84, 144.26, 135.53, 127.57, 115.02, 114.29 (CN), 114.13 (CN), 112.44, 106.79, 102.63, 54.31 ( $OCH_3$ ), 53.00 ( $OCH_3$ ). GC MS; 343

**Synthesis of Methyl 2-(3,4-dicyanophenoxy)-6-Methoxyisonicotinate (3):** Compounds 3 and 4 were synthesized as discussed above. Yield: 2.55 g (61%); mp: 153°C; anal. calcd. for  $C_{16}H_{11}N_3O_4$ : C, 62.14; H, 3.58; N, 13.59%. Found: C, 62.34; H, 3.48; N, 13.49%. FT-IR  $:\nu_{max}$ ,  $cm^{-1}$  3104 (Aromatic CH), 3078, 3047, 2965 (aliphatic CH), 2233 (CN), 1733 (Ester C=O), 1620, 1601, 1563, 1490, 1447, 1394, 1362, 10131, 770, 525.  $^1H$  NMR (400 MHz,  $CDCl_3$ ,  $\delta$ , ppm) 7.84-7.13 (m, Aromatic ve Pyridine CH, 5H), 3.97 (s,  $OCH_3$ , 3H), 3.78 (s,  $OCH_3$ , 3H).  $^{13}C$  NMR ( $CDCl_3$ ): $\delta$ , ppm 164.57 (C=O), 163.83, 159.93, 157.56, 144.14, 135.01, 125.41, 125.22, 117.26, 115.22 (CN), 114.86 (CN), 110.94, 107.11, 103.33, 54.35 ( $OCH_3$ ), 52.97 ( $OCH_3$ ). GC MS; 309

**Synthesis of Methyl 2-(2,3-dicyanophenoxy)-6-Methoxyisonicotinate (4):** Yield: 5.38 g (64%); mp: 155°C; anal. calcd. for  $C_{16}H_{11}N_3O_4$ : C, 62.14; H, 3.58; N, 13.59%. Found: C, 62.24; H, 3.52; N, 13.66%. FT-IR  $:\nu_{max}$ ,  $cm^{-1}$  3104 (Aromatic CH), 3123 (Aromatic CH), 3104, 3000, 2960 (aliphatic CH.), 2235 (CN), 1741 (Ester C=O), 1709, 1627, 1589, 1567, 1395, 1238, 1031, 872, 769, 552, 454..  $^1H$  NMR (400 MHz,  $CDCl_3$ ,  $\delta$ , ppm) 7.77-7.16 (m, Aromatic ve Pyridine CH, 5H), 3.98 (s,  $OCH_3$ , 3H), 3.74 (s,  $OCH_3$ , 3H).  $^{13}C$  NMR ( $CDCl_3$ ): $\delta$ , ppm 164.56 (C=O), 163.66, 160.26, 156.68, 144.22, 133.92, 129.29, 126.66, 117.03, 114.93 (CN), 112.34 (CN), 109.81, 106.70, 102.93, 54.16 ( $OCH_3$ ), 52.86 ( $OCH_3$ ). GC MS; 309

**Synthesis of zinc phthalocyanines (5):** The mixture of Methyl 2-(2-Chloro-4,5-dicyanophenoxy)-6-methoxyisonicotinate (2) 2.50 g (7.28 mmol),  $Zn(CH_3COO)_2 \cdot 2H_2O$  0.52 g (2.37 mmol) and dry quinoline (12 mL) was heated and stirred at 185-190°C for 24 h in a nitrogen atmosphere. Then, the mixture was cooled to room temperature; it was precipitated by adding methanol and filtered off. The green precipitate were washed with hot methanol, hot ethanol, diethyl ether, hexane and hot water. They were washed with methanol for 24 h in the soxhlet apparatus and dried in vacuo. The green products were stirred in LiOH solution at room temperature for 3 days and filtered. HCl solution was added to the filtrate and filtered off. Compound was washed with hot water and dried in vacuo. Yield: 1.81 g (72%); mp > 250°C; anal. calcd. for  $C_{60}H_{32}Cl_4N_{12}O_{16}Zn$ : C, 52.06; H, 2.33; N, 12.14%. Found: C, 52.12; H, 2.25; N, 12.24%. FT-IR  $:\nu_{max}$ ,  $cm^{-1}$  3818-2500 (Carboxylic acid OH), 2978 (aliphatic CH), 1730 (Carboxylic acid C=O), 1617, 1575, 1492, 1455, 1395, 1368, 1241, 1185, 1105, 1085, 876, 749.

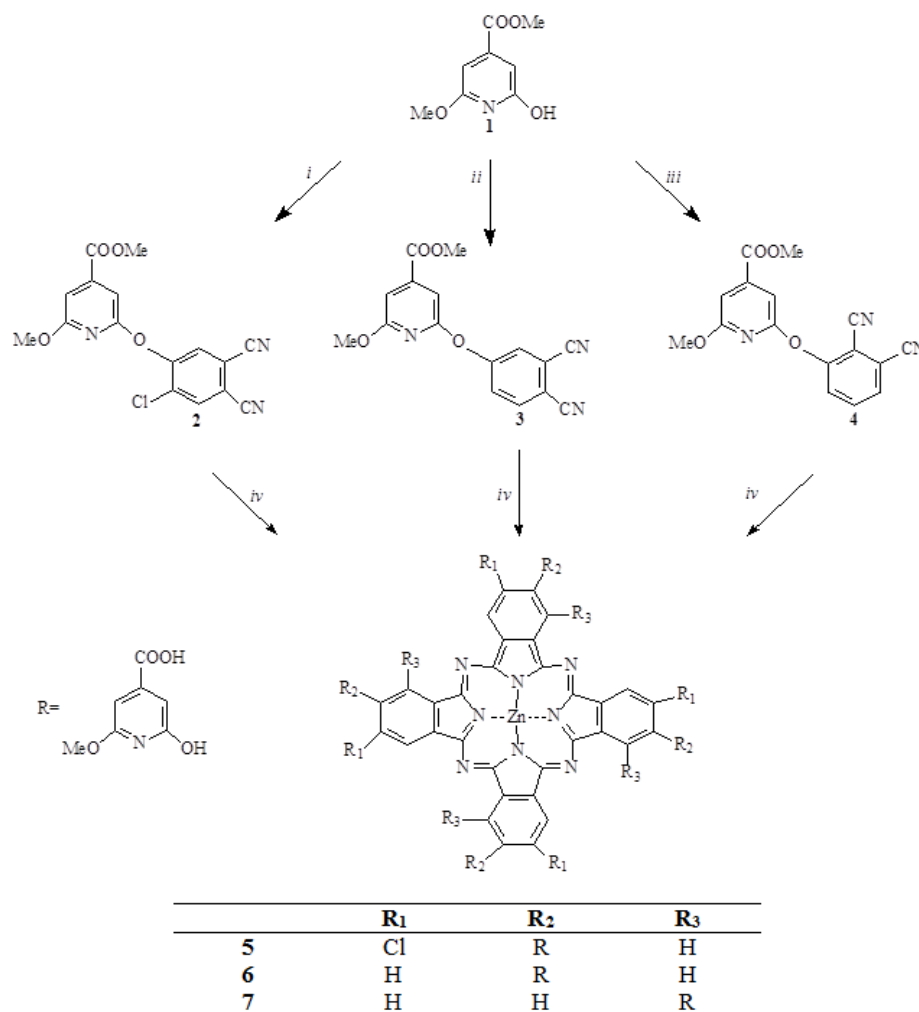
**Synthesis of zinc phthalocyanines (6):** Zinc phthalocyanines 6 and 7 were synthesized as discussed above. Yield: 1.14 g (56%); mp > 250°C; anal. calcd. for  $C_{60}H_{36}N_{12}O_{16}Zn$ : C, 57.82; H, 2.91; N, 13.49%. Found: C, 57.78; H, 2.86; N, 13.54%. FT-IR  $:\nu_{max}$ ,  $cm^{-1}$  3500-2500 (Carboxylic acid OH), 2957 (aliphatic CH), 1727 (Carboxylic acid C=O), 1615, 1573, 1474, 1472, 1394, 1347, 1220, 1211, 1098, 1052, 999, 974, 874, 776, 775.

**Synthesis of zinc phthalocyanines (7):** Yield: 1.03 g (51%); mp > 250°C; anal. calcd. for  $C_{60}H_{36}N_{12}O_{16}Zn$ : C, 57.82; H, 2.91; N, 13.49%. Found: C, 57.90; H, 2.96; N, 13.44%. FT-IR  $:\nu_{max}$ ,  $cm^{-1}$  3306-2500 (Carboxylic acid OH), 2957 (aliphatic CH), 1728 (Carboxylic acid C=O), 1616, 1570, 1486, 1465, 1392, 1344, 1238, 1185, 1129, 1096, 1042, 879, 752.

### 3 Results and Discussion

#### 3.1 Synthesis and Characterization

Scheme 1 presents the synthetic route to Zinc Phthalocyanines Containing 2-Hydroxy-6-methoxyisonicotinic Acid. The phthalonitriles containing methyl 2-hydroxy-6-methoxyisonicotinate (2, 3, 4) were firstly prepared by treating 4,5-dichlorophthalonitrile, 3 or 4-nitrophthalonitrile with 2-Hydroxy-6-methoxyisonicotinic Acid in DMF using  $K_2CO_3$  as the base for nucleophilic displacement reaction and gave moderate yield (59-64 %). The zinc phthalocyanines (5-7) containing 2-Hydroxy-6-methoxyisonicotinic Acid are obtained directly by cyclotetramerization of the corresponding phthalonitriles in the presence of the  $Zn(CH_3COO)_2 \cdot 2H_2O$  in quinoline. In these reactions, it was observed that some of the ester groups transformed into carboxylic acid. It was observed that the resulting product dissolved in aqueous sodium hydroxide and there were peaks belonging to carboxylic acid groups in the FT-IR spectra. Considering that not all ester groups were converted to carboxylic acid, the products were hydrolyzed in aqueous LiOH. The yields of phthalocyanines 5, 6 and 7 were 72%, 56% and 51%, respectively. The phthalocyanines showed solubility in DMF, DMSO and water, but insolubility in common organic solvents. The new phthalocyanines and phthalonitriles were characterized by UV-Vis, FT-IR,  $^1H$  NMR,  $^{13}C$  NMR, MS spectra and elemental analysis. All the spectroscopic results of compounds show good agreement with target structures. The FT-IR spectra of synthesized phthalocyanines and phthalonitriles are very similar with the exception of small stretching shifts. In the FT-IR spectrum of phthalonitriles (2, 3, 4), aromatic CH, aliphatic CH, nitrile CN, carbonyl C=O, aromatic C=C, ether Ar-O-Ar stretching vibrations appeared at ca. 3100, 2964, 2231, 1597 and 1278  $cm^{-1}$ , respectively. The new phthalocyanines (5-7) have carboxylic acid, aromatic CH, aliphatic CH, nitrile CN, carbonyl, aromatic C=C, ether Ar-O-Ar stretching vibrations appeared at ca. 3091, 2964, 2237, 1733, 1592 and 1251  $cm^{-1}$ , respectively. While the strong -CN band of phthalonitriles (2-4) appeared at ca 2231  $cm^{-1}$ , this band completely disappeared after cyclotetramerization to compounds (5-7) and strong carboxylic acid and



**Scheme: Synthetic route for Zn(II) Phthalocyanines (5, 6 and 7) i: 4,5-dichloro-1,3-dicyanobenzene, DMF, K<sub>2</sub>CO<sub>3</sub>, N<sub>2</sub>, 70°C, 72h ii: 4-nitro-1,3-dicyanobenzene, DMF, K<sub>2</sub>CO<sub>3</sub>, N<sub>2</sub>, 70°C, 72h iii: 3-nitro-1,3-dicyanobenzene, DMF, K<sub>2</sub>CO<sub>3</sub>, N<sub>2</sub>, 70°C, 72h iv: quinoline, Zn(CH<sub>3</sub>COO)<sub>2</sub> · 2H<sub>2</sub>O, N<sub>2</sub>, 24h, 190°C**

carbonyl band appeared at ca 3500-2500, 1730 respectively (Figure 1 and 2). In contrast to the phenoxy groups, the solubility of these phthalocyanines is very low in DMSO and DMF. <sup>1</sup>H NMR and <sup>13</sup>C NMR spectra of phthalocyanines (5-7) could not be measured due to the low solubility [23].

### 3.2 UV-Vis Spectra

UV-Vis spectrum of phthalocyanine is characteristic. The spectrum observed two strong absorption regions. These regions are B band Q band [1], [2]. The UV-Vis spectra of Zinc(II)phthalocyanines (5-7) were archived in DMSO, DMF and water (Figure 3, 6, 9). The results were shown in Table 1. Nonperipheral substitute zincphthalocyanine (7) showed monomeric behavior in DMSO, DMF and Water, evidenced by a single (narrow) Q-band at 688-696. However peripheral substitute zincphthalocyanines (5 and 6) showed aggregation in water (Figures 3 and 6). Also, compound 5 aggregated in DMSO (Figure 3, 4). B-Band absorptions of zinc phthalocyanines in different solvents were observed at 342-346 nm for 5, 338-352 for 6 and 306-330 nm for 7. Figure 4, 5, 7, 8, 10 and 11 show UV-Vis spectra of phthalocyanines (5, 6 and 7) in the concentration range  $1 \times 10^{-6} - 1.50 \times 10^{-5}$  M in DMSO and DMF. As shown in the 4, 5, 7, 8, 10 and 11, the Q band decreases in intensity with decreasing concentration of phthalocyanines (5, 6 and 7). Beer's law was obeyed for 5, 6 and 7 in the concentration range  $1 \times 10^{-6} - 1.50 \times 10^{-5}$  M.

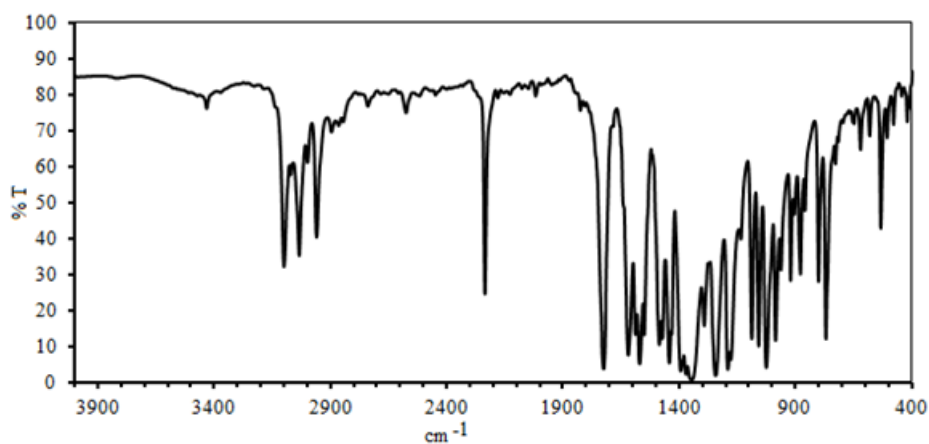


Figure 1: FT-IR Spectrum of Methyl 2-(2-Chloro-4,5-dicyanophenoxy)-6-methoxyisonicotinate (2)

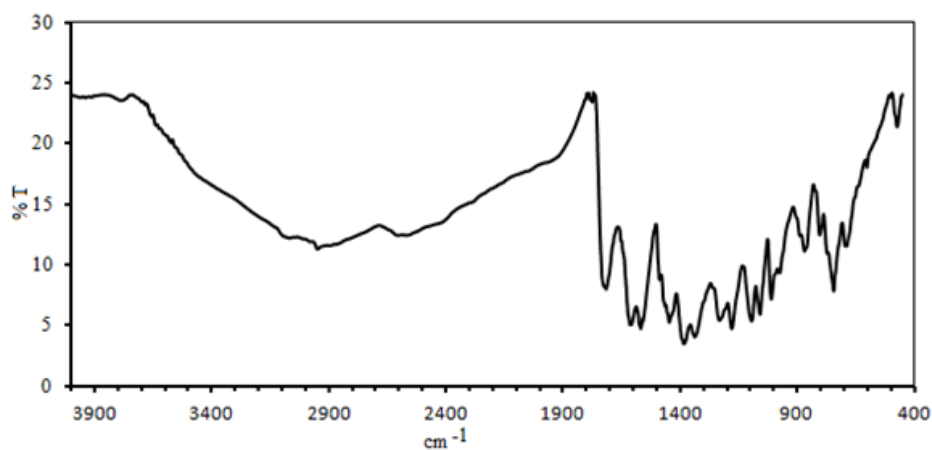


Figure 2: FT-IR Spectrum of the Zn(II)phthalocyanine (5) containing chlorine and methyl 2-hydroxy-6-methoxyisonicotinate in the peripheral position

Table 1: UV-vis spectral results for zinc(II)phthalocyanines (5-7) in various solvents at a concentration of  $0,8 \times 10^{-5}$  M

Compound	Solvent	Q-Band		B-Band	
		$\lambda_{max}$ (nm)	log $\epsilon$	$\lambda_{max}$ (nm)	log $\epsilon$
5	DMSO	676, 635, 607	4.624; 4.921; 4.235	346, 381	4.851; 4.542
5	DMF	676, 642, 611	5.083; 4.388; 4.379	353	4.768
5	Water	671, 639	4.284; 4.769	342	4.732
6	DMSO	677, 640, 611	5.199; 4.555; 4.513	352	4.858
6	DMF	675, 645, 609	5.153; 4.434; 4.457	353	4.765
6	Water	671, 639, 585	4.433; 4.892; 4.095	286, 338	4.579; 4.770
7	DMSO	690, 660, 622	5.123; 4.363; 4.375	317	4.742
7	DMF	688, 657, 621	5.190; 4.436; 4.454	330	4.693
7	Water	696, 627	4.752; 4.224	306	4.574

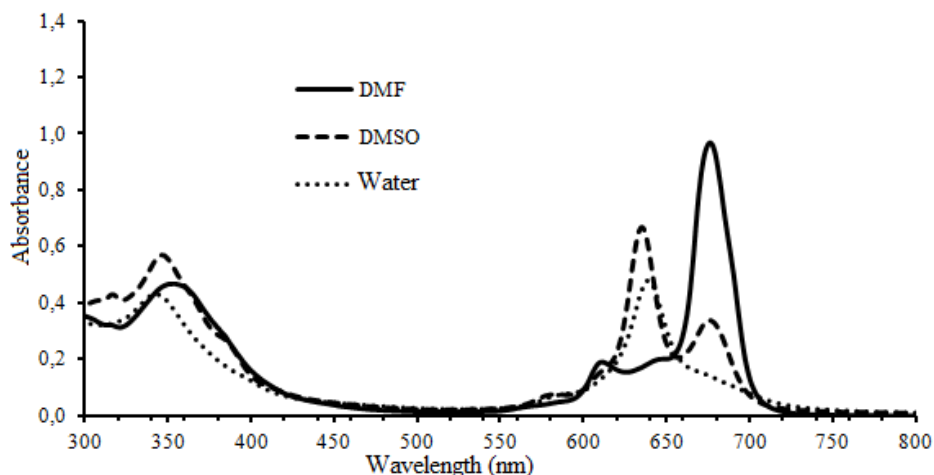


Figure 3: Uv-Vis Spectra of the Zn(II)phthalocyanine (5) containing chlorine and methyl 2-hydroxy-6-methoxyisonicotinate in the peripheral position in different solvents (Pc/NaOH mol ratio in aqueous solution: 1/4) (Concentration:  $0,8 \times 10^{-5}$  M

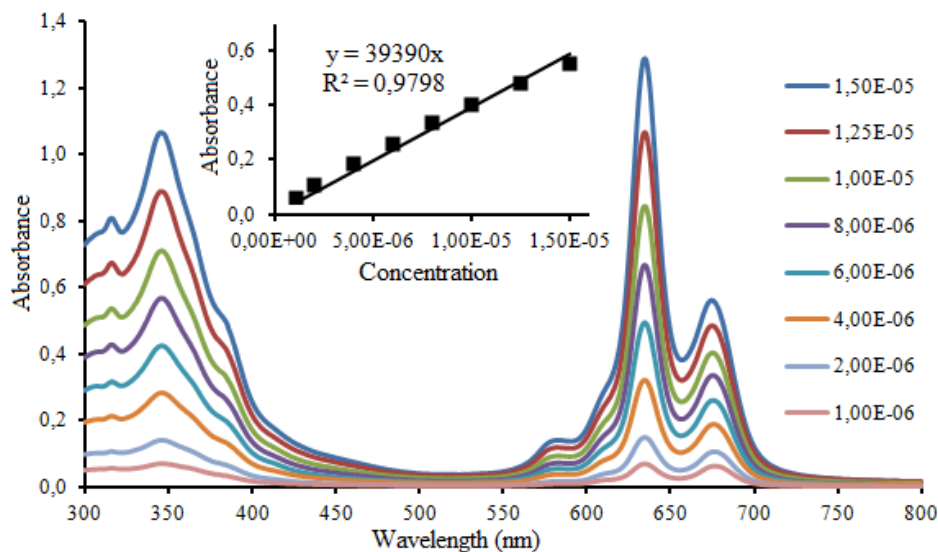


Figure 4: Uv-Vis Spectra of the Zn(II)phthalocyanine (5) containing chlorine and methyl 2-hydroxy-6-methoxyisonicotinate in the peripheral position in DMSO

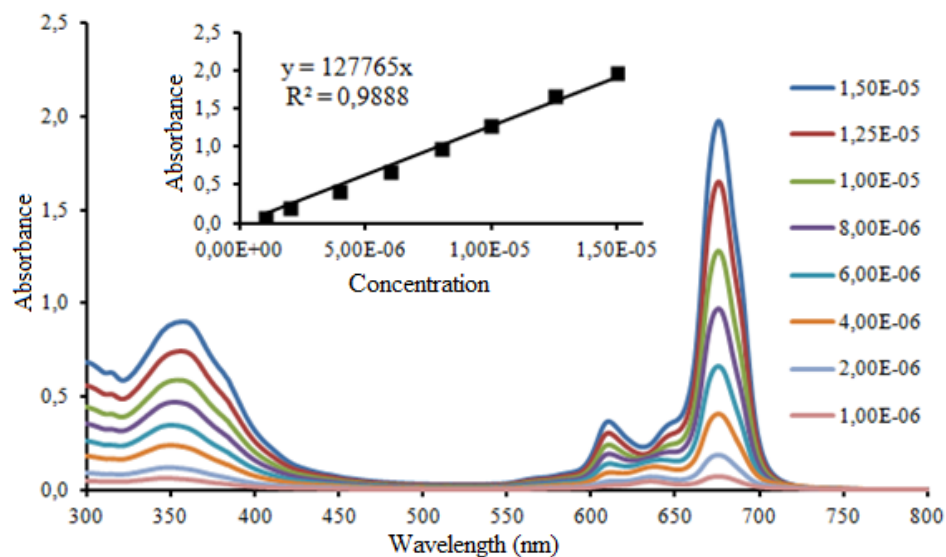


Figure 5: Uv-Vis Spectra of the Zn(II)phthalocyanine (5) containing chlorine and methyl 2-hydroxy-6-methoxyisonicotinate in the peripheral position in DMF

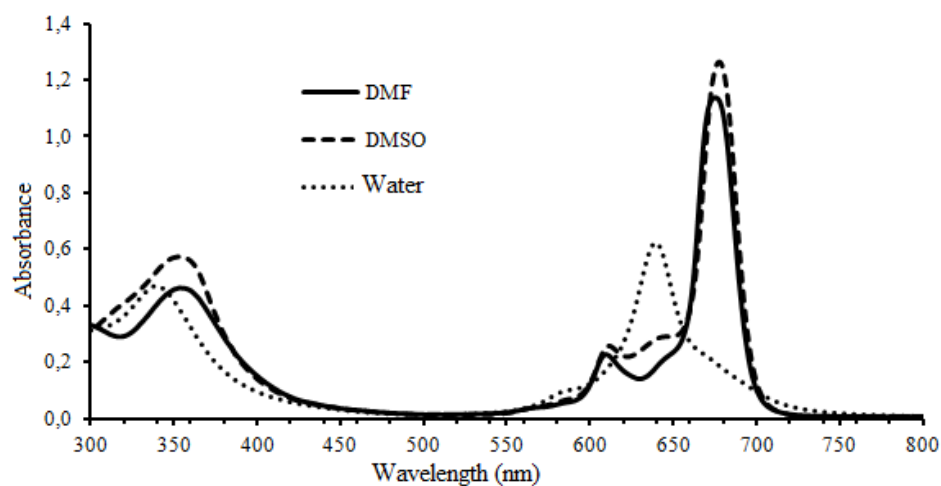


Figure 6: Uv-Vis Spectra of the Zn(II)phthalocyanine (6) containing methyl 2-hydroxy-6-methoxyisonicotinate in the peripheral position in different solvents (Pc/NaOH mol ratio in aqueous solution: 1/4) (Concentration:  $0,8 \times 10^{-5}$  M)

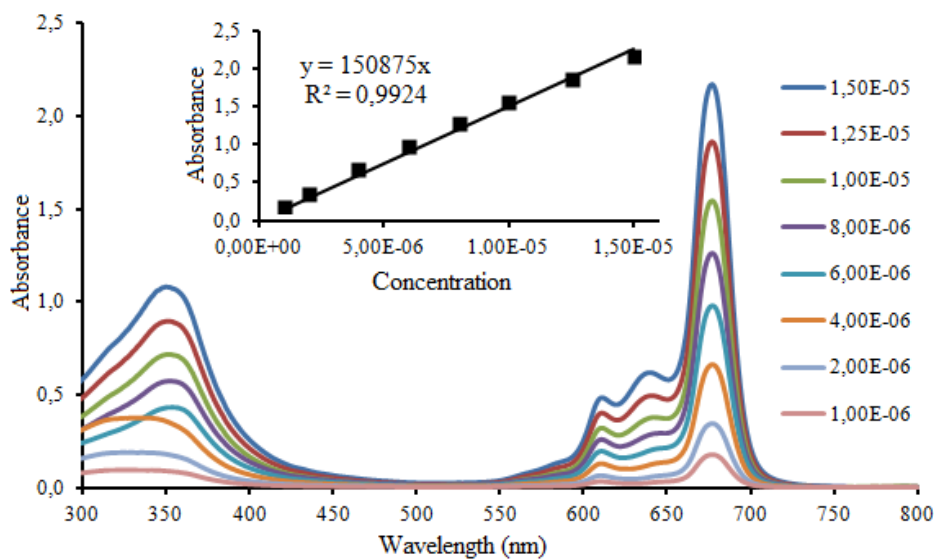


Figure 7: Uv-Vis Spectra of the Zn(II)phthalocyanine (6) containing methyl 2-hydroxy-6-methoxyisonicotinate in the peripheral position in DMSO

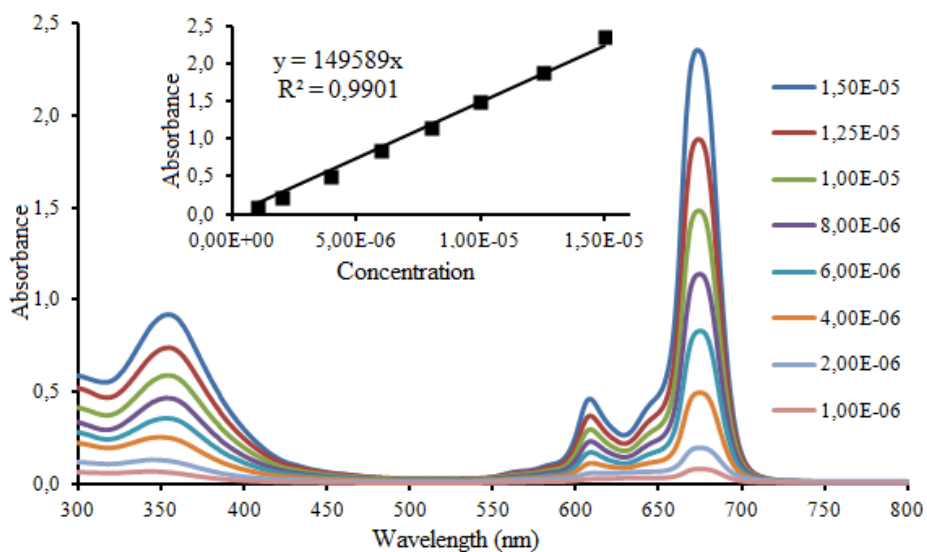


Figure 8: Uv-Vis Spectra of the Zn(II)phthalocyanine (6) containing methyl 2-hydroxy-6-methoxyisonicotinate in the peripheral position in DMF

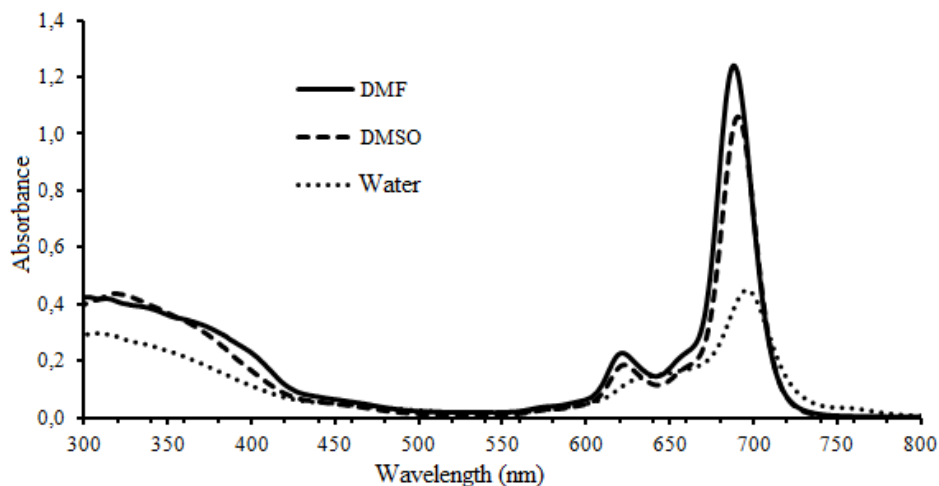


Figure 9: Uv-Vis Spectra of the Zn(II)phthalocyanine (7) containing methyl 2-hydroxy-6-methoxyisonicotinate in the nonperipheral position in different solvents (Pc/NaOH mol ratio in aqueous solution: 1/4) (Concentration:  $0,8 \times 10^{-5}$  M)

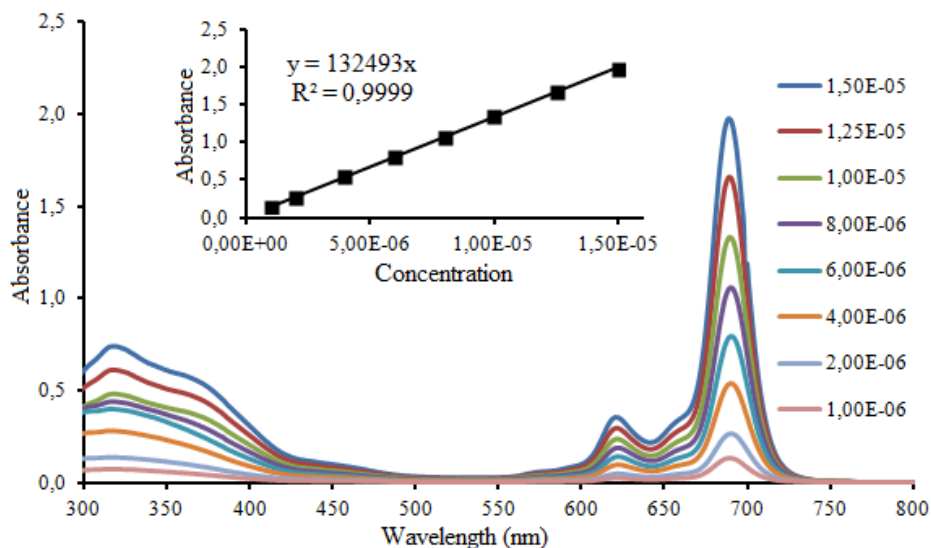


Figure 10: Uv-Vis Spectra of the Zn(II)phthalocyanine (7) containing methyl 2-hydroxy-6-methoxyisonicotinate in the peripheral position in DMSO

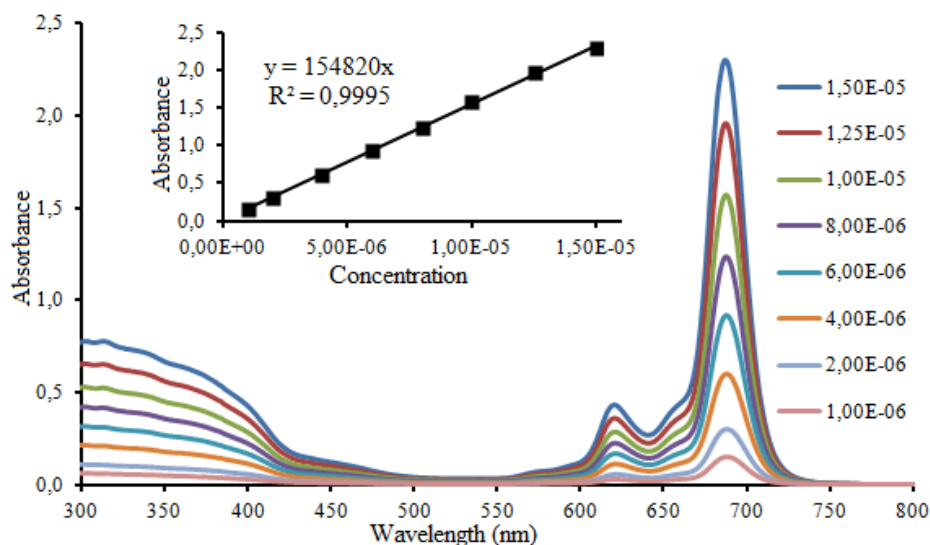


Figure 11: Uv-Vis Spectra of the Zn(II)phthalocyanine (7) containing methyl 2-hydroxy-6-methoxyisonicotinate in the nonperipheral position in DMF

#### 4 Conclusions

Zn(II) phthalocyanines containing 2-Hydroxy-6-methoxyisonicotinic Acid on the periphery or nonperiphery were successfully synthesized. Characterization of all synthesized phthalonitriles and phthalocyanines were determined by elemental analyses, UV-Vis,  $^1\text{H}$ NMR,  $^{13}\text{C}$ NMR, Mass spectra and FT-IR spectroscopy. The solubility of phthalocyanines is very low in DMSO and DMF but high in alkaline aqueous solution. The UV-vis spectra of the zinc phthalocyanines were recorded in different solvents. Peripheral substituted zincphthalocyanines (5 and 7) showed aggregation in water. Beer's law was obeyed for zinc phthalocyanines (5-7).

#### Acknowledgments

This work was supported by the research fund of the Amasya University (FMB-BAP 20-0449).

#### Authors' Contributions

NA and AY designed the structure, carried out the experiments work and wrote up the article. Both authors read and approved the final manuscript.

#### Competing Interests

The authors declare that they have no competing interests.

#### References

- [1] N. B. McKeown, *Phthalocyanine Materials: Synthesis, Structure and Function*. Cambridge University Press, 1998.
- [2] C. C. Leznoff and A. Lever, *Phthalocyanines: Properties and Applications*, vol. 1-4. VCH, Weinheim, 1998.
- [3] D. Wörhle, "Phthalocyanines in macromolecular phases-methods of synthesis and properties of the materials," *Macromol. Rapid Comm.*, vol. 22, pp. 68–97, Feb 2001.
- [4] J. A. Duro, G. Torre, J. Barbera, J. L. Serrano, and T. Torres, "Synthesis and liquid-crystal behavior of metal-free and metal-containing phthalocyanines substituted with long-chain amide groups," *Chem. Mater.*, vol. 8, no. 5, pp. 1061–6, 1996.
- [5] F. Yakuphanoglu, M. M. Durmuş, O. K. Okutan, and V. Ahsen, "The refractive index dispersion and theoptical constants of metal-free and nickel(ii) phthalocyanines liquid crystals," *Physica B:*, vol. 373, pp. 262–6, Mar 2006.
- [6] M. N. H. Xia, "Copper phthalocyanine bonding with gel and their optical properties," *Opt. Mater.*, vol. 15, pp. 93–8, Nov 2000.
- [7] S. Makhseed, M. Al-Sawah, J. Samuel, and H. Manaa, "Synthesis, characterization and nonlinear optical properties of non aggregating hexadeca-substituted phthalocyanines," *Tetrahedron Lett.*, vol. 50, pp. 165–8, Jan 2009.
- [8] E. Ben-Hur, J. Otjen, and B. Horowitz, "Silicon phthalocyanine pc 4 and red light causes apoptosis in hiv-infected cells," *Photochem Photobiol.*, vol. 65, pp. 456–460, Mar 1997.
- [9] H. Margolis-Nunno, E. Ben-Hur, P. Gottlieb, R. Robinson, and B. J. Oetjen, "Horowitz. inactivation by phthalocyanine photosensitization of multiple forms of human immuno deficiency virus in red cell concentrates," *Transfusion*, vol. 36, pp. 743–750, Aug 1996.
- [10] Y. S. Krasnov, G. Y. Kolbasov, I. N. Tretyakoya, L. A. Tomachynska, Y. Y. Chernii, and S. V. Volkov, "Dynamics of redox processes and electrochromism of films of zirconium (iv) phthalocyanines without-of-plane  $\beta$ -dicarbonylligands," *Solid State Ionics*, vol. 180, pp. 928–933, Jun 2009. Article 14-16.
- [11] P. Monk, R. J. Mortimer, and D. R. Rosseinsky, *Electrochromism: Fundamentals and Applications*. VCH, Weinheim, 2008.
- [12] T. Ikeuchi, H. Nomoto, N. Masaki, M. J. Griffith, S. Mori, and M. Kimura, "Molecular engineering of zinc phthalocyanine sensitizers for efficient dye-sensitized solar cells," *Chem. Commun.*, vol. 50, pp. 1941–3, 2014.

- [13] M. Kimura, H. Nomoto, H. Suzuki, T. Ikeuchi, H. Matsuzaki, T. N. Murakami, A. Furube, N. Masaki, M. J. Griffith, and S. Mori, "Molecular design rule of phthalocyanine dyes for highly efficient near-ir performance in dye-sensitized solar cells," *Chem Eur J.*, vol. 19, pp. 7496–7502, Jun 2013.
- [14] T. V. Basova, C. Taşaltın, A. G. Gürek, M. A. Ebeoğlu, Z. Z. Öztürk, and V. Ahsen, "Mesomorphic phthalocyanine as chemically sensitive coatings for chemical sensors," *Sensors and Actuators B: Chemical.*, vol. 96, pp. 70–5, Nov 2003.
- [15] L. Valli, "Phthalocyanine-based langmuir–blodgett films as chemical sensors," *Advances in Colloid and Interface Science*, vol. 116, pp. 13–44, Nov 2005.
- [16] Y. Zhang, X. Cai, Y. Bian, and J. Jiang, "Organic semiconductors of phthalocyanine compounds for field effect transistors (fets)," *Structure and Bonding*, vol. 135, pp. 275–321, Dec 2009.
- [17] M. Bouvet, "Phthalocyanine-based field-effect transistors as gas sensors," *Analytical and Bioanalytical Chemistry*, vol. 384, pp. 366–373, Jan 2006.
- [18] M. Durmuş and V. Ahsen, "Water-soluble cationic gallium(iii) and indium(iii) phthalocyanines for photodynamic therapy," *Journal of Inorganic Biochemistry*, vol. 104, pp. 297–309, Mar 2010.
- [19] D. Çakır, V. Çakır, Z. Bıyıklıoğlu, M. Durmuş, and H. Kantekin, "New water soluble cationic zinc phthalocyanines as potential for photodynamic therapy of cancer," *J Organomet. Chem.*, vol. 745-746, pp. 423–431, 2013.
- [20] E. Ranyuk, N. Cauchon, B. K. Klarskov, and J. E. v. L. Guerin, "Phthalocyanine–peptide conjugates: Receptor-targeting bifunctional agents for imaging and photodynamic therapy," *J. Med. Chem.*, vol. 56, no. 4, pp. 1520–1534, 2013.
- [21] F. Dumoulin, M. Durmuş, V. Ahsen, and T. Nyokong, "Synthetic pathways to water-soluble phthalocyanines and close analogs," *Coordination Chemistry Reviews*, vol. 254, p. 2793, 2010.
- [22] E. Açar, S. Şaşmaz, N. Akdemir, and I. Keskin, "Synthesis and characterization of new phthalocyanines containing four 15-membered tetrathiaoxa macrocycles," *Synth. React. Inorg. Met.-Org. Chem.*, vol. 29, no. 3, pp. 473–485, 1999.
- [23] S. Şaşmaz, E. Açar, N. Akdemir, and I. Keskin, "Synthesis and characterization of new phthalocyanines containing thio-oxa-ether moieties," *Dyes and Pigments*, vol. 37, pp. 223–230, May 1998.
- [24] E. Açar, S. Şaşmaz, N. Akdemir, and I. Keskin, "Synthesis and characterization of novel phthalocyanines containing four 15-membered oxathiadiaza mixed-donor macrocycles," 1997.
- [25] N. Akdemir, I. Gümrükçüoğlu, and E. Açar, "Synthesis and characterization of novel phthalocyanines containing n-(n-octyl)mercaptoacetamid substituents," *Synth. React. Inorg. Met.-Org. Chem.*, vol. 35, no. 10, pp. 819–824, 2005.
- [26] M. Özil, E. Açar, S. Şaşmaz, B. Kahveci, N. Akdemir, and I. Gümrükçüoğlu, "Microwave-assisted synthesis and characterization of the monomeric phthalocyanines containing naphthalene-amide group moieties and the polymeric phthalocyanines containing oxa-azabridge," *Dyes and Pigments*, vol. 75, no. 3, pp. 732–740, 2007.
- [27] C. Kantar, N. Akdemir, E. Agar, N. Ocak, and S. Sasmaz, "Microwave-assisted synthesis and characterization of differently substituted phthalocyanines containing 3,5-dimethoxyphenol and octanethiol moieties," *Dyes and Pigments*, vol. 76, no. 1, pp. 7–12, 2007.
- [28] S. Gorduk and O. Avcıata, "A3b type asymmetric metallo phthalocyanines bearing carboxylic acid and tert-butyl groups photophysical, photochemical and aggregation properties," *Journal of Photochemistry & Photobiology, A: Chemistry*, vol. 449, p. 115387, 2024.
- [29] R. Atajanov, B. Huraibat, Z. Odabaş, and A. R. Özkaya, "Electrochemical, spectroelectrochemical, and electrocatalytic properties of novel soluble phthalocyanines containing peripheral thiomethyl and chloride units," *Inorganica Chimica Acta*, vol. 547, p. 121360, 2023.
- [30] S. Moeno and T. Nyokong, "An investigation of the behaviour of quaternized peripherally tetra mercaptopyridine substituted metallophthalocyanines in the presence of quantum dots," *Journal of Photochemistry and Photobiology. A: Chem.*, vol. 215, pp. 196–204, 2010.
- [31] Z. Bıyıklıoğlu, E. Cekirge, H. Bas, N. Ozbek, U. Ocak, and M. Ocak, "New fluorescent manganese(iii) phthalocyanines bearing non-peripherally octa-(3-pyridin-3-ylpropoxy) and (4-pyridin-3-ylpropoxy) for the sensitive determination of pd<sup>2+</sup> in real water samples," *Inorganic Chemistry Communications*, vol. 159, p. 11182, 2024.
- [32] B. S. Bilen, M. Ozcesmeci, M. Akin, B. Cakir, K. Alsakini, A. Nalbantsoy, N. Saki, and E. Hamuryudan, "3', 3', 4', 4', 5', 5', 6', 6', 6'-nonafluoro-hexyloxy groups substituted phthalocyanines: Synthesis, characterization and their biological properties," *Dyes and Pigments*, vol. 221, p. 111814, 2024.
- [33] B. S. Bilen, M. Ozcesmeci, N. Kocuyigit, T. Elgun, A. G. Yurttas, and E. H. Glycosylated, "zinc(ii) phthalocyanine photosensitizer: Synthesis, photophysical properties and in vitro photodynamic activity on breastcancer cell line," *Journal of Molecular Structure*, vol. 1295, p. 136688, 2024.
- [34] A. Upton, C. B. Cooper, K. Marcel, J. E. Guillemont, W. V. D. Broeck, and B. D. Palmer, "Antibacterial compounds and uses thereof," *US Patent*, vol. US2017/21031, 2017.
- [35] D. Wöhrle, M. Eskes, K. Shigehara, and A. Yamada, "A simple synthesis of 4,5-disubstituted 1,2-dicyanobenzenes and 2,3,9,10,16,17,23,24-octasubstituted phthalocyanines," *Synthesis*, vol. 2, pp. 194–196, 1993.
- [36] R. D. George and A. W. Snow, "Synthesis of 3-nitrophthalonitrile and tetra- $\alpha$ -substituted phthalocyanines," *Journal of Heterocyclic Chemistry*, vol. 32, pp. 495–498, 1995.
- [37] J. G. Young and W. Onyebugu, "Synthesis and characterization of di-disubstituted phthalocyanines," *The Journal of Organic Chemistry*, vol. 55, pp. 2155–2159, 1990.

Research Article

# Implement Edge Pruning to Enhance Attack Graph Generation Using the Naïve Approach Algorithm

Zaid J. Al-Araji<sup>1a</sup>, Ammar Awad Mutlag<sup>1b</sup>, Sharifah Sakinah Syed Ahmad<sup>1c</sup>

<sup>1</sup> Technical Computer Engineering Department, Al-Hadba University, Mosul, Iraq

<sup>2</sup> Ministry of Education/General Directorate of Curricula, Pure Science Department, Baghdad 10065, Iraq

<sup>3</sup> Faculty of Information and Communication Technology, Universiti Teknikal Malaysia Melaka, Melaka, Malaysia

zaid.jm@hcu.edu.iq

DOI : 10.31202/ecjse.1375755

Received: 13.10.2023 Accepted: 18.01.2024

**How to cite this article:**

Zaid J. Al-Araji, Ammar Awad Mutlag, Sharifah Sakinah Syed Ahmad, " Implement Edge Pruning to Enhance Attack Graph Generation Using the Naïve Approach Algorithm ", El-Cezeri Journal of Science and Engineering, Vol: 11, Iss:3, (2024), pp.(298-306).

ORCID: "0000-0003-1768-7569; <sup>b</sup>0000-0002-4966-0232; <sup>c</sup>0000-0002-3803-4578.

**Abstract :** The use of network technologies has increased in recent years. Although the network is beneficial for individuals to work and live in, it does have security challenges that should be rectified. One of these issues is cyberattacks. The attack surface for hackers is growing as more devices are linked to the internet. The next-generation cyber defence concentrating on predictive analysis seems more proactive than existing technologies based on intrusion detection. Recently, many approaches have been proposed to detect and predict attacks; one of these approaches is attack graphs. The main reason for designing the attack graph is to predict the attack as well as to predict the attack's next step in the network. The attack graph depicts the many paths an attacker may attempt to get around a security policy by leveraging interdependencies between disclosed vulnerabilities. The attack graph is categorized into three sections: generation, analysis, and use of attack graph. However, current attack graphs are suffering from a few issues. Scalability is the main issue the attack graph generation is facing. The reason for this issue is that the increase in the usage of devices connected to the network leads to increased vulnerabilities in the network, which leads to an increment in the complexity as well as generation time of the attack graph. For this issue, this study proposes using the naïve approach prune algorithm and using Personal agents to reduce the reachability time in calculating between the nodes and to remove unnecessary edges, minimizing the attack graph's complexity. For the results, the proposed attack graph performs better than the existing attack graph by using a naïve approach and a personal agent. The proposed attack graph reduced the generation time by 20 percent and the attack graph complexity.

**Keywords :** Attack Graph, Fog computing, Cloud computing, Edge Computing, Edge Pruning

## 1 Introduction

The rapid development of telecommunications technology has profoundly altered people's lives. The networks have been actively involved in each life aspect to break the limits of space and time that have greatly enabled humanity. As more people invest in cyberspace to execute their everyday tasks, this trend reveals that people worldwide are utilizing internet capabilities. Security problems have grown as a result of the Internet's continuous rise in connections [1] The network becomes more vulnerable as a result of the rising utilization of the devices that are connected to the internet. Vulnerabilities are flaws in the design of a system that allows an outsider to execute commands, obtain unauthorized data, and launch numerous attacks [2] [3] [4]. According to the National Vulnerability Database (NVD), the number of vulnerabilities was over 18362 in 2020. Also, this is more significant compared to previous years (17,382 in 2019 and 17,252 in 2018) [5]. This increase in vulnerabilities through the years has led to increased attacks on organizations and individual networks [6]. However, these best security measures do not consider application, network service-based, or operating system vulnerabilities. Attackers abuse these vulnerabilities and get legal access to the network resources, evading access control and authentication measures, owing to the evolution of sophisticated hacking tools. An attack graph is a tool that provides a concise description of various attack scenarios relevant to a network [7] [8] [9] [10]. According to [11] [12] [13] [14], the generation of an attack graph could be divided into four phases: reachability analysis, modelling, core building, and analysis. The reachability analysis is the first phase. To summarize, this phase looks into the reachability circumstances within the target network, showing if two specific hosts can connect. The second step is an attack graph model, which can be thought of as an attack template that specifies the components of various attacks, the conditions (acquired or necessary attacker capabilities), and the relationships between the requirements. The rationale for several attacks is

**Table 1: Attack graph generation previous work**

Author	Strength	Limitation
[16]	The generation time is stable with Different numbers of vulnerabilities	- The complexity calculation is not considered - Consider the attack path discovery only in the analysis. - The starting node is assigned manually.
[19]	The attack graph generation has been done automatically.	- Generation time and complexity are not calculated. - The attack graph does not support large-scale networks.
[20]	Use Hadoop MapReduce to enhance the scalability	- The experiment used only eight machines
[21]	Use the partition graph to generate the attack graph faster	- Create an attack graph statically - The generating algorithm's complexity is not measured
[22]	Used two metrics to find the optimal path	- The complexity of the generation algorithm is not considered.
[23]	Relevant in the context of large-scale complex networks	- Calculating the time and algorithm complexity is not considered.
[24]	Use attack probability	- Time and complexity are not considered
[25]	Propose an algorithm to divide the services into segments	- The attack graph is generated based on connections, vulnerabilities, and services. - The attack graph analysis is not considered

defined by an attack template [15]. The third phase, known as attack graph core building, deals with the fundamental technique that generates the attack graphs. The fourth phase is attack graph analysis, which refers to attack path discovery, which means predicting the attack path from the initial node to the target node [12]. The attack graph represents the possible ways in which an attacker might violate a security policy [10], [16]. An attack graph may be created using known network vulnerabilities as well as network configuration details [17]. The attack graph shows how an attacker might utilize vulnerability dependencies to circumvent a security policy. However, the attack graph performance still suffers from different issues, the generation time is the main challenge of the attack graph [18]. Based on this, this paper proposed a naïve approach algorithm to prune the unnecessary edge in the attack graph which reduces the complexity of the attack graph, and used a personal agent to calculate the reachability of each node individually which leads to reducing the reachability calculation time. The rest of the paper is organized by, section 2 is the related work, section 3 explains the proposed model, section 4 shows the experiments, section 5 explains the results, and section 6 is the conclusion.

## 2 Related Work

Many attack graphs have recently been developed utilizing various methodologies and methods to improve attack graphs. The most current attack graphs will be discussed in this section as shown in Table 1.

[19] introduced Derivation of Attack Graphs Generation from Security Requirements (DAGGER), a novel attack graph-building approach that employs a comprehensive collection of threat models to automatically evaluate the security posture of heterogeneous and complex (both new and established) cyber-physical system designs. To increase readability, [20] proposes a graph segmentation algorithm for breaking apart a complex attack graph into several subgraphs while maintaining the original structure. The authors also suggest a distributed attack graph segmentation method based on Spark GraphX and a distributed attack graph synthesis method based on Hadoop MapReduce to handle enormous amounts of alert data. [21] proposed a hypergraph partitioning-based searching forward complete attack graph design strategy to assure that each computing agent parallels computational load is balancing. Furthermore, calculating the whole attack graph in the opposite order from the vulnerability nodes to the attacker reduces calculation duplication in real-time attack graph development, adds to real-time network vulnerability analysis, and ensures computational accuracy and efficiency. A supervised Kohonen neural network-based attack graph-generating algorithm is suggested by [22]. Using this strategy, the authors can predict the attack success rate and status types if attackers successfully exploit vulnerabilities. [16] presented a "compact planning graph"-based attack path discovery algorithm that may use goal-oriented information from penetration testing to sever recurring attack path branches [26]. In a complex network context, [23] recommended a graph database-based approach to network vulnerability assessment and its usefulness in addressing state explosion, too many attributes and high computational burden issues were investigated. [24] Proposed an attack path prediction method to find the optimal attack path based on the attack graph. The authors calculate the attack probability by attack cost and vulnerability value. A network segmentation-based scalable security state (S3) framework is presented by [25]. The framework divides the large-scale network region into smaller, more manageable units using the well-

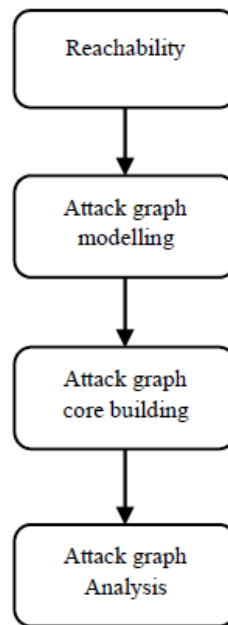


**Figure 1: Attack graph generation steps**

known divide-and-conquer strategy. To divide the system into segments based on how similar the services are to one another, this study used a well-known segmentation technique created from the K-means clustering algorithm. The segments are kept isolated by a distributed firewall (DFW), which also blocks lateral attacker movement that might compromise them. In conclusion, even though several techniques have been employed to enhance attack graph development, there are still certain problems with attack graphs, particularly scalability, which affects the attack graph generation time.

### 3 Proposed Model

The generation of the attack graph in this work can be divided into three steps which are reachability analysis, attack graph modelling, attack graph core building and attack graph analysis as the following as shown in Figure 1. In the following, each step will be explained in detail.

#### 3.1 Attack Graph Reachability

Calculating reachability is a time-consuming and difficult operation. It discovers paths between target and source nodes using network topology information. All the filtering devices in the networks must have their rulesets imported and simulated. There are several methods for calculating reachability. The reachability between nodes in the network will be calculated using a matrix and multi-graph in this paper. Here, the matrix is employed to determine the connection between the nodes using the IP addresses, while the multi-graph is used to visualize the network topology and the weaknesses in the network.

A multi-graph refers to a graph that allows for multiple edges (also known as parallel edges) [15], [27]. In other words, they are known as edges that possess similar end nodes. As a result, one node can connect to another node with one or more edges. The goal of calculating the reachability using the multi-graph is to reach every IP address in the network and show all the weaknesses between the nodes.

The accessibility of software programs placed on the target network is determined by reachability. The reachability conditions are determined by firewall filtering rules, trust relationships, router access control lists, and software programs. To develop our reachability multi-graph, all of these aspects will be considered.

A personal agent gathers these elements from the nodes, determines the node's reachability, and sends the results to the administrator server, which is in charge of producing the attack graph. Each personal agent is in charge of gathering information to calculate reachability; the personal agent is also responsible for the update to reduce the time complexity. For numerous software applications, the administrator server will be in charge of identifying information source usages, vulnerability exploits, and attacker privileges.

The graph-vertex represents the nodes in the network. On the other hand, a graph edge denotes a group of source and target software programs where the applications' source may access the target applications if certain requirements are met. The circumstances are saved in the edge, enabling direct reachability between software applications. Port numbers, network protocols, user passwords, and many others are examples of such situations.

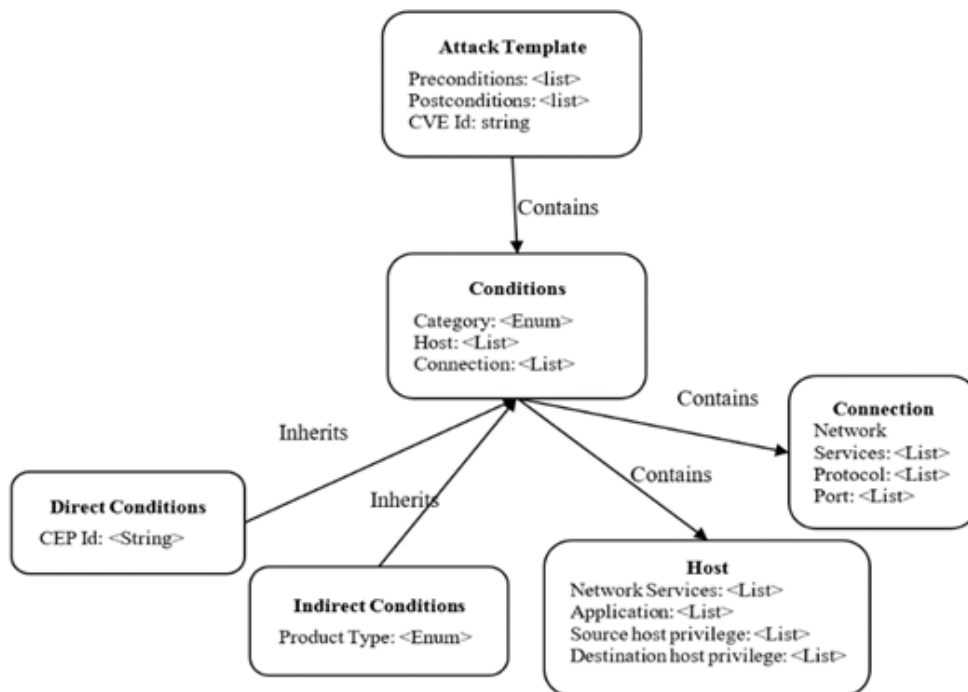


Figure 2: Attack Template

### 3.2 Attack Graph Modeling

Two components of attack graph modelling are figuring out the structure of attack graphs and modelling attack templates. The modelling of the attack template includes the pre- and post-conditions for vulnerabilities. It also contains a way for determining these requirements for particular vulnerabilities using weak databases and public vulnerability. Note that choosing the types of edges and nodes in an attack graph determines the attack graph structure. Network modelling aims to find the best depiction for network assets (such as hardware/software applications operating on network hosts). Each of these sub-parts is discussed in particular in the subsequent sub-sections.

#### 3.2.1 Attack Template Modelling

The attack template model is derived from the vulnerability data in CVE and NVD, which uses the formalization method to represent the attack template factors. It was developed by [28], who described a four-part attack template: network preconditions, attacker preconditions, network postconditions, and attacker postconditions. In this work, the same attack template as in [21] will be employed. Figure 2 depicts the attack template model employed in our system, followed by the formal descriptions of its elements.

Definition 1. A condition refers to a type of right obtained in a software program. It refers to a two-element tuple,  $\langle Category, Host \rangle$ , with *Category* denoting the gains on the programme and *Host* denoting the software application location where the right is earned. The attacker’s and victim’s software applications are used to ascertain the location.

Definition 2. In a condition tuple, a direct condition provides an additional component. The *CPE* product identifier of the software program in which the condition is gained is represented by this element, which is *CPEId*. The *CPEId* is provided by NVD.

Definition 3. A condition tuple with an indirect condition has an extra element. *ProductType* is an element that identifies the sort of software program based on the condition category. The *producttype* can be a mail server, mail client, database server application, and many others. Indicate the technology class of software application.

Definition 4. This thesis considers a vulnerability in a specific CVE entry in the CVE database.  $\langle CVEId, Preconditions, Postcondition \rangle$  is a three-element tuple that represents it. The *CVEId* element stores the unique CVE identification for each vulnerability. It possesses a list of preconditions that indicate which attacker privileges are necessary to exploit the vulnerability.

#### 3.2.2 Attack Graph Structure

The attack graph structure determines the generated attack graphs’ edges and nodes. As illustrated in Figure 3, the attack graph structure suggested by [15] will be employed.

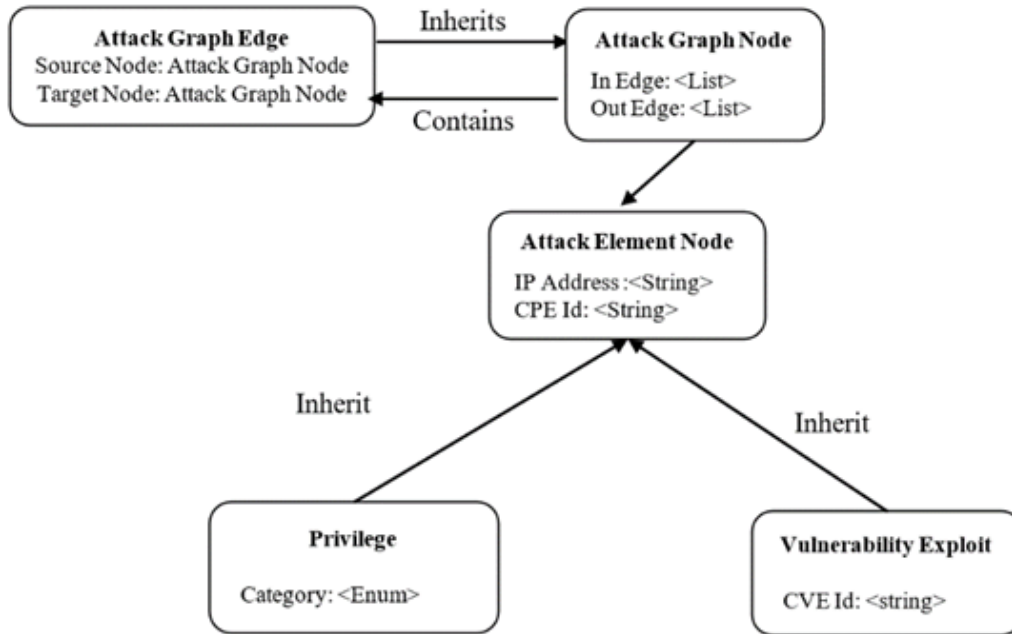


Figure 3: Attack Graph Structure

```

1. inputs:
   node_list; // network nodes list, Vul_list; // vulnerabilities list; P=0;
2- Process
   foreach node in node_list
       M = getinformation(node);
       MP = 0;
       foreach n in Mreachability
           F = getinformation(n);
           Vul_list = check_vulnerabilities(M.vulnerabilities, n.vulnerabilities)
           if (Vul_list != null)
               MP++;
               addedge(node, Vul_list, n);
           else
               addedge(node, privilege, n);
           endif
       endfor
       if (MP == 0)
           Privilege_nodes.add(node);
       else if (MP == 1)
           Vulnerability_nodes.add(node);
       else if (MP > 1)
           Conjunction_nodes.add(node);
       endif
   endfor
3. Output:
   Attack_graph, Vulnerability_nodes, Privilege_nodes, Conjunction_nodes
    
```

Figure 4: Attack graph generation

Definition 5. A privilege node resembles an attacker privilege on a software application on a network host Definition 6. In an attack graph, a vulnerability conjunction node represents a conjunction connector for several vulnerability nodes. Definition 7. A software application vulnerability on a network host is indicated by a vulnerability node.

### 3.3 Attack Graph Core Building

The administrator will generate the attack graph when data is collected from every node using a personal agent, as shown in Figure 4. The algorithm starts by extracting each node’s information in the network, comprising the vulnerabilities, reachability,

```

1- Input
G=(V, E)
(s, t), //Node pair with source and target
edges_list, app_list, vul_list, AHE
2- Process
AHE ← sort(edges_list);
While (AHE is not empty)
    (s, t) ← first edge in AHE
    Remove first edge from AHE
    sourceapp_list [] ← app_list[s]
    distapp_list [] ← app_list[t]
    vul_list = findvulnerabilities(sourceapp_list, distapp_list)
    sourcevul_list [] ← vul_list[s]
    distvul_list [] ← vul_list[t]
    gainprivileges = findgainprivileges(s, t)
    if (gainprivileges !=0)
        graphadddedge(s, gainprivileges)
        graphadddedge(gainprivileges, t)
        goto 2;
    elseif (vul_list !=0)
        graphadddedge(s, vul_list)
        graphadddedge(vul_list, t)
        goto 2;
    else
        goto 2;
    endif
end while
3- Output
Prune Attack Graph
    
```

Figure 5: Naïve approach pruning algorithm

application list, privileges, and connection information. The next step is checking the mutual vulnerability between the node and the reachability list for the node. If the reachability nodes list and the node are related by more than one vulnerability, the node will be classified as a conjunction node. If a vulnerability exists between the list of reachability nodes and the node, the node is assigned as a vulnerability node. If there is no vulnerability connected to the node, the node will be assigned as a privileged node.

3.3.1 Naïve Approach

The naïve approach pruning algorithm was presented first by [29]. A naïve approach was proposed to simplify the network visualization. Naïve approach algorithm is used to prune some of the edges in the graph to minimize the loss of connectivity.

In this work, a naïve approach will be used to prune unnecessary edges from the attack graph to reduce the complexity of the generation. The definitions of the algorithm will be the following:

Definition 8: Let a network be expressed using a graph  $G = (V, E)$ , in which  $V$  denotes the set of nodes and  $E$  denotes the set of links.

Definition 9: let the  $e \rightarrow E$  be a pair of  $e = s, t$  of nodes  $s$  and  $t \rightarrow V$ , as in Equation (1)

$$e \rightarrow E, E = e(s_0, t_0), e(s_1, t_1), \dots, e(s_n, t_n). \tag{1}$$

Definition 10: App edge: Suppose app  $m$  is denoted as an edge between nodes  $s$  and  $t$ . Here,  $m$  resembles an application of joint application list set  $M$  between nodes  $s$  and  $t$ , as in Equation (2)

$$m \rightarrow M, M(s, t) = app_1, app_2, \dots, app_n. \tag{2}$$

The algorithm’s first step is to get the full attack graph with  $V$ , which is nodes and  $E$ , which is edges, also gets the list of vulnerabilities in the network  $vul\_list$ , application list  $app\_list$  for all nodes in the full attack graph, as in Figure 5.

In the beginning, the algorithm started to sort all the edges ascendingly based on the weights of the edge. Then add them to  $AHE\_list$  which means (acceptable head edge) that it contains all the edges after sorting them.

After sorting the edges, the first edge in  $AHE\_list$  will be taken to the test. The edge will be removed from the  $AHE\_list$  then the edge will be checked by the vulnerabilities in each node. First, it will be checked if there is a gain privilege between these nodes which means there is an inappropriate behaviour in one of these nodes which could be an attacker; then add an edge between the nodes and the gain privileges. Secondly, if there are no gain privileges, check the vulnerabilities between these nodes that might be used by the attacker to attack the node or to move from one node to another, then add an edge between the nodes and the highest vulnerabilities score between all the vulnerabilities in the edge. Lastly, if there are no privileges or vulnerabilities between these nodes, go to another edge.

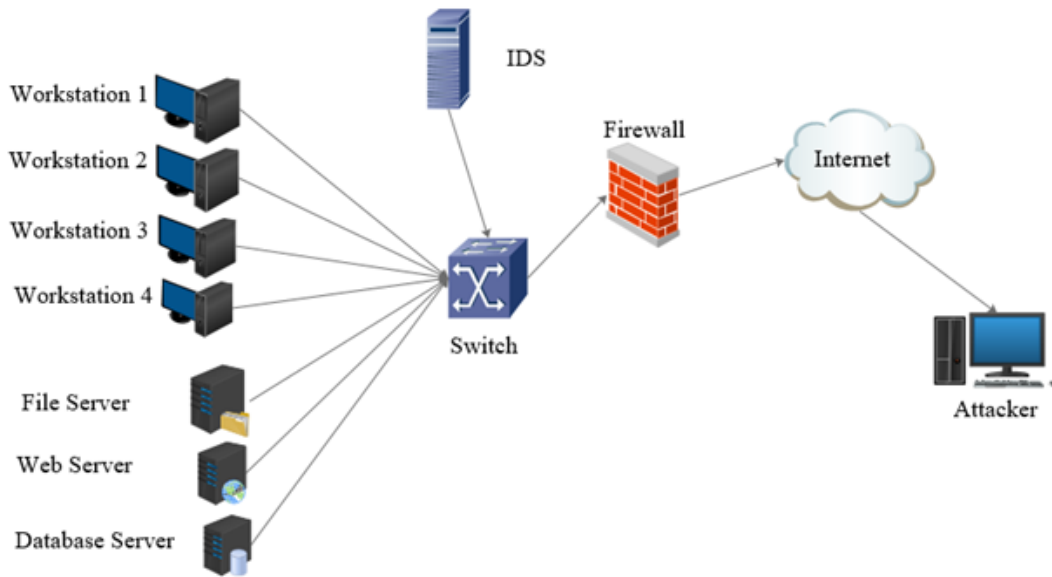


**Figure 6: Network Topology**

#### 4 Experiment

In order to compare our approach to other attack path-finding techniques, the experiment was run on a real enterprise network. The network topology shown in Figure 6 was used to test the created attack graph; due to the network's small size and low number of nodes, it is referred to as a small-scale network.

Three servers make up the network: a file server, a database server, and a web server. Additionally, it features an IDS device and four workstations, of which two are running Windows 10 and the other two are Windows 7. A perimeter firewall is present. In this network configuration, network connectivity is governed by the following firewall rules:

- The webservice and workstations are connected to the network in both directions.
- Workstations 1, 2, 3, and 4 are connected in both directions.
- The attacker's external host is connected to the internet and has access to the web server's HTTP protocol and HTTP port.
- Workstations 3 and 4 are in communication with one another in both directions.
- The four workstations and file servers can connect using the NFS protocol and NFS port.
- The four workstations and file servers have connections to the internet via the HTTP protocol, while workstation 4 has access to the network's database server. The studies used to assess the generating attack graph in this setting included a core i7 3.40 GHz processor, 32 GB of RAM, Windows 11 as the operating system, and Microsoft Visual Studio 2022 for coding.

#### 5 Results

As a result, there are no missing data when the attack graph is updated if any information has changed, according to the results of employing a personal agent to gather the data and communicate it to the administrator. By using a naive technique of pruning, the attack graph's complexity and generation time are both decreased. As a result, after applying the naive technique prune, the running time for the network design in Figure 5.1 is 0.247 seconds. These findings motivate us to test additional attack graph components, as well as larger nodes and servers (large-scale networks), to evaluate the complexity and running time of the graph using the personal agent and naive approach prune algorithm.

The first factor is the attack graph generation time. The experiment compares the running time in different stages of attack graph generation. The first stage is the full graph without applying any pruning algorithm and parallel process, while the second stage applies a parallel process to execute each sub-network individually. The last stage of our work includes the naive approach prune algorithm, a parallel process, as in Table 2. The results show the difference in each stage until reaching the last stage. The last stage records less generation time because it uses the parallel process and naive approach, which reduces the number of edges used in the generation and reduces the attack graph's generation time.

Other algorithms are used to generate the attack graph, which are greedy algorithm, breadth-first search, and depth-first on the same number of nodes and a similar topology. These path-pruning algorithms were chosen to compare because these algorithms have been used to prune the attack graph in previous works. The results show that the naive approach prune algorithm gets better results than other algorithms, as shown in Figure 7; the reason behind that is naive approach is based on edge pruning while other algorithms are search algorithms, so they depend on path pruning. The path pruning algorithms require more time because they need to identify the connection between the nodes, determine all the paths then check each path individually; while

**Table 2: Running time of the attack graph (seconds)**

Nodes Number	Full Graph	Parallel Process	Our Work
8 nodes	12.604	5.973	1.232
50 nodes	27.489	13.187	5.173
100 nodes	62.480	27.875	13.579
250 nodes	113.631	56.319	39.496
400 nodes	201.170	117.642	91.670

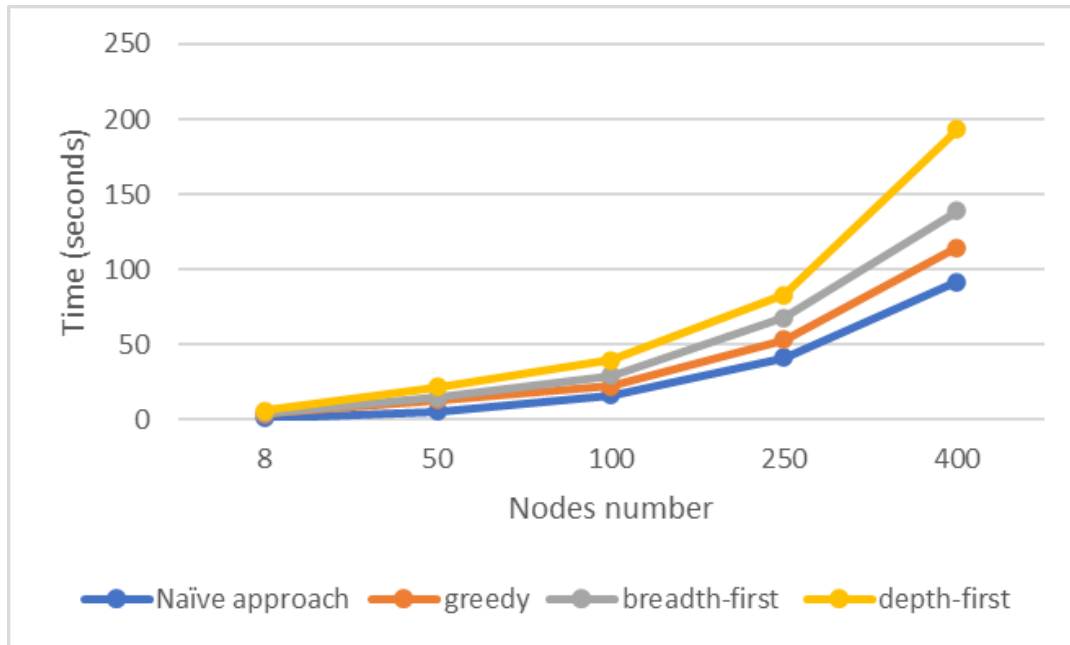


**Figure 7: Comparison results between the Naïve approach and other algorithms**

each pruning algorithm requires only the connection between the nodes and then directly checks the edge, also can check more than one edge at the same time.

As stated in Table 3, a further comparison with earlier research has been conducted. When comparing the outcomes, it can be seen that our work is more efficient than others because [15] relies on multiple agents to compute and produce the subgraphs, which are then "combined in the administrator to produce the full graph." While Li et al. [30] used the queue size to indicate the number of threats and reduce creation time, merging the sub-graphs is a problem because it takes a while to construct the whole graph. While Feng et al. [10] rely on a reduction in the number of vulnerabilities in each node to ensure that the attack graph won't be larger and that it won't increase generation time, the generating time will rise as the number of vulnerabilities increases because the attack graph is intended to reflect all of the network's vulnerabilities.

The complexity of the attack graph is measured next. The attack graph represents the connection between the nodes; however, the attack graph generally depends on the reachability calculation, so the general complexity in the worst scenario is  $O(N^2)$  where  $N$  is the number of nodes; in this thesis, a personal agent is used to calculate the reachability for each node, so the complexity of the attack graph will be divided to between each host, so the reachability's complexity is  $O(N)$ , while combining each reachability by the administrator which is  $O(N * \log N)$ , so the complexity is  $O(N + (N * \log N))$ . Also, the naive approach is used to prune unnecessary edges in the attack graph; the naive approach complexity is  $O(E)$ , where  $E$  denotes the number of the edges that must be checked; however, the network is divided into subnetworks so that each subnetwork will generate the attack graph individually then send it to the administrator, so the complexity for the naive approach become  $O(E/S)$  where  $S$  is the number for subnetworks. However, the attack graphs must be merged to get the full attack graph, so the merged graph complexity is  $O(N * \log N)$ , so basically, the naive approach complexity will be  $O((E/S) + (N * \log N))$ . In the end, the attack graph complexity will be  $O(N + 2(N * \log N) + (E/S))$ , so it will be  $O(N + (N * \log N) + (E/S))$ .

**Table 3: Running time of the attack graph (seconds)**

Network size	[15]	[30]	[10]	our work
8	4.102	9.350	5.616	1.232
50	9.830	13.610	11.381	5.173
100	14.670	21.583	16.620	13.579
250	47.38	52.172	49.521	39.496

## 6 Conclusion

Nowadays, networks have overgrown in both terms of complexity and size. However, with the widespread growth of network connectivity, the frequency of cyber-attacks on enterprises and government offices has risen dramatically, causing business interruptions and compromising the reputation and monetary stability of these organizations. To overcome with this issue, the researcher uses a graph model to predict, detect, and discover attack paths to represent the network, however, the attack graph generation is still having an issue of generation time. In this work, a naïve approach algorithm and personal agent are used to enhance the generation time by reducing the reachability calculations and pruning unnecessary edges in the graph. A personal agent gathers the information from the nodes, determines the node's reachability, and sends the results to the administrator server, which is in charge of producing the attack graph. Each personal agent is in charge of gathering information to calculate reachability; the personal agent is also responsible for the update to reduce the time complexity. While the naïve algorithm is used to prune the unnecessary edge that will reduce the probabilities of the paths that might be used by the attacker. The experiment shows that the proposed model reduced the generation by 20 percent. In future work, use more attack graph reachability content to increase the information that used in the attack graph which increases the ability to detect and predict the attacks. Also, propose a new pruning algorithm with more details to reduce the generation time and the complexity of the attack graph.

## Authors' Contributions

In this study, all authors studied in creating idea, designed the study and wrote up the article.

## Competing Interests

The authors declare that they have no conflict of interest.

## References

- [1] J. Jang-Jaccard and S. Nepal, "A survey of emerging threats in cybersecurity," *Journal of computer and system sciences*, vol. 80, no. 5, pp. 973–993, 2014.
- [2] E. Bertino, L. Martino, F. Paci, A. Squicciarini, E. Bertino, L. D. Martino, F. Paci, and A. C. Squicciarini, "Web services threats, vulnerabilities, and countermeasures," *Security for web services and service-oriented architectures*, pp. 25–44, 2010.
- [3] J. M. Kizza, W. Kizza, and Wheeler, *Guide to computer network security*, vol. 8. Springer, 2013.
- [4] M. Abomhara and G. M. Kjøien, "Cyber security and the internet of things: vulnerabilities, threats, intruders and attacks," *Journal of Cyber Security and Mobility*, pp. 65–88, 2015.
- [5] A. O'driscoll, "Cyber security vulnerability statistics and facts of 2022," *Comparitech*, 2021.
- [6] Y. Yang, L. Wu, G. Yin, L. Li, and H. Zhao, "A survey on security and privacy issues in internet-of-things," *IEEE Internet of things Journal*, vol. 4, no. 5, pp. 1250–1258, 2017.
- [7] J. Wang, "A generation method of attack graph based on evolutionary computation," in *2016 2nd International Conference on Advances in Energy, Environment and Chemical Engineering (AEECE 2016)*, pp. 28–31, Atlantis Press, 2016.
- [8] M. U. Aksu, K. Bicakci, M. H. Dilek, A. M. Ozbayoglu, and E. i. Tatli, "Automated generation of attack graphs using nvd," in *Proceedings of the Eighth ACM Conference on Data and Application Security and Privacy*, pp. 135–142, 2018.
- [9] M. Ibrahim and A. Alsheikh, "Automatic hybrid attack graph (ahag) generation for complex engineering systems," *Processes*, vol. 7, no. 11, p. 787, 2019.
- [10] Y. Feng, G. Sun, Z. Liu, C. Wu, X. Zhu, Z. Wang, and B. Wang, "Attack graph generation and visualization for industrial control network," in *2020 39th Chinese Control Conference (CCC)*, pp. 7655–7660, IEEE, 2020.
- [11] K. Kaynar, "A taxonomy for attack graph generation and usage in network security," *Journal of Information Security and Applications*, vol. 29, pp. 27–56, 2016.
- [12] M. Husák, J. Komárková, E. Bou-Harb, and P. Čeleda, "Survey of attack projection, prediction, and forecasting in cyber security," *IEEE Communications Surveys & Tutorials*, vol. 21, no. 1, pp. 640–660, 2018.
- [13] Z. J. Al-Araji, S. S. S. Ahmed, R. S. Abdullah, A. A. Mutlag, H. A. A. Raheem, and S. R. H. Basri, "Attack graph reachability: concept, analysis, challenges and issues," *Network Security*, vol. 2021, no. 6, pp. 13–19, 2021.
- [14] Z. J. Al-Araji, S. Sakinah Syed Ahmad, H. M. Farhood, A. Awad Mutlag, and M. S. Al-Khaldee, "Attack graph-based security metrics: Concept, taxonomy, challenges and open issues," in *BIO Web of Conferences*, vol. 97, p. 00085, EDP Sciences, 2024.
- [15] K. Kaynar and F. Sivrikaya, "Distributed attack graph generation," *IEEE Transactions on Dependable and Secure Computing*, vol. 13, no. 5, pp. 519–532, 2015.
- [16] Z. Yichao, Z. Tianyang, G. Xiaoyue, and W. Qingxian, "An improved attack path discovery algorithm through compact graph planning," *IEEE Access*, vol. 7, pp. 59346–59356, 2019.
- [17] Z. J. Al-Araji, S. S. S. Ahmad, and R. S. Abdullah, "Propose vulnerability metrics to measure network secure using attack graph," *International Journal of Advanced Computer Science and Applications*, vol. 12, no. 5, 2021.
- [18] Z. Al-Araji, S. S. Syed Ahmad, R. S. Abdullah, *et al.*, "Attack prediction to enhance attack path discovery using improved attack graph," *Karbala International Journal of Modern Science*, vol. 8, no. 3, pp. 313–329, 2022.
- [19] M. Moulin, E. Eyisi, D. M. Shila, and Q. Zhang, "Automatic construction of attack graphs in cyber physical systems using temporal logic," in *MILCOM 2018-2018 IEEE Military Communications Conference (MILCOM)*, pp. 933–938, IEEE, 2018.
- [20] Y. Chen, Z. Liu, Y. Liu, and C. Dong, "Distributed attack modeling approach based on process mining and graph segmentation," *Entropy*, vol. 22, no. 9, p. 1026, 2020.
- [21] H. Li, Y. Wang, and Y. Cao, "Searching forward complete attack graph generation algorithm based on hypergraph partitioning," *Procedia Computer Science*, vol. 107, pp. 27–38, 2017.
- [22] Y. Chen, K. Lv, and C. Hu, "Optimal attack path generation based on supervised kohonen neural network," in *Network and System Security: 11th International Conference, NSS 2017, Helsinki, Finland, August 21–23, 2017, Proceedings 11*, pp. 399–412, Springer, 2017.
- [23] B. Yuan, Z. Pan, F. Shi, and Z. Li, "An attack path generation methods based on graph database," in *2020 IEEE 4th Information Technology, Networking, Electronic and Automation Control Conference (ITNEC)*, vol. 1, pp. 1905–1910, IEEE, 2020.
- [24] P. Sun, H. Zhang, and C. Li, "Attack path prediction based on bayesian game model," in *Journal of Physics: Conference Series*, vol. 1955, p. 012098, IOP Publishing, 2021.
- [25] A. Sabur, A. Chowdhary, D. Huang, and A. Alshamrani, "Toward scalable graph-based security analysis for cloud networks," *Computer Networks*, vol. 206, p. 108795, 2022.

- [26] G. Frances and H. Geffner, "Modeling and computation in planning: Better heuristics from more expressive languages," in *Proceedings of the International Conference on Automated Planning and Scheduling*, vol. 25, pp. 70–78, 2015.
- [27] G. Chartrand and P. Zhang, *A first course in graph theory*. Courier Corporation, 2013.
- [28] S. Jha, O. Sheyner, and J. Wing, "Two formal analyses of attack graphs," in *Proceedings 15th IEEE Computer Security Foundations Workshop. CSFW-15*, pp. 49–63, IEEE, 2002.
- [29] F. Zhou, S. Malher, and H. Toivonen, "Network simplification with minimal loss of connectivity," in *2010 IEEE international conference on data mining*, pp. 659–668, IEEE, 2010.
- [30] M. Li, P. Hawrylak, and J. Hale, "Concurrency strategies for attack graph generation," in *2019 2nd International Conference on Data Intelligence and Security (ICDIS)*, pp. 174–179, IEEE, 2019.

Research Article

# Examining the Effect of Annealing Parameters on Surface Quality and Tensile Strength of ABS 3D-Printed Materials

Mohd Nizam Sudin<sup>1,2a</sup>, Shamsul Anuar Shamsudin<sup>1,2b</sup>, Nazri Md Daud<sup>1,2c</sup>, Mohd Asri Yusuff<sup>1,2d</sup>

<sup>1</sup> Faculty of Mechanical Technology and Engineering, Universiti Teknikal Malaysia Melaka (UTeM), 76100 Durian Tunggal, Melaka, Malaysia.

<sup>2</sup> Centre for Research on Energy (CARE), Universiti Teknikal Malaysia Melaka (UTeM), 76100 Durian Tunggal, Melaka, Malaysia

nizamsudin@utem.edu.my

DOI : 10.31202/ecjse.1369831

Received: 02.10.2023 Accepted: 24.04.2024

## How to cite this article:

Mohd Nizam Sudin, Shamsul Anuar Shamsudin, Nazri Md Daud, Mohd Asri Yusuff, " Examining the Effect of Annealing Parameters on Surface Quality and Tensile Strength of ABS 3D-Printed Materials", El-Cezeri Journal of Science and Engineering, Vol: 11, Iss:3, (2024), pp.(307-316).

ORCID: <sup>a</sup>0000-0001-7513-3826; <sup>b</sup>0000-0003-1740-8021; <sup>c</sup>0009-0007-0007-1430; <sup>d</sup>0000-0001-6736-8705.

**Abstract :** The primary objective of this research is to examine the effects of annealing temperature and duration on the surface quality and tensile strength of ABS-printed materials. ASTM 638 Type IV specimens were created in SolidWorks, sliced using Ultimaker Cura 4.4, and printed with a Creality Ender 3 3D printer using 1.75 mm ABS filament. The samples were subjected to thermal annealing at temperatures ranging from 120°C to 180°C. The annealing durations were set at 20, 40, and 60 minutes, after which the samples were cooled down to room temperature. The TR200 roughness tester and Instron 5585 tensile testing machine were utilized to measure surface roughness and tensile strength, respectively. The smoothest surface (0.622 $\mu$ m) was obtained when the temperature was set at 120°C for a duration of 20 minutes. On the other hand, the roughest surface (3.246 $\mu$ m) was observed when the temperature was increased to 180°C and maintained for a longer period of 60 minutes. The highest tensile strength of 75.681 MPa was observed at a temperature of 180°C for a duration of 60 minutes, indicating an optimal condition for maximizing the strength of ABS. However, there may be a limit, as suggested by previous research conducted at temperatures of 160°C and 180°C. In conclusion, it can be observed that the relationship between annealing temperature, duration, and surface roughness is not solely linear. The variations observed indicate the presence of interactions between these factors.

**Keywords :** ABS, Annealing parameters, FDM, surface roughness, tensile strength.

## 1 Introduction

Fused deposition modelling (FDM) is an economically viable additive manufacturing methodology that employs thermoplastics to fabricate personalized products. Despite being a cost-effective manufacturing technique, FDM exhibits certain limitations, including a restricted range of material choices, rough surface textures, and subpar mechanical characteristics. FDM parts are sensitive to slicing parameters. For example, infill density has the greatest impact on the tensile strength of 3D printed PLA+ samples (90.7%), followed by print speed and infill pattern. Previous research has shown that the diamond infill pattern demonstrates superior performance in influencing the structural strength of 3D printed objects [1], [2]. In investigating the wear behavior of gears, Kalani et al. [3] concluded that 3D-printed PA-12 Nylon gears manufactured using SLS exhibit reduced durability at high torque and rotational speeds, leading to failure due to increased contact surface at 1400 rpm and 2.4 Nm torque. They also found a higher specific wear rate at low rotational speeds. However, at low torque and speed, the gears operated smoothly without significant issues. The nozzle diameter has also affected the tensile properties of FDM-printed parts. However, the findings of [4] contradict those of [5]. Kartal and Kaptan [6] employed milling for post-processing and determined the optimum cutting tool for CNC milling of 3D-printed PLA parts.

Nevertheless, it is possible to overcome these limitations by implementing post-processing techniques that enhance both the mechanical properties and surface finish [7]. Annealing is a frequently utilized post-processing methodology that enhances the mechanical strength and crystallinity of parts produced through FDM [8], [9] but not at excessive temperature [10]. The methodology entails the application of gentle heat to the substance, elevating its temperature slightly beyond the threshold at which it transitions from a rigid to a more pliable state. The temperature is maintained at an elevated level for a specified duration, following which the substance is gradually cooled. The process of reheating and subsequent gradual cooling facilitates the development of substantial crystalline structures within the polymer, leading to the redistribution of internal stresses and, ultimately, an enhancement in crystallinity, strength, and stiffness [11].

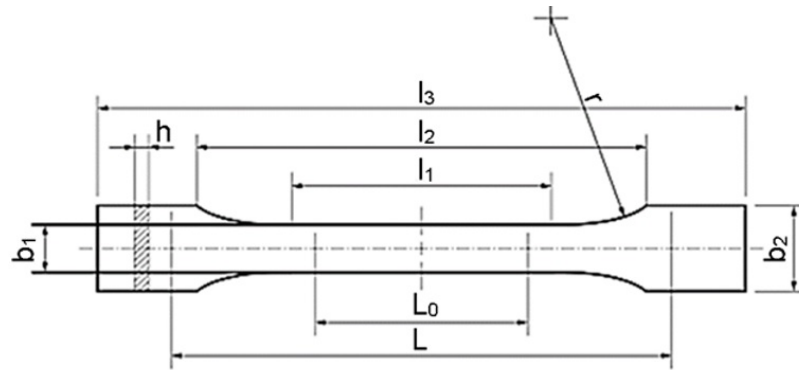
A number of studies have been conducted to examine the impacts of various annealing parameters on thermoplastic materials. The point being illustrated was demonstrated by [12] through the implementation of tensile and compressive tests on FDM-printed volcano Polylactic Acid (PLA). The material underwent annealing for durations of 20 and 60 minutes at a temperature of 110°C. As a result, the compressive strength of the PLA exhibited an increase, while its elongation demonstrated a decrease. Slavković et al. [13] conducted an experiment wherein annealing was carried out at a temperature of 75°C on a shape memory polymer composed of PLA. The researchers observed a significant increase in both tensile and compressive strength. The observed improvement can be attributed to the augmentation in crystallinity, mitigation of residual stress, and enhancement of interlayer bonding. In a similar vein, the authors Singh et al. [14] employed an annealing-based heat treatment methodology to enhance the surface characteristics of acrylonitrile butadiene styrene (ABS) components produced through FD. The implementation of this particular approach resulted in a decrease in porosity and interlayer gaps observed in the printed components. The predictive accuracy pertaining to tensile strength, flexural strength, and Charpy impact strength was found to be minimal. In a study conducted by [15], the manufacturing process of PLA was examined using FDM and subsequent annealing at temperatures above the glass transition temperature. The aforementioned methodology yielded a significant augmentation in flexural stress, a phenomenon that can be ascribed to the heightened crystallinity of the material. The findings presented in this study provide empirical evidence supporting a correlation between the mechanical properties of PLA and its crystalline structure. Butt and Bhaskar [7] conducted a recent study that demonstrated the efficacy of annealing treatments in improving the surface properties of ABS components produced through FDM. The annealing process is primarily influenced by temperature and time. The annealing process, when performed at temperatures below the glass transition temperature ( $T_g$ ), serves to mitigate the residual stresses that arise from the printing process. Nevertheless, the process of annealing performed above the glass transition temperature ( $T_g$ ) serves the purpose of not only relieving internal stresses but also modifying the molecular orientation. However, it has been demonstrated in prior studies that the impact of annealing on the properties of materials is intricate, resulting in different consequences depending on the precise annealing temperatures and durations [16], [17]. The phenomenon of annealing, carried out at temperatures surpassing the glass transition temperature ( $T_g$ ), in the case of ABS, facilitates the consolidation of separate filament layers, consequently augmenting the material's pliability and adhesion properties. This phenomenon has the capability to reduce the occurrence of stress concentrations, thereby potentially enhancing the mechanical properties and surface finish of a material. To attain an optimal equilibrium between the augmentation of properties and the potential distortion of the structure, it is imperative to exercise prudence in the selection of annealing parameters. The preservation of the original form requires the utilization of molds or bracing techniques [17].

FDM components have improved mechanical properties and surface quality after annealing. To achieve the desired results while minimizing side effects, annealing parameters must be carefully adjusted. Our primary objective is to investigate how annealing parameters such as temperature and time affect the surface roughness and tensile strength of ABS-printed materials. The effect of processing parameters of abrasive water jet on the surface roughness of ABS and PLA 3D printed parts was investigated by [18]. In contrast to previous studies, which focused on annealing near the glass transition temperature ( $T_g$ ), our research ranges from temperatures slightly above  $T_g$  to those near the melting point of the ABS material, with varying annealing times. Our research is based on three hypotheses: 1) Annealing above  $T_g$  improves interlayer adhesion and mechanical strength; 2) Annealing reduces surface imperfections such as porosity and interlayer gaps, thereby enhancing surface finish; and 3) The mechanical properties and surface quality of FFF-printed parts are dependent on annealing parameters. We expect that this research will aid in optimizing annealing for FDM applications.

## 2 Materials and Method

### 2.1 Material and Modelling

SolidWorks, a computer-aided design (CAD) application, was used to create a precise 3D model of the specimen. The design strictly adhered to the dimensions outlined in ASTM D638's dogbone configuration, as depicted in the Fig. 1. Specifically, it maintained the Type IV dimensions, ensuring precision with a length of 115mm, a grip width of 19mm, and a gauge width of 6mm, which all significantly contributed to the data's accuracy. The created model was saved in the STL file format to ensure compatibility with Ultimaker Cura 4.4 slicing software. The primary objective of this software platform is to optimize various critical parameters, encompassing layer height, wall thickness, top and bottom layers, infill density, and pattern. In order to achieve precision in the realm of 3D printing, these parameters must be accurately adjusted. The slicing of the specimen's 3D model was executed using Ultimaker Cura 4.4 software, a critical step in the process. After uploading the file, careful consideration was given to the creation of parameters and printing settings to ensure the accuracy of the printing procedure. Key printing parameters as in Table 1, including a layer height of 0.2 mm, were determined in order to achieve printing of standard quality. The wall thickness was determined to be 1.6mm, with four wall lines, and the top and bottom layers shared a thickness of 0.8mm, mirroring the wall thickness, with the number of lines matching the wall thickness for consistency. In addition, the infill density was set to 100% and the infill pattern was "lines," which had significant implications for the top and bottom layers, where a grid pattern was fully integrated into each layer. Fig. 2 provides further insight into the infill density (100%) and infill pattern (lines). The material chosen for this study is Acrylonitrile Butadiene Styrene (ABS).



Size	Type I	Type II	Type III	Type IV	Type V
Full length, $l_3$	165	185	165	115	
Parallel length, $l_2$	57	57	57	33	63.5
Gauge length, $l_1$	50	50	50	25	
Parallel section width, strong <sub>1</sub>	13	6	19	6	7.62
Thickness, $h$	7 mm or less		7mm to 14 mm	4 mm or less	
Grip section width, strong <sub>2</sub>	19	19	29	19	9.53
Distance between grips	115	135	115	65	25.4

Figure 1: ASTM specimen dimension [19]

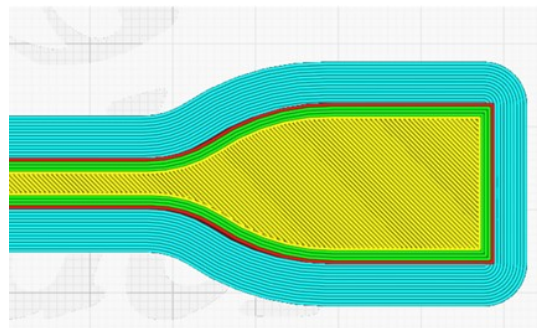


Figure 2: Infill density (100%) and the infill pattern (lines)

## 2.2 Printing Process

To ensure proper adhesion to the build plate, a raft with precise dimensions and a surface separation of 0.3 mm was implemented. Using this design, the printed object demonstrated a high degree of detachability. Following the slicing procedure, the G-code for the project was saved and sent to the Creality Ender 3 3D printer (Fig. 3a). Consequently, the bed was accurately levelled using a sheet of paper to ensure the proper nozzle-bed distance (Fig. 3b). To ensure consistency, three identical specimens were subsequently replicated three times. The scaffolding used to support the specimens was carefully removed following the printing process in order to preserve their structural integrity. Sample of printed specimens is shown in Fig. 4.

## 2.3 Annealing Process

Annealing is a post-processing technique used to enhance the strength of printed parts. In this process, the specimens, printed layer by layer, were placed on a flat Teflon-coated baking pan inside a forced convection bench oven. They were subjected to heating at temperatures of 120°C for durations of 20, 40, and 60 minutes and then allowed to cool to room temperature. The

Table 1: Parameters used for slicing the 3D model

Parameter	Value
Layer Height	0.2mm
Wall Thickness	0.8mm
Print Speed	45mm/s
Build Plate Adhesion	Raft
Nozzle Temperature	230 <sup>0</sup> C
Infill Density	100%
Infill Pattern	Lines
Material	ABS

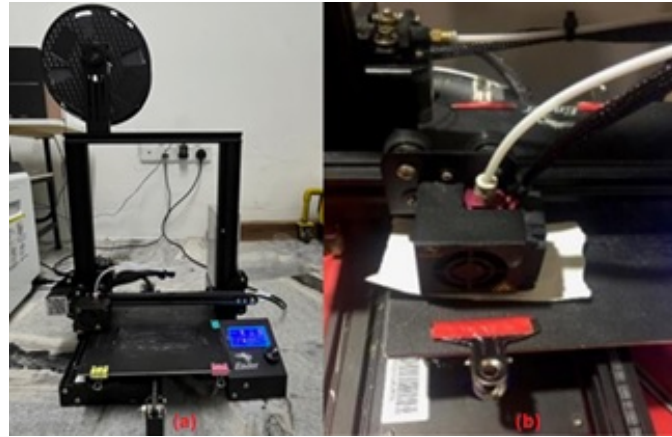


Figure 3: (a) Creality Ender 3 3D printer (b) The bed levelling process



Figure 4: Samples of printed specimens for various annealing times: 20, 40 and 60 min (from left to right)

process was then repeated for temperatures of 140°C, 160°C, and 180°C. Detailed information about the annealing temperature and duration for the specimens can be found in Table 2. This process was applied to samples printed with ABS wire filament with infill densities of 100%. Fig. 5 illustrates an example of an annealed 3D printed specimen for testing purposes.

**2.4 Surface Roughness**

The surface roughness tester, model TR200, with a measuring range of Ra from 0.005 to 16.000µm and Rz from 0.02 to 160.00µm, was utilized to record the average surface roughness. Three different spots on the sample were recorded, and the average of these three values was calculated. During the measuring procedure, the sensor moved linearly along the measured length, while the probe adapted to the surface profile. These movements were then converted into electric signals, subsequently amplified, filtered, and transformed into digital signals by an A/D converter. The main processor further processed these digital signals to provide Ra and Rz values (or Rq and Rt metrics), which were displayed on the screen. Fig. 6 depicted the surface roughness tester, model TR200.

**2.5 Tensile Test**

The tensile test was conducted on each specimen using an Instron 5585 Floor Model Testing System. The primary technical characteristic of the machine is its load cell capacity, which can reach up to 250 kN, making it suitable for conducting the tests in this research. The setup for the tensile test is illustrated in Fig. 7. In the tensile test, each specimen was subjected to a defined rate

**Table 2: Parameters for annealing process**

Experiment	Annealing temperature (°C)	Annealing time (min)
1	120	20,40,60
2	140	20,40,60
3	160	20,40,60
4	180	20,40,60



Figure 5: Samples of specimens after annealing process at variuos temperatures and times: (a) 20 min, (b) 40 min, (c) 60 min.

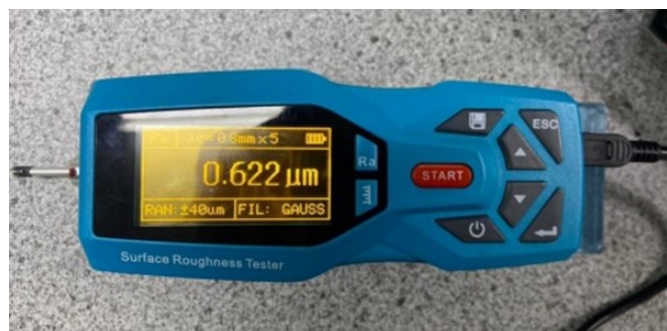
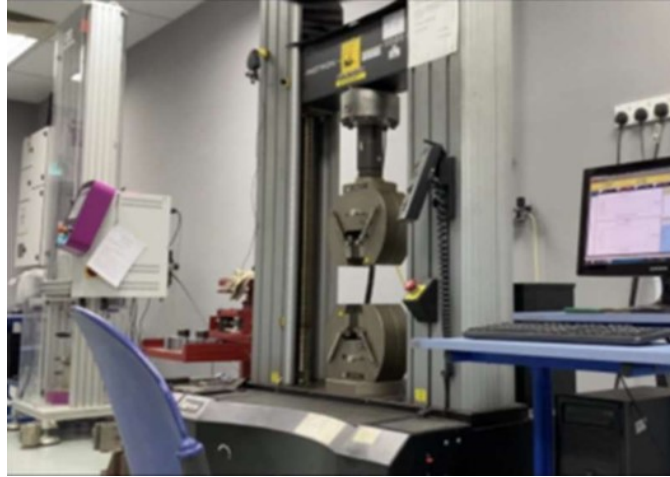


Figure 6: Portable surface profilometry



**Figure 7: Instron 5585 tensile testing machine**

**Table 3: Parameters used for the tensile test**

Parameter	Value
Distance between grip	115mm
Thickness of specimen	4 mm
Speed	4 mm/min
Temperature	25 <sup>0</sup> C
Humidity	60%

of extension until it reached failure. A total of thirty-six samples were evaluated, with three for each combination of annealing temperature and time. This experiment aimed to determine the mechanical properties of the specimens. Using the test results, parameters such as tensile strain, tensile strength, and modulus of elasticity were calculated. The experiment involved several key parameters, including gauge length, gauge width, thickness, specimen grip distance, and testing speed. These parameters were determined prior to conducting the experiment. Table 3 provides an overview of the tensile test parameters.

### 3 Results and Discussion

#### 3.1 Effect of Annealing Temperature on the Surface Roughness

The findings of surface roughness measurements conducted on annealed components produced through the FDM technique are presented in Table 4. The obtained measurements demonstrate a noticeable pattern of fluctuations in surface roughness, which can be attributed to the different annealing temperatures. This claim is supported by the noticeable differences in measurements of average roughness. Our study presents a notable departure from previous research by establishing a clear and positive association between the annealing temperature and the surface roughness of the specimens. The current findings are in opposition to the results documented by [7] and [20], who observed a decrease in surface roughness for 3D-printed ABS components when the annealing temperature was increased slightly above the glass transition temperature of ABS (ranging from 105°C to 115°C to 125°C). Conversely, the findings derived from our research demonstrate a divergent outcome. As an example, the surface roughness was measured to be 0.622µm after subjecting it to a heating duration of 20 minutes at a temperature of 120°C. Nevertheless, it was observed that there existed a clear relationship between the surface roughness and the annealing temperature. Specifically, as the annealing temperature increased to 140°C, 160°C, and 180°C, while maintaining a constant duration, the surface roughness values correspondingly increased to 1.576µm, 2.72µm, and 2.863µm. The abrupt transition in surface roughness is observed when the annealing temperature is increased from 120°C, which is in close proximity to the glass transition temperature (T<sub>g</sub>), to 180°C, a temperature that is significantly distant from T<sub>g</sub>. Singh et al. [17] have proposed that the application of annealing at a temperature of 120°C shows potential in reducing the occurrence of the "staircase effect" by facilitating the reflow of build material, leading to enhancements in surface roughness. Nevertheless, when subjected to temperatures outside of the optimal range or excessive heat, such as 180°C in the specific context mentioned, the material may undergo degradation, resulting in the appearance of surface irregularities, the generation of bubbles, or the development of roughness. The decrease in quality that has been observed can be attributed to the thermal decomposition of ABS. Therefore, the meticulous selection of the appropriate annealing temperature is imperative in order to achieve the optimal surface roughness of the specimen.

**Table 4: Effect of annealing parameters on surface roughness**

Annealing temperature (°C)	Annealing time (min)	Surface roughness ( $\mu\text{m}$ )
120	20	0.622
120	40	0.640
120	60	0.635
140	20	1.576
140	40	1.886
140	60	1.748
160	20	2.725
160	40	2.919
160	60	3.134
180	20	2.863
180	40	3.124
180	60	3.246

### 3.2 Effect of Annealing Time on the Surface Roughness

Two distinct patterns were identified with regards to the influence of annealing duration on the surface roughness of ABS-printed components. The results revealed a positive correlation between the length of the annealing process and the level of surface roughness. This was apparent based on the observed upward trend at both temperatures of 120°C and 140°C. However, a deviation from this established trend became apparent following a duration of 60 minutes, as a noticeable reduction in surface roughness was observed. For instance, the annealing temperature was established at 120°C, and the duration was systematically adjusted in 20-minute intervals, starting at 20 minutes, progressing to 40 minutes, and ultimately concluding at 60 minutes. Upon initial observation, there was a noticeable increase in surface roughness, as evidenced by an initial measurement of 0.622 $\mu\text{m}$ , which later advanced to a final reading of 0.640 $\mu\text{m}$ . Nevertheless, it is crucial to acknowledge that a subsequent marginal reduction in surface roughness occurred, leading to a final measurement of 0.635 $\mu\text{m}$ . A similar pattern was observed when the temperature was modified to 140°C.

On the other hand, the second pattern arose due to the elevation of the annealing temperature to 160°C and 180°C. Under the prevailing conditions, an increase in the duration of the annealing process led to a corresponding increase in surface roughness. The existence of an optimal duration for annealing at a particular temperature can explain the two patterns that have been observed. This enables the material to achieve the desired improvements in both its structural and mechanical properties, while also preserving its surface quality. Beyond this optimal duration, there exists the potential for encountering over-annealing, a phenomenon that may result in the deterioration of the material or the formation of imperfections on its surface. The decrease in surface roughness observed after a duration of 60 minutes implies that the material may have attained its optimal annealing state, subsequently experiencing a gradual degradation as a result of prolonged heat exposure. Furthermore, when exposed to elevated temperatures, specifically at 160°C and 180°C, acrylonitrile butadiene styrene (ABS) experiences significant softening and increased malleability, leading to the flow and deformation of the material. As a result, this phenomenon plays a role in the development of surface irregularities and a general augmentation in roughness.

### 3.3 Effect of Annealing Temperature on the Tensile Strength

The data presented in Table 5 and Fig. 8 offers valuable insights into the influence of annealing parameters on the tensile strength exhibited by ABS material. A noticeable pattern emerges as the annealing temperature varies between 120°C and 180°C, demonstrating a consistent increase in tensile strength. This observation suggests that increasing annealing temperatures has a positive effect on the tensile properties of ABS material. This result aligns with the discovery made in reference [21], which examined how different annealing temperatures affect the properties of PLA-printed components. Significantly, the shift from 120°C to 140°C demonstrates a noteworthy augmentation in tensile strength measurements, emphasizing the advantageous impact of higher annealing temperatures on the strength of the material. Nevertheless, when subjected to elevated temperatures of 160°C and 180°C, the tensile strength values display fluctuations, suggesting that there may be other contributing factors, apart from temperature alone, that impact the material's tensile properties. The heightened molecular mobility of the ABS material is considered to be a significant contributing factor to the observed trend of increased tensile strength at higher annealing temperatures. Increased temperatures impart higher thermal energy to polymer chains, thereby promoting enhanced mobility and reconfiguration. The heightened molecular mobility results in enhanced alignment of chains, diminished internal stresses, and augmented intermolecular interactions, ultimately leading to improved tensile properties, including heightened strength. Nevertheless, when exposed to extremely elevated temperatures, specifically 160°C and 180°C, the fluctuations in tensile stress that are observed can be ascribed to the initiation of material degradation or other complex interactions that impact the behavior of the material. This suggests that there may be a limit to the advantages of utilizing higher temperatures.

### 3.4 Effect of Annealing Time on the Tensile Strength

The data presented in Table 5 demonstrates a consistent pattern across various annealing temperatures, suggesting that longer durations of annealing generally lead to higher levels of tensile strength and, as a result, enhanced tensile properties. The

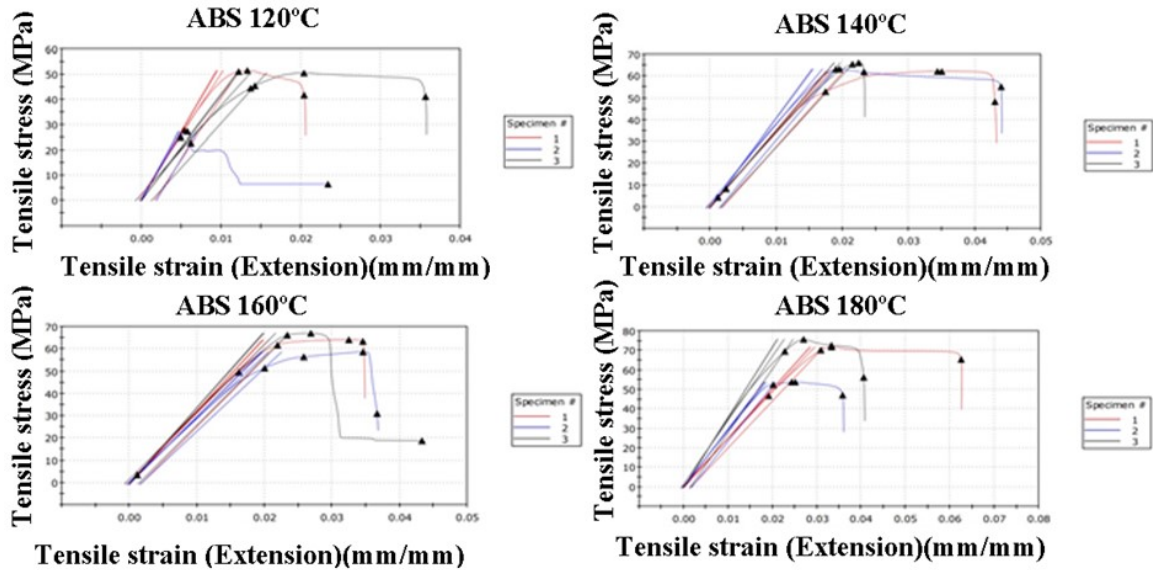


Figure 8: Graph of stress-strain for ABS specimens annealed at various temperatures (9 plots in each graphs reflecting 3 samples tested in each combination of annealing temperature and time)

Table 5: Effect of annealing parameters on tensile strength

Annealing temperature (°C)	Annealing time (min)	Tensile strength (MPa)
120	20	51.629
120	40	27.452
120	60	50.619
140	20	62.159
140	40	63.191
140	60	66.062
160	20	64.071
160	40	58.655
160	60	66.938
180	20	71.810
180	40	53.863
180	60	75.681

observed phenomenon is particularly prominent when the annealing process reaches the 60-minute mark, as the tensile strength values consistently surpass those observed at shorter durations of 20 and 40 minutes. When considering different annealing temperatures, such as 120°C and 140°C, the impact of varying annealing times ranging from 20 minutes to 60 minutes exhibits a complex pattern. A clear positive correlation between longer annealing times and higher tensile strength is observed at temperatures of 120°C and 140°C. This discovery underscores the positive impact of prolonged durations on the tensile strength, corroborating the results observed in reference [22], which used PLA material as the specimen for tensile testing. In contrast, when subjected to temperatures of 160°C and 180°C, the correlation between the duration of annealing and the tensile strength displays a more intricate nature, characterized by fluctuations in tensile strength values and less predictable patterns. The observed intricacy at elevated temperatures implies that there are additional factors, beyond the passage of time alone, that can impact the tensile properties. Stress relaxation is a significant contributing factor to the observed correlation between longer annealing durations and enhanced tensile properties. During the annealing process, the ABS material undergoes prolonged exposure to elevated temperatures, which facilitates the gradual reorganization of polymer chains and the subsequent relief of internal stresses. The aforementioned procedure serves to mitigate residual stresses and imperfections present in the material, thereby leading to an augmentation in its tensile strength. Nevertheless, it is worth noting that there is an optimal duration for annealing, beyond which further enhancements may be constrained. This limitation is evident in the fluctuating stress values observed at exceedingly high temperatures.

**4 Conclusions**

This research aims to investigate the influence of thermal annealing parameters, specifically temperature and duration, on both surface roughness and tensile strength in ABS material printed parts. Overall, both parameters exhibit significant effects on the studied outcomes. Notably, the lowest surface roughness values are achieved at 120°C with a 20-minute annealing duration, yielding a surface roughness of 0.622µm, suggesting an optimal condition for achieving smoother surface finishes. Conversely,

the highest surface roughness values are recorded at 180°C with a 60-minute annealing duration, resulting in a surface roughness of 3.246 $\mu\text{m}$ , indicating the roughest finish. It's important to acknowledge that the relationship between annealing temperature, duration, and surface roughness is not purely linear, with interactions between time and temperature leading to observed variations. This data suggests a potential trade-off between enhancing mechanical properties through annealing (as previously noted) and maintaining a smooth surface finish. Longer annealing times at higher temperatures appear to enhance mechanical properties but may result in rougher surfaces. Similarly, the effect of temperature and time on tensile strength is not strictly linear, with potential interactions between these variables. The highest tensile strength values are achieved at 180°C with a 60-minute annealing duration, reaching 75.681 MPa, possibly indicating an optimal condition for maximizing tensile strength in ABS material. However, it's essential to recognize that there may be a threshold beyond which further increases in temperature or annealing time do not lead to enhanced tensile properties, as indicated by variations at 160°C and 180°C. Manufacturers can utilize the results to enhance their annealing procedures for 3D-printed ABS components, achieving an optimal balance between surface quality and mechanical durability according to specific application needs. Further investigation into the microstructural changes induced by different annealing parameters could lead to deeper insights into the mechanisms that control the roughness and tensile stress of materials. To broaden the scope of this research, future studies could examine the effects of surface coatings, chemical treatments, and annealing on the properties of ABS components produced through 3D printing. It's important to note that the scope of this study is limited to ABS material and may not comprehensively reflect the characteristics of other 3D-printed materials. Additionally, this study does not consider the impact of build orientation or part geometry on the efficacy of annealing, which could be significant factors in real-world applications.

### Acknowledgments

The authors express their gratitude to Universiti Teknikal Malaysia Melaka (UTeM) for their valuable technical support.

### Authors' Contributions

MNBS made contributions to the literature review, experimental investigation, result interpretation, and article writing. NMD participated in result analysis and article writing. MAY played a role in defining the research subject, outlining the scope, handling manufacturing aspects, and contributing to article writing. The final version of the article received approval from all authors.

### Competing Interests

The authors declare that they have no competing interests.

### References

- [1] F. Yılan, İ. B. Şahin, F. Koç, and L. Urtekin, "The effects of different process parameters of pla+ on tensile strengths in 3d printer produced by fused deposition modeling," *El-Cezeri*, vol. 10, no. 1, pp. 160–174, 2023.
- [2] P. Demircioğlu, H. S. Sucuoğlu, I. Bögrekci, and A. Gültekin, "The effect of three dimensional printed infill pattern on structural strength," *El-Cezeri*, vol. 5, no. 3, pp. 785–796, 2018.
- [3] A. Kalani, J. Vadher, S. Sharma, and J. A. N. I. Rita, "Investigation of thermal and wear behaviour of 3d printed pa-12 nylon polymer spur gears," *El-Cezeri*, vol. 9, no. 3, pp. 1121–1135, 2022.
- [4] F. Kartal and A. Kaptan, "Investigating the effect of nozzle diameter on tensile strength in 3d-printed pla parts," *Black Sea Journal of Engineering and Science*, vol. 6, no. 3, pp. 276–287, 2023.
- [5] M. N. Sudin, N. M. Daud, F. R. Ramli, and M. A. Yusuff, "The effect of nozzle size on the tensile and flexural properties of pla parts fabricated via fdm," *Science, Engineering and Technology*, vol. 3, no. 1, pp. 33–43, 2023.
- [6] F. Kartal and A. Kaptan, "Experimental determination of the optimum cutting tool for cnc milling of 3d printed pla parts," *International Journal of 3D Printing Technologies and Digital Industry*, vol. 7, no. 2, pp. 150–160, 2023.
- [7] J. Butt and R. Bhaskar, "Investigating the effects of annealing on the mechanical properties of fff-printed thermoplastics," *Journal of Manufacturing and Materials Processing*, vol. 4, no. 2, p. 38, 2020.
- [8] I. Ferreira, D. Vale, M. Machado, and J. Lino, "Additive manufacturing of polyethylene terephthalate glycol/carbon fiber composites: An experimental study from filament to printed parts," *Proceedings of the Institution of Mechanical Engineers, Part L: Journal of Materials: Design and Applications*, vol. 233, no. 9, pp. 1866–1878, 2019.
- [9] M. Yılmaz, N. F. Yılmaz, and M. F. Kalkan, "Rheology, crystallinity, and mechanical investigation of interlayer adhesion strength by thermal annealing of polyetherimide (pei/ultem 1010) parts produced by 3d printing," *Journal of Materials Engineering and Performance*, vol. 31, no. 12, pp. 9900–9909, 2022.
- [10] M. O. Kabakçı, I. Karaağaç, and M. Y. Demirel, "The experimental investigation of annealing parameters effects on al2024-t3 materials' formability and mechanical properties," *European Journal of Technique (EJT)*, vol. 9, no. 2, pp. 338–346, 2019.
- [11] L. Wang, W. M. Gramlich, and D. J. Gardner, "Improving the impact strength of poly (lactic acid) (pla) in fused layer modeling (flm)," *Polymer*, vol. 114, pp. 242–248, 2017.
- [12] J. Beniak, M. Holdy, P. Križan, and M. Matuš, "Research on parameters optimization for the additive manufacturing process," *Transportation Research Procedia*, vol. 40, pp. 144–149, 2019.
- [13] V. Slavković, N. Grujović, A. Dišić, and A. Radovanović, "Influence of annealing and printing directions on mechanical properties of pla shape memory polymer produced by fused-deposition modeling," in *Proceedings of the 6th International Congress of Serbian Society of Mechanics Mountain Tara*, (Mountain Tara, Serbia), pp. 19–21, 2017.
- [14] R. Singh, L. Yadav, and T. Shweta, "Effect of annealing time on the structural and optical properties of n-cuo thin films deposited by sol-gel spin coating technique and its application in n-cuo/p-si heterojunction diode," *Thin Solid Films*, vol. 685, pp. 195–203, 2019.
- [15] R. A. Wach, P. Wolszczak, and A. Adamus-Włodarczyk, "Enhancement of mechanical properties of fdm-pla parts via thermal annealing," *Macromolecular Materials and Engineering*, vol. 303, no. 9, p. 1800169, 2018.

- [16] J. Torres, E. Abo, and A. J. Sugar, "Effects of annealing and acetone vapor smoothing on the tensile properties and surface roughness of fdm printed abs components," *Rapid Prototyping Journal*, vol. 29, no. 5, pp. 921–934, 2023.
- [17] J. Singh, R. Singh, and H. Singh, "Investigations for improving the surface finish of fdm based abs replicas by chemical vapor smoothing process: a case study," *Assembly Automation*, vol. 37, no. 1, pp. 13–21, 2017.
- [18] J. Lluch-Cerezo, R. Benavente, M. D. Meseguer, and S. C. Gutiérrez, "Study of samples geometry to analyze mechanical properties in fused deposition modeling process (fdm)," *Procedia Manufacturing*, vol. 41, pp. 890–897, 2019.
- [19] ASTM International, "Standard test method for tensile properties of plastics," tech. rep., ASTM International, 2014.
- [20] F. Kartal and A. Kaptan, "Influence of abrasive water jet turning operating parameters on surface roughness of abs and pla 3d printed parts materials," *International Journal of 3D Printing Technologies and Digital Industry*, vol. 7, no. 2, pp. 184–190, 2023.
- [21] F. Kartal and A. Kaptan, "Effects of annealing temperature and duration on mechanical properties of pla plastics produced by 3d printing," *European Mechanical Science*, vol. 7, no. 3, pp. 52–159, 2023.
- [22] S. U. Singh and R. U. Singh, "Effect of annealing on surface roughness of additively manufactured plastic parts: A case study," in *Proceedings of the National Conference on Production Engineering (COPE-2016)*, (Guru Nanak Dev Engineering college, Ludhiana, India), pp. 7–8, 2016.

Research Article

# Experimental Study on Clay Stabilization Using Waste Pumice, Waste Marble Dust, and Lime

Ömür Çimen<sup>1a</sup>, S. Nilay Keskin<sup>1b</sup>, Engin Kalay<sup>2c</sup>

<sup>1</sup> Department of Civil Engineering, Faculty of Engineering and Natural Sciences, Süleyman Demirel University, Isparta, 32260, Türkiye

<sup>2</sup> Technology Program of Civil Engineering, Inegöl Vocational High School, Uludağ University, Inegöl/Bursa, 16400, Türkiye

omurcimen@sdu.edu.tr

DOI : 10.31202/ecjse.1506870

Received: 28.06.2024 Accepted: 03.09.2024

**How to cite this article:**

Ömür Çimen, S. Nilay Keskin, Engin Kalay, "Experimental Study on Clay Stabilization Using Waste Pumice, Waste Marble Dust, and Lime", El-Cezeri Journal of Science and Engineering, Vol: 11, Iss: 3, (2024), pp.(317-326).

ORCID: <sup>a</sup>0000-0002-6138-6029; <sup>b</sup>0000-0002-0367-943X; <sup>c</sup>0000-0001-5185-8806.

**Abstract :** In high-plasticity clays, low unconfined compressive strength and high swelling pressure cause problems in engineering structures. In this study; pumice, marble dust, and lime were mixed with high-plasticity clay to investigate their effects on the engineering properties of clay. Atterberg's limits, standard compaction, unconfined compression test, and swelling experiments were performed by adding pumice, marble dust, and lime to clay in pre-defined ratios. After determining the optimum dosages for each additive, samples prepared at maximum dry density and optimum water contents were cured for 7, 28, and 90 days. Unconfined compression tests, triaxial compression tests, and CBR tests were performed on those samples. SEM, X-ray, and chemical analysis were also performed. It was observed that the additives used improved the engineering properties of high-plasticity clay.

**Keywords :** Soil Stabilization, Clay, Waste Material, Geotechnical Properties.

## 1 Introduction

Large quantities of domestic, industrial, and mining wastes are produced yearly. Recycling, incineration, and burial are procedures for the disposal of these waste materials. Many countries use landfills to eliminate waste materials that cannot be recycled or processed [1]. Mine wastes or by-products offer a great potential to meet the demand for large-volume low-cost mineral resources for road construction [2]. Bruder-Hubscher et al. [3] stated that the incineration of municipal solid wastes is a management option that can achieve up to 80% and 90% reduction in waste mass and volume, respectively. Puma et al. [4] reported that the most commonly used methods for processing non-recyclable solid wastes (about 426 kg per capita-1 year-1) in Italy are landfilling (60%) and incineration (18%).

Recent projects show that successful waste usage significantly saves construction costs [5]. One of the methods applied to improve the engineering properties of clay soil is to mix some waste additives with clay soil. Clay soils with a high expansion, high moisture capacity, low bearing value, and high shrinkage potential can cause problems in various engineering structures. Waste materials can be evaluated as a potential additive for structural fills such as roads, slopes, and dams. There are numerous studies on the various wastes used in fillings in the literature and many of these studies are on the stabilization of clayey soils.

Naganathan et al. [6] showed that kaolin addition delayed the initial setting time of controlled low-strength material mixtures, reduced bleeding, lowered compressive strength, and increased the values of water absorption, sorption, and initial surface absorption. Babu and Chouksey [7], and Peddaiah et al. [5] observed that plastic wastes increase soil resistance and significantly reduce compressibility.

Kamon and Nontananandh [8] examined the potential for burning various industrial wastes with lime to produce a by-product having cementing characteristics similar to those of ordinary Portland cement in stabilizing loam soil. They obtained that the percentages of the main cementitious compounds in this new cement-like stabilizer are comparable to those of cement for subgrade purposes. Attom and Al-Sharif [9] evaluated burned olive waste for usage as a soil stabilizer. They found that the 2.5% addition by weight of burned olive waste increases the Unconfined Compressive Strength (UCS) and maximum dry density (MDD) and the 7.5% addition by weight of olive ash minimizes the swelling pressure of the soil. Igwe and Adepehin [10] reported using granite and dolerite dust for clay stabilization. They found that a noticeable reduction in shrinkage and plasticity, as well as an increase in California Bearing Ratio (CBR), were observed in the treated soil samples. Cokca and Yilmaz [11] evaluated the feasibility of utilizing fly ash, rubber, and bentonite as a low hydraulic conductivity liner material. They implied that the rubber and bentonite with added fly ash showed good promise as a candidate for the construction of a liner based on

hydraulic conductivity, leachate analysis, unconfined compression, split tensile strength, one-dimensional consolidation, swell, and freeze/thaw cycle tests.

Forteza et al. [12] reported that bottom ash is an adequate soil for embankments and landfills and an excellent material for granular layers (bases and subbases). Baykal et al. [2] suggested a new technique for adding water to fly ash samples to enhance the conditions for cementitious mineral formation without sacrificing compressibility. They reported that the snow addition to fly ash noticeably increased the UCS and splitting tensile strength beginning from 14 days of curing, new technology will allow the construction of highway embankments, bases, and subbases during the wintertime in cold regions. Tonož et al. [13] investigated the performance of lime in powder form in laboratory-scaled models to improve the physical, swelling, and strength characteristics of Ankara clay in Turkey. They implied that the UCS increased by approximately 84% after 28 days and that if the curing period is less than 28 days, the UCS values of the lime-treated samples are higher than those of natural samples.

Senol et al. [14] presented the results of research that considered self-cementing fly ashes for stabilizing four different types of soft subgrades from various road sites in Wisconsin, USA. They reported that the fly ash stabilization substantially increased both the UCS and CBR values for the mixtures tested, and it has the potential to offer an alternative for the soft subgrade improvement of highway construction. Pahanikumar and Shankar [15] investigated the heave studies on fly ash-stabilized expansive clay liners. Hossain et al. [16] presented the characteristics of Papua New Guinea clayey soils stabilized with various percentages of volcanic ash, finely ground natural lime, cement, and their combinations. They reported that the stabilized soils exhibit enhanced mechanical properties, such as compressive and tensile strength, modulus of elasticity and CBR, and durability regarding water resistance, sorptivity, and shrinkage. They proposed that suitable stabilized soil mixtures using volcanic ash, lime, and cement and their combinations can be used to set up road pavements, airfields, earth dams, and low-cost housing. Sengupta et al. [17] investigated the improvement of the bearing ratio of clayey subgrade using a compacted fly ash layer. They determined the improvement of clayey soil when a compacted fly ash layer was placed on it with the different values of thickness ratio, placement moisture content, and compaction energy.

Dubois et al. [18] investigated the potential of using dredged marine sediments in road construction, and they reported the efficiency of lime in improving the mechanical characteristics of the mixtures. Brooks et al. [19] presented the results of a laboratory experimental program to evaluate the potential of limestone dust and coal fly ash to stabilize some problem soils in south-eastern Pennsylvania, showing that the plasticity and swell were reduced by 40% and between 40 and 70%, respectively. The results further showed a marked increase in the strength of the soils for CBR and UCS when stabilized with the additives.

Al-Mukhtar et al. [20] investigated the lime consumption by 10% of the lime treatment of five soils containing different major clay minerals. They assessed the short-term reaction (cation exchange and flocculation) and the long-term reaction (pozzolanic reaction) due to the highly alkaline medium induced by the dissolution of lime in the water contained in the soil. Zorluer and Gucek [21] investigated the reuse of marble dust and fly ash in soil stabilization finding that their addition to clay soil increased the UCS, CBR, and freeze-thaw strength but decreased the swelling potential and grain loss after freeze-thaw. Guney et al. [22] reported that sepiolite is the dominant material affecting both the geo-mechanical and geo-environmental properties of liners of kaolinite, zeolite and their mixtures. Modarres and Nosoudy [23] evaluated the environmental and technical impacts of coal waste usage at stabilization of the hydrated lime-additive medium-plastic clay. They implied that a coal waste powder addition and its ash with lime extent enhanced the soil-bearing capacity. Jamsawang et al. [24] determined the free swell potential of expansive clays stabilized with the shallow bottom ash mixing method. They show the free swell potential values of the stabilized expansive samples decreased with increasing bottom ash content.

The effect of pumice material on high-plasticity and low-plasticity clay soils was evaluated. It has been shown that pumice can be used as a stabilization material in high-plasticity clays [25]. Çimen et al. [26] examined waste pumice's use to stabilize the high-plasticity clayey subgrade, which is inappropriate for road construction. It improved the mechanical properties and reduced the swelling potential.

In the present study, waste pumice, waste marble dust, and lime as the soil stabilizer were added to high-plasticity clay soil to investigate their effects on the engineering properties of clay. Liquid limit, plastic limit, standard compaction test, unconfined compression test, and swelling test were performed by adding these additives according to the weight ratios of the additives. The optimum dosages for pumice, marble dust, and lime were first determined. Then triple mixture samples were prepared using those optimum dosages. For these mixture samples, first CBR tests and then 7, 28, and 90-day cured unconfined compression tests were performed. The change in engineering properties of high plasticity clay was investigated by using different percentages of waste materials. It is aimed to obtain a cheap, effective and sustainable improvement by using waste materials in clay soil stabilization.

## 2 Material and Experimental Study

In this study, the materials used for soil stabilization are supplied from pumice, marble, and lime factories in Isparta, Turkey, and the high-plasticity clay is taken from the construction field of the Fethiye – Esen 1 hydroelectric power plant in Türkiye. The samples used are presented in Figure 1 below.

The chemical properties of the high-plasticity clay, pumice (P), marble dust (M), and lime (L) are determined with XRF test equipment. The chemical test results are given in Table 1. X-ray analyses were performed for the mineral properties of the samples. The minerals obtained are shown in Table 2.



Figure 1: Images of the samples used

Table 1: Results of Chemical Analysis for Used Materials [27]

Sample	Na <sub>2</sub> O	MgO	Al <sub>2</sub> O <sub>3</sub>	SiO <sub>2</sub>	P <sub>2</sub> O <sub>5</sub>	K <sub>2</sub> O	CaO	TiO <sub>2</sub>	MnO	Fe <sub>2</sub> O <sub>3</sub>	L.I.
Clay (C)	<0.1	17.4	4.3	47.1	<0.1	0.3	2.8	0.2	0.1	16.6	9.85
Pumice (P)	5.3	1.1	17.1	60.9	0.2	5.0	3.0	0.3	0.1	3.2	2.80
Marble Dust (M)	<0.1	0.3	<0.1	0.2	<0.1	<0.1	57.0	<0.1	<0.1	0.1	42.35
Lime (L)	<0.1	0.4	<0.1	0.1	<0.1	<0.1	79.3	<0.1	<0.1	0.1	19.85

L.I: Loss of ignition

Table 2: Results of Mineralogical Analysis for Used Materials [27]

Materials	Minerals
Clay	Simectite group, serpentine group, quartz, calcite, amorphous silica, amphibole group (very few), feldspar (very very few), chlorite (very very few).
Pumice	Feldspar, opal-CT, quartz, mica group, amphibole group.
Marble Dust	Calcite
Lime	Portlandite, aragonite (few), calcite (few), illite (very very few)

For engineering properties of samples, liquid limit tests, plastic limit tests (as described in the ASTM D4318-05), standard compaction tests (as described in the ASTM D698-00), unconfined compression tests (as described in the ASTM D2166-00) and free volume swelling tests (as described in the ASTM D4546 method A) are conducted [28], [29], [30], [31]. Those tests were carried out to determine the geotechnical properties of clay both in its natural state and when mixed with varying percentages at weight (5, 10, 15, 20, 25, 30, 35% of passed No40 sieve pumice for 2, 4, 5, 6, 10, 15, 20, 25, 30% of passed No40 sieve marble dust for 1, 2, 3, 4, 5, 6, 7% of passed No40 sieve lime). After determining the optimum dosages of clay-pumice, clay-marble dust, and clay-lime, triple-mixed samples were prepared. Then, the same experiments were made. Images of some samples after unconfined compression tests are shown in Figure 2.

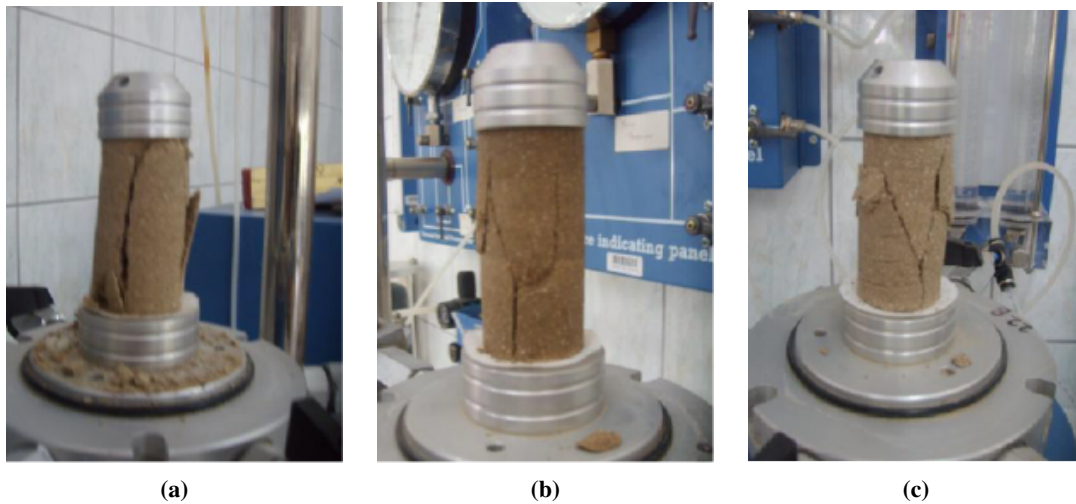


Figure 2: Images of some samples after unconfined compression tests

Unconfined compression tests are conducted for dry curing periods of 7, 28 and 90 days on the samples determined optimum additive ratios according to the ASTM D2166-00 standard test method [30]. The samples are compacted in a right circular cylinder with a diameter of 3.5 cm and a height of 7 cm according to the ASTM D 698-00 Standard Test method, and they are kept in a desiccator by covering with a stretch film during curing [29]. The shear characteristics of the samples are measured by triaxial compression tests using 50, 100, and 200 kPa cell pressures under undrained conditions according to the ASTM D4767-95 standard test method [32]. The California bearing ratio (CBR) test is implemented to evaluate the potential strength of the samples for use in the design of roads according to the ASTM D1883-07e2 standard test method [33]. The swelling percentage is determined after the samples are soaked underwater for 4 days. Scanning Electron Microscopy (SEM) images of used samples were taken using FEI Quanta 400 equipment.

### 3 Results and Discussions

Liquid limit ( $WL$ ), plastic limit ( $WP$ ), plasticity index ( $PI$ ), maximum dry density ( $\gamma_{dmax}$ ), optimum water content ( $W_{opt}$ ), Unconfined compressive strength ( $q_u$ ), free volume swelling potential ( $SP$ ), and swelling pressure ( $P_s$ ) were shown in Table 3.

These results presented that the liquid limit, plastic limit, and plasticity index of clay have decreased with the pumice additive. It was observed the maximum dry density and unconfined compressive strength of clay were increased and optimum water content, swelling potential, and swelling pressure were decreased with the addition of pumice. An ideal pumice mixing ratio was determined as 25-30%.

With the addition of marble dust, the liquid limit, plastic limit, and plasticity index of clay were decreased by 20% marble dust additive. However, there is an increase of over 20% in the liquid limit of marble powder. Therefore, the plasticity index increased. By increasing the amount of marble dust, it was seen that the maximum dry unit weight and the unconfined compressive strength of clay were increased and optimum water content, swelling potential, and swelling pressure were decreased. An ideal marble dust mixing ratio was determined as 5%. With the addition of lime, the liquid limit, plastic limit, and plasticity index of clay decreased rapidly. When the lime ratio increases, maximum dry unit weight and unconfined compressive strength increase, optimum water content, swelling potential, and swelling pressure decrease. An ideal lime mixing ratio was determined as 6%. The effects of pumice, marble dust, and lime on the unconfined compressive strength, swelling potential, and swelling pressure of the clay used are shown in Figure 3.

As seen in Figure 3a; Increasing the amount of additive increases the unconfined compressive strength. This increase is different for pumice, marble dust and lime. After a certain amount of additive, the unconfined compressive strength decreases. As seen in Figure 3a and 3b; Increasing the amount of additive generally decreases swelling potential and swelling pressure. This decrease is different for pumice, marble dust and lime.

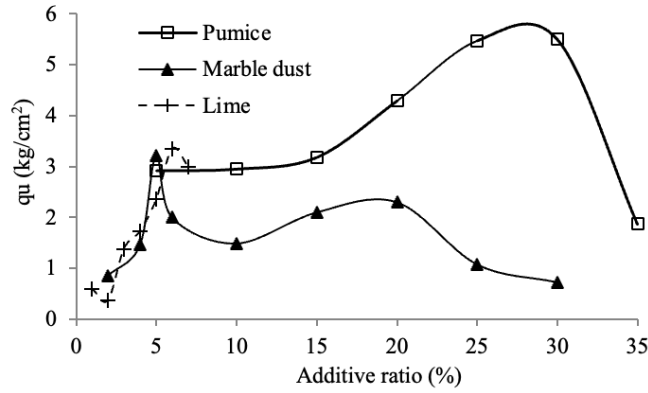
It can be seen in Table 3 that the results of the triple mixture (pumice-lime-clay, pumice-marble dust-clay, lime-marble dust-clay) are quite different from the results of the binary mixture (pumice-clay, marble dust-clay, lime-clay). When 30% pumice additive is kept constant and the amount of lime additive is increased, the liquid limit, plastic limit, plasticity index, optimum water content, swelling potential, and swelling pressure of the mixture are decreased. Maximum unconfined compressive strength at these mixtures is obtained at 30% pumice and 3%lime. When 30% pumice additive is kept constant and the amount of marble dust additive is increased, the liquid limit, plastic limit, plasticity index, optimum water content, swelling potential, and swelling pressure of the mixture are decreased. Maximum unconfined compressive strength at these mixtures is obtained at 30% pumice and 6% marble dust.

**Table 3: Results of liquid limit tests, plastic limit tests, standard compaction tests, unconfined strength tests, and free volume swelling tests for samples [25], [27]**

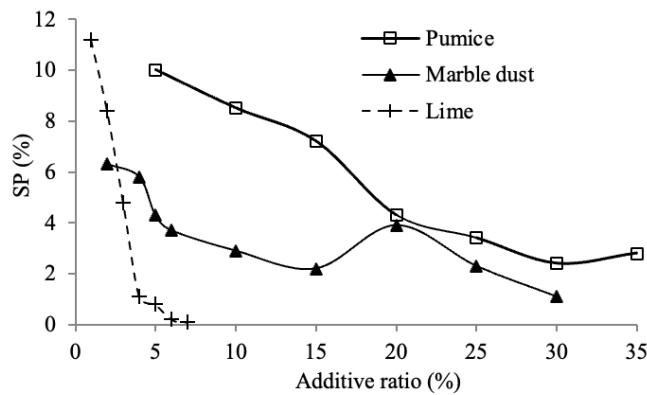
Samples Properties	WL (%)	WP (%)	PI (%)	$\gamma_{dmax}$ (gr/cm <sup>3</sup> )	$W_{opt}$ (%)	$q_u$ (kg/cm <sup>2</sup> )	SP (%)	$P_s$ (kg/cm <sup>2</sup> )
100% C	108	38	70	1.16	38	1.96	12.0	1.50
100% P	-	-	-	1.18	29	0.45	-	-
100% M	-	21.5	-	1.63	20	2.16	-	-
5% P + 95% C	100	34.5	65.5	1.20	34	2.92	10.0	0.75
10% P + 90% C	95	32.5	62.5	1.16	29	2.95	8.5	0.40
15% P + 85% C	90	30	60	1.21	35	3.18	7.2	0.33
20% P + 80% C	89	27	62	1.23	35	4.29	4.3	0.37
25% P + 75% C	88	27	61	1.30	32	5.47	3.4	0.20
30% P + 70% C	80	27	53	1.30	32	5.50	2.4	0.25
35% P + 65% C	77	26	51	1.31	28	1.87	2.8	0.10
2% M + 98% C	115	34	81	1.16	37	0.86	6.3	1.32
4% M + 96% C	102	34	68	1.20	33	1.46	5.8	1.17
5% M + 95% C	112	38	74	1.19	37	3.22	4.3	1.05
6% M + 94% C	98	32	66	1.21	26	2.00	3.7	1.08
10% M + 90% C	100	34	66	1.16	36	1.49	2.9	1.02
15% M + 85% C	84	33	51	1.23	30	2.10	2.2	1.25
20% M + 80% C	80	32	48	1.31	29	2.30	3.9	1.03
25% M + 75% C	90.5	28	62.5	1.30	31	1.08	2.3	1.41
30% M + 70% C	90	26	64	1.34	29	0.73	1.1	0.93
1% L + 99% C	96	32	64	1.16	37	0.60	11.2	1.46
2% L + 98% C	84	53	31	1.14	35	0.36	8.4	1.41
3% L + 97% C	81	58	23	1.12	42	1.38	4.8	1.03
4% L + 96% C	78	56	22	1.24	37	1.73	1.1	0.77
5% L + 95% C	80	61	19	1.24	34	2.35	0.8	0.75
6% L + 94% C	73	59	14	1.26	34	3.35	0.2	0.65
7% L + 93% C	72	-	-	1.21	36	3.00	0.1	0.60
30% P + 1% L + 69% C	80	36	44	1.24	27	2.84	1.0	0.80
30% P + 2% L + 68% C	73	51	22	1.26	34	2.21	0.8	0.05
30% P + 3% L + 67% C	71	53	18	1.29	20	4.18	0.6	0.05
30% P + 4% L + 66% C	71	51	20	1.27	22	2.39	0.5	0.04
30% P + 5% L + 65% C	65	52	13	1.23	29	2.78	0.2	0.02
30% P + 6% L + 64% C	65	-	-	1.28	26	3.39	0.1	0.02
30% P + 7% L + 63% C	69	-	-	1.32	25	2.20	0.1	0.01
30% P + 4% M + 66% C	78	27	51	1.34	33	1.43	0.8	0.52
30% P + 5% M + 65% C	77	23	54	1.33	18	2.01	0.6	0.50
30% P + 6% M + 64% C	80	23	57	1.34	23	4.02	0.8	0.34
30% P + 7% M + 63% C	76	28	48	1.21	36	0.93	0.7	0.15
6% L + 10% P + 84% C	85	64	21	1.31	31	3.52	0.6	0.81
6% L + 20% P + 74% C	78	63	15	1.31	24	3.84	0.4	0.49
6% L + 4% M + 90% C	80	63	17	1.32	31	2.04	0.9	0.15
6% L + 5% M + 89% C	80	66	14	1.30	32	4.36	0.5	0.04
6% L + 6% M + 88% C	79	62	17	1.31	36	3.08	0.4	0.04
5% M + 10% P + 85% C	96	63	10	1.31	36	1.92	6.5	1.03
5% M + 20% P + 75% C	90	36	54	1.31	36	1.51	3.5	0.53
5% M + 5% L + 90% C	80	61	19	1.28	38	3.10	0.3	0.40
5% M + 7% L + 88% C	83	63	20	1.26	37	3.38	0.2	0.10
5% M + 8% L + 87% C	72	55	17	1.25	37	2.44	0.1	0.08
30% M + 3% L + 67% C	66	40	26	1.42	19	2.50	1.0	0.80

Then, 6% lime was kept constant, and pumice and marble dust were mixed in different ratios. In this case, the amount of pumice increased while the liquid limit, plastic limit, plasticity index, optimum water content, swelling potential, and swelling pressure of the mixture decreased. Maximum unconfined compressive strength in this mixture is obtained by 20% pumice. When 6% lime was kept constant and the amount of marble dust was increased, the liquid limit, plastic limit, plasticity index, optimum water content, swelling potential and swelling pressure of the mixture did not change much. Maximum unconfined compressive strength in this mixture is obtained at 5% marble dust.

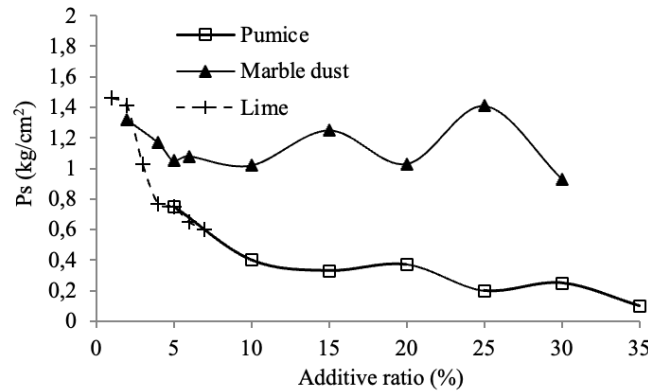
The last, 5% marble dust was kept constant, and pumice and lime were mixed in different ratios. When 5% marble dust was kept constant and the amount of pumice was increased, liquid limit, unconfined compressive strength, swelling potential, and



(a) Relationship between unconfined compressive strength and additive ratio



(b) Relationship between swelling potential and additive ratio



(c) Relationship between swelling pressure and additive ratio  
**Figure 3: Effects of additive ratio on high plasticity clay**

swelling pressure decreased, but plastic limit, maximum dry unit weight and optimum water content were unchanged. When 5% marble dust was kept constant and the amount of lime was increased, the liquid limit, plastic limit, plasticity index, swelling potential, and swelling pressure of the mixture were decreased and unconfined compressive strength and maximum dry unit weight were increased. Maximum unconfined compressive strength in this mixture is obtained at 6% lime.

All mixture ratios were evaluated among themselves and the optimum proportions of each mixture were determined. The optimum values for mixing a single additive into clay and mixing two different additives are given in Table 4. In general, it is found that with an increase in the amounts of marble dust, pumice, and lime in the clay sample, the maximum dry unit weight ( $\gamma_{dmax}$ ) of the clayey mixture increases, the optimum water content ( $W_{opt}$ ) decreases, and the unconfined compressive strength ( $q_u$ ) increases. As a result, it is determined that the optimum addition to the clayey mixture with the marble dust is 5%, and those

of the crushed pumice and quick-lime are 30% and 6%, respectively. In the mixing with the marble dust additive, the liquid limit (*WL*) is determined to be 112%, higher than the 108% of the clay; the plastic limit (*WP*) is obtained as 38%, equal to that of the clay; and the plasticity index (*PI*) is obtained as 74%, higher than the 70% of the clay. In the mixing with the crushed pumice additive, Atterberg's limits are determined to be lower than those of clay. In the mixture with lime, lower values of the liquid limit and plasticity index are obtained, while a higher value of the plastic limit is obtained. When these three additives are compared, pumice is more effective in the increase of the maximum dry unit weight and reduction of the optimum water content however lime is more effective in the plasticity index reduction.

When two additives (*M + P*, *M + L* and *P + L*) at the optimum ratios are added to the clay, the highest maximum dry unit weight and the lowest optimum water content are obtained from sample #9 ( 30% *M* + 3%*L* + 67% *C*) and the lowest plasticity index is obtained from sample #8 (5%*M* + 6%*L* + 89%*C*).

The results of the unconfined compression tests (7, 28, and 90-day curing), triaxial compression tests, and CBR tests are shown in Table 4. The strengths of the mixture samples are determined to be higher than that (1.96 kg/cm<sup>2</sup>) of clay. After a 7-day curing time, there is an increase in the strengths of mixture samples, except for samples # 4, #5, and #7 with *M* and *P*, while the strength values of all of the mixtures increase after 28- and 90-day curing times. According to the test results, the additives affecting the UCS of the clay can be ordered by impact as lime, pumice, and marble dust. The mixtures can also be ordered as samples #10, #6, and #8 (20%*P* + 6%*L*+74%*C*, 6%*L* +94%*C*, and 5%*M* + 6%*L*+89%*C*). This effect can also be seen in Fig. 1. It is determined that the strengths of samples #10, #6, and #8 are, respectively, 13.4, 12.8, and 11.4 higher than those of the high-plasticity clay after 90 days of curing. It is known that the lime-clay reactions continue for quite a long time and that the water content, temperature, and curing time influence the reactions [34], [35], [36], [37]. Consoli et al. [38] reported for Botucatu residual soil (12.5% fly ash) - lime mixtures that the percentage increase in the UCS over the curing time is approximately 62% higher for specimens molded after 60 days of curing compared to 28 days of curing, and there is a further 38% increase in strength in the specimens molded after 90 days of curing compared to the results obtained at 60 days of curing. This implied that the crushed pumice–clay and marble dust–clay reactions also proceed over a long period. Ural et al. [39] have shown that the unconfined compressive strength of high plasticity clay increases when waste PVC is used, through 28-day curing experiments. Yılmaz and Duman [40] showed that when waste Midyat stone and 6% lime were added to low plasticity clay, the 28-day cured unconfined compressive strength increased.

The shear characteristics of the samples are measured by the triaxial compression tests using 50, 100, and 200 kPa cell pressures under undrained conditions according to the ASTM D4767-95 standard test method [31]. The values of the cohesion (*C*), which is equal to the shear strength when the compressive stress is equal to zero, and the angle of internal friction ( $\phi$ ), which is the angle of shear resistance, of the samples are given in Table 4. The highest cohesion is obtained as 1.0 kg/cm<sup>2</sup> for sample #10 (20%*P* + 6%*L*+74%*C*), while that of the clay is 0.2 kg/cm<sup>2</sup>. The next highest mixtures are #11 (0.75 kg/cm<sup>2</sup>) and #8 (0.7 kg/cm<sup>2</sup>). The highest angle of internal friction is determined to be  $\phi = 36.4^\circ$  for sample #6 (6%*L*+94%*C*), followed by  $\phi = 32.3^\circ$  and  $\phi = 30.9^\circ$  for samples #11 (30%*P*+ 3%*L*+67%*C*) and #7 (30%*P* + 6%*M* +64%*C*), compared to a value for the clay of  $\phi = 6^\circ$ . Changes of the unconfined compressive strengths of samples at various curing times are given in Figure 4. It is observed that as the curing time increases, the unconfined compressive strength also increases.

**Table 4: Results of the unconfined compression, triaxial compression, swelling, and CBR tests [27]**

#	Sample properties	$q_u$ (kg/cm <sup>2</sup> )	$q_u$ (kg/cm <sup>2</sup> )			<i>C</i> (kg/cm <sup>2</sup> )	$\phi$ (°)	Swelling (%)	CBR (%)
			7-days	28-days	90-days				
1	100% <i>C</i>	1.96	-	-	-	0.20	6.0	5.78	0.9
2	100% <i>M</i>	-	-	-	-	-	-	-	-
3	100% <i>P</i>	-	-	-	-	-	-	-	-
4	5% <i>M</i> + 95% <i>C</i>	3.22	1.94	4.62	5.40	0.50	13.4	2.98	2.1
5	30% <i>P</i> + 70% <i>C</i>	5.50	2.42	5.51	7.14	0.35	11.8	1.84	4.1
6	6% <i>L</i> + 94% <i>C</i>	3.35	7.37	17.91	25.18	0.60	36.4	0.76	15.2
7	30% <i>P</i> + 6% <i>M</i> + 64% <i>C</i>	4.02	3.98	6.61	7.85	0.60	30.9	0.94	2.0
8	6% <i>L</i> + 5% <i>M</i> + 89% <i>C</i>	4.36	8.85	16.15	22.33	0.70	16.7	0.31	25.1
9	3% <i>L</i> + 30% <i>M</i> + 67% <i>C</i>	2.50	8.50	8.62	12.13	0.15	18.4	0.21	30.1
10	6% <i>L</i> + 20% <i>P</i> + 74% <i>C</i>	3.84	8.63	10.50	26.35	1.00	26.5	0.26	22.1
11	3% <i>L</i> + 30% <i>P</i> + 67% <i>C</i>	4.18	6.65	8.69	19.61	0.75	32.3	0.26	34.3

The California bearing ratio (CBR) test is implemented to evaluate the potential strength of the samples for use in the design of roads according to the ASTM D1883-07e2 standard test method [33]. The samples are soaked under water for 4 days and the swelling percentage is calculated. The CBR values are also determined from the load–penetration curves. Table 4 shows the results of the swelling percentage and CBR for the mixtures. The General Directorate of Highways in Türkiye recommends that subgrade soils have a swelling percentage of  $\leq 3$  and  $CBR > 10$ . As seen in Table 4, all of the mixtures have values of swelling percentage less than 3, and except for samples #4, #5, and #7, all of the mixtures have CBR values greater than 10. According to these results, it is clear that the mixtures with quick-lime can be used as a stabilization material. The highest CBR ratios

are obtained from sample #11 (30%P+ 3%L+67%C), 34.3; sample #9 (30%M + 3%L+67%C), 30.1; and sample #8 (5%M + 6%L+89%C), 25.1. It is significant that the CBR values of samples #11 and #9, with 3% L, are greater than those of samples #6 and #8, with 6% L, resulting in a lower cost for the subgrade. The reasons that sample #11, containing P, has the highest CBR value may include the flocculation, accumulation, and pozzolanic reactions, together with the cation exchange capacity.

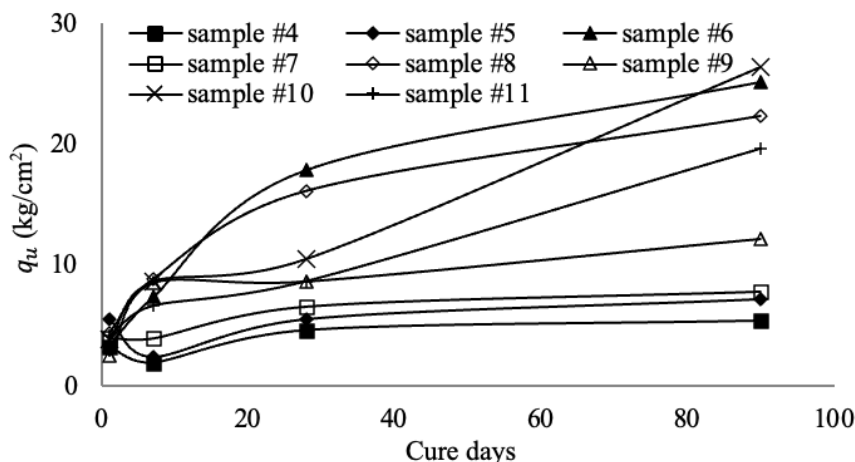


**Figure 4: Unconfined compressive strengths of samples at various curing times**

Morphological analyses of samples were carried out using SEM. SEM images are shown in Figure 5. Comparing SEM images at stabilized with additives clays and pure clay, showed very different morphological structures. It has occurred that open pores of pumice are filled with lime and clay from Figures 5e and 5h. It is thought that portlandite crystals in lime can fill the pore structures and give strength-increasing properties.

It has been shown that the change in engineering properties of high plasticity clay is also possible by mixing waste materials. The use of waste materials in soil stabilization will reduce the storage areas of these materials. In this way, more environmentally appropriate solutions can be produced.

#### 4 Conclusions

The effects of pumice, marble dust, and quick-lime additives in high-plasticity clay are evaluated in the study. The in situ test fillings are prepared according to the optimum mixture ratios obtained from test results in the laboratory. The conclusions obtained from this study are listed below:

- 1) With the addition of crushed pumice, marble dust, and lime into high plasticity clay, it is observed that the values of the dry unit weight, unconfined compressive strength, cohesion, angle of internal friction, and CBR increase, while those of the optimum water content, liquid limit, plasticity index and percentage of swelling decrease. Evaluating these results, the changes in the consistency limits, optimum water content, and maximum dry unit weight stem from short-term reactions while those in the unconfined compressive strength, CBR, percentage of swelling, cohesion, and internal friction angle are from long-term ones.
- 2) It is seen that the curing duration has a greater effect on the unconfined compressive strength of the lime-supplemented mixtures in laboratory tests with 7, 28, and 90-day curing. Among the samples at 90 days' curing, the highest unconfined compressive strength value is obtained from the mixture of 20%P + 6%L + 74%C as 26.35 kg/cm<sup>2</sup> (13.4 times more than that of clay), and the others are in the order of 6%L + 94%C (25.18 kg/cm<sup>2</sup>) and 5%M + 6%L + 89%C (22.33 kg/cm<sup>2</sup>).
- 3) It is determined from the triaxial compression tests that the highest cohesion is found in the mixture of 20%P + 6%L + 74%C (1.0 kg/cm<sup>2</sup>, 5 times more than that of clay), followed by 30%P + 3%L + 67%C (0.75 kg/cm<sup>2</sup>) and 5%M + 6%L + 89%C (0.7 kg/cm<sup>2</sup>). Also, the highest angle of internal friction is found in the mixture of 6%L + 94%C (36.4°, 6 times more than that of clay), followed by 30%P + 3%L + 67%C (32.3°) and 30%P + 6%M + 64%C (30.9°).
- 4) It is determined that all of the mixtures have values of percentage of swelling less than 3 and that the highest CBR ratios are obtained from the mixtures of 30%P + 3%L + 67%C (34.3), 30%M + 3%L + 67%C (30.1), and 5%M + 6%L + 89%C (25.1). The highest values of CBR are obtained from the mixtures with 3% lime.
- 5) From the overall results, it is seen that mixtures of crushed pumice and marble dust with little lime can be effectively used for stabilization for high plasticity clay soil.

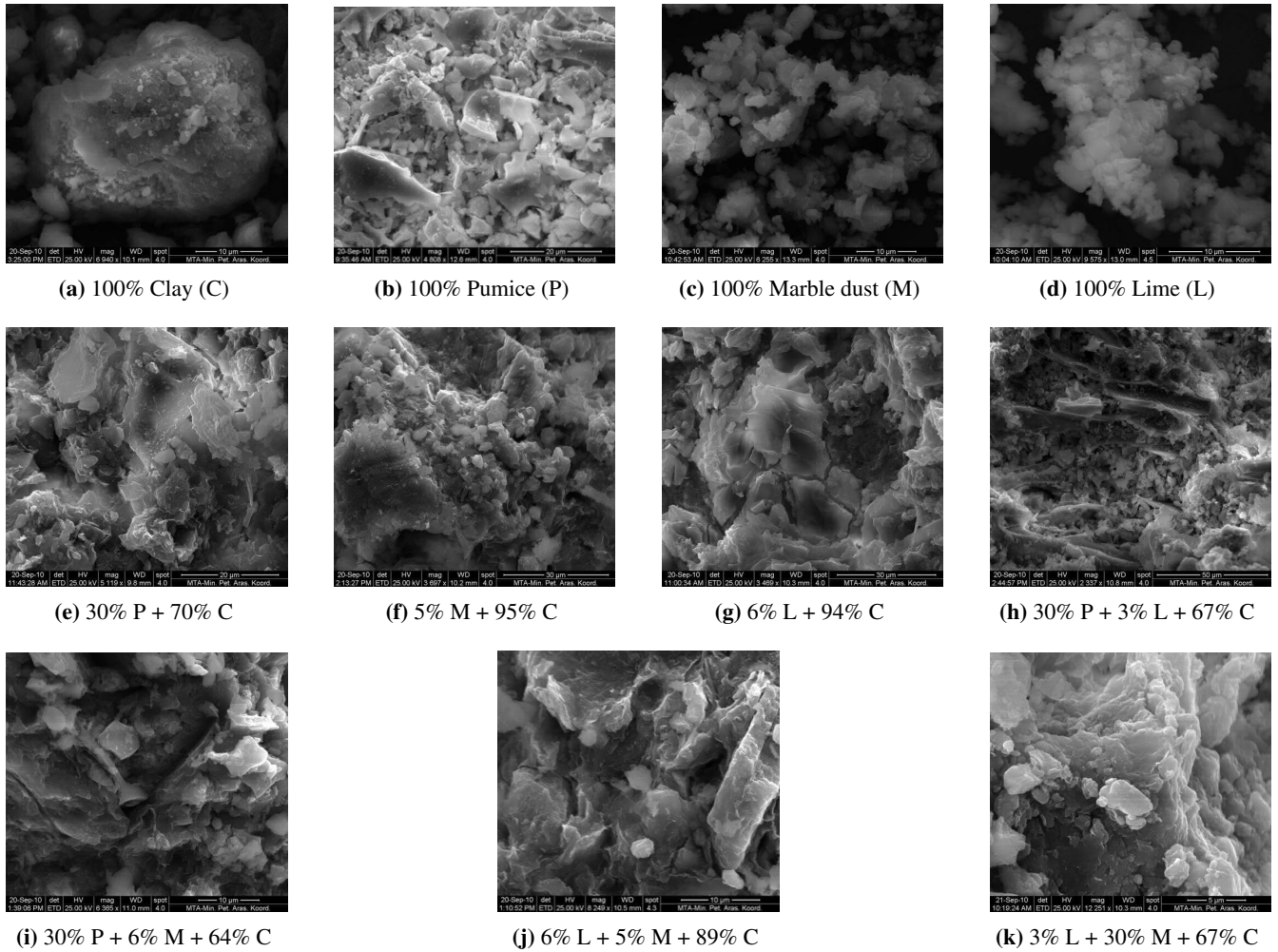


Figure 5: SEM images of pure and mixed samples

### Acknowledgments

This study was supported by the Scientific and Technological Research Council of Turkey [grant number 109M344]; and the Scientific Research Project Management Unit of Süleyman Demirel University [grant number 98-DES-10]. The authors thank both institutions for their support.

### Authors' Contributions

In this study, all authors wrote up the article.

### Competing Interests

The authors declare that they have no conflict of interest.

### References

- [1] H. Scharff, A. Van Zomeren, and H. A. Van Der Sloot, "Landfill sustainability and aftercare completion criteria," *Waste Management & Research*, vol. 29, no. 1, pp. 30–40, 2011.
- [2] G. Baykal, A. Edinçliler, and A. Saygılı, "Highway embankment construction using fly ash in cold regions," *Resources, Conservation and Recycling*, vol. 42, no. 3, pp. 209–222, 2004.
- [3] V. Bruder-Hubscher, F. Lagarde, M. Leroy, C. Coughanowr, and F. Enguehard, "Utilisation of bottom ash in road construction: a lysimeter study," *Waste management & research*, vol. 19, no. 6, pp. 557–566, 2001.
- [4] S. Puma, F. Marchese, A. Dominianni, and M. Manassero, "Reuse of mswi bottom ash mixed with natural sodium bentonite as landfill cover material," *Waste management & research*, vol. 31, no. 6, pp. 577–584, 2013.
- [5] S. Peddaiah, A. Burman, and S. Sreedeeep, "Experimental study on effect of waste plastic bottle strips in soil improvement," *Geotechnical and Geological Engineering*, vol. 36, pp. 2907–2920, 2018.
- [6] S. Naganathan, H. A. Razak, and S. N. A. Hamid, "Effect of kaolin addition on the performance of controlled low-strength material using industrial waste incineration bottom ash," *Waste management & research*, vol. 28, no. 9, pp. 848–860, 2010.
- [7] G. S. Babu and S. K. Chouksey, "Stress-strain response of plastic waste mixed soil," *Waste management*, vol. 31, no. 3, pp. 481–488, 2011.
- [8] M. Kamon and S. Nontananandh, "Combining industrial wastes with lime for soil stabilization," *Journal of geotechnical engineering*, vol. 117, no. 1, pp. 1–17, 1991.

- [9] M. F. Attom and M. M. Al-Sharif, "Soil stabilization with burned olive waste," *Applied clay science*, vol. 13, no. 3, pp. 219–230, 1998.
- [10] O. Igwe and E. J. Adepehin, "Alternative approach to clay stabilization using granite and dolerite dusts," *Geotechnical and Geological Engineering*, vol. 35, no. 4, pp. 1657–1664, 2017.
- [11] E. Cokca and Z. Yilmaz, "Use of rubber and bentonite added fly ash as a liner material," *Waste management*, vol. 24, no. 2, pp. 153–164, 2004.
- [12] R. Forteza, M. Far, C. Segui, and V. Cerdá, "Characterization of bottom ash in municipal solid waste incinerators for its use in road base," *Waste management*, vol. 24, no. 9, pp. 899–909, 2004.
- [13] M. C. Tono, R. Ulusay, and C. Gokceoglu, "Effects of lime stabilization on engineering properties of expansive ankara clay," *Engineering Geology for Infrastructure Planning in Europe: A European Perspective*, pp. 466–474, 2004.
- [14] A. Senol, T. B. Edil, M. S. Bin-Shafique, H. A. Acosta, and C. H. Benson, "Soft subgrades' stabilization by using various fly ashes," *Resources, Conservation and Recycling*, vol. 46, no. 4, pp. 365–376, 2006.
- [15] B. Phanikumar and M. Uma Shankar, "Heave studies on fly ash-stabilised expansive clay liners," *Geotechnical and Geological Engineering*, vol. 35, pp. 111–120, 2017.
- [16] K. Hossain, M. Lachemi, and S. Easa, "Stabilized soils for construction applications incorporating natural resources of papua new guinea," *Resources, Conservation and Recycling*, vol. 51, no. 4, pp. 711–731, 2007.
- [17] A. Sengupta, S. Mukherjee, and A. Ghosh, "Improvement of bearing ratio of clayey subgrade using compacted flyash layer," *Geotechnical and Geological Engineering*, vol. 35, pp. 1885–1894, 2017.
- [18] V. Dubois, N. E. Abriak, R. Zentar, and G. Ballivy, "The use of marine sediments as a pavement base material," *Waste management*, vol. 29, no. 2, pp. 774–782, 2009.
- [19] R. Brooks, F. F. Udoeyo, and K. V. Takkalapelli, "Geotechnical properties of problem soils stabilized with fly ash and limestone dust in philadelphia," *Journal of Materials in Civil Engineering*, vol. 23, no. 5, pp. 711–716, 2011.
- [20] M. Al-Mukhtar, A. Lasledj, and J. Alcover, "Lime consumption of different clayey soils," *Applied Clay Science*, vol. 95, pp. 133–145, 2014.
- [21] I. Zorluer and S. Gucuk, "The effects of marble dust and fly ash on clay soil," *Science and Engineering of Composite Materials*, vol. 21, no. 1, pp. 59–67, 2014.
- [22] Y. Guney, B. Cetin, A. H. Aydılek, B. F. Tanyu, and S. Koparal, "Utilization of sepiolite materials as a bottom liner material in solid waste landfills," *Waste Management*, vol. 34, no. 1, pp. 112–124, 2014.
- [23] A. Modarres and Y. M. Nosoudy, "Clay stabilization using coal waste and lime—technical and environmental impacts," *Applied clay science*, vol. 116, pp. 281–288, 2015.
- [24] P. Jamsawang, B. Adulyamet, P. Voottipruex, P. Jongpradist, S. Likitlersuang, and K. Tantayopin, "The free swell potential of expansive clays stabilized with the shallow bottom ash mixing method," *Engineering Geology*, vol. 315, p. 107027, 2023.
- [25] O. Cimen, "Versatile investigation of improvement of geotechnical properties of soils," M.S. thesis, Suleyman Demirel University, Graduate School of Applied and Natural Sciences, Isparta, Türkiye, 1996.
- [26] Ö. Çimen, M. Saltan, and S. N. Keskin, "Stabilization of clayey subgrade with waste pumice for road infrastructure," *Science and Engineering of Composite Materials*, vol. 22, no. 5, pp. 583–590, 2015.
- [27] E. Kalay, "Using pumice, marble dust and lime for stabilization of compacted high plasticity clay. süleyman demirel university graduate school of applied and natural sciences department of civil engineering," Ph.D. dissertation, Master Thesis, 2010.
- [28] *Standard Test Methods for Liquid Limit, Plastic Limit, and Plasticity Index of Soils (ASTM D 4318-05)*. Philadelphia: American Society for Testing and Materials, 2005.
- [29] *Standard Test Methods for Laboratory Compaction Characteristics of Soil using Standard Effort (ASTM D 698-00)*. Philadelphia: American Society for Testing and Materials, 2000.
- [30] *Standard Test Methods for Unconfined Compressive Strength of Cohesive Soil (ASTM D 2166-00)*. Philadelphia: American Society for Testing and Materials, 2002.
- [31] *Standard Test Methods for One-Dimensional Swell (ASTM D 4546-Method A)*. Philadelphia: American Society for Testing and Materials, 2000.
- [32] *Standard Test Method for Consolidated Undrained Triaxial Compression Test for Cohesive Soils (ASTM D 4767-95)*. Philadelphia: American Society for Testing and Materials, 2003.
- [33] *Standard Test Method for CBR (California Bearing Ratio) of Laboratory-Compacted Soils (ASTM D 1883-07e2)*. Philadelphia: American Society for Testing and Materials, 2007.
- [34] J. E. Gillott, *Clay in engineering geology*. Elsevier, 2012.
- [35] T. M. Petry and E. A. Berger, "Impact of moisture content on strength gain in lime-treated soils," Tech. Rep., 2006.
- [36] T. Shibi and Y. Ohtsuka, "Influence of applying overburden stress during curing on the unconfined compressive strength of cement-stabilized clay," *Soils and Foundations*, vol. 61, no. 4, pp. 1123–1131, 2021.
- [37] A. Petcherdchoo, S. Pochalard, and K. Piriyakul, "Use of bender element tests for determining shear modulus of fly-ash and cement admixed bangkok clay with considering unconfined compressive strength," *Case Studies in Construction Materials*, vol. 18, p. e02040, 2023.
- [38] N. C. Consoli, A. D. Rosa, and R. B. Saldanha, "Variables governing strength of compacted soil-fly ash-lime mixtures," *Journal of Materials in Civil Engineering*, vol. 23, no. 4, pp. 432–440, 2011.
- [39] N. Ural, Ü. Kut, and N. Gülsevinç, "Atık pvc ile zemin iyileştirme," *El-Cezeri*, vol. 7, no. 3, pp. 1471–1481, 2020.
- [40] F. Yılmaz and V. Duman, "Zemin stabilizasyonunda midyat taşı atıklarının kullanılabilirliği," *El-Cezeri*, vol. 7, no. 2, pp. 848–857, 2020.



Research Article

# A Study on Impatient Pedestrian Effect on Bi-directional Pedestrian Movement by Using Ant Algorithms

Tarik Kunduraci<sup>1a</sup>

<sup>1</sup>Department of Electricity and Energy, Manisa Celal Bayar University, Akhisar, Manisa, Türkiye

tarik.kunduraci@cbu.edu.tr

DOI : 10.31202/ecjse.1430803

Received: 02.02.2024 Accepted: 01.09.2024

**How to cite this article:**

Tarik Kunduraci, "A Study on Impatient Pedestrian Effect on Bi-directional Pedestrian Movement by Using Ant Algorithms", El-Cezeri

Journal of Science and Engineering, Vol: 11, Iss: 3, (2024), pp.(327-337).

ORCID: "0000-0002-1854-1361.

**Abstract :** This paper aims to revisit the bidirectional walking of pedestrians to contribute to a more realistic definition of the case of the presence of impatient pedestrians and to depict the effect of including impatient walkers in the pure bi-directional system of "normal" walking pedestrians. It is found that when a trace amount of impatient pedestrians is added to the system, it affects traffic in a disruptive way at low densities, however, it affects constructively at medium and high densities interestingly. In addition, when adding a comparable amount of impatient pedestrians to the system, it is seen that at low and medium densities, the flux of motion and the order parameter change in parallel. In contrast, at high densities, the high number of impatient pedestrians positively affects lane formation, so pedestrian mobility remains high despite high density and disorder. As a result, more impatient pedestrians may not always mean more congested traffic. Sometimes, a certain density of impatient pedestrians can positively affect the bi-directional pedestrian traffic flow.

**Keywords :** Cellular Automata (CA), Computer Simulation, Bi-Directional Pedestrian Flow.

## 1 Introduction

In the literature, pedestrian dynamics have been investigated using several methods. The most frequently used ones are the social force model (SFM), continuum model (CM), and cellular automaton model (CA). The SFM is based on Newtonian mechanics and is one of the well-known microscopic simulation models for describing pedestrian dynamics [1]–[7]. The model that describes specific situations, like arching, lane formation, clogging, and the faster-is-slower effect was first introduced by Helbing. One of the social insects, as known, are ants that communicate with each other by a hormone called pheromone while they forage for food. Recently, it was shown that human travel behaviors seem to carry some similarities with those of ants [8]. So, one can use the ant communication path in the pedestrian movement in such a manner that each person will drop a "visual pheromone" to communicate with other ones [9]–[11]. As known, the pheromone dropped by an ant evaporates with time. Similarly, our visual pheromone does the same: The commonly preferred routes will be preferred again with a great probability by pedestrians as we know our daily observations. This means that the visual pheromone will be refreshed if pedestrians keep using the same routes. The non-preferred or less preferred ones will vanish due to evaporating of the visual pheromone. As an example, for this analogy, the collective behavior of other biological entities to design a safe evacuation scenario has been studied in the literature: a mathematical model is proposed based on the approach that is used to describe animal dynamics to simulate the collective traffic [12], [13].

Some ant species, for example, Pharaoh's ants drop repelling pheromone to warn others that there is no entry [14]. This keeps other forager ants away from unrewarding paths. The lane formation phenomenon in pedestrian movement includes two behavioral elements known as "following" and "avoidance" that may correspond to the visually attractive and repellent pheromones, respectively [15], [16].

In literature, a theoretical model for ant trail traffic was studied including two distinct types of ant species one of which "smells" reasonably good than the other [17]. The flux vs evaporation rate of pheromone was investigated comprehensively. In another study, the traffic on a unidirectional ant trail was investigated theoretically on the base of CA by mixing good-smelling and poor-smelling ants on the trail. In the study, ants were thought of as vehicles that travel, and TASEP (Totally Asymmetric Simple Exclusion Principle) was employed, known as Nagel-Schreckenberg Model (NaSch Model) in traffic modeling [18]. In addition, the unidirectional ant traffic flows with a U-turn in an ant trail was studied by using a one-dimensional CA model [19], [20].

All these similarities between movement rules given above have been a motivating point to examine the bi-directional pedestrian

traffic by imposing ant algorithm. A study has been done in this context where pedestrians decide to move according to the amount of visual pheromone. The movement probabilities are calculated as a function of repellent and attractive pheromones. This work is an extended version of the study performed earlier [21]. All the movement rules in this reference are valid, but in this study, all pedestrians are not identical, some of those are “impatient” and tend to move two times faster. A similar study has been done very recently, in which the Kinetic Monte Carlo method was employed [22]. In there, the bi-directional pedestrian flows with different walk speeds are studied in the CA context choosing Moore neighborhoods. Very recent studies, “the phase behaviors of counterflowing stream of pedestrians” and, “the pedestrian evacuation model of impatient queuing” have been examined, respectively [23], [24].

**2 The Model**

The system is constructed as a two-dimensional cell grid with the size of  $L \times L$ , where  $L$  defines here system size. In the work,  $L$  is taken as 50. The cells may be occupied by just one pedestrian or may be empty. All pedestrians move synchronously in a time step. If a pedestrian is an “impatient” one and if there are two empty cells in his/her neighborhood then he/she is permitted to move double cells per time step, which may be introduced as an extension of Von Neumann neighborhood<sup>1</sup>, else he/she obeys ordinary Von Neumann neighborhood rules of motion in CA (Fig.1). Moving backward is not allowed. The simulations are

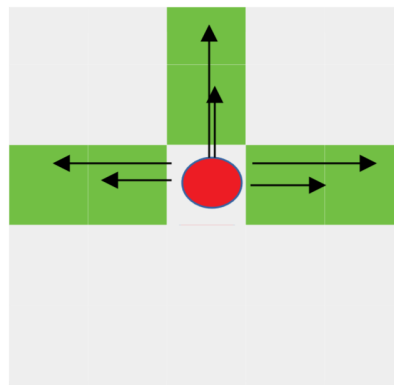


**Figure 1: An extended version of Von Neumann neighborhood for a pedestrian who is represented as a red full circle. The green cells are empty, and the pedestrian can move to them in next time step.**

performed in a square corridor, which is populated by two species of pedestrians, i.e., the top-down walkers and the bottom-up walkers who also include the “impatient” population (Fig. 2). The numbers of top-down and bottom-up walkers are set to be equal. At initial, they are randomly distributed in the corridor. The periodic boundary conditions are applied at the bottom and the top boundaries. While the top-down walkers arrive at the bottom, they continue the movement and enter the corridor from the upper boundary. When the bottom-up walkers arrive at the top boundary, they continue to move and enter the corridor from the bottom boundary. The right and left boundaries are assumed to be walls, so pedestrians are not allowed to cross; the closure boundary conditions are applied to the right and left boundaries. The colored arrows shown in Fig. 2 represent pedestrians

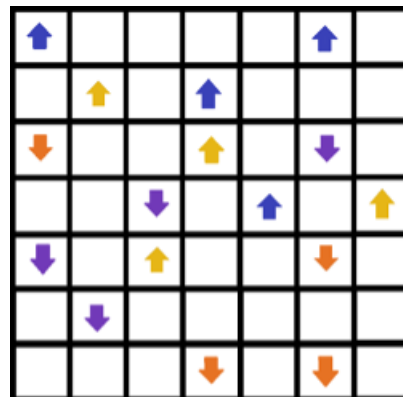
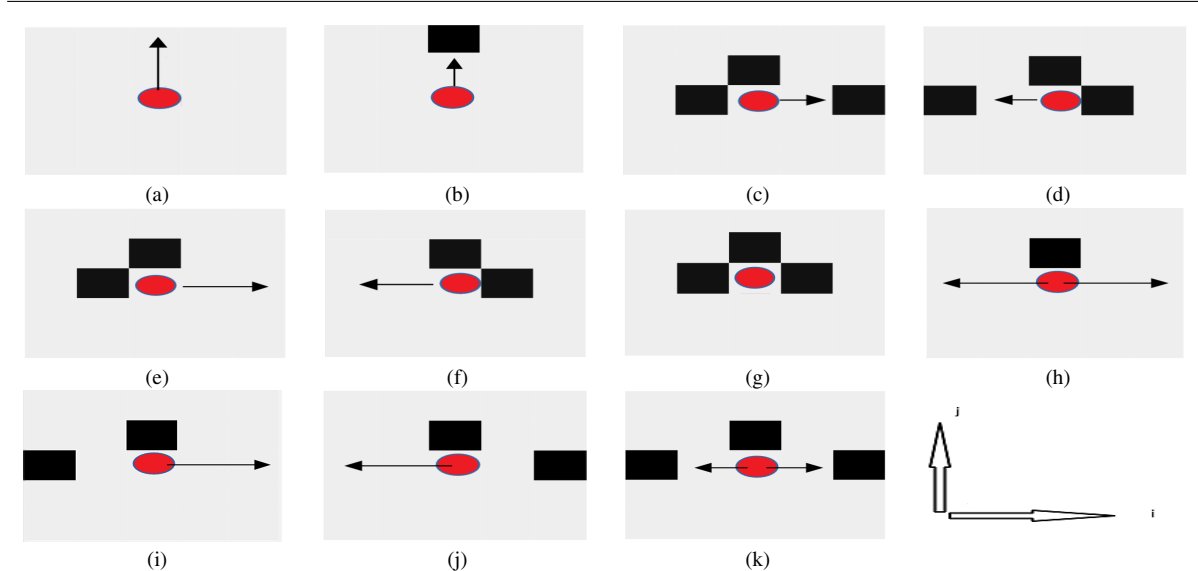


**Figure 2: A Schematic diagram to illustrate the bottom-up and top-down walkers in two opposite main directions (south-north and north-south). The different colored arrows stand to distinguish the impatient pedestrians.**

1. A discussion about the extended version of Von Neumann and Moore neighborhoods can be found in [25].

**Table 1: The bottom-up walker updating rules. The dark cells are occupied. The impatient walker prefers to move with  $v_{max} = 2$  if the neighboring two adjacent cells are empty; if not, it obeys the updating rules corresponding to the ordinary Von Neumann neighboring ( $v_{max} = 1$ ). The top-down walker updating rules, which are not presented here, are the same but the reverse movement direction must be held.**



moving in two specific directions i.e., south-north and north-south. In the south-north direction, the bottom-up walkers are represented by yellow- and blue-colored arrows, whereas in the north-south direction, the top-down walkers are represented by orange- and purple-colored arrows. Yellow arrows stand for patient bottom-up walkers while blue ones stand for impatient bottom-up walkers, conversely, orange arrows stand for top-down patient walkers while purple arrows for top-down impatient walkers. All pedestrians/walkers are assumed to drop visual pheromones according to the direction they move. The pheromone dropped from a bottom-up walker is attractive for the same kind of walker but is repellent for a top-down walker, and vice versa.

At each time step, the update of the state of the system is carried out synchronously in two stages, as follows: In the first stage, all the pedestrians are sequentially moved by imposing the rules that have been mentioned above, and the new configuration  $(W(t + 1), p(t + 1))$  is composed of the old configuration  $(W(t), p(t))$  at time  $t$ , where  $W$  and  $p$  refer to pedestrian and pheromone states, respectively. In the second stage, the pheromone is allowed to evaporate for updating of  $p(t)$ .

The updating rules are given in Table 1 for a bottom-up walking pedestrian. In the table, an impatient bottom-up walker moves to another cell according to the updating rule corresponding to the extended Von Neumann neighborhood. This updating rule is one of the updating rules of the Nagel-Schreckenberg traffic model with  $v_{max} = 2$  [18], [21]. The impatient bottom-up walker primarily prefersto move to the second neighboring cell in front (Table 1(a)), if the first and second two adjacent neighboring cells in front are simultaneously empty. Namely, a transformation, when

$$t \rightarrow t + 1; (W_{i,j}(t) = 1, W_{i+2,j}(t) = 0) \rightarrow (W_{i,j}(t + 1) = 0, W_{i+2,j}(t + 1) = 1)$$

takes place with a probability where  $i, j$  refer to the coordinates of the current cell. If a cell is empty at time  $t$ , the state of the cell is  $W_{i,j}(t) = 0$  or if occupied by a pedestrian, it is  $W_{i,j}(t) = 1$ . The bottom-up walker may also move right and left neighboring empty cells if the up-neighboring cell is occupied at time  $t$ , which means the transformation

$$(W_{i,j}(t) = 1, W_{i\pm 2,j}(t) = 0) \rightarrow (W_{i,j}(t + 1) = 0, W_{i\pm 2,j}(t + 1) = 1)$$

takes place with a probability as  $t \rightarrow t + 1$  (Table 1(h)). In cases (i) and (j), it is seen that the bottom-up walker makes the decision likely to move to the side where the two adjacent empty cells exist. If only one neighboring cell is empty as shown in cases (e) and (f) in Table 1, the walker moves to the empty cell with a probability. In (e) and (f), the second neighboring empty cell is visited with a probability if two adjacent left/right cells are empty at time  $t$ . The probability of the movement is determined fully by the visual pheromone concentration left by pedestrians in cells. The net pheromone concentration is obtained by subtracting pheromone 2 from pheromone 1, where pheromones 1 and 2 indicate attractive and repellent visual pheromones, respectively. Namely,

$$ph_{net} = ph_1 - ph_2 \tag{1}$$

For both walker types, the first pheromone i.e., pheromone 1 is attractive and pheromone 2 is repellent. That is, when investigating the movement of the bottom-up walkers, pheromone 1 belongs to the bottom-up walkers and pheromone 2 to

the top-down walkers, but when investigating the movement of the top-down walkers, pheromone 1 belongs to the top-down walkers and pheromone 2 to the bottom-up walkers. Pheromone concentrations are chosen as 0.0, 0.5, and 1.0. Thus, the net pheromone may be negative, meaning that it is not permitted to move, and if it equals 0.0 the probability to move is only 5%.

**Table 2: Movement probabilities according to the net pheromone concentration in a cell.**

$ph_{net}$	Probability to move
< 0	0.00
=0.0	0.05
+ 0.5	0.15
+ 1.0	0.80

In Table 2, all the movement probabilities are given. It seems that the most probable motion occurs when the net pheromone

**Table 3: The visual pheromone updating rules. When a cell is occupied by a pedestrian at the end of the first stage, a pheromone is leaved. If the cell is empty, the pheromone concentration will gradually decrease by 0.5 with the probability  $f$ .**

Probability of Evaporation	$W_{i,j}(t + 1)$	$p_{i,j}(t)$	$p_{i,j}(t + 1)$
–	1	1.0	1.0
$1 - f$	0	1.0	1.0
$f$	0	1.0	0.5
$1 - f$	0	0.5	0.5
$f$	0	0.5	0.0

concentration is +1.0 in a cell. When the concentration is +0.5, the probability of motion for a walker decreases to 15%. Pheromones evaporate over time, thus in a cell, the concentration of pheromone decreases with the evaporation rate  $f$  which is also a probability and  $f \in [0, 1]$ . If a cell is occupied by a pedestrian then the pheromone concentration is set to 1.0 for all types at the end of the first stage, namely if  $W_{i,j}(t + 1) = 1$  then  $p_{i,j}(t + 1) = 1.0$ . But, if the cell is empty i.e.,  $W_{i,j}(t + 1) = 0$  then the pheromone concentration decreases with the probability of evaporation. The pheromone updating rules are summarized in Table 3.

### 3 The Order Parameter and Flux and Velocity

The order parameter is a useful value that enables us to follow a system ordering degree. The evolution of a stochastic system can be followed by a few parameter sets; for example, the order parameter and the flux of the system. To calculate the order parameter, it is proposed to use, [15], [21], [26]

$$\phi_n = \left[ \frac{N_{jn}^{\uparrow} - N_{jn}^{\downarrow}}{N_{jn}^{\uparrow} + N_{jn}^{\downarrow}} \right]^2 \tag{2}$$

where  $N_{jn}^{up}$  and  $N_{jn}^{down}$  stand for the number of bottom-up and top-down walkers at the corresponding column,  $jn$  respectively. The calculation is performed over the column  $jn$ . Then the global order parameter  $\Phi$  is calculated over all pedestrians from the formula

$$\Phi = \frac{1}{N} \sum_{n=1}^N \phi_n, \tag{3}$$

where  $\phi_n$  is being individual order parameter described in Eq.(2) and  $N$  is the number of whole pedestrians.

Another parameter is the flux of the movement defined as  $\langle J \rangle = \rho \langle v \rangle$  where  $\langle v \rangle$  is the total velocity calculated over the Metropolis Monte Carlo (MMC) cycles as an average can carry important information about the phase transformation points of the bi-directional system. Also, the speed of the walkers  $v$  is known as one of the features of pedestrian traffic. Indeed, the velocity and flux for top-down and bottom-up walkers are calculated separately (without distinguishing as patient-impatient) as  $v \uparrow = N \uparrow / N$ ,  $v \downarrow = N \downarrow / N$  and  $J \uparrow$ ,  $J \downarrow$ , respectively. Then, the total velocity is calculated as

$$\langle v \rangle = (N \uparrow + N \downarrow) / N \tag{4}$$

and the total flux is calculated as

$$\langle J \rangle = (N \uparrow + N \downarrow) / L^2, \tag{5}$$

where  $\rho = N / L^2$ . In the following section, these observables are calculated as the average values over the Metropolis Monte Carlo (MMC) cycles for studying the pedestrian movement where half of the walkers are let walk from the top to the bottom and vice versa.

## 4 Results and Discussion

In this section, the results of the MMC simulations are given. In each simulation, the data is taken after  $2 \times 10^5$  MMC cycles and the system is assumed to reach equilibria in which all the mentioned observables has no longer large fluctuations. The results are given in two sections: In the first section, the bi-directional walking system is simulated so that the impatient pedestrian population number is set fairly low. In the beginning, the system consists of a pure patient pedestrian population. Then, a trace amount of the impatient pedestrian population is added increasingly at every three stages which are explained below. In the second section, simulations are performed with comparable amounts of the impatient pedestrian population. This population is added to the bi-directional walking system at two stages. In the first stage, the impatient pedestrian population size is selected as small, while the patient pedestrian population size is selected as large. Subsequently, in the second stage, these population amounts are exchanged.

### 4.1 Adding Trace Amount of the Impatient Pedestrians (ImP) to the Bi-Directional Pedestrian Movement

Firstly, it is aimed to study how pedestrian walking behavior is affected by “adding” a few “impatient” walkers labeled as ImP into both walking directions. The patient pedestrians walking at normal or average speed are labeled as PaP. If there is no ImP as a walker in the system, this state is labeled as the initial pure state of the system. In the pure state, where all pedestrians are patient (PaP), the situation is equivalent to that of in [21] except for some rules, therefore the simulation results have similar patterns.

If a certain amount of ImP is added, the system has an impure state. The inserted ImP walkers affect the system so that the observed phenomena such as “faster is slower” and “lane formation” in the initial pure state are deformed. The simulations are reperformed in each case and, the average values of observables (velocity, flux, and order parameter) are calculated over the last  $10^3$  MC cycles. In Fig. 3, the order parameter  $\Phi_0$  that changes by the density  $\rho$  and evaporation rate  $f$  is given. The subscript “0” in  $\Phi_0$  and in  $J_0$  stands for indicating the pure state where no ImP does exist.

- **Inserting ImP as 1% of patient pedestrians (PaP):** In this case, a few numbers of walkers that make 1% of PaP are inserted as “impatient walkers (ImP)” into the system to create impurity in the pedestrian walking. This is similar to “introducing impurities” in a pure crystal structure to alter the conducting properties. In an oppositely walking pedestrian system, the amount of flux may correspond to the conductivity or resistivity of a semiconductor. The order parameter here is  $\Phi_1$ , and the flux is  $J_1$ .
- **Inserting ImP as 2% of patient pedestrians (PaP):** As in the previous case, 2% of PaP is inserted as ImP into the system to simulate. The rate is now two times bigger. The 3<sup>rd</sup> row in Fig. 3, the change of the order parameter  $\Phi_2$  and flux  $J_2$  vs. the density  $\rho$  are given.
- **Inserting ImP as 4% of patient pedestrians (PaP):** In the last case, ImP is 4% of PaP. In the last row of Fig. 3, the simulation results for order parameter and flux are plotted vs. the density  $\rho$ .

It is seen from Fig. 3 that a discontinuous phase transition at  $\rho \approx 0.30$  for  $f = 0.01$  (red-colored) and for all percentage values of ImP has been clearly observed. This means that the transition does not depend on the change of the percentage of ImP, but depends on the change of  $f$ , which pertains to the motivation level to move. Moreover, the order parameters  $\Phi_k$  and fluxes  $J_k$ , ( $n = 1, 2, 4$ ) both decrease smoothly for each fixed  $f$  value smaller than 0.01, which indicates second-order phase transitions. All transitions that occur take place from the ordered phase to the disordered phase. The less  $f$  value does not always result in more flux or mobility of the pedestrians, contrarily, it is observed from the simulations that it causes congestion in the bi-directional motion. The decomposition of the order parameters is less because contributions of regular flow on the remaining lanes to the order parameter still exist. Some snapshots in Fig. 4 are given, where the colored small squares represent pedestrians moving. Results shown in Figs. (4-8) are done by averaging over the last  $10^3$  MMC simulation cycles. The orange squares are bottom-up walkers and the light brown squares are top-down walkers, as shown in (a), (c), and (e) parts of the figure, where no ImP exists. In (b), (d), and (f), ImP is added to the motion as 1% of PaP. In each case, the simulation starts at the beginning. The ImP are colored purple for bottom-up walkers and burgundy for top-down, respectively. The walls of the corridor are colored yellow and the empty squares are seen as black. The evaporation rate is taken as  $f = 0.0001$ .

The first two snapshots of Fig. 4 belong to the case that  $\rho = 0.13$  and  $N = 300$ . For the Fig. 4(a), the lanes are seen in both directions in the corridor. The total flux  $J_1$  calculated is 0.0017 and the average velocity  $v$  is 0.63 where  $\Phi_1 = 0.78$ . When 1% of  $N$  is added, the number of lanes decreases, and some small clusters appear as seen in 4(b). And flux, velocity, and order parameters both decrease to the values  $J_1 = 0.0013$ ,  $v = 0.57$ , and  $\Phi_1 = 0.57$  respectively. In 4(c) the density is  $\rho = 0.21$  and  $N = 500$  where  $J_1 = 0.0012$ ,  $v = 0.36$  and  $\Phi_1 = 0.44$ . The values surprisingly increase when  $N \rightarrow (1 + 1\%)N$  is held. The situation is shown in 4(d). The new values are  $J_1 = 0.0019$ ,  $v = 0.49$ , and  $\Phi_1 = 0.47$ , respectively. It is observed that the number of lanes doesn't change but that of clusters decreases and the size of those becomes narrower. This makes a positive contribution to the traffic flow in the system in both directions.

In the first part of the last snapshots of Fig. 4, where  $\rho = 0.39$  and  $N = 900$ , an aggregation formed by the bottom-up walkers

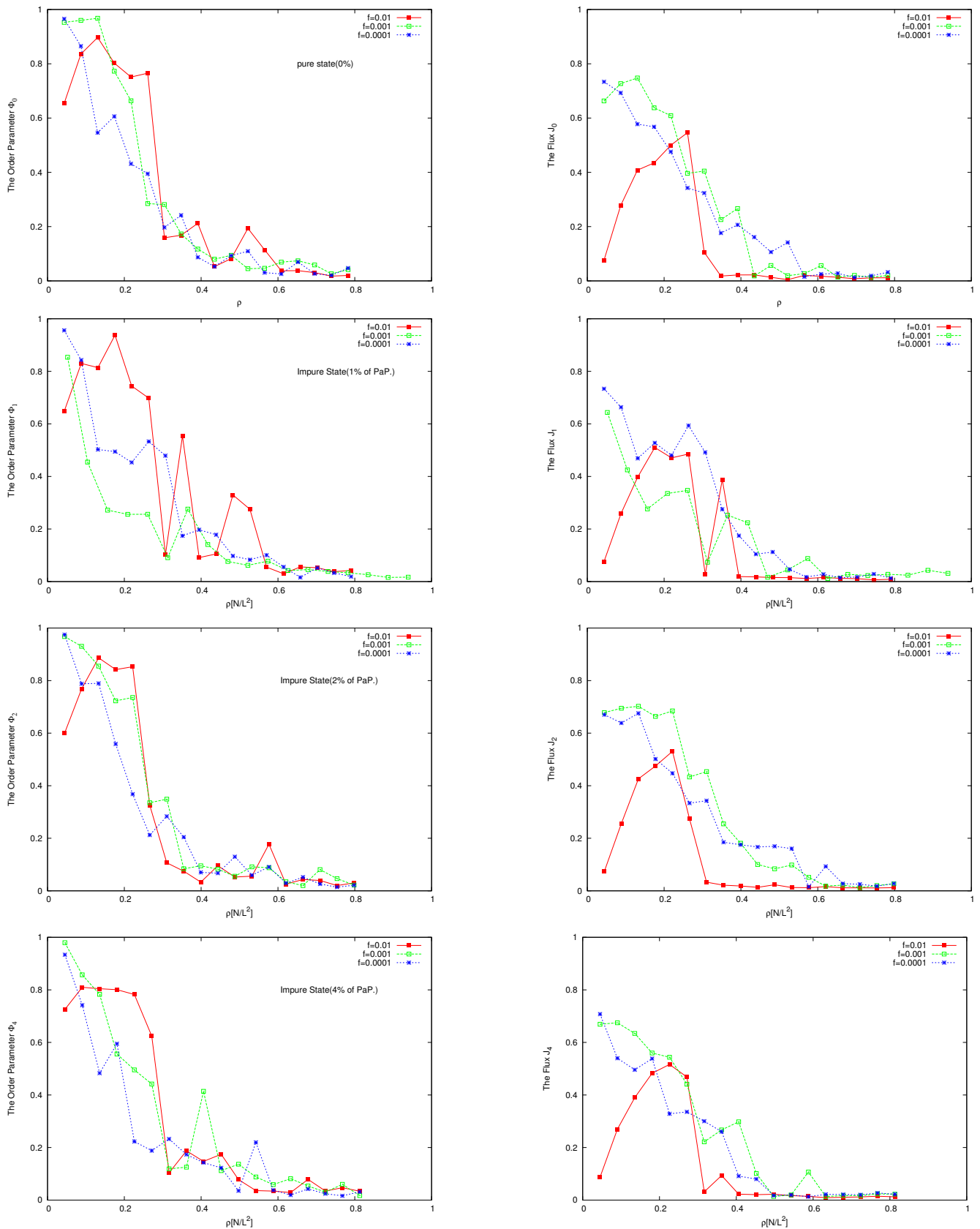
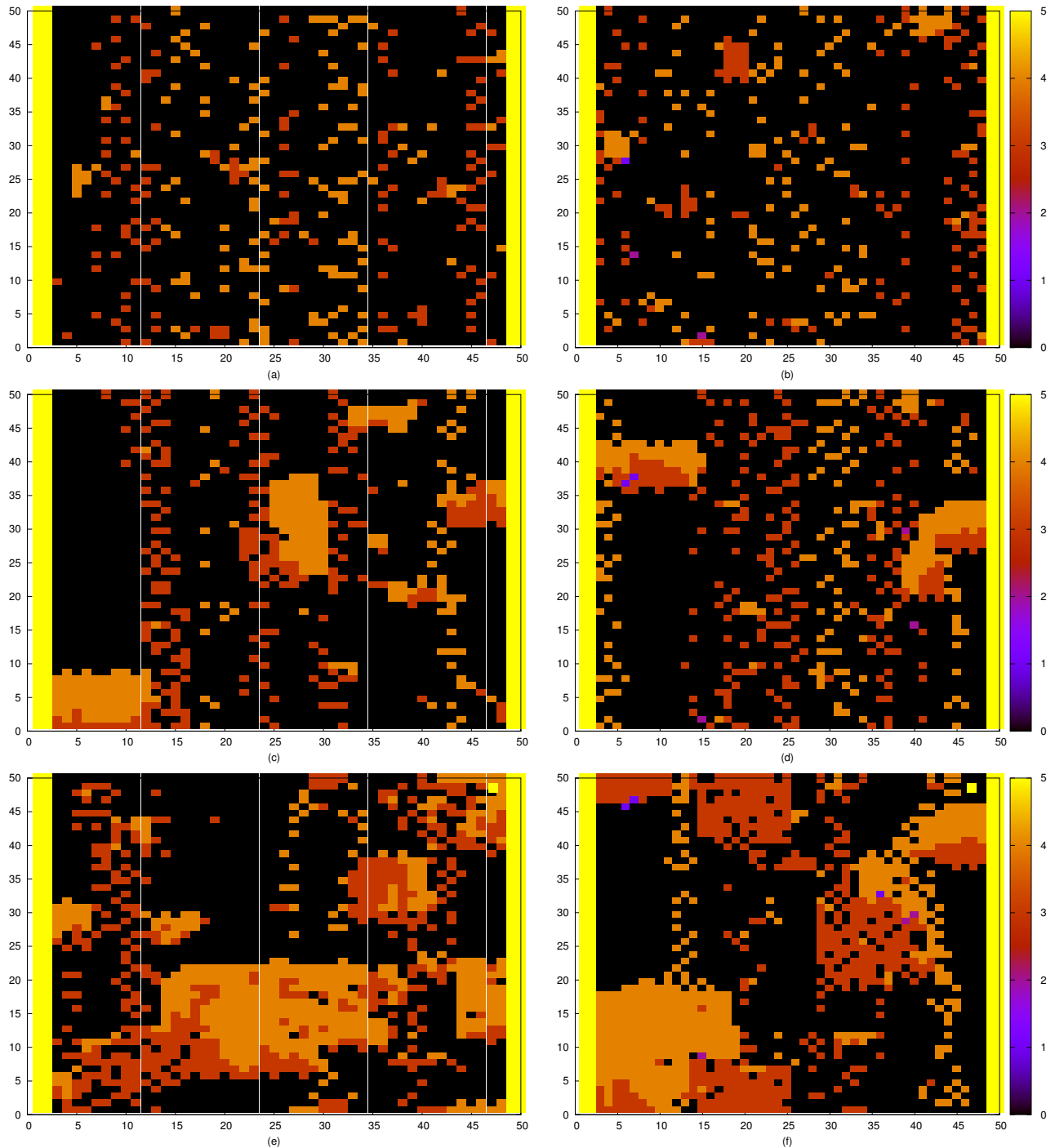
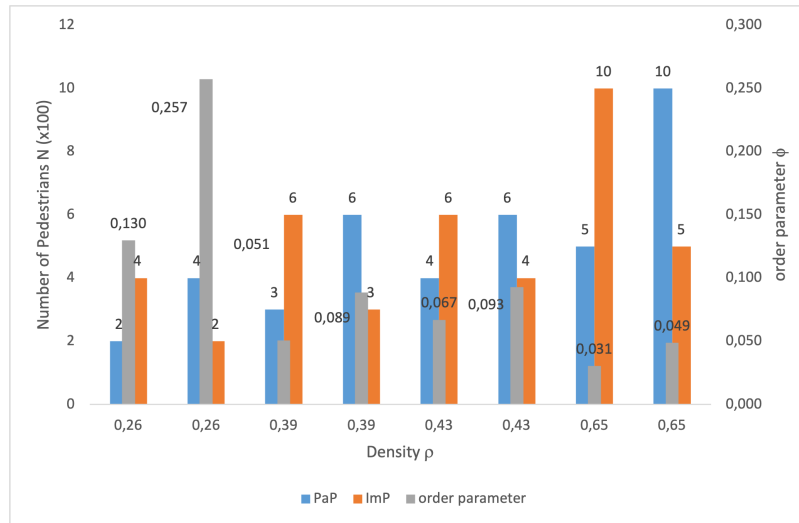


Figure 3: When the impatient walkers (ImP) are inserted into the system. The Order Parameter  $\Phi_k$  and the flux  $J_k$  vs.  $\rho$  with different  $f$  values. The subscripts indicate the percentage of ImP.



**Figure 4:** Some snapshots about the trace amount of ImP where  $f = 0.0001$  is taken. The bottom-up walkers are colored by orange and the top-down walkers by light brown. In all cases, half of the population walks oppositely:  $N/2 \uparrow, N/2 \downarrow$ .



**Figure 5: The total pedestrian number is set to  $N = 600, 900, 1000,$  and  $1500,$  respectively where  $f = 0.001$ . There are four successive bar groups illustrated for the case when a comparable amount of ImP is added.**

colored by orange is seen in the corridor. This leads to big congestion. In addition, some partially formed lanes and some cluster formations are observed. In this case, the observables are as follows: total flux is  $J_1 = 0.0012$ , the average velocity  $v = 0.27$ , and the order parameter is found as  $\Phi_1 = 0.23$ . The second part (i.e., 4(f)) includes slightly different patterns giving those observables as  $J_1 = 0.0013$ ,  $v = 0.28$ , and  $\Phi_1 = 0.35$ . As seen, there is no remarkable change in flux and velocity, but the order parameter increases fairly, most likely, due to the disappeared blockage when the transformation  $N \rightarrow (1 + 1\%)N$  holds. Similarly, at other ratios (2% and 4) the simulations give roughly the same results as understood while looking at Fig. 3. All those studies show that such a few ImP addition into a system including a large number of “normal-speeded” pedestrians (PaP) affects traffic in a disruptive way at low densities, however, it affects constructively at middle and high densities, interestingly.

#### 4.2 Adding Comparable Amount of ImP to the Pedestrian Bi-Directional Movement

Secondly, the simulation of the bi-directional motion of the walkers including comparable amounts of PaP and ImP has been studied. In this subsection, the number of total pedestrian  $N$  is selected arbitrarily as 600, 900, 1000, and 1500, respectively, and  $f = 0.001$ . There are exactly four cases for each density as shown in Fig. 5. Here, a condition is made. The condition is that the sum of the number of PaP  $N_P$  and the number of ImP  $N_I$  equals  $N$  which remains constant in each case, where  $N_P$  and  $N_I$  are chosen reciprocally unequal. In the first situation,  $N_P$  is large which means that the PaP population dominates over the ImP population ( $(N_P > N_I)$ ), and vice versa in the second: ( $(N_P < N_I)$ ). Simulations for each case aim to determine how the movement of walkers walking oppositely is affected under this population size condition. To show this situation, Fig. 5 is constructed.

In the figure, there are four successive bar groups each of which stands for distinct population size and density and are colored blue and orange. At the top of each bar,  $N_P$  and  $N_I$  are given. The order parameter values  $\Phi$ 's are given at the corresponding grey narrower bars. For example, for  $\rho = 0.26$ , there are two bar groups colored. The blue bar in the first group indicates the number of PaP as  $N_P = 200$  and the orange bar indicates the number of ImP as  $N_I = 400$ . In the second group, the blue bar indicates again the number of PaP but as  $N_P = 400$ , and the orange one indicates again the number of ImP but this time as  $N_I = 200$ . It seems that the order parameter  $\Phi$  takes 0.130 at first and increases then to  $\Phi = 0.257$  as the values  $N_P$  and  $N_I$  are exchanged.

The same procedure is valid for other cases as well. The second case is for  $\rho = 0.39$  where  $N = 900$ . In this case,  $N_P = 300$  and  $N_I = 600$  and the corresponding order parameter equals 0.051. The order parameter takes the value  $\Phi = 0.089$  when the values of  $N_P$  and  $N_I$  are exchanged and take values 600 and 300. In the third and fourth cases, as in the previous two cases, it was observed that the order parameter gets higher values when  $N_P < N_I \rightarrow N_P > N_I$  holds. That is when the population of ImP is low relative to that of PaP or, in other words, the population of PaP is high concerning that of ImP, the order parameter has been found to take high values. This means that a large population of ImP leads to a less ordered system than a system that dominates with PaP.

The same procedure is valid for other cases as well. The second case is for  $\rho = 0.39$  where  $N = 900$ . In this case,  $N_P = 300$  and  $N_I = 600$  and the corresponding order parameter equals 0.051. The order parameter takes the value  $\Phi = 0.089$  when the values of  $N_P$  and  $N_I$  are exchanged and take values 600 and 300. In the third and fourth cases, as in the previous two cases, it was observed that the order parameter gets higher values when  $N_P < N_I \rightarrow N_P > N_I$  holds. That is when the population of ImP is

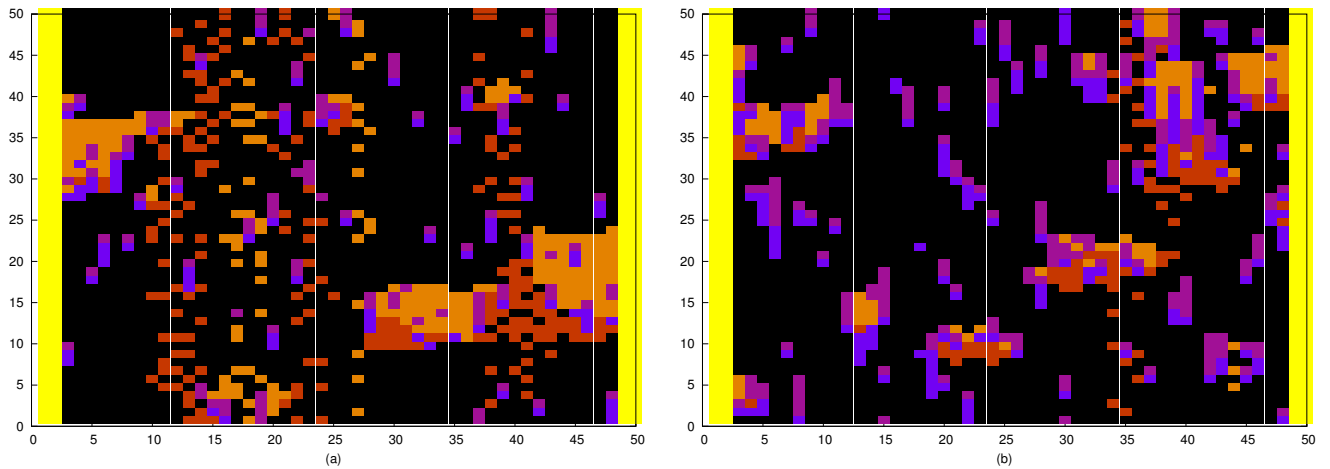


**Figure 6: The snapshots of the simulation of bottom-up and top-down walkers at a square corridor with  $L = 50$ . Here,  $N = N_p + N_t = 600$ ,  $\rho = 0.26$ , and  $f$  is 0.001. In all cases, half of walkers walk oppositely:  $N/2 \uparrow, N/2 \downarrow$ . The ImP part of bottom-up walkers are colored by purple while the PaP part of those are colored by orange, however, the ImP part of top-down walkers are colored by burgundy while PaP part of those are colored by light brown.**

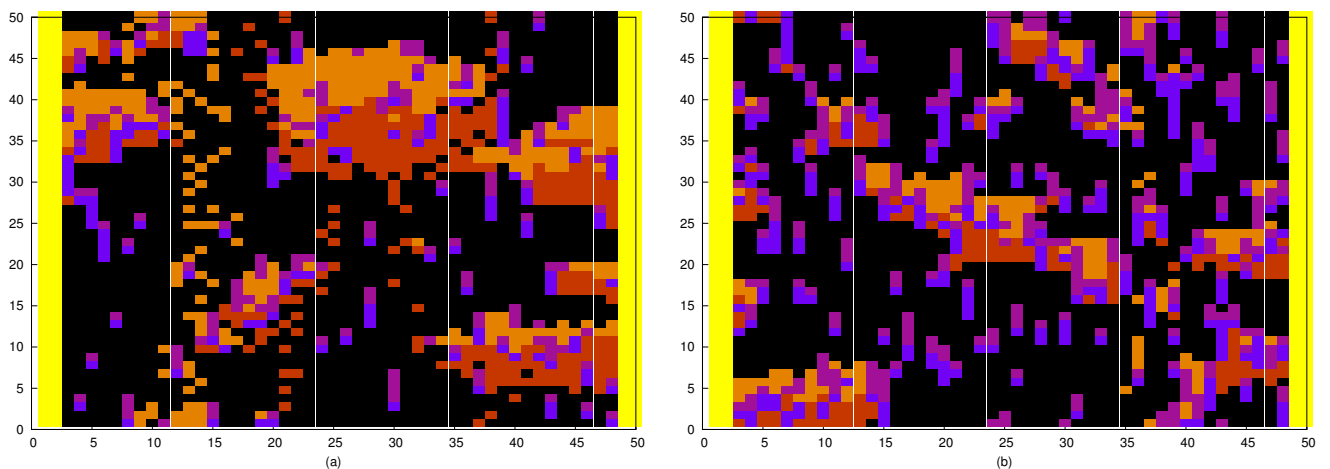


**Figure 7: Another snapshot of the simulation of bottom-up and top-down walkers at a square corridor with  $L = 50$ . Here,  $N = N_p + N_t = 900$ ,  $\rho = 0.39$  and  $f = 0.001$ . In all cases, half of the populations walk oppositely:  $N/2 \uparrow, N/2 \downarrow$ . The colorizing rules are also the same as in Fig. 6.**

low relative to that of PaP or, in other words, the population of PaP is high concerning that of ImP, the order parameter has been found to take high values. This means that a large population of ImP leads to a less ordered system than a system that dominates with PaP. The first snapshots of the simulation of this movement are given in Fig. 6. Here, results are done by averaging over the last  $10^3$  MC simulation cycles as mentioned before. The ImP part of the bottom-up walkers is colored purple while the PaP part of those is colored orange, however, the ImP part of the top-down walkers is colored burgundy while the PaP part of those is colored light brown. In the figure, the total pedestrian number is set to  $N = 600$  thus, the density of pedestrians equals 0.26 and  $f = 0.001$ . In the first case (a), where the number of PaP is taken as  $N_p = 400$  and the number of ImP  $N_t = 200$ , the lanes built by the bottom-up and top-down part of PaP are clearly seen, where  $\Phi = 0.257$  and flux is  $J = 0.275$ . In (b), where  $N_p \leftrightarrow N_t$  exchange is made, both  $\Phi$  and  $J$  get lower values and local clusters emerge in some parts of the corridor:  $\Phi = 0.129$  and flux is  $J = 0.071$ . In Fig. 7, snapshots of MC simulation of the bottom-up and the top-down walkers at a square corridor are given. The deformations of the lane formations are seen. In (a),  $N_p > N_t$  and  $\Phi = 0.089$ , lanes produced by PaP for both walker types colored light brown and orange are observed. And also, some small full lanes consisting of ImP that intercept mutually each other's walk are seen. Here, the flux of the movement is computed as  $J = 0.150$ . In (b), on the contrary,  $N_p < N_t$  and  $\Phi = 0.051$ , lower than the previous case. The lanes produced by PaP disappear but small ones remain, which give rise to a crowd at about the center of the corridor. The flux computed is  $J = 0.036$ , which is significantly lower. The snapshots for  $\rho = 0.43$  and  $N = 1000$  are given in Fig. 8. In 8(a), lane formations are almost gone relative to Figs. 6 and 7, but a few remain, and a big

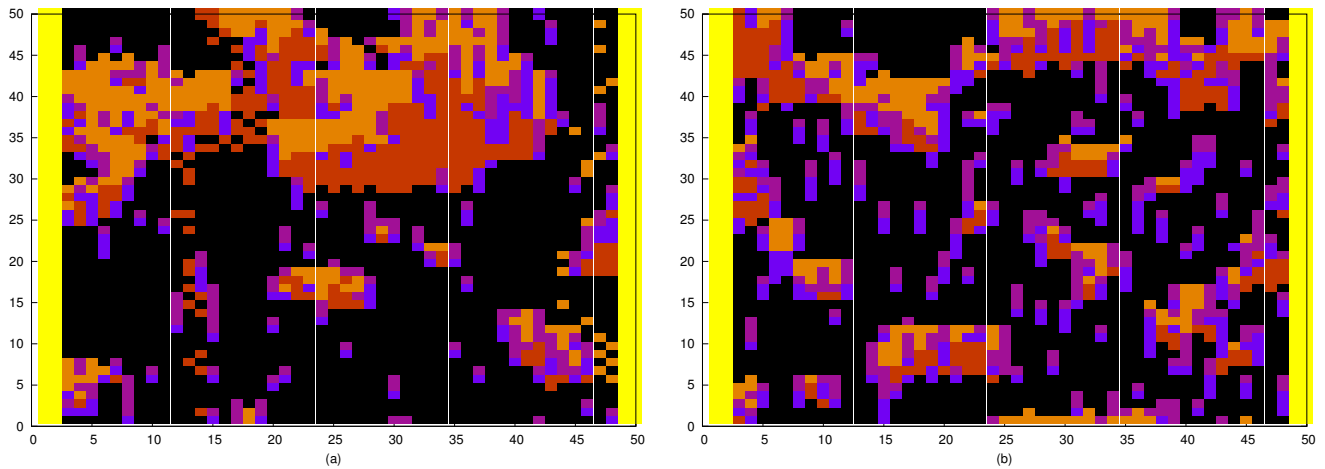


**Figure 8:** Other snapshots of the simulation of bottom-up and top-down walkers at a square corridor with  $L = 50$ . Here,  $N = N_P + N_I = 1000$ ,  $\rho = 0.43$  and  $f$  is the same. The colorizing rules are also the same as in Fig. 6. In all cases, half of the populations walk oppositely:  $N/2 \uparrow, N/2 \downarrow$ .

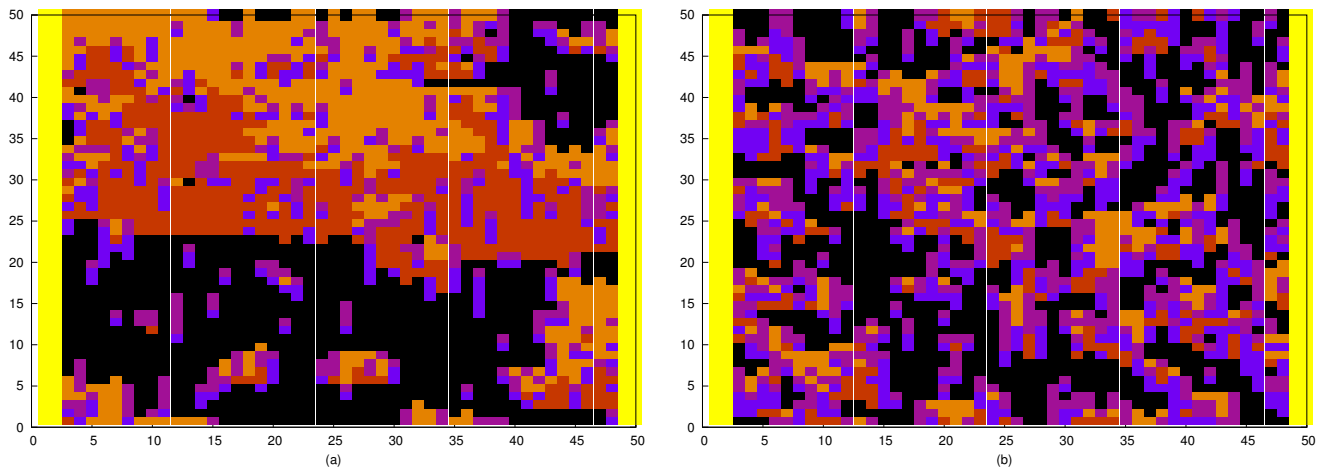


**Figure 9:** The last snapshots of the simulation of bottom-up and top-down walkers at a square corridor with  $L = 50$ . Here,  $N = N_P + N_I = 1500$ ,  $\rho = 0.65$  and  $f$  is the same. The colorizing rules are also the same as in Fig. 6. In all cases, half of the populations walk oppositely:  $N/2 \uparrow, N/2 \downarrow$ .

cluster caused by PaP is seen on the north side of the corridor. The ImP are seen as responsible for this cluster because they force the PaP to come together. In 8(b), after the exchange of pedestrian numbers, it is seen that the cluster becomes narrower and spreads out due to the existence of more ImPs who block mutually each other. The last snapshots of the bi-directional walkers’ simulation are given in Fig. 9, where the total number of pedestrians is the largest:  $N = 1500$ . The density  $\rho$  is 0.65 and the average speed of walkers along the corridor, unlike the previous ones, almost vanishes. In the first case (a), the number of PaP is larger than that of ImP:  $N_P = 1000, N_I = 500$ . A crowd, causing congestion is obviously observed along the north side of the corridor, produced by the top-down and the bottom-up walkers of PaP. Also, the walkers of ImP block themselves oppositely along the corridor. All these together point out a jammed phase. In case (b), surprisingly, the crowd disappears and clusters produced by burgundy and purple walkers remain, who are impatient. Another conclusion is that, although the system order decreases ( $\Phi : 0.049 \rightarrow 0.030$ ) by taking large number of ImP, the flux increases ( $J : 0.013 \rightarrow 0.029$ ). This happens probably due to the termination of the huge cluster appeared in (a) after exchanging pedestrian numbers of PaP and ImP. This leads to relatively high pedestrian mobility alongside the corridor which means that after the exchange of numbers, an increase in the mobility (emerging in the flux) is due to the new lane formations made by the ImP.

### 5 Conclusion

This work aims to study the effect of the “modified” agents on the bi-directional walking system in general when the interacting item is a “visual pheromone” that is assumed as the communication tool between humans [8]–[11]. The Metropolis Monte

Carlo (MMC) simulation method with  $v_{max} = 2$  as hopping speed is performed. The modified Von Neumann neighborhood is preferred. In this study, the modified agents are considered impatient pedestrians beside the patient pedestrians in the walking system. It is found that when a trace amount of impatient pedestrians are added to the system, some remarkable differences in fundamental patterns of pedestrian traffic have been observed with the help of the general observables such as flux and order parameters. In particular, a few ImP additions into a system including a large number of “normal speeded” pedestrian (PaP) affects traffic in a disruptive way at low densities. However, it affects constructively at middle and high densities interestingly. As an ambulance helps manage vehicle traffic in congested areas, some people in pedestrian traffic can play a constructive role in reordering the walking path.

When adding a comparable amount of impatient pedestrians to the bi-directional walking system it is seen that at low and middle densities, the flux of motion and the order parameter change in parallel. They both decrease while exchanging the number of patient and impatient pedestrians, i.e., while the transformation  $N_P > N_I \rightarrow N_P < N_I$  is carried out under the same density. On the other hand, in the case of high densities, the situation is different. Under the above transformation, the flux and the order parameter do not change in parallel but flux increases while the order parameter decreases. The reason for this is that the high number of ImP positively affects lane formation, therefore, pedestrian mobility remains high despite high density and disorder.

### Acknowledgments

The authors greatly thank Dr. Coskun Deniz for their support in conducting the characterization.

### Authors' Contributions

In this study, TK created the idea, designed the structure, evaluated the characterized results, performed a literature review, produced the samples, completed experimental works, wrote up the article.

### Competing Interests

The authors declare that they have no conflict of interest.

### References

- [1] Molnar P. Helbing D. Social force model for pedestrian dynamics. *Phys. Rev. E*, 51:4282, 1995.
- [2] Vicsek T. Helbing D., Farkas I. Simulating dynamical features of escape panic. *Nature*, 407, 2000.
- [3] Moldovan H. Parisi D. R., Gilman M. A modification of the Social Force Model can reproduce experimental data of pedestrian flows in normal conditions. *Physica A*, 388:3600, 2009.
- [4] Chao G. Xiaoping Z., Wei L. Simulation of evacuation processes in a square with a partition wall using a cellular automaton model for pedestrian dynamics. *Physica A*, 389:2177, 2010.
- [5] Löhner R. On the modeling of pedestrian motion. *Applied Mathematical Modelling*, 34:366, 2010.
- [6] Schadschneider A. Chraïbi M., Seyfried A. Generalized centrifugal-force model for pedestrian dynamics. *Phys. Rev. E*, 82:046111, 2010.
- [7] Schadschneider A. Seyfried A. Chraïbi M., Wagoum U.K. Force-based models of pedestrian dynamics. *Networks and Heterogeneous Media*, 692:425, 2011.
- [8] Nishinari K. Schadschneider A., Kirchner A. From Ant Trails to Pedestrian Dynamics. *Applied Bionics and Biomechanics*, 1(11), 2003.
- [9] Nishinari K. Schadschneider A. Chowdhury D., Guttal V. A cellular-automata model of flow in ant trails: non-monotonic variation of speed with density. *J.Phys. A*, 35:573, 2002.
- [10] Schadschneider A. Nishinari K., Chowdhury D. Cluster formation and anomalous fundamental diagram in an ant-trail model. *Phys. Rev. E*, 67:036120, 2003.
- [11] Chowdhury D. Nishinari K. John A., Schadschneider A. Collective effects in traffic on bi-directional ant trails. *Journal of Theoretical Biology*, 231:279, 2004.
- [12] Rose G. Burd M. Shiwakoti N., Sarvi M. Enhancing the Safety of Pedestrians during Emergency Egress: Can We Learn from Biological Entities? *Transportation Research Record*, page 2137, 2002.
- [13] Rose G. Burd M. Shiwakoti N., Sarvi M. Biologically Inspired Modeling Approach for Collective Pedestrian Dynamics under Emergency Conditions. *Transportation Research Record*, 2196:176, 2010.
- [14] Francis L. W. R. Duncan E. J. Communication in ants. *Current Biology*, 16:570, 2006.
- [15] Schadschneider A. Nowak S. Quantitative analysis of pedestrian counterflow in a cellular automaton model. *Phys. Rev. E*, 85:066128, 2012.
- [16] Nishinari K. Suma Y., Yanagisawa D. Pedestrian dynamics: Modeling and experiment. *Physica A*, 391:248, 2012.
- [17] Kayacan O. A theoretical model for uni-directional ant trails. *Physica A*, 390:1111, 2011.
- [18] Kayacan O. Kunduraci T. A Monte Carlo study of ant traffic in a uni-directional trail. *Physica A*, 392:1946, 2013.
- [19] Kayacan O. Kunduraci T. Uni-directional trail sharing by two species of ants a Monte Carlo study. *J. Stat. Mech.*, page P06038, 2015.
- [20] Kayacan O. Gökçe S. A cellular automata model for ant trails. *Pramana*, 80:909, 2013.
- [21] Kayacan O. Gökçe S. Study on bi-directional pedestrian movement using ant algorithms. *Chinese Phys. B*, 25:010508, 2016.
- [22] Sun Y. Kinetic Monte Carlo simulations of bi-direction pedestrian flow with different walk speeds. *Physica A*, 549:124295, 2020.
- [23] Hao Q. Y. et al. Phase behaviors of counterflowing stream of pedestrians with site-exchange in local vision and environment. *Physica A*, page 125688, 2021.
- [24] You L. et al. A study of pedestrian evacuation model of impatient queueing with cellular automata. *Phys. Scr.*, 95:095211, 2020.
- [25] Kretz T. Pedestrian Traffic, Simulation and Experiments, 2007. PhD. thesis.
- [26] Löwen H. Rex M. Lane formation in oppositely charged colloids driven by an electric field: Chaining and two-dimensional crystallization. *Phys. Rev. E*, 75:051402, 2007.